Vertex Based Missing Mass Calculator for 3-prong Hadronically Decaying Tau Leptons in the ATLAS Detector

Harvey Maddocks

MPhys

Lancaster University

Physics

Department of Physics

Lancaster University

September 2014

1. Reviewer: Name

2. Reviewer:

Day of the defense:

Signature from head of PhD committee:

Abstract

In this thesis my personal contributions to the ATLAS experiment are presented, these consist of studies and analyses relating to tau leptons.

The first main section contains work on the identification of hadronically decaying tau leptons, and my specific contribution the electron veto. This work involved improving the choice of variables to discriminate against electrons that had been incorrectly identified as tau leptons. These variables were optimised to be robust against increasing pile-up, which is present in this data period. The resulting efficiencies are independent of this pile-up.

The second main section contains an analysis of $Z \rightarrow \tau\tau$ decays, my specific contribution was the calculation of the detector acceptance factors and systematics.

The third, and final section contains an analysis of the performance of a new vertex based missing mass calculator for 3-prong hadronically decaying tau leptons. It was found that in its current state it performs just as well as the existing methods. However it has a much greater scope for improvement with the introduction of the Insertable B-Layer in the ATLAS detector that will dramatically increase the ability to track and vertex particles.

Dedicated to Camila and to my family.

Acknowledgements

Declaration

This thesis is my own work and no portion of the work referred to in this thesis has been submitted in support of an application for another degree or qualification at this or any other institute of learning.

Contents

List of Figures

List of Tables

Chapter 1

Introduction

This thesis is about the Standard Model (SM) Higgs boson and its decay into a pair of τ leptons, specifically those that then decay hadronically. The data used here were collected with the ATLAS detector at the Large Hadron Collider (LHC) located at CERN.

The Higgs boson arises as a consequence of spontaneous electroweak symmetry breaking, and when introduced to the SM it gives masses to the massive fundamental particles and ensures the internal consistency of the SM. This particle has been for a long time the missing link of the SM, which, despite this passed many tests successfully, including the correct predictions of the W and Z boson masses. It was with great joy to all those involved that in 2012, the Higgs boson was discovered at the LHC in decays into vector boson pairs. Subsequent analysis of this particle has shown that it is in agreement with the predictions made by the Standard Model. The work presented in this thesis focuses on $H \rightarrow \tau\tau$, specifically where the tau leptons decay hadronically. This is an interesting point of research because it is one of the most sensitive channels for the Higgs to couple directly to fermions.

Chapter 2 gives an overview of some of the theoretical foundations which underpin the analysis and physics for the Higgs boson searches. Chapter 3 describes the LHC accelerator complex and the ATLAS detector, including some of the peripheral systems. Chapter 4 discusses how the hadronically decaying τ leptons are reconstructed and identified. Chapter 5 overviews a study on the reconstruction

of $Z \to \tau\tau$. The final chapter 6 details an analysis focusing on the development of an improved method for determining the vertices of hadronically decaying τ leptons. There are some very valid reasons for wanting to study this specific channel, hadronically decaying τ leptons have a very high signal acceptance which arises from the larger branching ratio and the higher invariant mass resolution. This last point is because there are only two neutrinos involved in the final state. However, this channel has a very high background from QCD jet production, which can be easy to miss identify as hadronically decaying τ leptons. One method to reduce this background is to search specifically for the Higgs boson with the Vector Boson Fusion (VBF) production method, this means that two highly energetic jets are produced in line with the proton beam direction. Or, alternatively, to search for $\tau\tau$ pairs that have a high transverse momentum, to target the Higgs produced via the gluon-gluon fusion. This makes identification and background rejection easier.

The personal contributions of the author are the electron veto in chapter 4. Which consisted of creating a new list of variables to better discriminate against misidentified tau leptons[1]. In chapter 5 I calculated the fiducial acceptance for the $Z \to \tau\tau$ decay channel [2]. Finally in chapter 6 I participated in the development of the algorithm used to try and better improve the calculation of the missing mass of hadronically decaying 3-pronged tau leptons. The fourth body of work which is not mentioned in this thesis, was a dedicated argument parser for the ATLAS job transforms software, detailed here [3]. This piece of work was purely software based and not well suited for inclusion into this thesis, nonetheless it was still a significant amount of work that was undertaken, and contributed to the experiment as a whole. This work allowed the author to obtain their ATLAS authorship qualification, allowing them to be included on ATLAS public papers. The chronology of this thesis is as follows, the contents of chapter 5 were performed in 2011. Inbetween the work in chapter 5 and chapter 4 the author attained his ATLAS authorship qualification that was previously mentioned. The contents in chapter 4 were performed in 2012 and chapter 6 was performed from the Winter of 2012 thereafter.

Chapter 2

The Standard Model of Particle Physics and the Higgs Boson

2.1 General Overview of the Standard Model of Particle Physics

According to our current understanding of the universe, all of the building blocks of matter and their interaction through the fundamental forces can be described by the Standard Model of Particle Physics (SM). This model is an agglomeration of knowledge and theories that describe the strong, weak and electromagnetic interactions. It has been vigorously tested and has been found to agree exceptionally well with results of numerous experiments.

In the SM all interactions are mediated by exchange of particles, known as force carriers, these force carriers follow the Bose-Einstein Statistics. Matter is described in terms of fermions, particles that follow the Fermi-Dirac statistics. The fundamental particles are: three families of leptons and quarks, force carriers and the Higgs boson. The full list of these particles and some of their properties is shown in figure 2.1. Bosons are mediators of the fundamental forces in physics, specifically the strong, electromagnetic and weak forces. Each one of these forces has its own boson:

Figure 2.1: The Standard Model, showing the elementary particles, with some of the particles' properties: mass, charge, colour and spin. The particles that interact through the strong nuclear, electromagnetic and weak forces are shown. The graviton, the mediator of the gravitational force is also shown, even though it is not part of the Standard Model [4].

- The electromagnetic interaction is mediated by the photon, γ, a massless particle with no electrical charge,

- The strong interaction holds quarks together to form baryons (protons, neutrons etc.) and mesons (pions and kaons etc.), is mediated by gluons, g. Gluons are massless, have no electrical charge and have *colour charge* (or *anticolour charge*), referred to as, *red, blue* or *green* (*antired, antiblue* or *antigreen*),

- The weak interaction, which is responsible for some nuclear decays e.g. β decay, is mediated by the massive charged $W^\pm$ and the neutral Z bosons,

- The gravitational interaction is by far the weakest of all the fundamental forces (inside of the Planck scale 10^{19} GeV) and is not included in the SM.

Fermions (quarks and leptons) are separated into three generations of identical structure, aside from the particle mass. Amongst the charged leptons, the electron, e, is the lightest followed by the muon, μ and the tau τ. Whilst the electron is stable, the muon and the tau leptons are both unstable and decay spontaneously (with decay times of 2.2 μs and $2.9 \times 10^{-7} \mu s$ respectively). They are all sensitive to the weak and electromagnetic interactions, have integer electrical charge and are paired with a neutral lepton of the same *flavour* called a neutrino (ν_e, ν_μ and ν_τ). The quarks have a fractional electric charge of $+2/3e$ (u, c and t) or $-1/3e$ (d, s and b), they also have a colour charge which is necessary for their strong interaction which binds them together to form colourless particles, baryons or mesons. Quarks are also affected by the weak and electromagnetic interaction, however both of these are considerably less strong than the strong force so aren't usually taken into consideration.

The SM is a quantum field theory that is built from the principle that physics must be invariant under local symmetry transformation (referred to as gauge symmetry), it provides a framework in which to describe the electromagnetic, weak and strong interactions based on a combination of local gauge symmetry groups: $SU(2)_I \otimes U(1)_Y \otimes SU(3)_C$. The conserved quantities in this case are I, the weak isospin, Y the weak hyper-charge and C colour.

In the 1960s Glashow, Salam and Weinberg proposed a theory that describes the

interaction between quarks and leptons, thus combining the electromagnetic and weak interaction into one, the Electroweak Force [5, 6, 7]. The Electroweak (EW) theory is based on the gauge symmetry group $SU(2)_I \otimes U(1)_Y$ and postulates four massless mediating bosons, of which three belong to the non-abelian group $SU(2)$, and the fourth, is an isoscalar ($I = 0$) and belongs to the abelian group $U(1)$ of weak hypercharge.

Additionally to the matter and force mediating particles described above, a scalar $SU(2)$ doublet is introduced into the SM, this generates a spontaneous breaking of the Electroweak symmetry. This mechanism allows three of the gauge bosons to acquire mass, the remaining scalar field from this is called the Higgs field. Before the discovery in 2012, the mass of the boson associated with this field was the only unknown parameter of the theory.

Quantum Chromodynamics (QCD) is a theory based on the gauge symmetry group $SU(3)_C$, it describes the strong interaction between the quarks. The gauge bosons which mediate the interaction carry a colour and an anti-colour and belong to an octet of the symmetry group $SU(3)_C$.

2.2 Gauge Symmetries in Quantum Electrodynamics

Quantum Electrodynamics (QED) is a quantum field theory that is based on a local gauge symmetry. The QED symmetry group is the abelian $U(1)$, a gauge transformation is defined by applying an arbitrary phase to the state function of the system (a $U(1)$ transformation), in the following way:

$$\psi(x) \rightarrow e^{i\phi(x)}\psi(x) \tag{2.1}$$

where ψ is a Dirac spinor. The transformation is local due to the dependency of ϕ on the space time coordinate. The Lagrangian that describes a Dirac fermion

with spin 1/2 and mass, m, is:

$$\mathcal{L}_{Dirac} = \bar{\psi}(i\gamma_\mu\partial^\mu - m)\psi \tag{2.2}$$

where γ_μ are the Dirac matrices. The Lagrangian is invariant under a $U(1)$ transformation like that in equation 2.1, only if the phase, ϕ, is an arbitrary real constant. However, considering that this is not the case, and that the transformation $U(1)$ is local, equation 2.1 does not remain invariant under the transformation:

$$\partial^\mu\psi \rightarrow e^{i\phi(x)}(\partial_\mu + ie\partial_\mu)\psi \tag{2.3}$$

In order for the gauge invariance to be restored under the local $U(1)$ transformation a new vector field, A_μ, is introduced, this transforms in the following way:

$$A_\mu(x) \rightarrow A'_\mu(x) = A_\mu(x) + \frac{1}{e}\partial_\mu\phi \tag{2.4}$$

A covariant derivative is defined as:

$$D_\mu = \partial_\mu - ieA_\mu \tag{2.5}$$

This transforms in a way that is similar to that of the field itself:

$$D_\mu\psi \rightarrow D'_\mu\psi = e^{i\phi}D_\mu\psi \tag{2.6}$$

The Lagrangian for a vector field A^μ, associated with a particle with spin 1, is:

$$\mathcal{L} = -\frac{1}{4}F^{\nu\mu} + \frac{1}{2}m_A^2 A^\mu A_\mu \tag{2.7}$$

where $F^{\nu\mu} = \partial^\mu A^\mu - \partial^\nu A^\nu$, is the fields kinetic term. The first term of the Lagrangian is invariant under a local $U(1)$ transformation, conversely the second term is not. This means that the vector field has to be be massless ($m_A = 0$), to keep the local gauge invariance. After introducing the vector field, the resultant

Lagrangian is one that represents Quantum Electrodynamics:

$$\mathcal{L}_{QED} = \bar{\psi}(i\gamma_\mu \partial^\mu - m)\psi + e\bar{\psi}\gamma^\mu \psi A_\mu - \frac{1}{4}F^{\nu\mu}F_{\mu\nu} \tag{2.8}$$

The vector field A_μ represents the photon field, the Lagrangian describes the interactions between Dirac (fermions) fields and the photon field.

2.3 The Basics of Quantum Chromodynamics

The strong nuclear interaction is based on the $SU(3)_C$ symmetry group, this describes the quark colours (of which there are three, and their associated anticolours). The gauge fields $G^a_{\mu\nu}$ correspond to the 8 generators, T_a, with all the possible combinations of colour (and anti-colour), these combinations are identified as gluons. The gluon gauge fields have self-couplings this means that they are able to interact with themselves.
The Lagrangian for QCD is:

$$\mathcal{L}_{QCD} = \sum \bar{\psi}_{q,j}(i\gamma^\mu(D_\mu))_{j,k} - m_q\delta_{j,k})\psi_{q,k} - \frac{1}{4}G^a_{\mu\nu}G^{a\mu\nu} \tag{2.9}$$

where $\psi_{q,j}$, is the quark field for flavour, q carrying a colour, j. The covariant derivative D_μ and the gluon field strength tensor $G^a_{\mu\nu}$ are defined as:

$$D_{\mu\nu} = \partial_\mu + ig_s T^a A^a_\mu \tag{2.10}$$

$$G^a_{\mu\nu} = \partial_\mu A^a_\nu - \partial_\nu A^a_\mu - g_s f^{abc}A^b_\mu A^c_\nu \tag{2.11}$$

where A^a_ν are the gluon fields with index a, where a=1,2 .. 8. The generators of the SU(3) group are the Gell-Mann matrices T_a, which satisfy the algebra $[T^a, T^b] = if^{abc}T^c$, where f^{abc} are the group structure constants. $g_s = \sqrt{4\pi\alpha_s}$, where α_s is the strong coupling constant.
The properties of QCD are often considered strange, specifically the principles of asymptotic freedom and confinement. The former can be described as when

quarks and gluons behave as quasi-free particles at high energies or at short distances. The latter is when the same particles are at low energies or at large distance, in these conditions they are confined into hadrons.

2.4 Electroweak Theory and the Higgs Mechanism

2.4.1 Electroweak Theory

The combined theory of electromagnetism and the weak nuclear force, known as Electroweak (EW) theory, is based on the gauge symmetry group $SU(2)_I \otimes U(1)_Y$. As was previously stated, the $SU(2)_I$ group has the weak isospin (I) as its conserved quantity and the $U(1)_Y$ group has the weak hypercharge (Y) as its conserved quantity. These conserved quantities are connected to the non-conserved quantity, electric charge (Q) by:

$$Q = I_3 + \frac{Y}{2} \qquad (2.12)$$

where I_3 is the third component of the weak isospin.

EW theory is constructed under the principle of gauge invariance, in a similar fashion as described for QED in section 2.2. There is only one gauge field that is associated to the $U(1)_Y$ symmetry, B_μ and three fields associated to the $SU(2)_I$ group, W_μ^i. These W_μ^i fields only couple to the left-handed component of the fermion fields, the B_μ gauge field couples to both left and right-handed components, ψ_L and ψ_R.

The EW Lagrangian has to be invariant, this is ensured by introducing the derivatives $D_{\mu L}$ and $D_{\mu R}$. These are defined as follows:

$$D_{\mu L}\psi_L = (\partial_\mu + ig\frac{\sigma_i}{2}W_\mu^i + ig'\frac{Y_L}{2}B_\mu)\psi_L \qquad (2.13)$$

$$D_{\mu R}\psi_R = (\partial_\mu + ig'\frac{Y_R}{2}B_\mu)\psi_R \qquad (2.14)$$

where g and g' are the coupling constants of $SU(2)_I$ and $U(1)_Y$ respectively. σ_i are the Pauli matrices, and Y_L and Y_R are the weak hypercharges for the left and right-handed components of the fermion fields.

From this we can then formulate the full Lagrangian for EW theory as being:

$$\mathcal{L}_{EW} = i\bar{\psi}_L\gamma^\mu D_{\mu L}\psi_L + i\bar{\psi}_R\gamma^\mu D_{\mu R}\psi_R - \frac{1}{4}W^i_{\mu\nu}W_i^{\mu\nu} - \frac{1}{4}B^i_{\mu\nu}B_i^{\mu\nu} \quad (2.15)$$

where the first two terms describe the kinetic terms for the interaction between fermions and the gauge fields and the last two terms are the gauge field terms, which can be further described with:

$$W^i_{\mu\nu} = \partial_\mu W^i_\nu - \partial_\nu W^i_\mu - g\epsilon^{ijk}W^j_\mu W^k_\nu \quad (2.16)$$

$$B^i_{\mu\nu} = \partial_\mu B^i_\nu - \partial_\nu B^i_\mu \quad (2.17)$$

where ϵ^{ijk} are the $SU(2)_I$ structure constants. The electroweak gauge bosons, γ, Z and $W^\pm$ are linear combination of the four gauge fields, which are described by:

$$A_\mu = B_\mu \cos\theta_W + W^3_\mu \sin\theta_W \quad (2.18)$$

$$Z_\mu = -B_\mu \sin\theta_W + W^3_\mu \cos\theta_W \quad (2.19)$$

$$W^\pm_\mu = \frac{W^1_\mu \mp W^2_\mu}{\sqrt{2}} \quad (2.20)$$

The Weinberg angle (or weak mixing angle), θ_W is defined as:

$$\cos\theta_W = \frac{g'}{\sqrt{g^2 + g'^2}} \quad (2.21)$$

$$\sin\theta_W = \frac{g}{\sqrt{g^2 + g'^2}} \quad (2.22)$$

In the same way as in section 2.2, the EW Lagrangian (equation 2.15) describes fermions and gauge bosons as massless, because inserting a mass term into the Lagrangian would break gauge invariance. However, the $W^\pm$ and Z^0 bosons that

mediate the weak interaction are known to be massive from experimentation, having a mass of approximately 80 and 90 GeV respectively. To fix this problem, Higgs [8] [9] [10], Brout and Englert [11] and others [12] proposed in 1964, the mechanism for the spontaneous breaking of the symmetry, more often known as the Higgs Mechanism.

2.4.2 The Higgs Mechanism

The Higgs mechanism, introduces a doublet of complex scalar fields to the EW theory:

$$\Phi_H = \frac{1}{\sqrt{2}} \begin{pmatrix} \Phi^+ \\ \Phi^0 \end{pmatrix} = \frac{1}{\sqrt{2}} \begin{pmatrix} \phi_1 + i\phi_2 \\ \phi_3 + i\phi_4 \end{pmatrix} \tag{2.23}$$

where Φ^+ and Φ^0 are a charged and a neutral field respectively. The scalar field Φ_H is introduced into the EW Lagrangian via:

$$\mathcal{L}_H = (D^\mu \Phi_H)^\dagger (D_\mu \Phi_H) - V(\Phi_H) \tag{2.24}$$

where the covariant derivative has the form:

$$D_\mu \Phi_H = (\partial_\mu + ig\frac{\sigma_i}{2}W_\mu^i + ig'\frac{Y_{\Phi_H}}{2}B_\mu)\Phi_H \tag{2.25}$$

$V(\Phi_H)$ is a potential, that is defined as:

$$V(\Phi_H) = -\mu^2 \Phi_H^\dagger \Phi_H + \lambda(\Phi_H^\dagger \Phi_H)^2 \tag{2.26}$$

In Diagram 2.2 a representation of the potential can be seen for $\mu^2 < 0$ and $\lambda > 0$. The negative sign of the μ^2 term forces Φ_H to take a non-vanishing vacuum expectation value. The ground state of the Higgs field is given by the minimum of the potential. One state is chosen as the reference for the local gauge transformation, it is formulated as:

$$\Phi_{min} = \frac{1}{\sqrt{2}} \begin{pmatrix} 0 \\ v \end{pmatrix}, (\phi_1 = \phi_2 = \phi_4 = 0, \phi_3 = v) \tag{2.27}$$
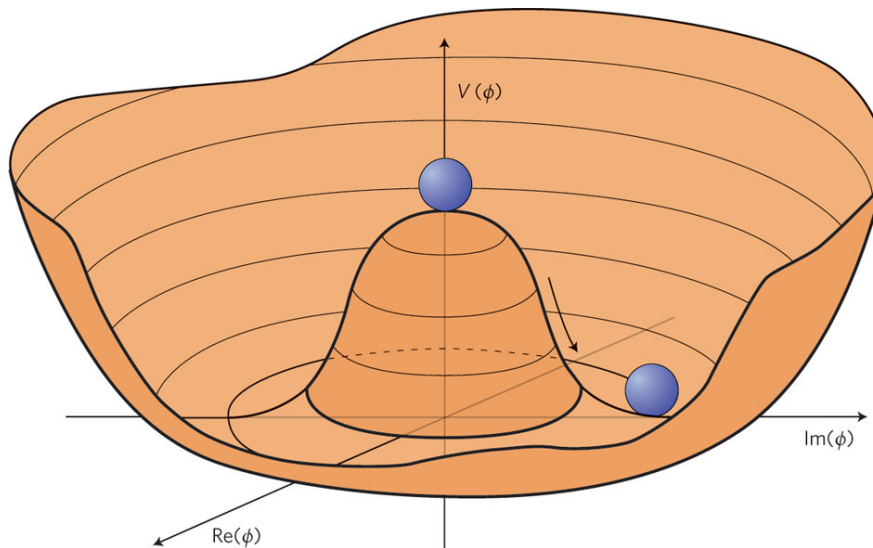
Figure 2.2: The Higgs potential $V(\Phi_H)$ in the $\Re(\Phi_H) - \Im(\Phi_H)$ plane [13].

where $v = \sqrt{\mu^2/\lambda}$ is referred to as the "vacuum expectation value" of the Higgs field. This minimum, or ground state of the Higgs field is not invariant under $SU(2) \otimes U(1)$, and therefore the gauge symmetry of this system is broken spontaneously. However, Φ_{min} has to be kept invariant under $U(1)$ so that the electric charge is a conserved quantity and that the photons remain massless. This is achieved by assigning a weak hypercharge to Φ, from equation 2.12 therefore it follows that the component, v, has to be neutral.

2.4.3 The Standard Model Higgs Boson

The Higgs field can be parametrised using four real fields θ_a (where $a = 1, 2, 3$) and $H(x)$, formulated as:

$$\Phi_H = \frac{1}{\sqrt{2}} e^{i\sigma^a \theta_a(x)} \begin{pmatrix} 0 \\ v + H(x) \end{pmatrix} \qquad (2.28)$$

The fields θ_a are known as Goldstone bosons, these are absorbed by a unitary gauge transformation of the W_i^μ fields. This process is colloquially described by saying that the Goldstone bosons have been *eaten* by the gauge fields. This forms the longitudinal components of the $W^\pm$ and Z weak gauge bosons. With this,

these gauge bosons have gained mass.

Substituting equations 2.19, 2.20 and 2.28 into the Lagrangian shown in equation 2.24 you obtain the following Lagrangian for the Higgs:

$$\mathcal{L}_H = \frac{1}{2}\partial^\mu H \partial_\mu H + \left(\frac{gv}{2}\right)^2 \frac{(W_\mu^+ W^{+\mu} + W_\mu^- W^{-\mu})}{2} + \left(\frac{gv}{2\cos\theta_W}\right)^2 \frac{Z^\mu Z_\mu}{2} - V(\Phi_H)$$

(2.29)

The mass terms for the Z and $W^\pm$ bosons are provided by the symmetry breaking, and are related by the weak mixing angle, thus the coupling constant g via:

$$m_W = \cos\theta_W m_Z = \frac{gv}{2}$$

(2.30)

Using equation 2.28 for the potential term, $V(\Phi_H)$, one can obtain the Higgs mass:

$$m_H = \sqrt{-2\mu^2} = \sqrt{2\lambda v^2}$$

(2.31)

The vacuum expectation value is, $v = \sqrt{2}/\sqrt{G_F} = 246$ GeV, this result is from the relation of the Fermi coupling constant, $\frac{G_F}{\sqrt{2}} = \frac{g^2}{8M_W^2}$.

The fermion masses can be introduced through the Higgs field and Yukawa interactions, these have a coupling (λ_f) that is proportional to their mass and to the value of the vacuum ground state:

$$m_f = \frac{\lambda_f v}{\sqrt{2}}$$

(2.32)

This leaves the couplings of the Higgs to all the other particles to be well defined and easy to calculate, after the fermion mass is measured.

2.5 Constraints on the SM Higgs Boson Mass

The Higgs mass is a free parameter of the SM, there are however some theoretical constraints that can be placed on it, that are derived from assumptions on the energy range where the SM is valid, that is to say before perturbation theory breaks down. Experimental constraints come from the direct searches that were

performed at LEP, Tevatron and the LHC, and from experimental measurements of some of the other SM parameters that have correlations with the Higgs mass.

2.5.1 Theoretical

The main theoretical constraints for the Higgs mass are discussed in this section.

Perturbative

The interactions of the longitudinal components of the massive gauge bosons increase with their momentum, therefore cross-sections of processes that involve them lead to energies that would violate unitarity. The best example of this is elastic WW scattering. When the Higgs mechanism is introduced into this process, it balances against the contribution that increases with the scattering energy. Furthermore, it is important to consider that since the WW can couple with other processes, such as ZZ, HH, ZH, W^+H and W^+Z, this constrains the Higgs mass with an upper limit of approximately $m_H < 700$ GeV. Simply put, this means that if the mass of the Higgs boson is greater than 700 GeV, unitarity would have to have been violated, unless there were some new phenomena that would restore this principle.

Triviality

The masses and couplings that appear in the SM Lagrangian depend on the energy. Additionally, the Higgs coupling monotonically increases proportionally to the energy scale, this leads to constraints on this coupling and therefore on the Higgs mass. The variation of the Higgs coupling (λ) with the energy scale $|Q|$ is described by the renormalisation group equation:

$$\frac{d}{dQ^2}\lambda(Q^2) = \frac{3}{4\pi^2}\lambda^2(Q^2) + ...$$
(2.33)

This equation can be solved by choosing as a reference point the energy at which the electroweak symmetry breaking scale, $Q_0 = v$, i.e.:

$$\lambda(Q^2) = \lambda(v^2)\left(1 - \frac{3}{4\pi^2}\lambda(v^2)\log\left(\frac{Q^2}{v^2}\right)\right)^{-1}$$
(2.34)

Equation 2.34, shows that the coupling increases logarithmically with respect to Q^2. When the energy is much smaller than the electroweak symmetry breaking scale ($Q^2 \ll v^2$), the coupling becomes negligibly small to the point of vanishing. When this occurs it is said that the theory is trivial, that is to say that there is no longer any interaction since the coupling is zero. In the opposite limit, when the energy is much higher than the weak scale ($Q^2 \gg v^2$), the coupling grows to the point of infinity, creating a Landau pole:

$$\Lambda_C = v e^{4\pi^2/3\lambda} = v e^{4\pi^2 v^2/M_H^2} \tag{2.35}$$

Inside this the energy scale limit the SM is valid. This means that below the energy cut-off, Λ_C, the self-coupling (λ) remains finite. For a large value of Λ_C, the Higgs mass is required to be small to avoid a Landau Pole. Conversely, a small Λ_C implies that a large Higgs mass is required. Setting the cut-off to be equal to the Higgs mass ($m_H = \Lambda_C$), the Higgs mass has to be smaller than 700 GeV, to have the coupling remain finite.

Similar to the perturbative constraints from the WW scattering (when λ or M_H are too large) perturbation theory can no longer be used and this constraint is no longer valid. However, from gauge theory simulations of lattices, where non-perturbative effects are taken into account, the mass limit is calculated to be $M_H < 640$ GeV [14].
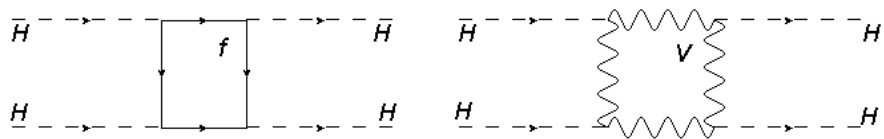
Figure 2.3: Diagrams showing one-loop contributions of fermions and gauge (Vector) bosons to λ

Stability Whilst talking about the triviality constraint, only the contributions from the Higgs boson itself are included in the calculation of the coupling, λ. When additional contributions from gauge bosons and fermions, as can be seen in figure 2.3, are included the coupling λ must not be small. If this was not the case then the vacuum would have the scalar potential $V(Q^2) < V(v)$, as this has no minimum it would mean an unstable vacuum. This puts a strong constraint on the Higgs boson mass, depending on the value of the cut-off Λ_C.

Figure 2.4 shows the stability (lower band) and triviality (upper band) constraints, which provide an allowed range of M_H as a function of the scale of new physics, Λ_C. If this is at the TeV scale then the Higgs boson mass is allowed in the range:

$$50\text{GeV} \lesssim M_H \lesssim 800\text{GeV} \tag{2.36}$$

This requires the SM to be valid up the scale of the Grand Unification theory, Λ_{GUT} 10^{16} GeV, otherwise the Higgs boson mass would be in the range of:

$$130\text{GeV} \lesssim M_H \lesssim 180\text{GeV} \tag{2.37}$$
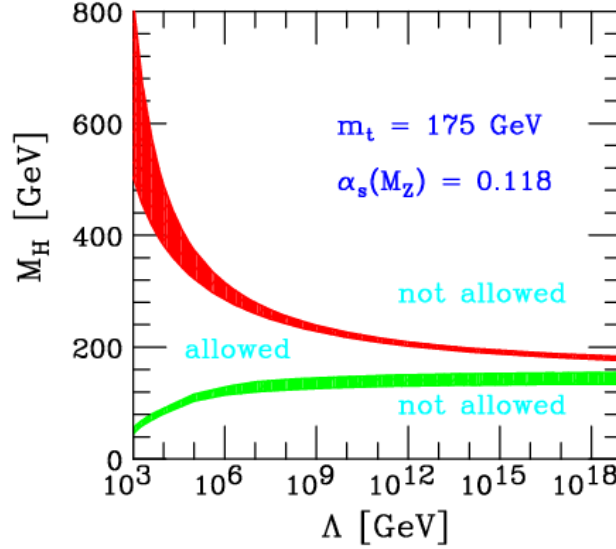
Figure 2.4: The triviality boundary (red) and the vacuum stability boundary (green) on the Higgs boson mass as a function of the new physics or cut-off scale for a top quark mass ($m_t = 175 \pm 6$ GeV and $\alpha_s(MZ) = 0.118 \pm 0.002$). The allowed region lies between the bands [15].

Fine-tuning constraint
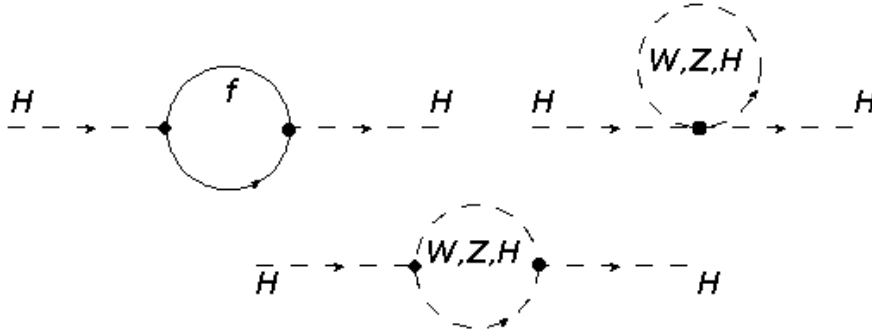
Figure 2.5: Diagrams showing one-loop corrections to the SM Higgs boson mass.

The fine-tuning problem comes from radiative corrections to the Higgs boson mass, these are shown in Figure 2.5, which can involve fermions, massive gauge bosons and Higgs boson loops. Cutting off the loop integral momenta at a scale Λ, keeping only the dominant contributions in this scale the following relation

was found:

$$\Delta M_H^2 = \frac{\Lambda^2}{8\pi^2 v^2} \left[M_H^2 + 2M_W^2 + M_Z^2 - 4m_t^2 \right] \tag{2.38}$$

In this only contributions from top quark loops are retained. Equation 2.38 shows an unusual phenomena within the SM. There are some quadratic divergences instead of the more usual logarithmic ones discussed in previous sections. In the case of a very large cut-off Λ, around 10^{16} GeV, there has to be a very fine arrangement between the Higgs mass and the EW corrections to have a physical M_H in the range of the EW symmetry breaking scale. This results in M_H being in a range from 100 GeV to 1 TeV which is required for the SM to be consistent. For low values of the scale Λ (less than 1 TeV), there is no problem of fine-tuning for any reasonable Higgs boson mass value. More detailed information for this section can be found in reference [14].

2.5.2 Experimental

Direct Higgs Searches

Before the start of LHC operations, the search for the Higgs boson had been performed by experiments situated on two large accelerators. The Large Electron Positron collider (LEP), which ran from 1989 to 2000 with a varying centre of mass energy of 91-210 GeV. LEP excluded the existence of the SM Higgs boson below 114.4 GeV at 95% confidence level [16]. At LEP, the Higgs Boson was expected to be produced via the Higgs-strahlung process (see 2.7) this is where the Higgs boson is radiated by a vector boson. The final results from LEP are shown in figure 2.6.
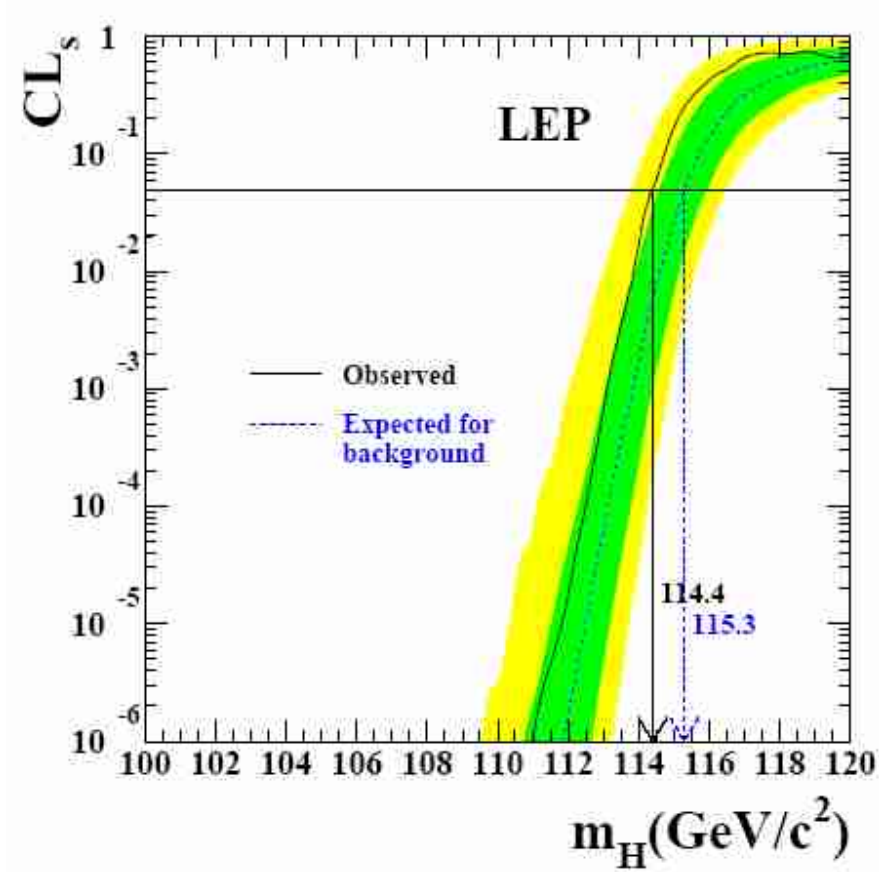
Figure 2.6: The CL_s ratio as a function of the mass of the Higgs boson. The observed exclusion limit is shown with the solid line and the expected limit is shown with the dashed. The bands show the 68% and 95% probability levels. The line $CL_s = 0.05$ defines the 95% CL [16].

The Tevatron, was a proton-antiproton collider that had a centre of mass energy of 1.96 TeV, also set exclusions for the SM Higgs boson mass. This can be seen in Figure 2.7, which shows the results published by the Tevatron in the summer of 2011 with 8 fb^{-1} of data [17].
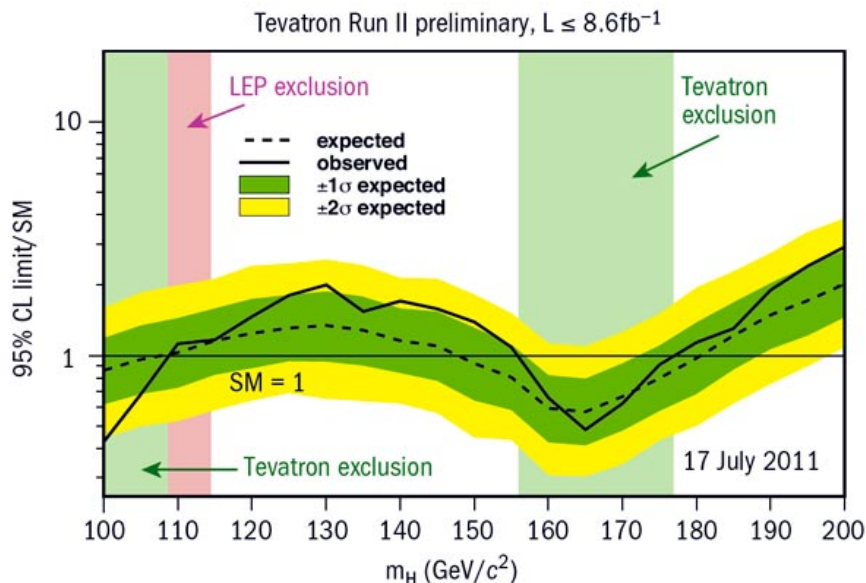
Figure 2.7: The 95% confidence level on the upper limits of a SM Higgs boson production cross-section, normalised to the SM prediction as a function of the Higgs boson mass hypothesis, m_H, obtained by experiments at the Tevatron. With data recorded up to the summer of 2011 [17].

Indirect experimental constraints

In addition there have been some constraints gathered from indirect experimental methods. The SM Higgs boson contributes to the radiative correction to the EW observables through the gauge bosons self energies. Constraints on the mass of the Higgs bosons can be derived from precision measurements of these EW observables. Specifically, the mass of the W and Z bosons, the EW mixing angle, the top quark mass and the Fermi coupling constant. These measurements have been performed at LEP and Tevatron, however these constraints are weak since the dependence with the Higgs mass is logarithmic.

The constraints set on the Higgs mass are extracted from global fits to these EW parameters, the result from groups at LEP and early data from the LHC is shown in figure 2.8. From the minimum of the curve, the preferred value for the Higgs mass is found to be $m_H = 94^{+29}_{-24}$ GeV.
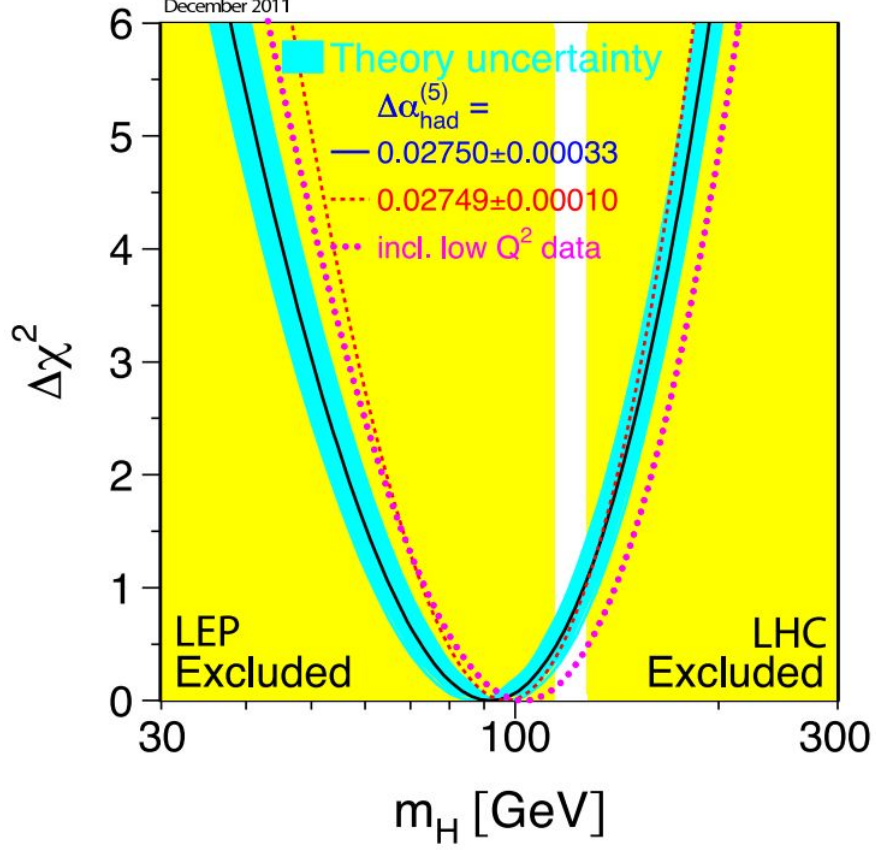
Figure 2.8: $\Delta\chi^2$ against m_H, this is the result from the fit to the EW parameters, the band represents an estimate of the theoretical error. The yellow band shows the exclusion from the direct searches from LEP and the LHC [18].

However, whilst this was not proof for the existence of the SM Higgs boson, it did provide a strong hint on what mass range to look for it. The results of the fit implies that m_H is lower than about 152 GeV. In figure 2.9, using results available before the summer of 2011, of the direct searches for the Higgs boson at LEP and Tevatron, the global fit gives the following constraint for the Higgs boson mass:

$$m_H = 120.6^{+17.9}_{-5.2}\text{GeV} \tag{2.39}$$

21
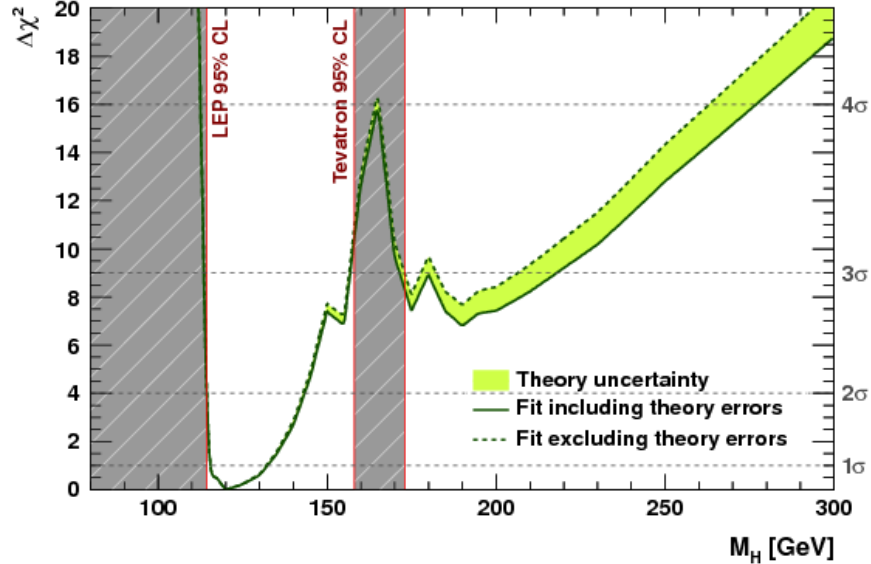
Figure 2.9: $\Delta\chi^2$ as a function of m_H. The solid (dashed) line line corresponds to the result including (ignoring) the theoretical errors [19]

2.6 The SM Higgs Boson at the LHC

2.7 The Higgs Production

In the SM the Higgs boson preferentially couples to heavy particles like the Z and W bosons and the top quark. There are four main production methods in proton collisions, shown diagrammatically in figure 2.10. The cross-sections for the different Higgs production methods at both 7 TeV and 8 TeV are shown in figure 2.11.

- The dominant method is gluon-gluon fusion (ggF), this is where the Higgs boson couples indirectly to gluons via a triangular loop of quarks dominated by the top quark,

- Vector Boson Fusion (VBF), this is where the Higgs boson is produced by the fusing together of two weak vector bosons radiated from quarks. Two

final quarks fragments into two forward jets, this, coupled with no expected QCD activity between them produces a very clean Higgs signal,

- The associated production with vector bosons is called Higgs-strahlung (WH or ZH), it is useful for the study of the couplings to vector bosons,

- Higgs production association with top pairs (ttH) is the smallest mode contributing to LHC Higgs production. However, it is important to note that this process is useful for measuring the Yukawa coupling between the Higgs and the top quark.
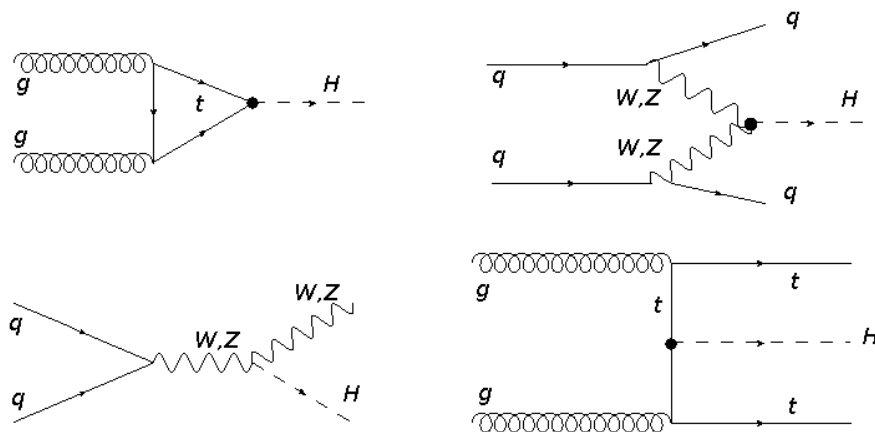
Figure 2.10: The four main SM Higgs boson production methods in hadron hadron collisions. Top-left, gluon-gluon fusion. Top right, vector boson fusion. Bottom left, Higgs-strahlung. Bottom right, associated production with pairs of top quarks.
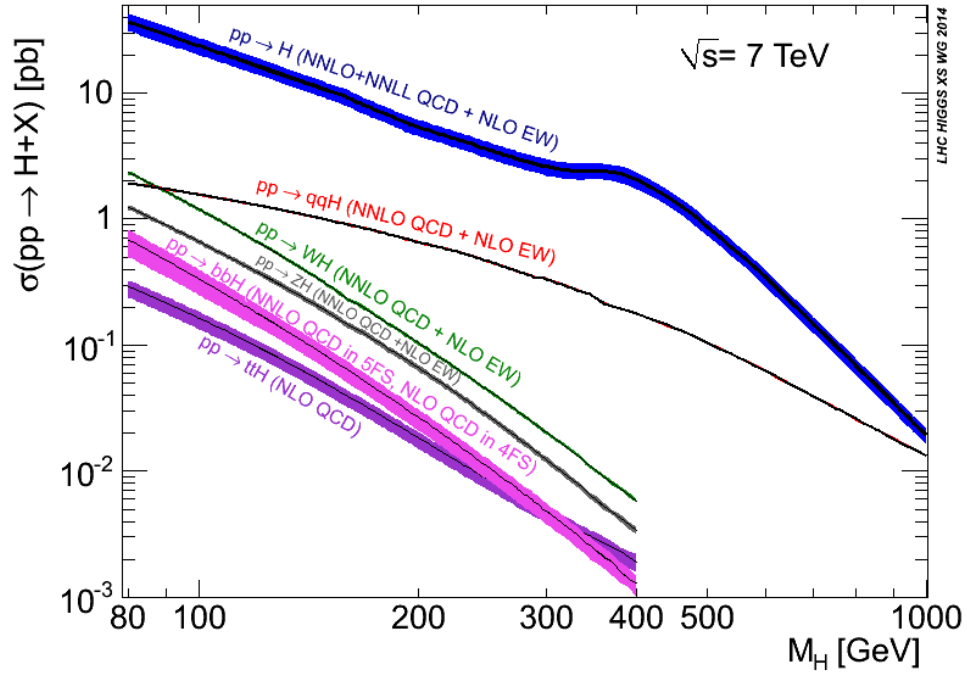
(a)
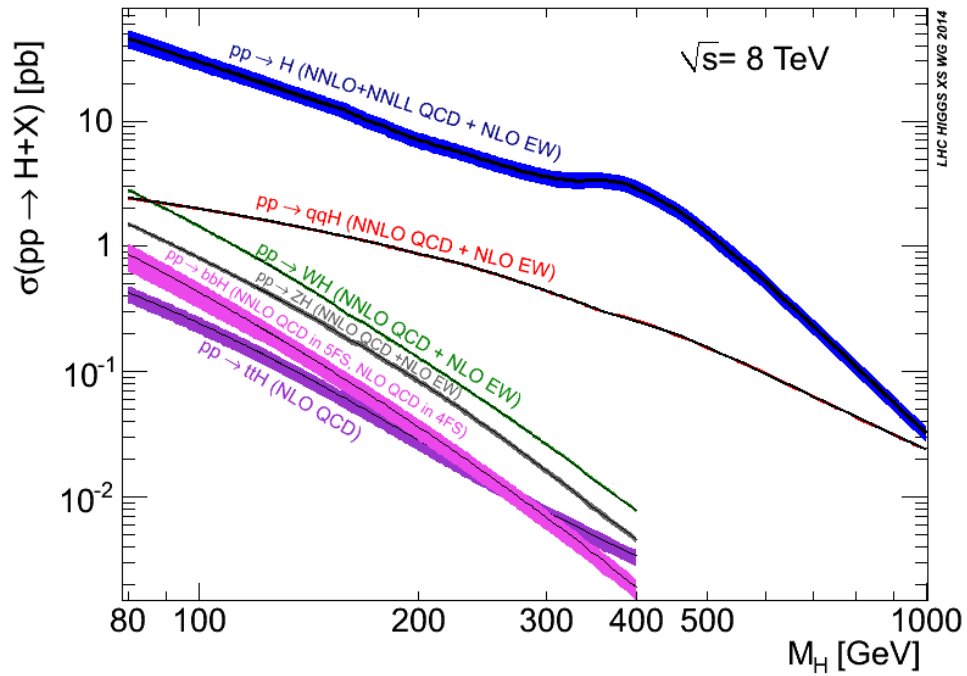
(b)

Figure 2.11: Cross section of various Higgs production modes at 7TeV (left) and 8TeV (right) as a function of the Higgs mass [20].

2.8   The Higgs Decay Modes
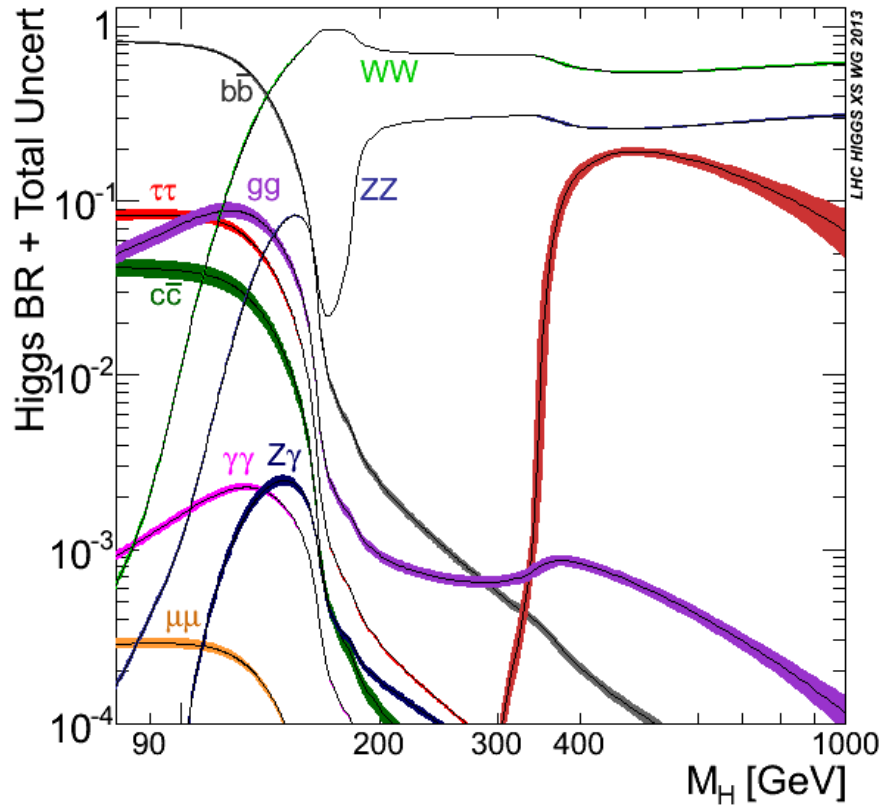
Figure 2.12: The decay mode branching fractions of the SM Higgs boson, displayed as a function of the Higgs boson mass [20].

Figure 2.12 shows the Higgs boson branching fractions as a function of m_H. It can split into three regions the Low, Intermediate and High mass ranges.

Low Mass Range

In the low mass range, 100 GeV $\leq m_H \leq 130$ GeV the Higgs bosons primarily decays into $b\bar{b}$ quark pairs, this has a branching fraction of approximately 70% at $m_H = 120$ GeV. This is because the Higgs coupling to fermions is proportional to their mass. However, despite this at the LHC this channel has a low sensitivity due to the very large QCD background inherent from proton-proton collisions. The $H \to \tau\tau$ (the main channel that is discussed in this thesis) has a branching ratio of about 8%, it has a large background from $Z \to \tau\tau$ events. The $\gamma\gamma$ and $Z\gamma$

decay channels have a contribution of about 10^{-3}. These are the more important Higgs decay channels in the low mass region.

Intermediate Mass Range

In the Intermediate mass range, 130 GeV $\leq m_H \leq$ 200 GeV, the dominant channels are the WW and the ZZ. From these two the most promising was the WW that has a branching fraction close to 100% in this range. The ZZ decay channel is still important in the Low mass range because the two Z bosons decay into pairs of leptons, which create a very unique and clean signature.

High Mass Range

When the Higgs mass is greater than twice that of the top quark ($m_H > 2m_t$) the top pair decay appears and has an increasing branching fraction due to its very strong coupling to the Higgs boson. Despite this the WW and ZZ channels are still dominant.

2.9 The $H \to \tau\tau$ channel

The τ lepton was first discovered in 1975 by a group lead by Martin Lewis Perl on the SPEAR e^+e^- collider, located at the SLAC National Accelerator Laboratory in the USA, uing the Mark I detector, which was one of the first large-solid-angle, general purpose detectors built. The search was initiated by the so called $e - \mu$ problem, this was the puzzling difference between the electron and the muon. Measuring the difference between the cross-sections in the elastic scattering of electrons and muon off protons, it was hypothesised that there was a third, heavier, charged lepton. They discovered an anomalous number of events of the form:

$$e^+ + e^- \to e^\pm + \mu^\pm + ? \tag{2.40}$$

The unknown in this equation was hypothesised to be two or more undetected particles. This was needed as the energy and momentum would not be conserved if there was only one solitary undetected particle. Furthermore, no other muons, electrons, photons or hadrons were detected. From this it was proposed that the

same process should be:

$$e^+ + e^- \rightarrow \tau^+\tau^- \rightarrow e^\pm + \mu^\mp + 4\nu \qquad (2.41)$$

After a confirming study that was performed at DESY in Hamburg, the τ lepton was officially discovered. This lepton has shown to be invaluable in the discovery process of the latest particle, the Higgs boson. As discussed in a previous section, it is important to ascertain to which particles the Higgs boson couples directly, thus without doubt gives mass to. If it couples to a boson it can be reasonably state that all bosons are affected by the Higgs field, similarly with the fermions. In Figure 2.12 it can be seen that the $\tau\tau$ final state for Higgs decays offers a very attractive opportunity for measuring a direct Higgs coupling to fermions. This makes the in-depth study of this decay branch to be a fairly high priority for the Higgs groups on the LHC.

2.10 Beyond the SM

Currently, the SM is very successful at describing the phenomena we observe in experiments. The results of a global SM fit to precision EW data, has severely constrained the SM Higgs to be in the low mass range, $m_H < 150$ GeV. This give experimentalists a clear energy window in which to look for it. There are however some unresolved problems in the SM:

- The SM does not describe in any way the gravitational force, this becomes more important at higher energies,

- The number of generations (3) for quark and leptons with such different mass scales,

- The SM does not provide any explanation for dark matter and dark energy. Neither does it explain CP violation, which is responsible for the matter-antimatter asymmetry in the universe.

Even though the SM has been proven to be very effective at describing the phenomena at the EW scale, it is still an incomplete theory. The general opinion is that the SM is a low energy limit of a much more complete and fundamental theory, this could provide the unification of all the fundamental interactions found in nature. Beyond the SM theories (BSM theories), aim to extend the SM in order to provide answers for some of the unresolved puzzles. the LHC was designed to try and shed some light on the energy scales that could be the domain of BSM theories.

2.10.1 Fourth Generation of Quarks and Leptons
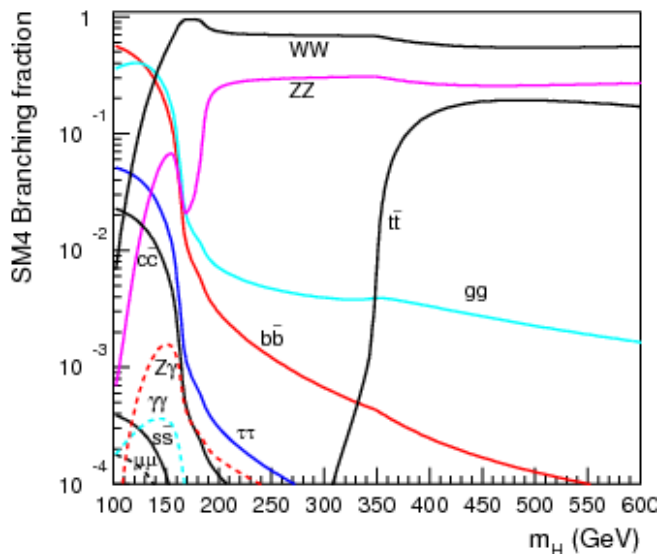
Figure 2.13: The branching fractions of fourth generation model Higgs decays, with $m_{d4} = m_{l4} = 400$ GeV [21]

Thus far there have only been three families of charged and neutral fermions have been observed in accordance with the SM. In a fourth generation model, the production cross-section of the Higgs boson produced via ggF is significantly increased due to additional loops of quarks. In figure 2.13 the branching fractions of Higgs bosons produced in fourth generation models, where the 4th generation

of leptons and quarks have masses of around 400 GeV [21, 22].

2.10.2 Fermiophobic Higgs Bososn
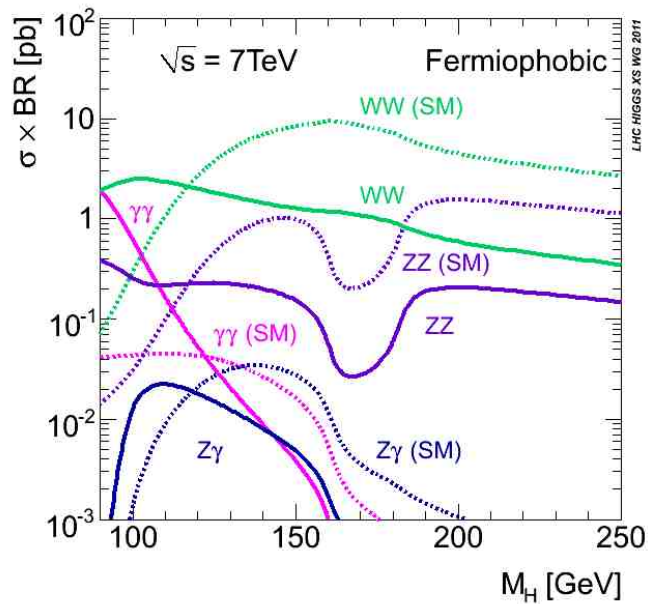
Figure 2.14: The branching ratio times cross-section for a fermiophobic Higgs model at a centre of mass energy of 7 TeV [20].

In some models such as the 2 Higgs Doublet Model (2HDM) [23] or Higgs Triplet Models [24], the Higgs field couplings to some or all fermion generations can be substantially suppressed. This is referred to as a fermiophobic Higgs, and means (if true) that the mechanism that generates the fermion masses is independent of the Higgs mechanism. The fermiophobic Higgs decaying into photons does not couple to fermions and only goes through W loops. See figure 2.14. Because the main SM Higgs boson decay channels, $b\bar{b}$ and $\tau\tau$ are forbidden at tree-level, the branching fraction for a low mass fermiophobic Higgs boson decaying to two photons is significantly enhanced.

2.11 Results from Run I of the LHC

The first run of the LHC bought many major advances in particle physics, including the discovery of a new particle announced on 4 July 2012 [25]. This was then confirmed by a full analysis of the complete dataset by the ATLAS and CMS collaborations to be the sought after Higgs boson in March of the next year [26]. The data collected during the LHC Run I were also used to test and set limits of several BSM theories, as described in section 2.10. Models such as an SM4 Higgs boson from a fourth generation of fermions with masses up to 600 GeV or a fermiophobic Higgs boson have been ruled out [27]. Limits on heavy or charged [28] Higgs bosons predicted by models with Higgs extensions have been set [29].

The most recent results from the ATLAS and CMS experiments, both the individual and the combined result can be seen in Figures 2.15, 2.16 and 2.17. The results from the ATLAS and the CMS experiments show all the measured decay channels, but the combined result only focuses on the $H \rightarrow ZZ \rightarrow 4\ell$ and the $H \rightarrow \gamma\gamma$ channels because they have the most precise measurements out of the decay channels that were studied. As can be seen the mass of the Higgs boson was measured to be:

$$m_H = 125.09 \pm 0.24 \text{GeV} \tag{2.42}$$

$$m_H = 125.09 \pm 0.21 \text{ stat. } \pm 0.11 \text{ syst. GeV} \tag{2.43}$$

The total uncertainty is dominated by the statistical term, with the systematic uncertainty dominated by effects related to the photon, electron, and muon energy or momentum scales and resolutions. Compatibility tests are performed to ascertain whether the measurements are consistent with each other, both between the different decay channels and between the two experiments. All tests on the combined results indicate consistency of the different measurements within 1σ, while the four Higgs boson mass measurements in the two channels of the two experiments agree within 2σ. The combined measurement of the Higgs boson mass improves upon the results from the individual experiments and is the most precise measurement to date of the mass of this newly discovered particle.
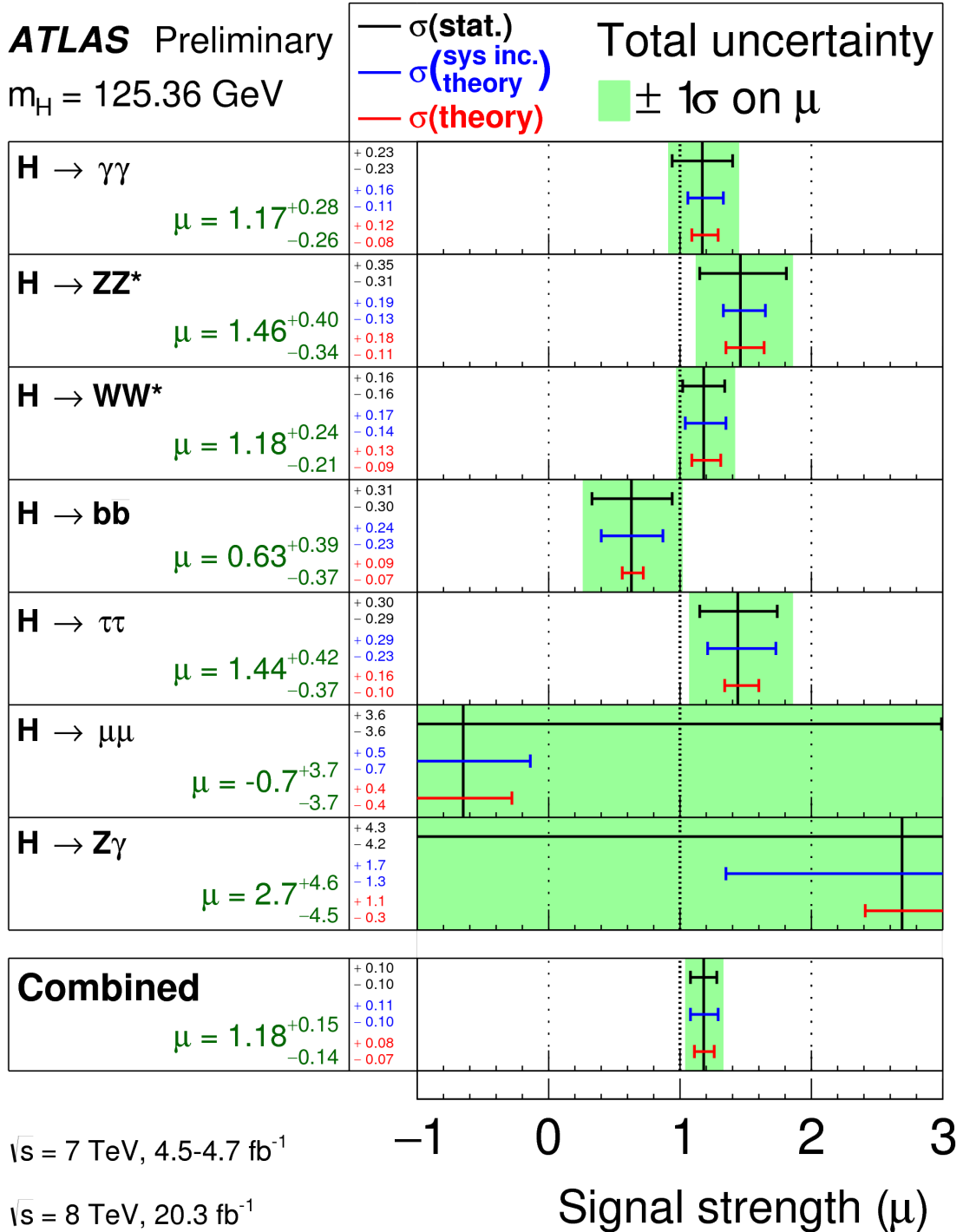
Figure 2.15: The observed signal strengths and uncertainties for different Higgs boson decay channels and their combination for $m_H = 125.36$ GeV. Higgs boson signals corresponding to the same decay channel are combined together for all analyses. The best-fit values are shown by the solid vertical lines. The total 1 uncertainties are indicated by green shaded bands, with the individual contributions from the statistical uncertainty (top), the total (experimental and theoretical) systematic uncertainty (middle), and the theory systematic uncertainty (bottom) on the signal strength shown as horizontal error bars [30].
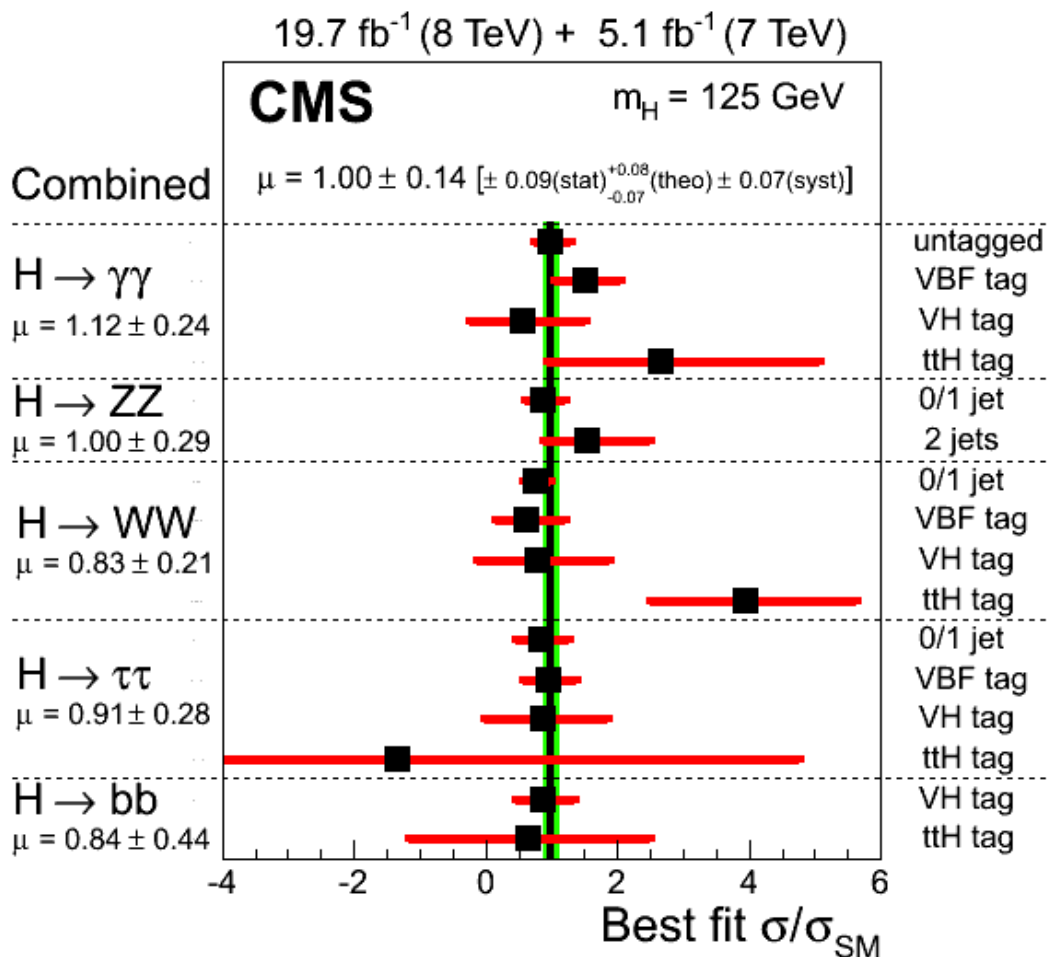
Figure 2.16: Values of the best-fit σ/σ_{SM} for the combination (solid vertical line) and for subcombinations by predominant decay mode and additional tags targeting a particular production mechanism. The vertical band shows the overall σ/σ_{SM} uncertainty. The σ/σ_{SM} ratio denotes the production cross section times the relevant branching fractions, relative to the SM expectation. The horizontal bars indicate the 1 standard deviation uncertainties in the best-fit /SM values for the individual modes; they include both statistical and systematic uncertainties [32].
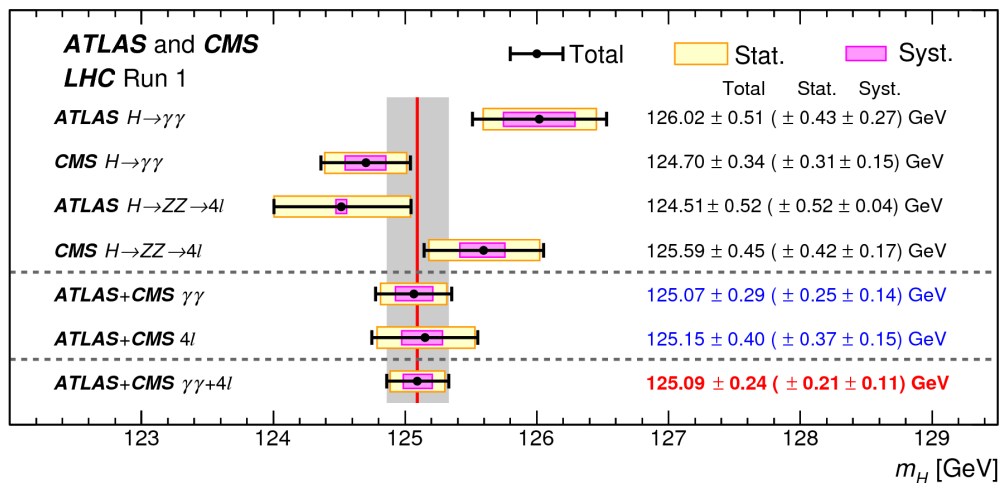
Figure 2.17: Higgs mass from combined $H \to ZZ \to 4\ell$ and $H \to \gamma\gamma$ channels in the ATLAS and CMS detectors and showing the overall combined mass. The systematic (narrower bands), statistical (wider bands), and total (black error bars) uncertainties are indicated. The (red) vertical line and corresponding (gray) shaded column indicate the central value and the total uncertainty of the combined measurement, respectively.

Chapter 3

The ATLAS Experiment

3.1 Introduction

The ATLAS (A Toroidal Lhc ApparatuS) experiment is the largest of the four main experiments (the others being CMS, LHCb and ALICE) located on the Large Hadron Collider (LHC) at the European Organization for Nuclear Research, CERN. The ATLAS detector is a general purpose detector, meaning that it was designed so that it could cover the largest range of physics, and to completely enclose the collision point with interactive material. In this chapter the layout and functioning of the ATLAS detector is described, however a special emphasis will be put on the sections that are most used in the identification of tau leptons.

3.1.1 The Large Hadron Collider

The LHC is a 27 km subterranean superconducting particle accelerator [33]. It has been designed to collide bunches of up to 10^{11} protons at a rate of 40 million times per second, and to generate proton-proton (PP) collisions with a centre of mass energy of 14 TeV and an instantaneous luminosity of $\mathcal{L} = 10^{34} cm^{-2} s^{-1}$. This increase will extend the energy and luminosity frontiers by around two orders of magnitude compared to previous hadron colliders. In addition to PP collisions

the LHC was also designed to accelerate and collide heavy ions, in this case lead nuclei. However this topic won't be discussed in great detail in this thesis.

The LHC was designed to have up to 2808 circulating bunches of protons in each beam, each bunch has a temporal separation of about 25ns, i.e. there is 25ns between each bunch crossing. The bunches of protons are separated into two separate beam pipes and sent in opposite directions around the accelerator. The beams are directed by 8.3 T magnetic fields generated by over 1200 super-conducting dipole magnets. The beams are focused by around 400 quadrupole magnets, and then focused into colliding at the four interaction points (where the main experiments are located) simply by dipole magnets. As with any large accelerator, one cannot get to the highest energies with a single machine, many have to be used to incrementally increase the energy and the shape of the beam before being injected into the final stage (in this case the LHC). This is shown in figure 3.1.

At the present time the LHC is in the first planned shut-down phase, this phase is to allow time to upgrade important computing systems in the Tier-0 grid site and replace and repair any broken or otherwise systems inside the detector itself. A brief time-line of the main milestones of the LHC is given below:

- 10 Sep 2008: First colliding protons at the LHC.

- 23 Nov 2009: First collisions at 450 GeV in all 4 detectors.

- 30 Nov 2009: First collisions at 1.18 TeV per beam.

- 30 Mar 2010: First collisions at 7 TeV.

- 5 Apr 2012: First collisions at 8 TeV.

- 4 July 2012: Announcement of the observation of a new boson consistent with the Higgs boson.

- 8 Nov 2012: Announcement of the observation of the decay of the B_s meson in to two muons $B_s^0 \to \mu^+\mu^-$.

- 14 Feb 2013: Beginning of the first long shut-down.

- 26 Nov 2013: Announcement of the observation of the Higgs boson decaying into Fermionic final states.
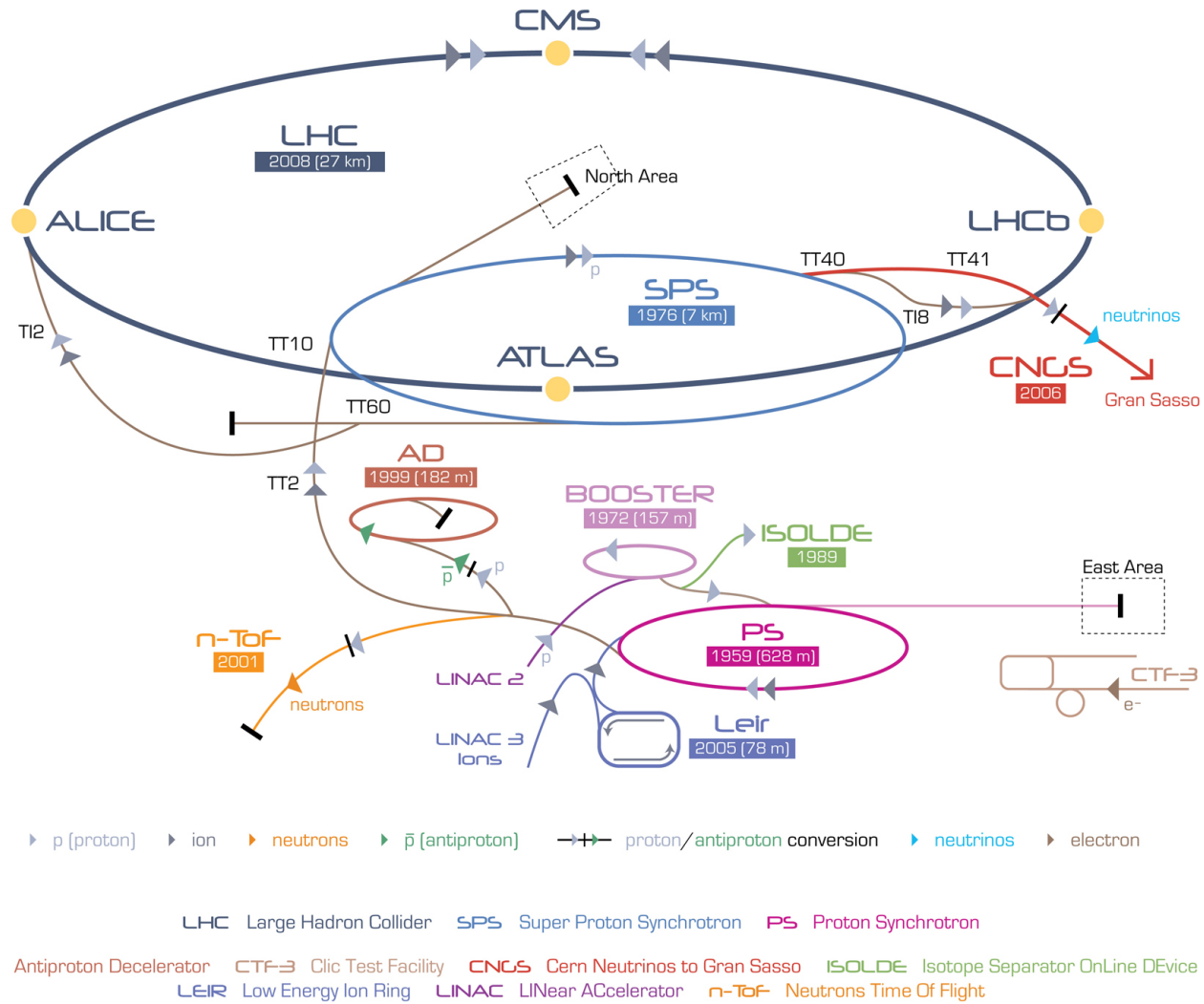
Figure 3.1: A schematic diagram showing the accelerator complex and the four main experiments. [34]

3.1.2 ATLAS Coordinate system

In this section the coordinate system used to define the space inside the detector will be outlined and be used throughout the remainder of this thesis. The beam circulating in the anti-clockwise direction is travelling in the positive z-direction and vice versa, while the $x - y$ plane is perpendicular (transverse) to this plane, more specifically the positive x direction is pointing towards the centre of the LHC ring and the positive y direction is pointing directly upwards. However, in practice it is much easier and makes more sense to use cylindrical coordinates instead of Cartesian; the polar angle θ and the azimuthal angle ϕ are used instead. With this system there is one problem the angle θ is not Lorentz invariant, instead the pseudorapidity is defined using the particles 4-momentum (p_x, p_y, p_z, E) as:

$$\eta = \frac{1}{2} \ln \frac{|\vec{p}| + p_z}{|\vec{p}| - p_z} = -\ln \tan \frac{\theta}{2} \tag{3.1}$$

The limits of this equation show that as $\theta \longrightarrow 0 \therefore \eta \longrightarrow \infty$.

Another often used variable is the transverse momentum (P_t) this is, as the name suggests, the momentum that is pointing in the $x - y$ (transverse) plane. A variable is also needed to define and angular separation of any two objects in the detector:

$$\Delta R = \sqrt{\Delta \eta^2 + \Delta \phi^2} \tag{3.2}$$

3.1.3 The ATLAS detector

Due to the high beam energies and the high interaction rates at the LHC, there is a massive potential for discovering new physics. However this sets very high requirements for the detector to operate efficiently and extract the important information from the voluminous amounts of background. An overview of these requirements are:

- Electromagnetic calorimetry sufficient enough to measure the energy and shower shapes of electrons and photons with a good angular coverage,

- A high precision hadronic calorimeter for identification and reconstruction of jets and missing transverse energy with a large angular coverage,

- A muon spectrometer for high-precision muon momentum measurements outside the calorimeters,

- A strong magnetic field to increase the curvature of tracks from charged particles especially muons,

- An efficient tracking detector for measuring the momentum and charge of high p_T particles and enable good reconstruction of particle vertices,

- Fast and radiation-hard electronics,

- A fast triggering and data-acquisition system.

The ATLAS detector was therefore designed to be able to handle more than 40×10^6 inelastic scattering events per second, most of these are 'minimum bias' i.e. QCD interactions with a low momentum transfer. When operating with a luminosity of, $\mathcal{L} = 10^{33} cm^{-2} s^{-1}$ there would be about 100 W and 10 Z gauge bosons produced each second, with a rate of many of orders of magnitude less for a Standard Model Higgs boson. This high rate of weak gauge bosons means that with the ATLAS detector there is a massive increase in statistics, thus allowing for incredibly precise measurements of the Standard Model and its predictions. However, at the same time, in the $H \rightarrow \tau\tau$ search the Z boson is a large irreducible background, this will be discussed in more detail in a later chapter.

In figure 3.2 you can see a detailed layout of the ATLAS detector, it is made up of several sub-detector systems:

- The Inner Detector (ID), is responsible for tracking and vertexing of the particles, and is itself made up of 3 smaller detector systems:

  - A pixel Detector;

  - The Transition Radiation Tracker (TRT);

  - The Semiconductor Tracker (SCT);

- A superconducting solenoid magnet system;

- Electromagnetic Calorimeters;

- Hadronic Calorimeters;

- A superconducting toroidal magnet system;

- Muon Spectrometers.

Figure 3.2: Diagram showing the scale of the ATLAS detector and the positions of its sub-detector systems [35].

44m

25m

Tile calorimeters

LAr hadronic end-cap and
forward calorimeters

Pixel detector

LAr electromagnetic calorimeters

Toroid magnets

Solenoid magnet   Transition radiation tracker

Semiconductor tracker

Muon chambers
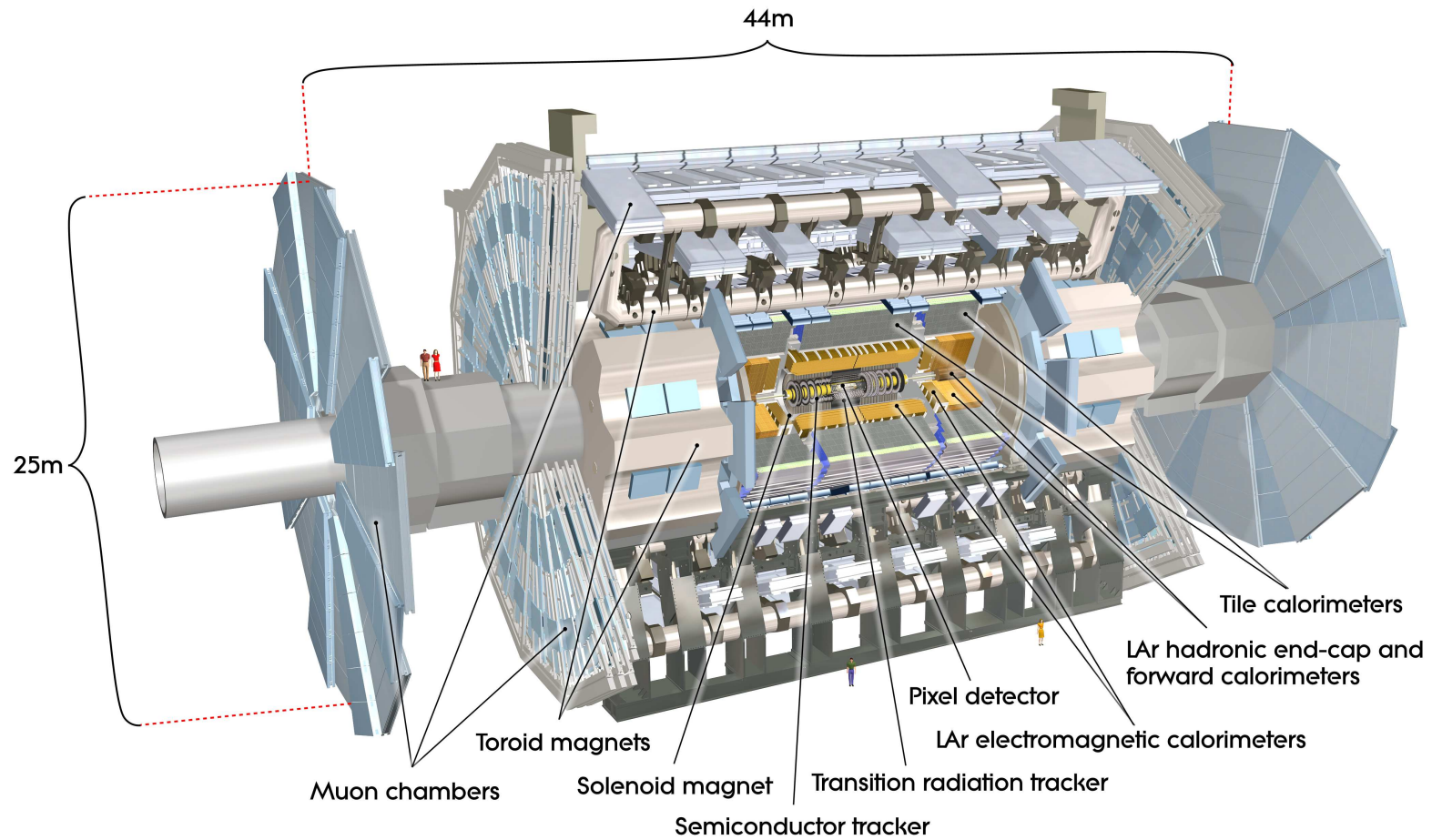
3.2   The Magnet System

So that measurements can be made about the particle's charge and its transverse momentum, there are two magnetic fields employed within the ATLAS detector: the Central Solenoid (CS) cryogenically cooled to superconducting temperatures, and an air cooled toroidal system. The CS which as stated previously surrounds the ID, provides a 2 T magnetic field, this causes the trajectories of the particles in the ID system to be curved. Measuring the curvature of the tracks allows very precise measurements to be made of a particle's charge and its momentum.

In addition there is a 0.5-1 T magnetic field provided by a toroidal magnetic system which is air-cooled, it is made of three individual systems, one barrel magnet and two endcap magnets. The barrel magnet applies a field to the central i.e. low $|\eta|$ region, whilst the endcap magnets placed on the z-axis provide the field for the higher $|\eta|$ region. Due to the nature of the barrel section of the toroidal magnet, it is eight individual coils, it produces a strongly non-uniform magnetic field, this has to be heavily monitored and taken into consideration upon particle reconstruction [33, 36].

3.3   The Inner Detector

The Inner Detector (ID) shown in figure 3.3 is responsible for the tracking of charged particles and consists of three sub-detectors using different technologies: closest to the beam's the silicon pixel detector, outside of which is the Semi-Conductor Tracker (SCT) and furthest away from the beam axis is the Transition Radiation Tracker (TRT). The outer dimensions of the ID are 5.6 m (length) and 2.1 m (diameter). The Inner Detector is required to be able to very accurately track a particle's path and measure its momentum. The detector with the highest granularity and precisions is placed closest to the beamline, but a trade off must be made, it is not wise to have a high density of material close to the beam line, but there must be enough so that a high accuracy can be maintained.
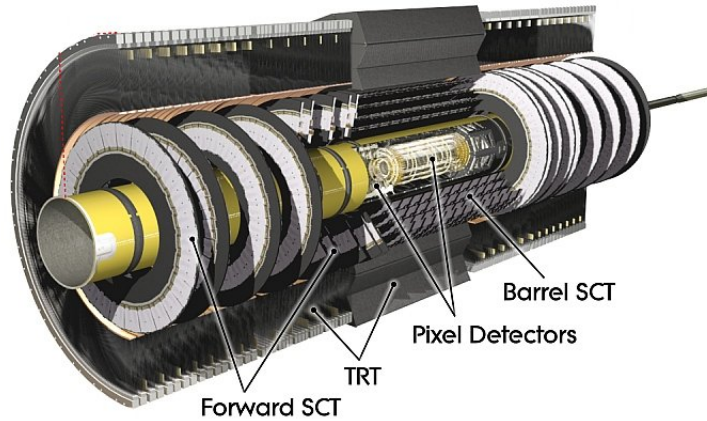
Figure 3.3: A cut away schematic showing all the sub-sections of the Inner Detector. [37]

3.3.1 Pixel Detector

The pixel detector is the closest detector to the beam in ATLAS, this is so the highest precision measurements for the vertexing can be be performed. It consists of 80 million read-out channels placed in three concentric cylinders around the beam axis in the barrel, and in three disks in the transverse direction in each end-cap. The size of each pixel is $5 \times 400\mu m^2$ and generates a hit precision of 10 $\mu m(r - \phi)$ and 115 $\mu m(z)$ in the barrel regions and 10 $\mu m(r - \phi)$ and 115 $\mu m(r)$ in the end-caps. This part of the ID covers an η range from -2.5 to 2.5 [38].

3.3.2 SCT

The SCT consists of 6.3 million silicon strip channels grouped into 4088 modules of 1536 channels per module [39]. In each module, the stripes are placed back to back at a 40 mrad stereo angle to each other. This ensures the 3-dimensional space point inside the detector can be formed. The modules are arranged in 4 barrel cylinders and 18 end-cap disks. The SCT covers an the same η range as

the pixel detector described in section 3.3.1. It has a precision of $17\mu m(r-\phi)$ and $580\mu m(z)$ in the barrel and $17\mu m(r-\phi)$ and $580\mu m(r)$ in the end-caps.

3.3.3 TRT

The final part of the ID is the TRT, this is not a silicon detector instead it has about 351,000 readout channels. The purpose of which is provide tracking measurements by hits generated in straws (4 mm × 144 cm), in each straw there is a 30 μm tungsten wire and a mixture of 70% Xe and 30% CO_2 gas (there is also a trace amount of O_2 gas). Typically there are enough hits in the TRT to allow for an almost continuous tracking of the particles in the $|\eta| < 2.0$ region. In addition to this the TRT provides information on r and ϕ with an accuracy of about 130 μm per straw. However due to the design the position of the hit along the axis of the straw cannot be determined intrinsically. In the barrel section, the straws are placed parallel to the beam axis with the wires divided into two halves at $\eta = 0$. In the end-caps the straw are arranged radially to maximise the number of straws passed by any particle.

The design of the ID with the TRT combines a large area of very precise trackers with a full set of track co-ordinates that has a very robust pattern recognition abilities. This is especially true for high p_T tracks where the TRT can really contribute significantly the track resolution.

With respect to tau leptons the TRT is very good at discriminating between electrons and other charged pions, this is very useful for identifying 3-pronged τ_h decays. This is for two reasons. Firstly, because the difference in mass between the pion and the electron effects the transition radiation of the two highly relativistic particles. Secondly, the electron creates transition radiation in the radiative material and in the straw material.

3.4 The Calorimeters

On the outside of the ID is the calorimeter system, this can be seen in figure 3.2, and in much more detail in 3.4. The calorimetry consists of two parts; a liquid-argon electromagnetic calorimeter (ECAL) and steel and scintillating tile hadron
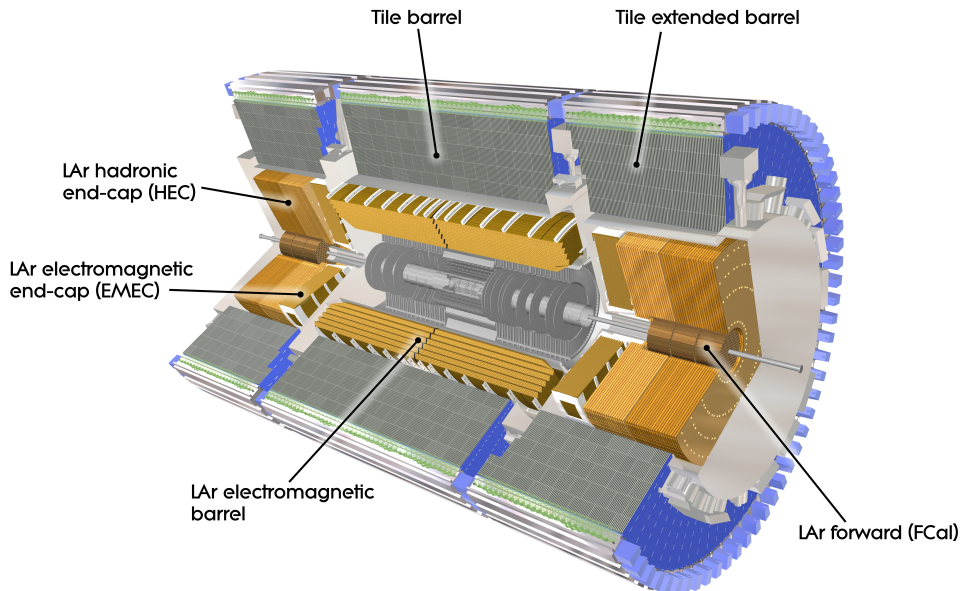
Figure 3.4: A computer generated image of the ATLAS calorimetry, marking all important sections. [40]

calorimeter (HCAL). The ECAL has a pseudorapidity range of $|\eta| < 3.2$, this completely encompasses the ID and provides information on photons and charged particles. The HCAL has a pseudorapidity range of $|\eta| < 4.9$, different segments with differing technologies involved.

The energy resolution of the ECAL is parametrised with a 'sampling' and a constant term, the sampling term has a $\sqrt{E}$ dependence due to the statistical nature of the energy deposition in the calorimeters, the constant term is independent of E is also present due to the non-uniformities when the detector was calibrated. The resolution of the ECAL is; $\sigma/E \approx 10\%/\sqrt{E} + 0.07$, and for the HCAL it is; $\sigma/E \approx 50\%/\sqrt{E} + 0.03$.

The ECAL has a high granularity, this is essential for the identification of electrons and photons. In comparison the HCAL has a much coarser granularity that is designed for jet reconstruction and measurements of missing transverse momentum. Another function of the calorimetry is to complete contain the EM and hadronic showers and thus limit any EM or hadronic particles from entering into the muon detectors. This is accomplished with a minimum calorimeter depth

of 22 interaction lengths (χ_0) in the barrel and 24 in the endcaps.

3.4.1   Electromagnetic Calorimeter

The Electromagnetic Calorimeter consists of a central barrel region that covers $|\eta| < 1.475$ with two endcap sections covering $1.375 < |\eta| < 3.2$. The barrel is composited of two identical halves around $z = 0$, each one is comprised of 16 modules that cover $\pi/8$ of the ϕ plane. Each of the endcaps has two coaxial wheels, where the outer most wheel makes precise measurements of particles inside $1.375 < |\eta| < 2.5$ and the inner wheel makes lower resolution measurements in the region $2.5 < |\eta| < 3.2$. In the higher precision area of the ECAL ($|\eta| < 2.5$), it is split longitudinally into three sections.

It is a Liquid Argon (LAr) and lead sampling calorimeter designed to have complete ϕ symmetry without any gaps. The lead absorber plates are for initiating the EM showers of incident electron and photons. In between these plates are LAr sampling layers in which the particles in the EM shower ionise the Argon. The resultant current is collected by electrodes, these have a drift time of about 250 ns resulting in 2kV potential [33].

A digram showing the make up of the ECAL is shown in figure 3.5. There you can see the three different layers in the ECAL, the first being the $|\eta|$ strip layer. After that there is the middle layer that has a depth of $16\chi_0$, and a coarser granularity than the $|\eta|$ strip layer, this section is also designed to contain most of the energy of an EM shower. The back layer is twice as coarse in granularity than the middle layer and is primarily for stopping and leaking into the HCAL. There are some energy loses from 'dead material' in front of the ECAL, this is accounted for with the addition of a thin liquid argon layer called, the pre-sampler layer.
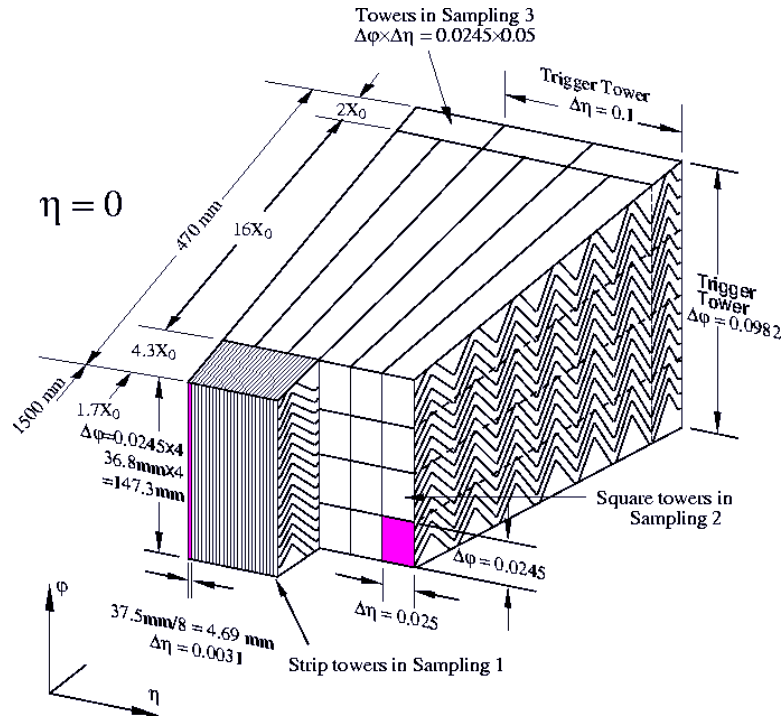
Figure 3.5: A sketch showing a cut-away of the barrel ECAL, and the granularity of the transverse and longitudinal layers [33].

3.4.2   Hadronic Calorimeter

The HCAL is very dense, this is to ensure that any entering hadrons come close enough to the nuclei in order to interact strongly with them, this causes the maximal number of particles are created. The hadronic shower is more complicated than the electromagnetic one, because leptons and neutrinos resulting from hadronic decays can also be created, making it tricky to get a good resolution on any energy measurements.

The HCAL is composed of three sub-detectors

- The tile calorimeter,

- The LAr hadronic end-cap calorimeter (HEC),

- The LAr forward calorimeter (FCal).

47

The tile calorimeter is situated just after the ECAL, starting at about $r = 2.28$ m and going out to about 4.25 m, it covers $|\eta| < 1.7$. The HEC is situated next to the electromagnetic end-cap calorimeter and is comprised of two wheels at each end-cap. The wheels have an outer radius of about 2 m, the HEC is in the range $1.5 < |\eta| < 3.2$. The FCALs are situated close to the beam axis around 4.7 m from the interaction point and cover the range $3.1 < |\eta| < 4.9$ [33].

3.5   The Muon Spectrometer

The muon spectrometers are the outermost layer of the ATLAS detector, completing the coverage around the interaction point. They are designed to measure the transverse momentum of charged particles with $|\eta| < 2.7$ that have passed through all the calorimetry by measuring the curvature of their path as they pass through the non-uniform toroidal magnetic field. This is mostly just muons, as they lose very little momentum in the rest of the detector. There is a however small probability that so called "punch through" hadrons can make it into the muon spectrometer, these are just hadrons that have enough momentum to make it all the way the HCAL.

A cross section of the muon system can be seen in 3.6. The p_T of the muons is measured very precisely by the Monitored Drift Tube (MDT) chambers in the $R - z$ plane. In this figure the MDTs are labelled with a three letter initialism, the first letter of which, 'B' or 'E' refers to the barrel and endcap sections of the muon system. The second letter refers to the position of the layer, either Inner, Middle or Outer and the final letter simply stands for Layer.
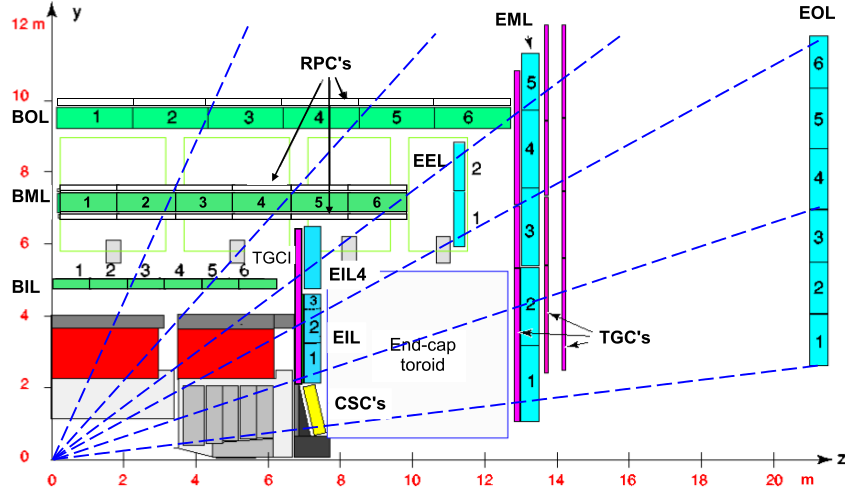
Figure 3.6: Cross-section of the muon system in a plane containing the beam axis, the bending plane. Muons with infinite momentum would move with straight trajectories, these are illustrated by the dashed lines and typically traverse three muon stations [41].

Each MDT is a pressurised drift tube (d=29.97mm) filled with an Argon CO_2 mixture the gas is held at a pressure of about 3 MPa. As a muon (or charged particle) passes through the tube, it ionises the gas, the electrons produced are collected by a tungsten wire (centrally located) which has a potential of 3080 V. Each chamber contains around 8 individual MDTs with an average resolution of around $80\mu m$ per tube. The chambers located closer to the barrel wheels, have the MDTs replaced with Cathode Strip Chambers (CSC, shown as the yellow box in figure 3.6), these have a higher resolution than the MDTs which means they are better suited to cope with the high particle fluxes in that region. The CSCs have radial anode wires with the cathode strips located perpendicular, they generate hits by interpolating the ionisation charge on adjacent cathode strips. The muon system as a whole was designed to provide a resolution on the p_T of about 10% and to make precise p_T and charge measurements for tracks of up to $\sim 3\text{TeV}$ [41]. This was a requirement as many new physics models will have a high p_T muon involved in the event, including one of the channels in which the Higgs Boson was first observed, $H \to ZZ(^*) \to \ell\ell\ell\ell$. Figure 3.7 shows the momentum resolution measured with 2.54fb^{-1} of 7 TeV data from $Z \to \mu\mu$ decays.
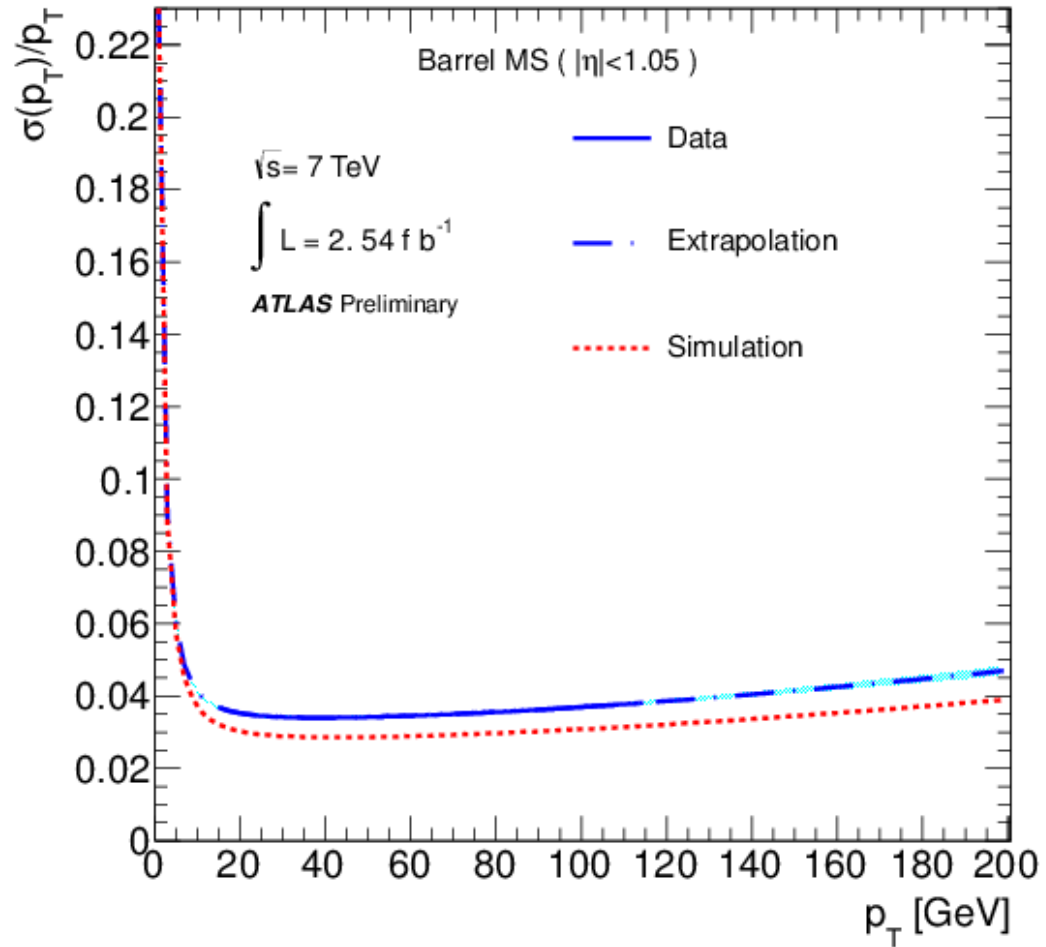
Figure 3.7: Resolution curve from the fitted parameter values on the MS (top) in collision data and simulation as a function of the muon p_T, for the barrel region. The solid blue line shows determinations based on data, the dashed blue line shows the extrapolation to a p_T range not accessible in this analysis and the dashed red line shows the determination from simulation [42].

3.6   Triggers

The high luminosities that are present at the LHC provide a problem for experiments searching for new and interesting physics, there are a lot of events that are uninteresting, that is to say events that have no potential to contain anything new. So to get around this a system was put into place so that not all of the events were recorded for further analysis, an event is classified as scientifically "interesting" and deserves to be recorded by this three-levelled system that is known as the Trigger. It was designed to operate at a luminosity of $10^{34}cm^{-2}s^{-1}$ where the event rate is expected to be around 1 GHz, and to reduce the rate to be recorded to about 200 Hz for further analysis. This requires that approximately 5×10^6 events per second need to be rejected, coupled with the fact there are bunch crossings at the interaction point every 25 ns, means that the system needs to be incredibly fast. It is comprised of an algorithm that works inside the detector (referred to as 'online') to decided if the event is interesting, this is known as the 'level 1' (L1) trigger. If an event passes the L1 trigger it gets saved and can then be processed offline by a High Level Trigger (HLT), this is itself split into two parts, the 'level 2' (L2) and the Event Filter (EF).

For many of the ATLAS analyses (including the ones presented in this thesis), the L1 trigger is used to find high p_T objects. For this, a subset of the detector systems, including the calorimeters and parts of the muon system (TPCs and TPCs), but excluding the ID, are used to provide the L1 with the information required to select which events to save. When an event is found to have passed the L1 trigger threshold, it is passed onto the HLT, otherwise it is deleted. Additionally to this, a randomly triggered selection of events are saved to disk; these are used to calibrate recognition and reconstruction algorithms.
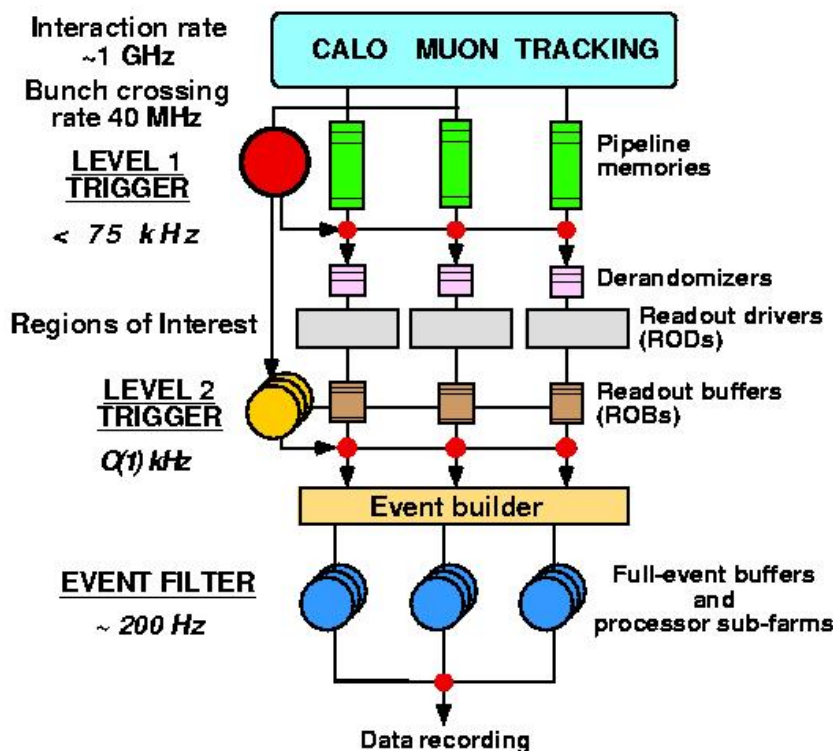
Figure 3.8: A sketch of the layout of the ATLAS trigger system [43].

3.6.1 L1 Trigger

After each bunch crossing has occurred all the detector information is time stamped and sent to memory located on the readout electronics. The decision by the L1 trigger has to get to the electronics, to reject or save the event data, within 2.5 μs of the bunch crossing having occurred (otherwise it will get overwritten). Due to this constraint this process can handle a maximum event rate of about 75 kHz. Those events that pass through the L1 trigger are then moved in to the readout drivers (RODs) and then into the readout buffers (ROBs), of which there are around 1700 in total. To make sure that the data can be read out of the memories with the available bandwidth of the RODs, there is an intermediate buffer system, all of these components of the L1 trigger can be seen in figure 3.8.

3.6.2 HLT

The HLT is very different to L1, the L1 is completely based in hardware, conversely the HLT is software based. It runs on a dedicated cluster farm of around 2000 computing elements (using commercially available hardware). The L2 and the EF trigger algorithms utilise the full calorimetry and muon sub detectors combined with some information from the inner detector.

The HLT acts on the detector data whilst it is being held in the ROBs, they are then either rejected or transferred to a storage area to be further processed by the EF trigger. The L2 trigger functions by looking at 'regions of interest' that have been passed on by the L1 algorithms, these are geometric regions of the detector in which physics objects have been identified by the L1 trigger. The L2 trigger then runs further analysis on these objects to identify them more precisely, this process takes about 40 ms and reduces the event rate fed into the EF to about 3.5 kHz

3.7 Event Reconstruction

When all the trigger decisions have been processed, the events that have passed have to be reconstructed. The specific reconstruction algorithms will not be discussed here. The output of the EF is directly used for the reconstruction algorithms, which can take one of three forms varying on the intended purpose. For calibration efforts there is the Event Summary Dataset (ESD), for analyses there is the Analysis Object Dataset (AOD) and there is also the TAG datasets which were created to enable rapid searches through all the events by providing thumbnail information about all the individual events. The AOD and the ESD are both "object orientated" this means that they are classified as to what the data set actually contains, "muon candidates", "tau candidates" etc.
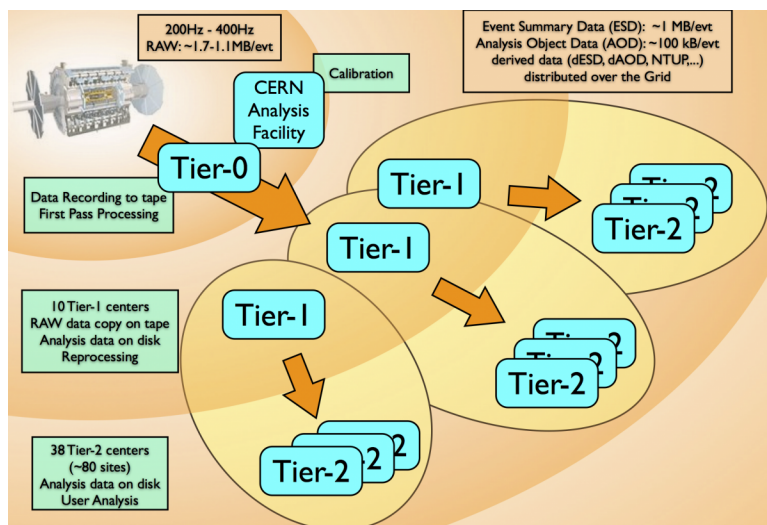
Figure 3.9: A digram showing the different Tiers of ATLAS [44].

This process is incredibly computationally intensive and can only be realistically achieved using large scale computing centres. This is the purpose of the Grid, the tier structure of the grid is shown in figure 3.9. Tier-0 is located centrally at CERN and houses all the initial events outputted directly from the EF, copies are sent to one of the 10 tier-1 centres, where they are processed into either AOD, ESD or TAG datasets. Further processing is still required to make these datasets more readily usable, individuals or specific physics groups can then, using the Athena software tools [45], make smaller more specific datasets called Derived Physics Datasets (DPD). As it is still very computationally heavy this is done at tier-2 sites, of which there are many. From these sites, datasets that are being used in analyses can be gotten and used by individual analysts and investigated using the ROOT analysis framework [46].

Chapter 4

The Identification of Hadronically Decaying Tau Leptons

4.1 Introduction

Tau leptons are the heaviest of the known leptons, they have a mass of 1.777 GeV [47] and a decay length of 87 μm. They decay before reaching the inner detector, and can only be identified from reconstructing their decay products. Because of their high mass, they have a unique (among leptons) decay mode, that is that they can decay to hadrons. In this decay mode (around 65% of the total), the tau lepton decays into a neutrino and a virtual W boson, which then decays into a pair of quarks, which, in the one prong case form a charged pion, but with mush less frequency can also form other mesons as well, such as a ρ or a a_0 meson, which then decay into further charged pions. You can see Feynman diagrams of tau decays in Figures 4.1 and 4.2. The neutrino in the decay is undetected by ATLAS, which leaves a problem for a full reconstruction of the system. One solution to this will be dealt with later on in Chapter 6. Aside from the neutrinos, the tau leptons are reconstructed as a jet of particles in the detector,

this feature means that one of the main sources of backgrounds is gluon or quark initiated jets (i.e. QCD jets). The narrow shower shape and a distinct number of tracks characterise hadronic tau decays, 1-prong with 1 track and 3-prong with 3 tracks. Neutral pions are not taken into account for tau identification and reconstruction.

The remaining 35% of the tau lepton decays, are leptonic where the decay products principally are electrons or muons. In these modes, because of the short lifetimes of τ leptons and the associated neutrino (which is also present in the hadronic decay but is slightly less of a problem) accurately identifying and discriminating the decay products of tau leptons from prompt electrons and muons is very difficult. As such, leptonically decaying tau leptons will not be covered in depth in this section.
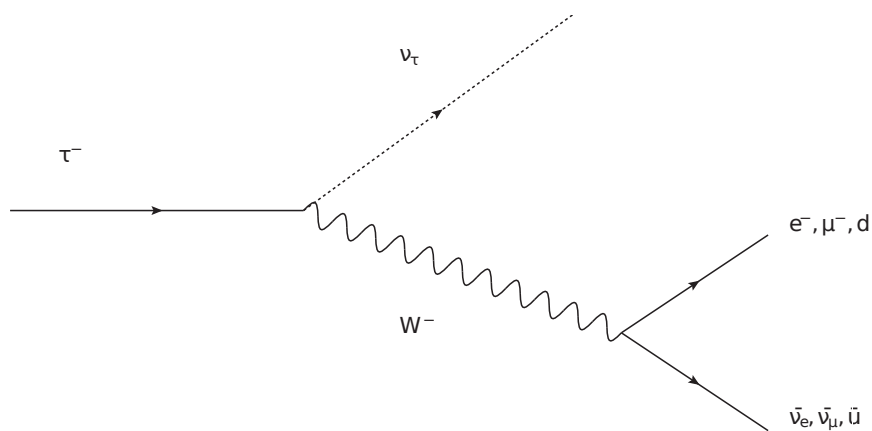
Figure 4.1: τ^- decay showing leptonic and hadronic modes.
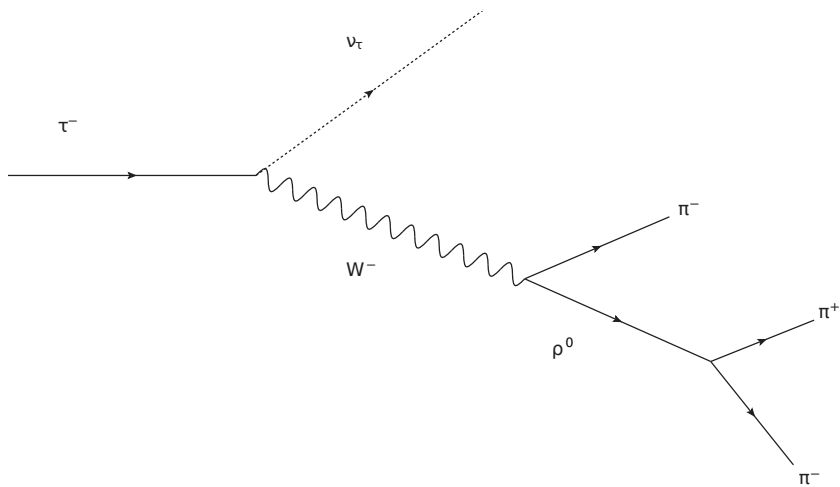
Figure 4.2: τ^- 3 pronged decay.

Hadronically decaying tau leptons play a very important role in various physics analyses in ATLAS, they can cover Standard Model measurements, Higgs searches and beyond the Standard Model searches. This means that the work on the identification and reconstruction of visible τ_h (hadronically decaying tau lepton) is continuously being updated, optimised and expanded upon; to better suit the needs of all of the tau analyses.

In the studies presented in this section the following simulated event samples were used. Z, W and $t\bar{t}$ events were produced using PYTHIA [48] and ALPGEN [49]. PYTHIA is also used to produce Z' samples with masses of 250 GeV, 500 GeV, 750 GeV, 1 TeV and 1.25 TeV. The response of the ATLAS detector is simulated using GEANT4 [50] with the `QGSP_BERT` shower model for the description of the hadronic showers [51]. In addition, samples simulated using the `QGSP` and `TFTP_BERT` shower model are used for the estimation of systematic uncertainties [52].

4.2 Reconstruction of Hadronic Tau Decays

The signature in the detector for hadronically decaying tau leptons is similar to that associated with jets and other leptons. Therefore, it is of critical importance to use combined information from as many sub-detectors as possible to

reconstruct hadronically decaying taus and differentiate them from objects with similar detector signatures. In order to accomplish this, dedicated reconstruction algorithms are used for visible τ_h, combining both tracking and calorimeter information. The following section describes the basic reconstruction of hadronically decaying taus in ATLAS.

4.2.1 Overview

The visible τ_h reconstruction in the ATLAS detector is seeded from reconstructed jet objects by considering each jet object as a visible τ_h candidate. The calorimeter cluster associated to each of these candidates is then refined and used to calculate kinematic quantities. Tracks satisfying the dedicated selection criteria are associated to the calorimeter clusters. Identification variables are then calculated using both tracking and calorimeter information. The variables are combined into multi-variate methods in order to discriminate jets as leptons that have been falsely identified as visible τ_h.

There are pre-defined selection criteria, based on the output of the discriminants, used at the analysis level to select a sample of visible τ_h candidates with the desired level of background rejection and signal efficiency.

4.2.2 Reconstruction Seeds

The reconstruction algorithms for visible τ_h are seeded from jet-objects that have been reconstructed using the anti-k_t algorithm [53], with a distance parameter $R = 0.4$. Topological clusters [54] made of calorimeter cells calibrated using the Local Hadron Calibration (LC) [55] are used as an input for the jet object algorithm. All jet objects with a $p_T \geq 10$ GeV and with an $|\eta| \leq 2.5$ (which corresponds to the η coverage of the ATLAS tracking system), are used as seeds. More information on the co-ordinate system used in the ATLAS detector can be found in Section 3.1.2.

4.2.3 Vertexing and Track Association

Tracks are associated with each visible τ_h candidate if they are within the "core cone", which is a region defined to be within $\Delta R < 0.2$ of the axis of the seed jet. They must also satisfy the following quality control criteria from the inner detector, pixel and SCT sub-detector systems:

- $p_T > 1$ GeV,

- Number of pixel hits ≤ 2,

- Number of pixel hits + number of SCT hits ≤ 7,

- $|d_0| < 1.0$ mm,

- $|z_0 \sin \theta| < 1.5$ mm.

Where d_0 is the distance of closest approach of the track to the reconstructed primary vertex in the transverse plane, while z_0 is the longitudinal distance of closest approach.

As the number of interaction vertices per beam crossing (pile-up), increases, the ability for general tracking to correctly identify the primary vertex decreases when using the default primary vertex. This is defined as the candidate with the highest $\sum (p_T^{trk})^2$ [56]. The visible τ_h track association, specifically the $|z_0 \sin \theta|$ requirement is sensitive to the primary vertex reconstruction; this sensitivity therefore affects the visible τ_h reconstruction and identification. To account for this the Tau Jet Vertex Association (TJVA) algorithms were created and will be described later in this section.

The visible τ_h candidates are classified as n-prong which depends on the number n of tracks counted in the core cone. Multi-prong, refers to the visible τ_h candidates with more than one track. Tracks within the isolation annulus, defined as $0.2 < \Delta R < 0.4$ of the axis of the seed jet, are counted for the calculation of some variables, and are also required to satisfy the same track quality criteria.

The probability of incorrectly reconstructing a primary vertex is much higher with the increased pile-up that comes as a result of higher beam luminosities in the LHC. This causes tracks to fail the z_0 impact parameter requirement, as
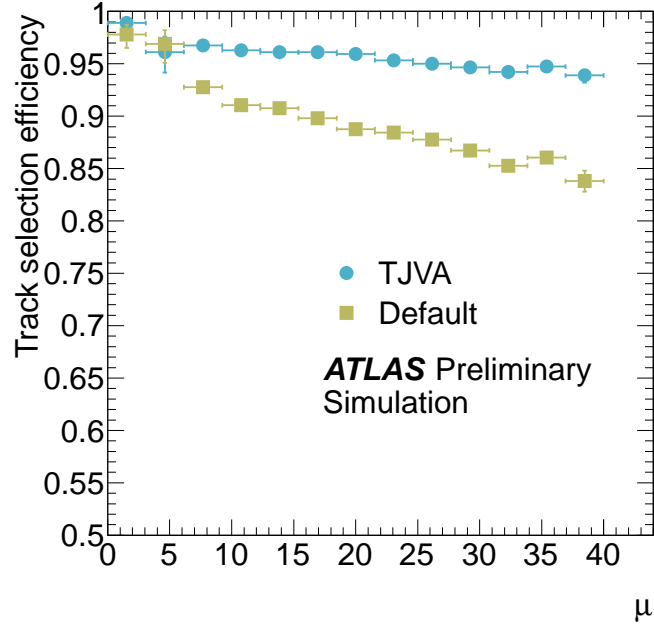
(a) Truth matched 1-prong τ
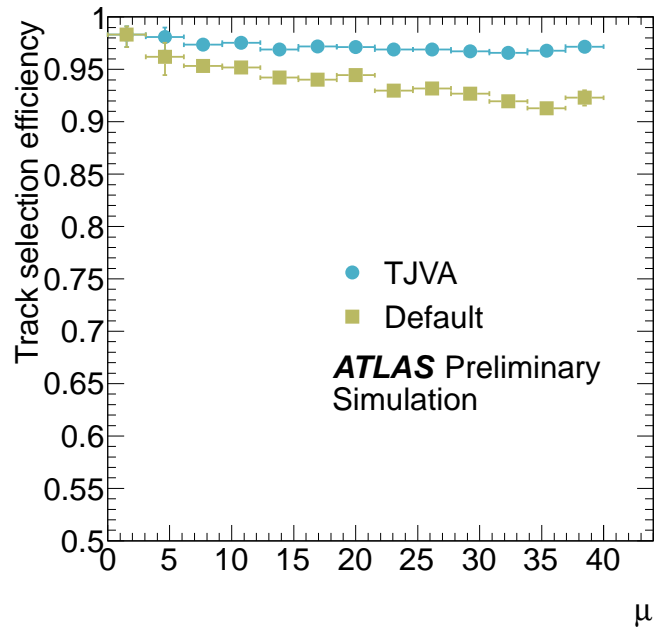
(b) Truth Matched 3-prong τ

Figure 4.3: The visible τ_h track selection efficiency with respect to the average number of pile-up interactions per bunch crossing (μ) for reconstructed visible τ_h candidates in $Z \to \tau\tau$ simulated events. Only visible τ_h candidates with $p_T > 15$ GeV matching to a true-tau within $\Delta R < 0.2$ are considered. With TJVA, the visible τ_h track multiplicity is less sensitive to pile-up and with increasing μ, a smaller degradation in the efficiency is observed [57].

60

observed in simulated $Z \to \tau\tau$ events. In Figures 4.3a and 4.3b, the visible τ_h track selection performance is degraded with increased pile-up conditions. These inefficiencies affect the number of tracks associated with the reconstructed visible τ_h objects as well as the calculation of many variables used for the visible τ_h identification algorithms(4.2.4).

To make sure that the visible τ_h track association method is pile-up robust, an algorithm was developed to correctly identify the primary vertex for each visible τ_h candidate. This algorithm, the TJVA is built using the existing Jet Vertex Association (JVA) algorithm. The JVA algorithm works by finding for each jet a vertex candidate with the highest Jet Vertex Fraction (f_{JVF}), calculated using the following formula:

$$f_{JVF}(jet|vtx) = \frac{\sum p_T^{trk|vtx}}{\sum p_T^{trk}} \tag{4.1}$$

Where $f_{JVF}(jet|vtx)$ is the jet vertex fraction of a jet given a vertex candidate, "$trk|vtx$" refers to a track matched to a given vertex and "trk" in the denominator refers to tracks in the jet. The track-vertex matching can be customised using the impact parameter and the longitudinal distance. Also, the set of tracks used in the calculation of the f_{JVF} can be customised by applying selection criteria on the track kinematics and quality criteria. This is illustrated in Figure 4.4.

TJVA uses the Tau Jet Vertex Fraction (f_{TJVF}), which is calculated similarly to f_{JVF}. The track vertex match criteria are the same as for the f_{JVF} but the track selection parameters for f_{TJVF} were optimised for tracks originating from a τ_h decay. These optimised track selection criteria are the same criteria described above, apart form the impact parameters that were not used for this track selection.
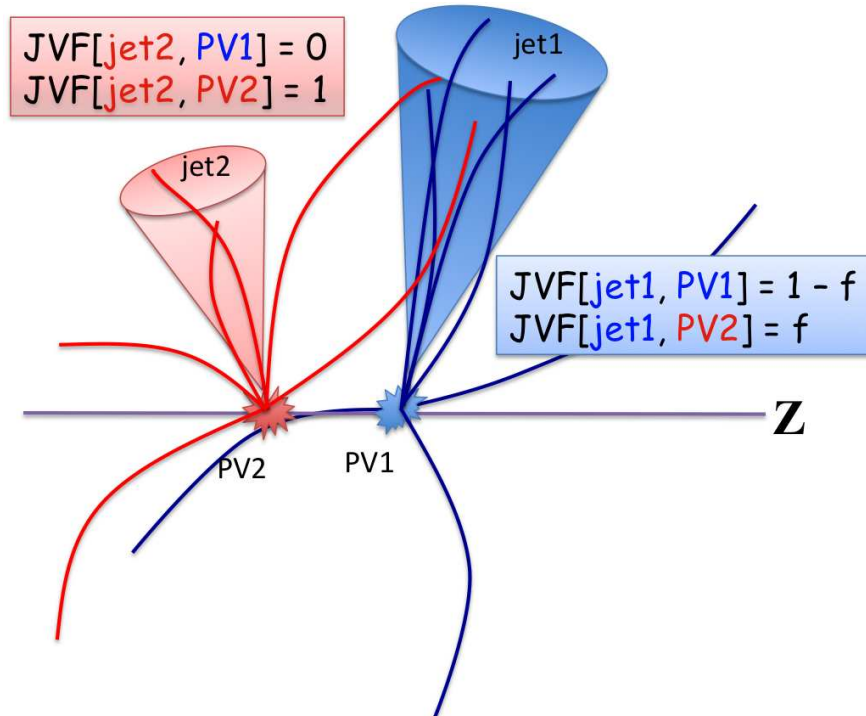
Figure 4.4: Depiction of the jet-vertex fraction discriminant [57].

4.2.4 Definition of Discriminating Variables

Throughout this project many different variables were used to help define or discriminate hadronically decaying tau lepton events. The definitions of these variables are given in the following section, and Table 4.1 outlines which specific part of the analysis they were used for.

Variable prongs	LLH ID 1-prong	LLH ID multi-prong	BDT ID 1-prong	BDT ID multi-prong	BDT e-veto 1-prong	Cut muon-veto 1-prong
f_{core}^{corr}	•	•	•	•	•	
f_{track}^{corr}	•	•	•	•	•	
f_{track}					•	•
R_{track}	•	•	•	•	•	
$S_{lead\ track}$	•		•			
N_{track}^{iso}	•		•			
ΔR_{max}		•		•		
S_{T}^{flight}		•		•		
m_{tracks}		•		•		
f_{EM}					•	•
f_{HT}					•	
$E_{T,max}^{strip}$					•	
$f_{HCAL}^{leadtrk}$					•	
$f_{ECAL}^{leadtrk}$					•	
f_{PS}					•	
$f_{EM}^{\pi^{\pm}}$					•	
f_{iso}					•	
R_{Had}					•	

Table 4.1: Comparison of variables used by the identification algorithms: projective likelihood identification (LLH ID), boosted decision tree identification (BDT ID), boosted decision tree based electron veto (BDT e-veto) and cut based muon veto (Cut muon-veto).

Many of these use two definitions for the transverse energy, $E_{T,i}$, is deposited in cell i of the calorimeters inside a cone of $\Delta R < 0.1$. $E_{T,j}$ is over all cells in the calorimetry inside a cone of $\Delta R < 0.2$ and both are calibrated using the EM energy scale [58].

Core Energy Fraction (f_{core}):

Fraction of transverse energy in the central region ($\Delta R < 0.1$) of the τ_h candidate such that:

$$f_{core} = \frac{\sum_{i\in\{all\}}^{\Delta R_i < 0.1} E_{T,i}^{EM}}{\sum_{j\in\{all\}}^{\Delta R_i < 0.2} E_{T,j}^{EM}} \tag{4.2}$$

The subscripts i and j represent the cells in all layers associated with the τ_h candidate and all of the cells in all of the layers in total, respectively. $E_{T,ij}$ is defined as above.

Pile-up Corrected core energy fraction (f_{core}^{corr}):

Pile-up corrected fraction of transverse energy in the central region ($\Delta R < 0.1$) of the τ_h candidate such that:

$$p_T < 80 GeV, f_{core}^{corr} = f_{core} + 0.03 \times N_{vtx} \tag{4.3}$$

$$else, f_{core}^{corr} = f_{core} \tag{4.4}$$

Where N_{vtx} is the number of good vertices in the event, defined as the number of pile-up vertices with at least 2 tracks plus the primary vertex, which is required to have at least 4 tracks. The p_T of the τ_h candidate is calibrated using the tau energy scale [58].

Leading Track Momentum Fraction (f_{track}):

$$f_{track} = \frac{p_T^{leadtrk}}{\sum_{j\in\{all\}}^{\Delta R_j < 0.2} E_{T,j}^{EM}} \tag{4.5}$$

Where, $p_T^{leadtrk}$ is the transverse momentum of the leading p_T core track of the τ_h candidate. $E_{T,j}$ is defined as above.

For candidates with one track, f_{track} is the fraction of the candidates momentum attributed to the track, compared to the total momentum of the candidate, which can have contributions from the calorimeter deposits from π^0s and other neutral particles.

Pile-up Corrected Leading Track Momentum Fraction (f_{track}^{corr}):

Pile-up corrected momentum for the leading track.

$$f_{track}^{corr} = f_{track} + 0.03 \times N_{vtx} \tag{4.6}$$

Where N_{vtx} is the number of good vertices in the event, defined as the number of pile-up vertices with at least 2 tracks plus the primary vertex, which is required to have at least 4 tracks.

Track Radius (R_{track}):
p_T-Weighted track width:

$$R_{track} = \frac{\sum_i^{\Delta R_i \leq 0.4} P_{T,i} \Delta R_i}{\sum_i^{\Delta R_i \leq 0.4} P_{T,i}} \tag{4.7}$$

Where, i runs over all core and isolation tracks of the τ_h candidate, within $\Delta R_i \leq 0.4$. ΔR_i is defined relative to the τ_h intermediate axis and $P_{T,i}$ is the track transverse momentum.
For candidates with only one track in the core cone and isolation annulus, R_{track} simplifies to the ΔR between the track and the intermediate axis.

Maximum ΔR (ΔR_{max}):
The maximal ΔR between a track associated to the τ_h candidate and the intermediate axis. Only core tracks are considered.

Transverse Flight Path Significance (S_T^{flight}):
The decay length significance of the secondary vertex for multi-track τ_h candidates in the transverse plane:

$$S_T^{flight} = \frac{L_T^{flight}}{\delta L_T^{flight}} \tag{4.8}$$

Where, L_T^{flight} is the reconstructed decay length and δL_T^{flight} is its estimated uncertainty. Only core tracks are used for the secondary vertex fit.

Electromagnetic Fraction (f_{EM}):
Fraction of transverse energy of the τ_h candidate deposited in the EM

calorimeter:

$$f_{EM} = \frac{\sum_{i \in \{EM0-2\}}^{\Delta R_i < 0.2} E_{T,i}^{EM}}{\sum_{j \in \{all\}}^{\Delta R_j < 0.2} E_{T,j}^{EM}} \tag{4.9}$$

Where, $E_{T,i}$ $(E_{T,j})$ is defined as above however it only takes into account first three layers of the EM calorimeter (0,1,2). ΔR_i is defined relative to the τ_h candidates intermediate axis.

Leading Track Impact Parameter Significance ($S_{leadtrack}$):

Impact parameter significance of the leading track of the τ_h candidate in the core region:

$$S_{leadtrack} = \frac{d_0}{\delta d_0} \tag{4.10}$$

Where, d_0 is the distance of closest approach of the track to the tau vertex in the transverse plane and δd_0 is its estimated uncertainty.

Number of Tracks in Isolation Annulus (N_{track}^{iso}):

Number of tracks reconstructed within $0.2 < \Delta R \leq 0.4$ around the intermediate axis.

Number of Isolation Tracks (N_{track}^{iso}):

The number of tracks in the isolation annulus.

Calorimetric Radius (R_{Cal}):

The shower width in the electromagnetic and hadronic calorimeter weighted by the transverse energy of each calorimeter part:

$$R_{Cal} = \frac{\sum_{i \in \{all\}}^{\Delta R_i < 0.4} E_{T,i} \Delta R_i}{\sum_{i \in \{all\}}^{\Delta R_i < 0.4} E_{T,i}} \tag{4.11}$$

Where, i runs over all cells in all layers of the EM and hadronic calorimeters. Only cells in the wide cone ($\Delta R < 0.4$) are considered.

Cluster Mass ($m_{eff.clusters}$):

The invariant mass computed from the constituent clusters of the seed jet,

calibrated at the LC energy scale.

$$m_{\text{eff. clusters}} = \sqrt{\left(\sum_{clusters} E\right)^2 - \left(\sum_{clusters} \mathbf{P}\right)^2} \qquad (4.12)$$

To minimise the effect of pileup, only the first N leading E_T clusters (effective clusters) are used in the calculation, defined as:

$$N = \frac{\left(\sum_i E_{T,i}\right)^2}{\sum_i E_{T,i}^2} \qquad (4.13)$$

Where, i runs over all clusters associated to the tau candidate, and N is rounded up to the nearest integer.

Track Mass (m_{tracks}):

The invariant mass of the track system, where both core and isolated tracks are used for the invariant mass calculation:

$$m_{tracks} = \sqrt{\left(\sum_{tracks} E\right)^2 - \left(\sum_{tracks} \mathbf{P}\right)^2} \qquad (4.14)$$

Corrected Cluster Isolation Energy ($E_{T,corr}^{iso}$):

The transverse energy of isolated clusters:

$$E_{T,corr}^{iso} = E_T^{iso} - \sigma E_T^{iso} \qquad (4.15)$$

$$= \sum_i^{0.2 < \Delta R_i < 0.4} E_{T,i} - \sigma E_T^{iso} \qquad (4.16)$$

Where, i runs over all clusters associated to the τ candidate. ΔR_i is defined between the cluster and the tau candidate axis. The pileup correction term is defined as $\sigma E_T^{iso} = (1 - JVF) \times \sum P_{T,trk}$, where JVF is the jet vertex fraction of the jet seed of the tau candidate, calculated with respect to the primary vertex and $\sum P_{T,trk}$ is the sum of the transverse momentum of the

tracks associated to that jet.

The following Variables are only used in the electron veto, this will be discussed in more detail in Section 4.3.2:

TRT HT fraction (f_{HT}):

The ratio of high-threshold to low-threshold hits (including outlier hits), in the Transition Radiation Tracker (TRT) for the leading p_T core track. Since electrons are lighter than pions, and therefore have higher Lorentz γ factors, they are more likely to produce the transition radiation that causes high threshold hits in the TRT [59]. This variable can be used to discriminate hadronic 1-prong τ_h candidates from electrons.

Secondary Energy Deposited in the Strip Layer ($E_{T,max}^{strip}$):

The energy in the strip layer of the EM Calorimeter is summed over three cells in ϕ and local maxima are searched for and summed for cells in an η region centred around the impact point of the leading track associated to the tau candidate. The energy associated to the leading track is excluded. This variable is only calculated for $|\eta^{leadtrk}| \leq 1.7$ where the TRT provides discrimination power between electrons and hadrons.

Ratio Between Energy in the Hadronic Calorimeter and Leading Track Momentum ($f_{HCAL}^{leadtrk}$):

$$f_{HCAL}^{leadtrk} = \frac{\sum_{l=0}^{N_{cell}} E_T^l}{p_T^{leadtrk}} \tag{4.17}$$

Where, l runs over calorimeter cells associated to the τ_h candidate. The energy deposit in the first layer of the hadronic calorimeter in a window of $\Delta\phi \leq 0.2$ and $\Delta\eta \leq 0.2$ around the extrapolation of the leading track to the calorimeter surface is summed up. To compensate for the missing of the first layer of the hadronic calorimeter in the transition region of the barrel, the energy of the full hadronic calorimeter depth is collected in the region of $0.8 \leq |\eta| < 1.2$. $p_T^{leadtrk}$ denotes the transverse momentum of the leading track associated to the τ_h candidate in the core region.

Ratio Between Energy in the EM Calorimeter and Leading Track Momentum ($f_{ECAL}^{leadtrk}$):

$$f_{ECAL}^{leadtrk} = \frac{\sum_{l=0}^{N_{cell}} E_T^l}{p_T^{leadtrk}} \qquad (4.18)$$

Where l runs over all calorimeter cells associated to the τ_h candidate. Only cells from the presampler and first three layers of the barrel are taken into account. The energy is calculated in the window $(\Delta\eta \times \Delta\phi)$ around the extrapolation of the leading track to the calorimeter surface: 0.075×0.3 in presample, 0.0475×0.3, 0.075×0.075, 1.5×0.075 for the first, second and third layer, respectively. $p_T^{leadtrk}$ denotes to the transverse momentum of the leading track associated to the τ_h candidate in the core region.

Presample Strip Energy Fraction (f_{PS}):

$$f_{PS} = \frac{\sum_{l=0}^{N_{clus}} E_l^{PS}}{\sum_{l=0}^{N_{clus}} E_l} \qquad (4.19)$$

Where, l runs over calorimeter clusters associated to τ_h candidates, E_l^{PS} denotes the part of the cluster energy, calibrated using the Local Hadron Calibration (LC) scale, deposited in the presampler layer of the calorimeter and E_l is the total energy of a calorimeter cluster.

Electromagnetic Energy of Charged Pions Over Calorimetric Electromagnetic Energy ($f_{EM}^{\pi^\pm}$):

$$f_{EM}^{\pi^\pm} = \frac{\sum_i^{\Delta R \leq 0.2} P_i^{trk} - \sum_{l=0}^{N_{clus}} E_l^{Had}}{\sum_{l=0}^{N_{clus}} E_l^{EM}} \qquad (4.20)$$

Where, l runs over calorimeter clusters associated to τ_h candidates, E_l^{Had} denotes the part of the cluster energy deposited in the hadronic part of each cluster (including the third layer of the EM calorimeter), E_l^{EM} is the part of the cluster energy deposited in the electromagnetic part of each the calorimeter (pre-sampler and first two layers) and i runs over tracks

associated to the τ_h candidate in the core region. All clusters are calibrated using the LC energy scale.

Ring Isolation (f_{iso}):

$$f_{iso} = \frac{\sum_{i\in\{Had\}}^{0.1<\Delta R<0.2} E_{T,i}^{EM}}{\sum_{j\in\{Had\}}^{\Delta R<0.2} E_{T,j}^{EM}} \tag{4.21}$$

Where, $E_{T,i}$ ($E_{T,j}$) is the transverse energy, calibrated at the EM energy scale, deposited energy scale, deposited in cell i (j), and i is run over all calorimeter cell in all layers in the associated topocluster of the τ_h candidate in an annulus of $0.1 < \Delta R < 0.2$ around the intermediate axis, while j runs over cells in a cone of $\Delta R < 0.2$.

Hadronic Radius (R_{Had}):

Transverse energy weighted shower width in the hadronic (Had) calorimeter:

$$R_{Had} = \frac{\sum_{i\in\{Had\}}^{\Delta R_i<0.2} E_{T,i}^{EM} \Delta R_i}{\sum_{i\in\{Had\}}^{\Delta R_i<0.2} E_{T,i}^{EM}} \tag{4.22}$$

Where, $E_{T,i}$ is the transverse energy, calibrated at the EM energy scale, deposited in cell i and i runs over cells in the hadronic calorimeter and also layer 3 of the EM calorimeter within $\Delta R_i \leq 0.2$. ΔR_i is defined relative to the τ_h candidate intermediate axis.

4.3 Identifying Hadronic Tau Decays

For the identification of hadronically decaying tau leptons, cut-based and multivariate techniques are used. This section describes two approaches to discriminate visible τ_h from jets: a Log Likelihood Function method (LLH) and a Boosted Decision Tree (BDT) method. It is followed by a description of BDTs used for the rejection of electrons and a cut-based method for the rejection of muons.

4.3.1 Jet Discrimination

In the LHC there is a high rate of quark and gluon seeded jets, these have a detector signature that is very similar to that of hadronically decaying τ leptons. That is why they are one of the main source of backgrounds for them. The reconstruction method offers very little rejection against them, which is why a dedicated algorithm for this purpose, generally referred to as the tau ID, is required.

For the training of these algorithms, simulated $Z \to \tau\tau$, $W \to \tau\nu$ and $Z' \to \tau\tau$ samples are used for the signal samples. Z' samples with a mass of 250-1250 GeV (in 250 GeV steps) are used to enhance the number of high p_T visible τ_h candidates. However, only properly reconstructed τ_h candidates that satisfy $|\eta| < 2.3$ and $p_T > 15$ GeV are considered for the training and have to lie within a cone of $\Delta R < 0.2$ of the visible position of the truth match τ_h decay. For the visible part of the decay, the neutrino is ignored. The visible true τ_h decays have to be in the fiducial region $|\eta_{vis}^{true}| < 2.5$, P_{Tvis}^{true} and $N_{prong}^{true} = 1$ or 3. In the tau ID algorithms, three groups of visible τ_h candidates are used:

a) *1-prong* candidates with one reconstructed track matched to a true τ_h with one charged hadron,

b) *3-prong* candidates with three reconstructed tracks matched to a true τ_h with three charged hadrons,

c) *multi-prong* candidates with two or three reconstructed tracks matched to a true τ_h with three charged hadrons.

For the QCD backgrounds, a jet enriched data sample from 2011 (for the BDT) and 2012 (for the LLH) is used for training purposes. For the validation of both methods, data from early 2012 were used. The background visible τ_h candidates have to fulfil the same cut as before ($|\eta| < 2.3$ and $p_T > 15$ GeV). The three groups of candidates are defined as above, requiring one reconstructed track (1-prong), three reconstructed tracks (3-prong) and two or three reconstructed tracks (multi-prong).

Reconstruction and identification efficiencies for signal events are defined as the

number of truth matched visible τ_h candidates passing identification divided by all true hadronic decays. Similarly the background efficiency is defined as the number of background visible τ_h candidates passing identification divided by the number of all background visible τ_h candidates.

4.3.1.1 BDT Method

The BDT based tau ID uses two individual training methods for 1-prong and 3-prong visible τ_h candidates, using the TMVA package [60]. The variables used in this method are listed and explained in Table 4.1 and in section 4.2.4. The BDT trained for 3-prong events is used for classifying all visible τ_h candidates with two or more tracks. Three working points *loose*, *medium* and *tight* are defined, corresponding to target efficiencies of 70%, 60% and 40% for 1-prong and 65%, 55% and 35% for multi-prong visible τ_h candidates, respectively.

In order to correct for the p_T dependence of the BDT in low-momentum region, the working points are determined in bins of true visible p_T. Using the $Z \to \tau\tau$ sample, 30 bins are chosen each with an equal number of visible τ_h candidates. The cut on the BDT score to attain the target efficiency is estimated separately for 1-prong and multi-prong candidates. The thresholds are then interpolated between bin centres and they are constrained to above 50 GeV. Plots showing the efficiencies as a function of the momentum are shown in Figures 4.5a- 4.5d. The sudden change of the efficiency at 80 GeV is because of a different pile-up correction applied to one of the calorimeter variables below and above this threshold (see Section 4.2.4). The BDT training is approximately independent of the pile-up conditions as shown in Figures 4.5e- 4.5h, therefore no binning (in order to the flatten the distribution) of the number of the number of vertices per event was performed.
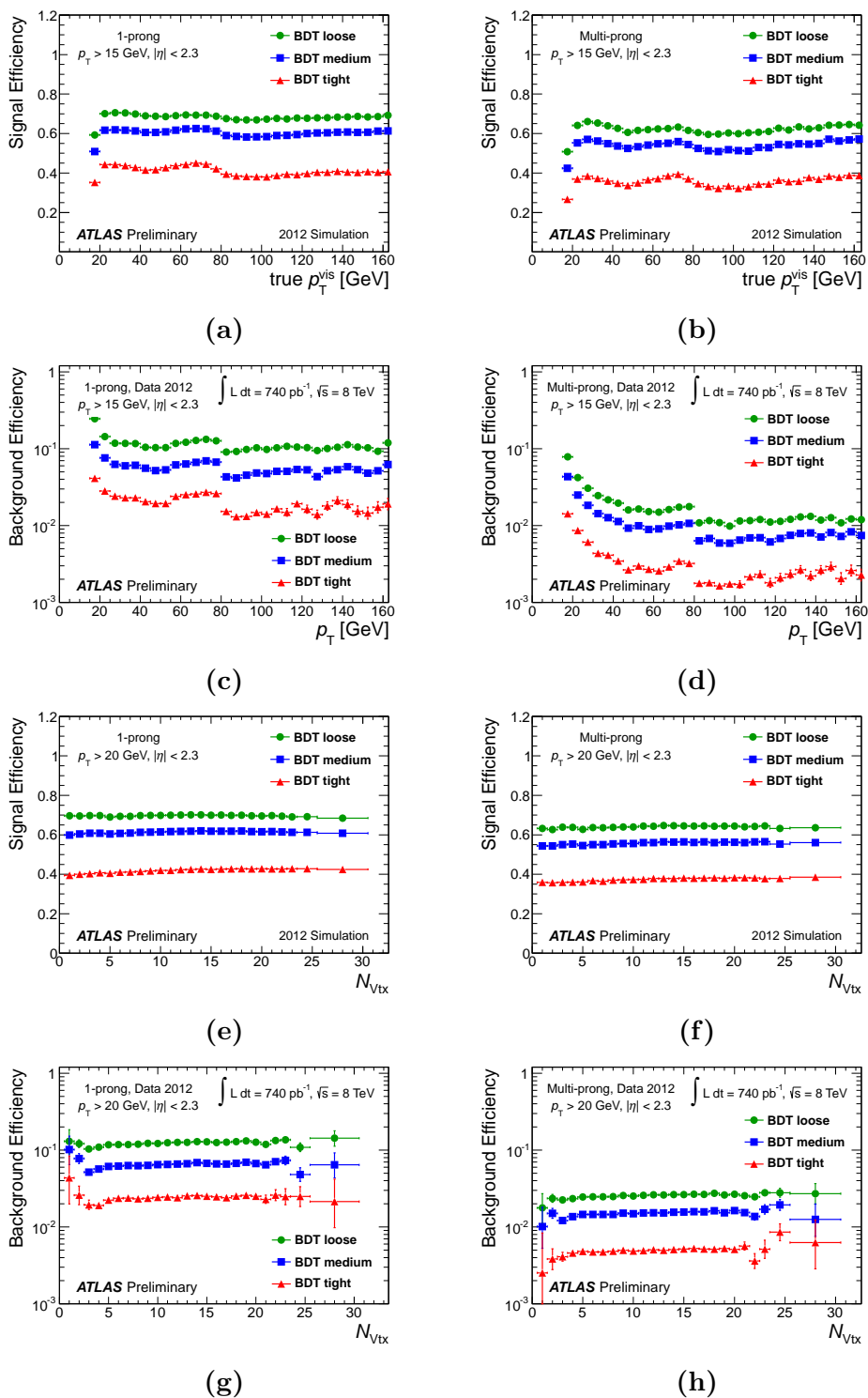
Figure 4.5: Signal and background efficiencies for 1-prong (left) and multi-prong (right) visible τ_h candidates for the three working points of the BDT tau ID as a function of true visible tau p_T for signal candidate (a) and (b), reconstructed p_T for background candidates (c) - (d) and number of vertices (e)-(h). The efficiencies were obtained using $Z \to \tau\tau$, $Z' \to \tau\tau$ and $W \to \tau\nu$ simulated samples for signal and multi-jet events from data for background [1].

4.3.1.2   Log Likelihood Function

The likelihood function $L_{S(B)}$ for signal (background) is defined as the product
of the distributions of the identification variables:

$$L_{S(B)} = \prod_{i=1}^{N} p_i^{S(B)}(x_i) \tag{4.23}$$

Where $p_i^{S(B)}(x_i)$ is the signal (background) probability density function of iden-
tification variable x_i of N variables. The likelihood function represents the joint
probability distribution for the identification variables [61], neglecting correla-
tions between the variables. The discriminant used by the likelihood method is
defined as the log-likelihood ratio between signal and background:

$$d = \ln\left(\frac{L_S}{L_B}\right) = \sum_{i=1}^{N} \ln\left(\frac{p_i^S(x_i)}{p_i^B(x_i)}\right) \tag{4.24}$$

The projective likelihood function uses the same set of discriminating variables as
the BDT ID(as shown in Table 4.1) to create one dimensional probability density
functions (PDFs).These PDFs are binned with according to the number of tracks
associated with the visible τ_h candidate (both 1 and 3 prong) and with the p_T
of the candidate. The p_T bins in this case are < 45 GeV, $45 - 100$ GeV and
> 100 GeV. Calculating the final likelihood score requires a liner interpolation
at the borders of each of the p_T bins. For each border, a symmetric window of
$[-10, +10]$ GeV is used, except for the 100 GeV border 1-prong visible τ_h, where
an asymmetric window of $[-30, +60]$ GeV is used.

To be consistent with the BDT ID, the same working points for *loose*, *medium* and
tight were used corresponding to target efficiencies of 70%, 60% and 40% for 1-
prong and 65%, 55% and 35% for multi-prong visible τ_h candidates, respectively.
To account for the p_T dependence of the likelihood score, cuts were determined
as a function of the true visible tau p_T so as to get an (approximately) flat
efficiency distribution (with respect to the p_T for each of the working points, and
each number of associated tracks. This can be seen for signal Monte Carlo and

background di-jet samples in Figure 4.6.

4.3.1.3   Performance

Both methods have compatible performance, as as shown in Figure 4.7. Background rejection factors of 10-40 for signal efficiencies of 70% are achieved, going up to 500 for 35% signal efficiency. In practice the background efficiency will depend on the event selection as it depends on the kinematics of the candidates considered and the type of partons that seeded the jets. The upper bound on the signal efficiency is subject to the efficiency loss due to the track selection during visible τ_h reconstruction.

4.3.2   Electron Discrimination

The characteristic signature of a 1-prong τ_h can be mimicked by electrons. This creates a significant background contribution after all the jet related backgrounds are suppressed via kinematic, topological and τ_h identification criteria. Despite all the similarities between the τ_h and electron signatures, there are several properties that can be used to discriminate between the two. The most useful examples of such properties are the emission of transition radiation of the electron track and the longer and wider shower produced by the hadronic tau decay products in the calorimeter, compared to the one created by an electron. The full list of variables used in the electron veto is shown in Table 4.1, these variables are specialised in the rejection and discrimination against, electrons that have been miss-identified as a τ_h. Before this, the only method for this used a Boosted Decision Tree (BDT) utilising the TMVA package [60]. Prior studies showed that the 3-prong τ_h could also be "faked" by electrons, however at the time of writing this has not been fully investigated.

The BDT for vetoing electrons is trained and optimized using simulated $Z \rightarrow \tau\tau$ events for the signal, and simulated $Z \rightarrow ee$ events for the background. Events from the signal sample are required to be truth matched to 1-prong τ_h decays, whilst those from the background sample are matched to truth matched electrons. Additionally, both signal and background events have to pass a cut of $p_T > 20$
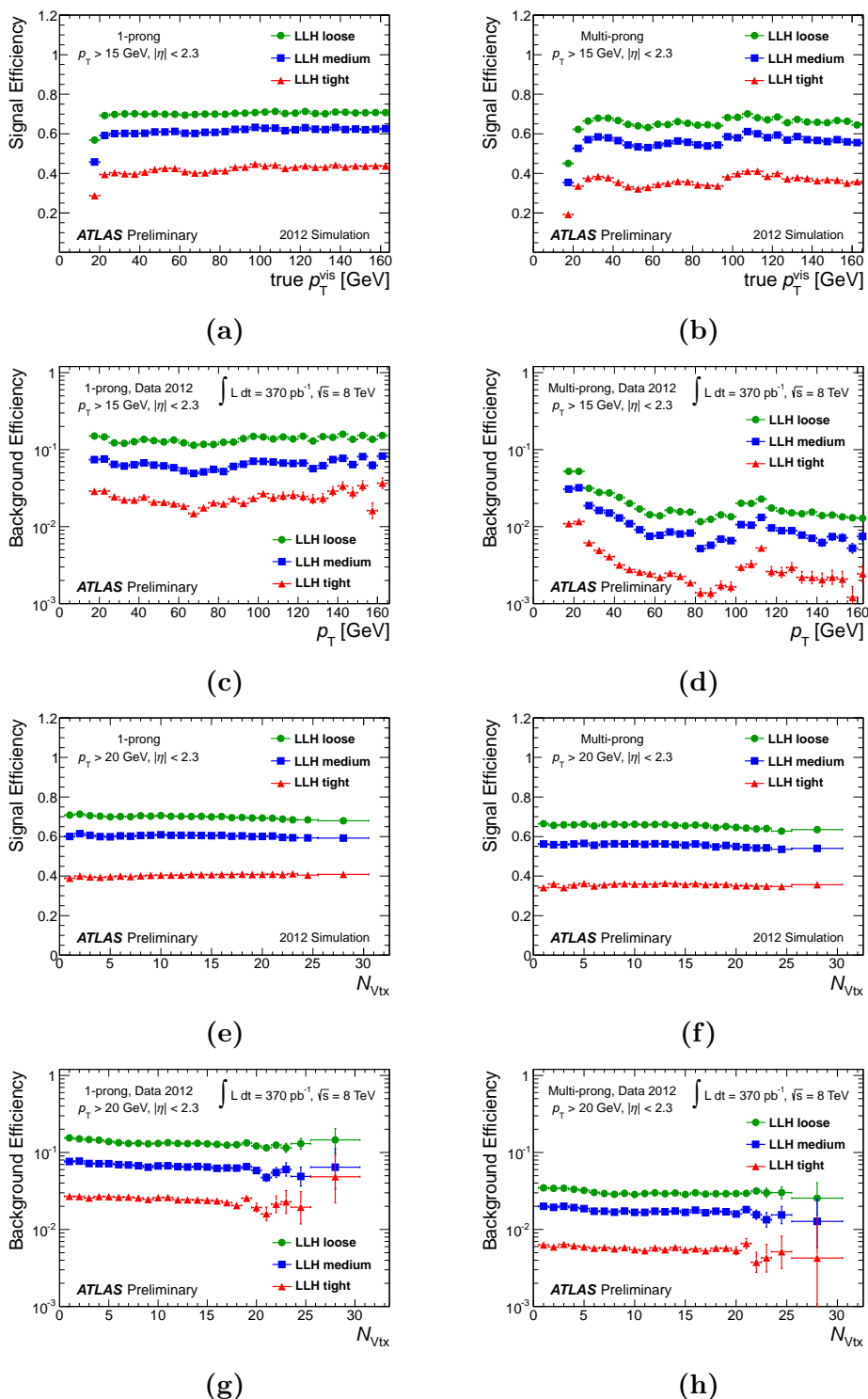
Figure 4.6: Signal and background efficiencies for 1-prong (left) and multi-prong (right) visible τ_h candidates for the three working points of the LLH tau ID as a function of true visible tau p_T for signal candidate (a) and (b), reconstructed p_T for background candidates (c) - (d) and number of vertices (e)-(h). The efficiencies were obtained using $Z \to \tau\tau$, $Z' \to \tau\tau$ and $W \to \tau\nu$ simulated samples for signal and multi-get events from data for background [1].
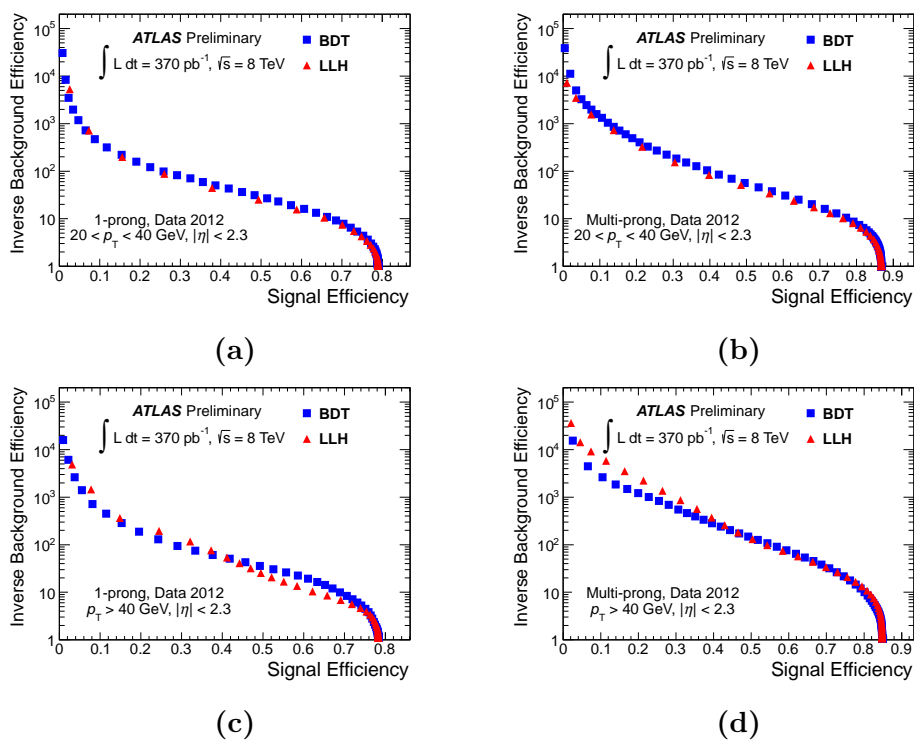
Figure 4.7: Inverse background efficiencies as a function of signal efficiency for 1-prong (left) and multi-prong (right) candidates, in low (top) and high (bottom) p_T ranges, for the two tau ID methods BDT and LLH. The signal efficiencies were obtained using $Z \to \tau\tau$, $Z' \to \tau\tau$ and $W \to \tau\nu$ simulated samples and the inverse background efficiencies from data multi-jet events [1].

GeV and a loose BDT tau ID. The electron veto BDT is trained for several different η regions, these are:

$$\text{Barrel - } |\eta| < 1.37$$

$$\text{Crack - } 1.37 < |\eta| < 2.0$$

$$\text{Endcap - } 2.0 < |\eta| < 2.3$$

$$\text{Beyond the endcap - } |\eta| > 2.3$$
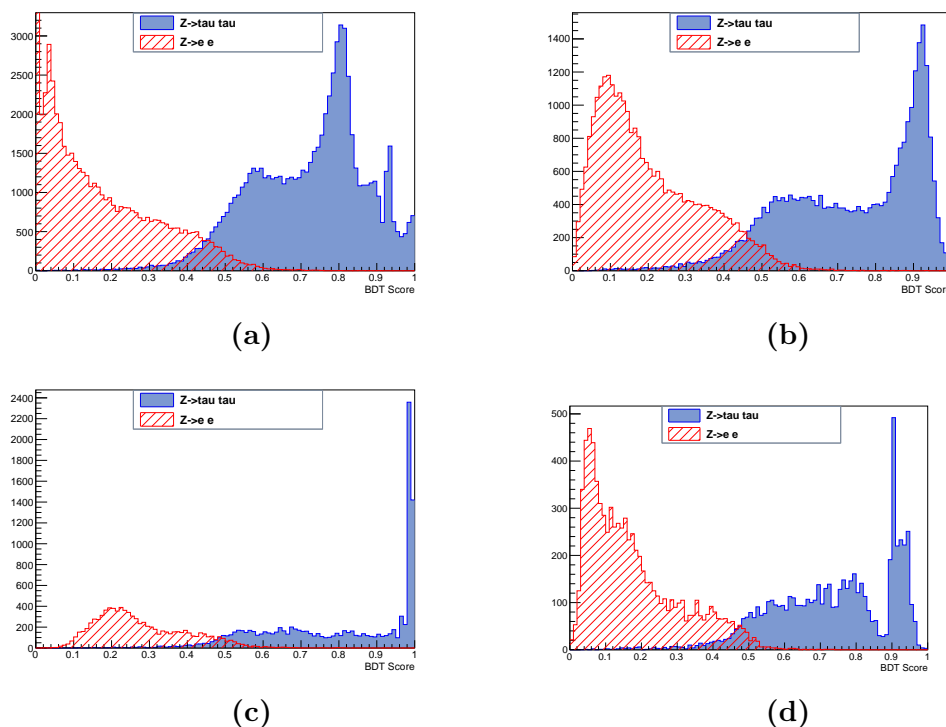
Figure 4.8: The level of discrimination between signal ($Z \to \tau\tau$) and background ($Z \to ee$). Each of the η regions are shown a) barrel, b) crack, c) endcap and d) beyond the endcap.

A plot showing signal against background efficiencies for each of the different η regions is shown in Figure 4.9. The electron veto BDT performance was tested for dependencies on a number of different variables: the number of inelastic proton-proton interactions per event (μ), the transverse momentum (p_T) and the pseudo-rapidity (η). The dependence on η and μ was not considered significant enough

to warrant a dedicated flattening of the signal efficiency with respect to these variables. This can be seen in Figure 4.10, which shows that there is not a significant difference between the Loose, Medium and Tight working points with respect to the variable μ. The general outcome of the BDT that was trained to discriminate against electrons can be seen in Figure 4.8, which shows the score in each of the η regions separately. The dependence on p_T was such that a sliding cut on the electron veto BDT score was used implementing the three efficiency working points *loose*, *medium* and *tight*. This can be seen in Figures 4.11 to 4.14, the working points correspond to yield signal efficiencies of 95%, 85% and 75%, respectively. Plots showcasing the efficiency dependence of the electron veto on μ, p_T and η are shown in Figures 4.15 to 4.17.
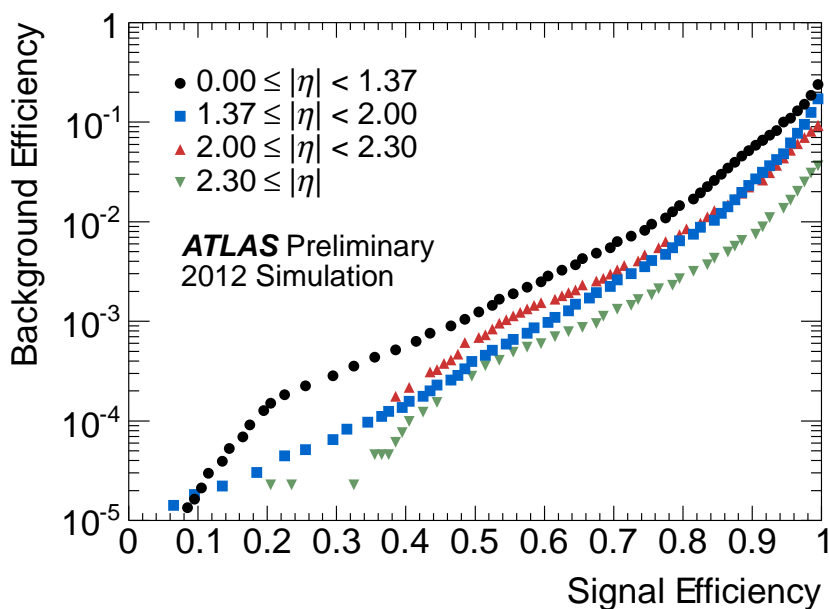
Figure 4.9: Background efficiency as a function of signal efficiencies of the electron veto for each of the different η regions. The efficiencies are obtained using simulated $Z \to \tau\tau$ events for signal and simulated $Z \to ee$ events for background [1].
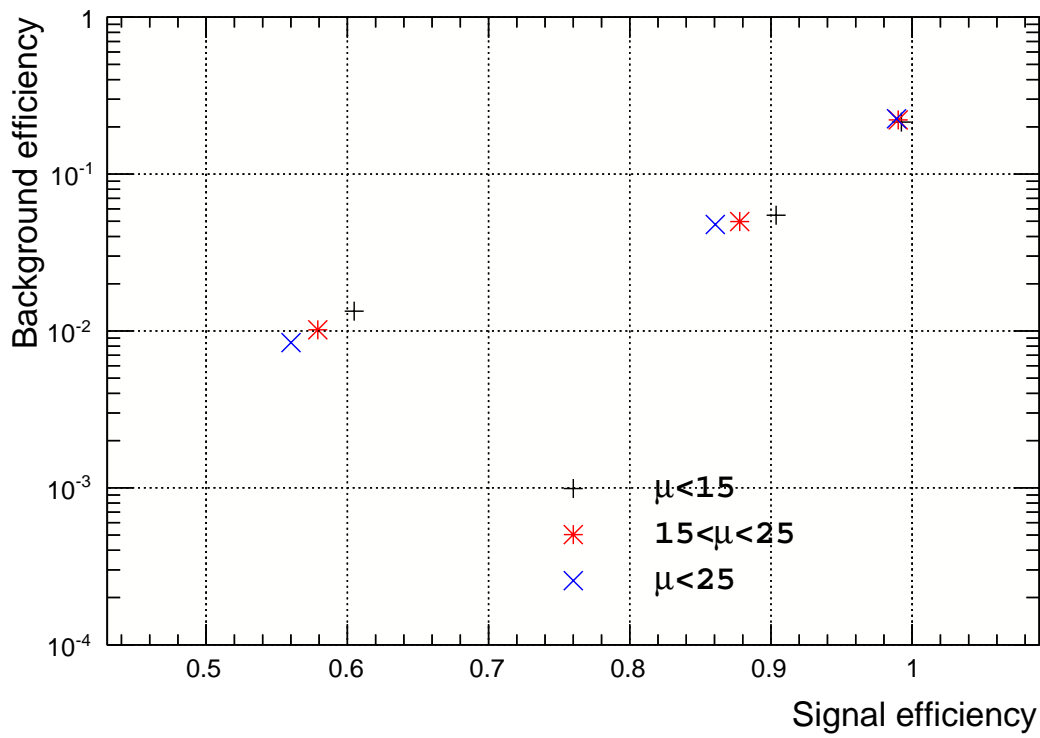
Figure 4.10: The Average interactions per bunch crossing, μ shown as a function of background and signal efficiencies.
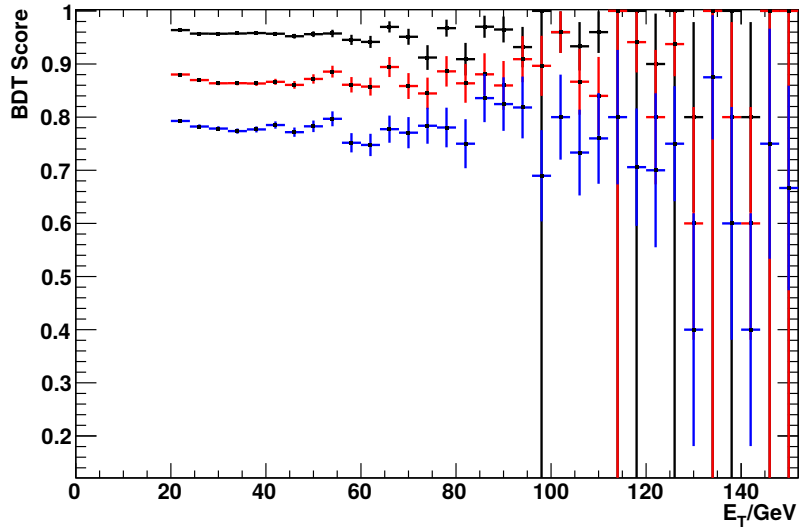
(a)
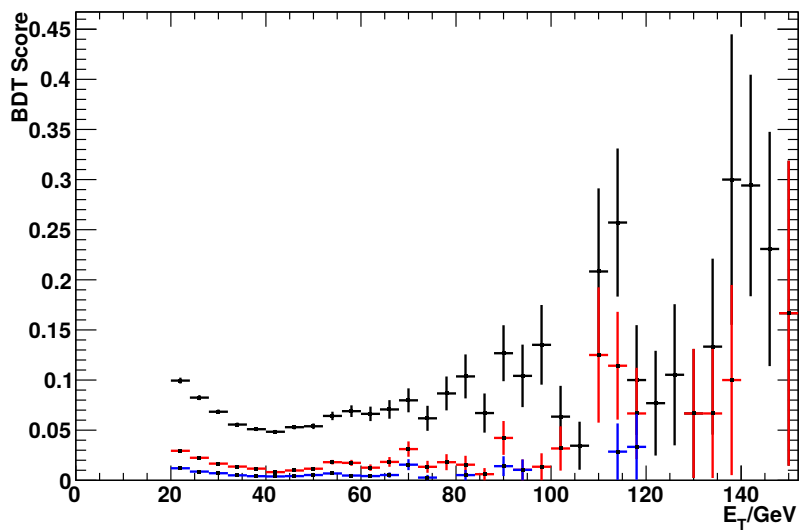
(b)

Figure 4.11: Tau Identification efficiency in the barrel region for the signal sample 4.11a and for the background sample 4.11b.
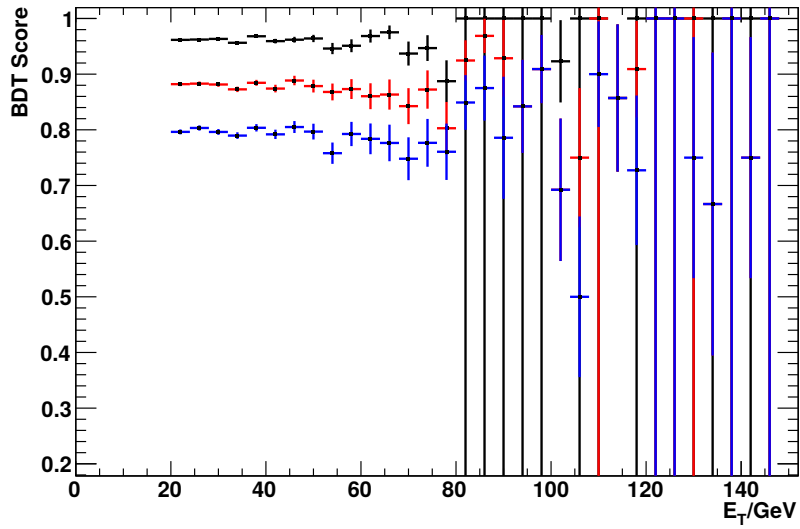
(a)
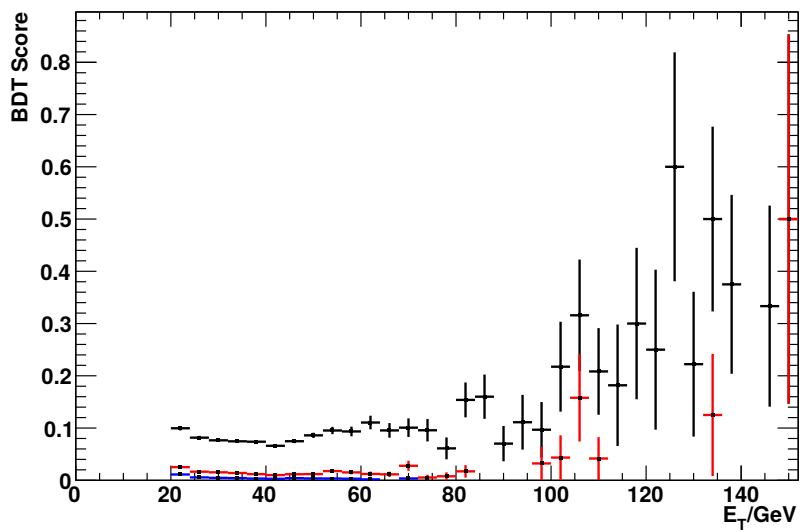
(b)

Figure 4.12: Tau Identification efficiency in the barrel region for the signal sample 4.12a and for the background sample 4.12b.
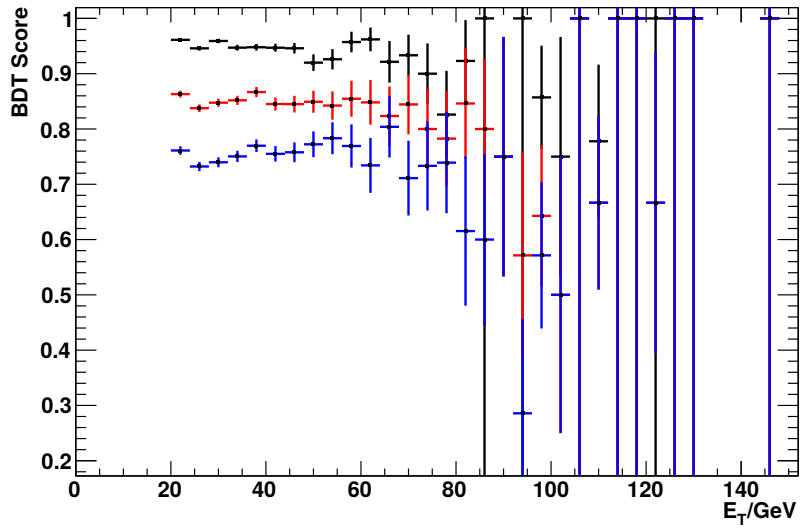
(a)
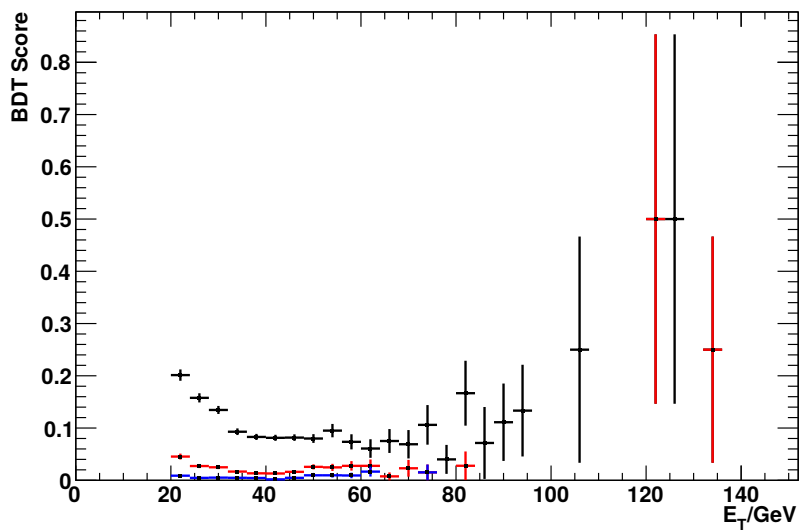
(b)

Figure 4.13: Tau Identification efficiency in the barrel region for the signal sample 4.13a and for the background sample 4.13b.
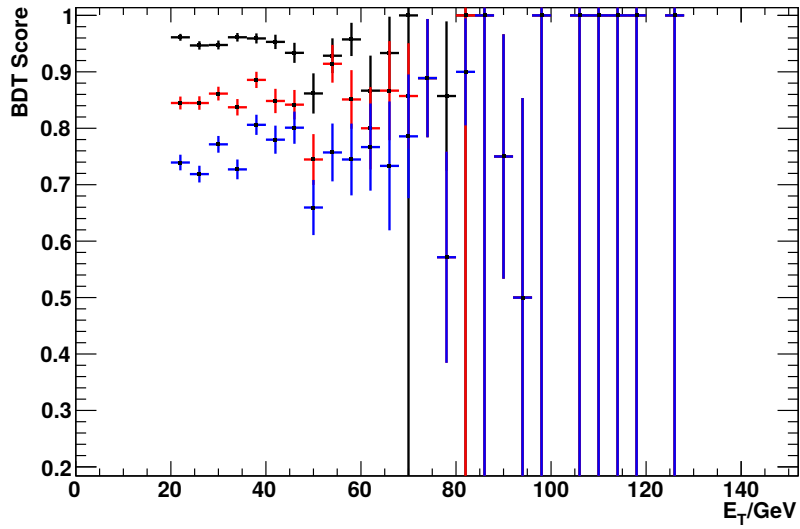
(a)
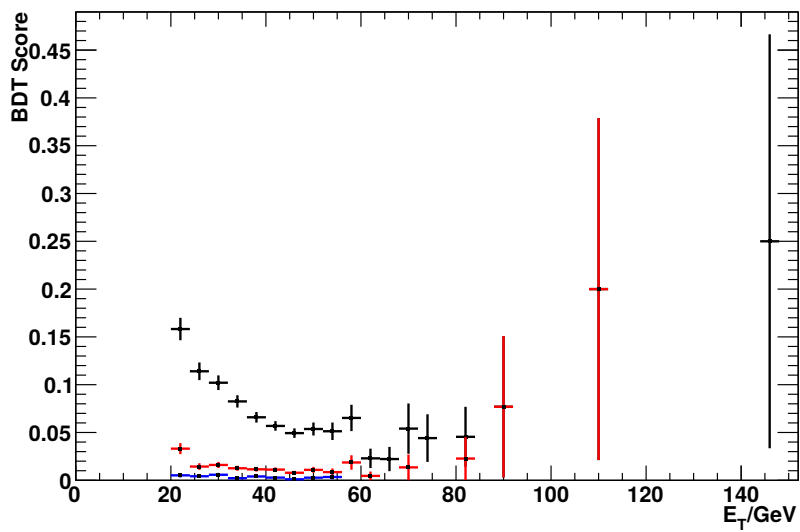
(b)

Figure 4.14: Tau Identification efficiency in the barrel region for the signal sample 4.14a and for the background sample 4.14b.
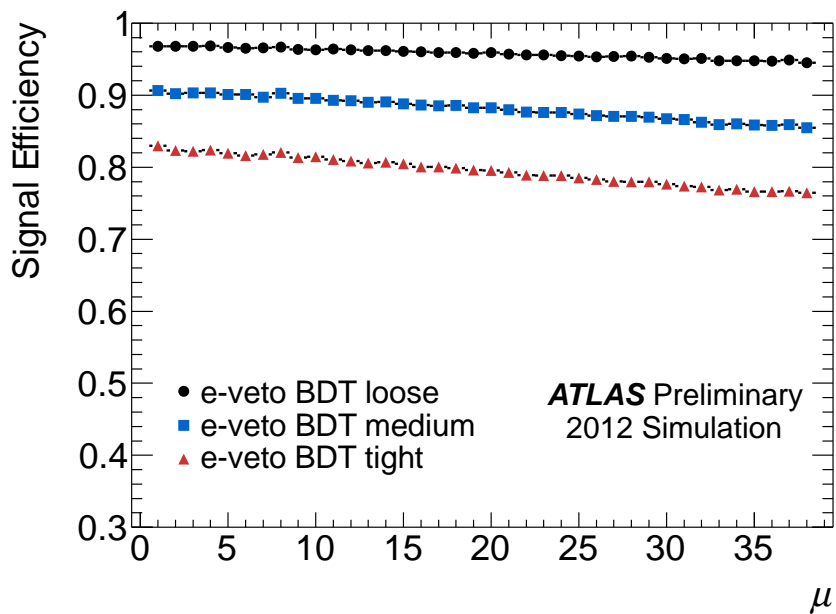
(a)
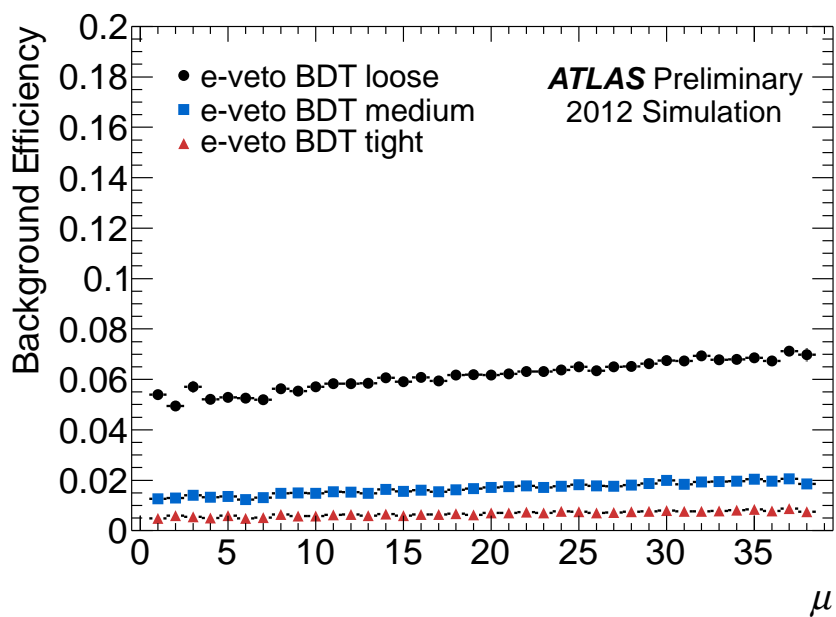
(b)

Figure 4.15: Signal (left) and background (right) efficiencies for the three BDT electron veto working points as a function of μ. The efficiencies are obtained using 1-prong τ_h candidates from simulated $Z \to \tau\tau$ events for signal and simulated $Z \to ee$ events for background [1].
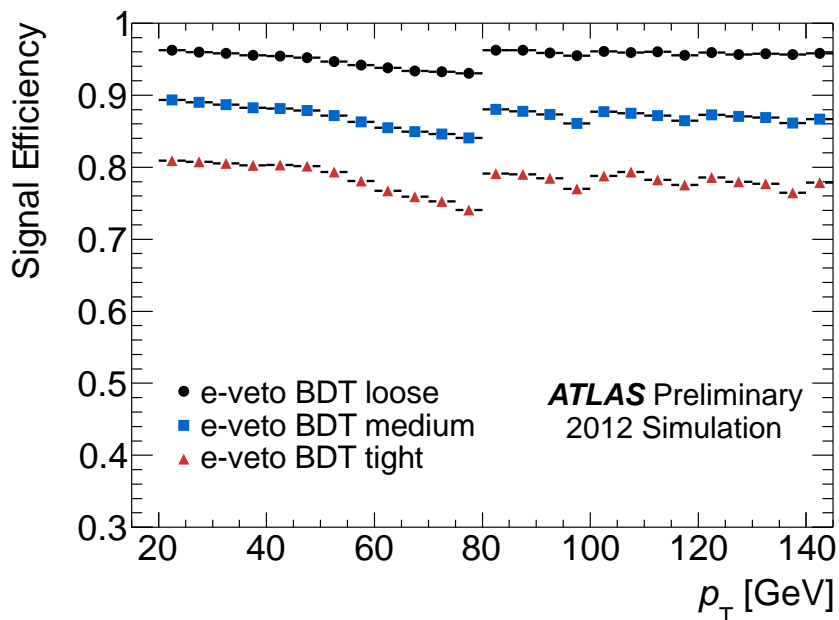
(a)
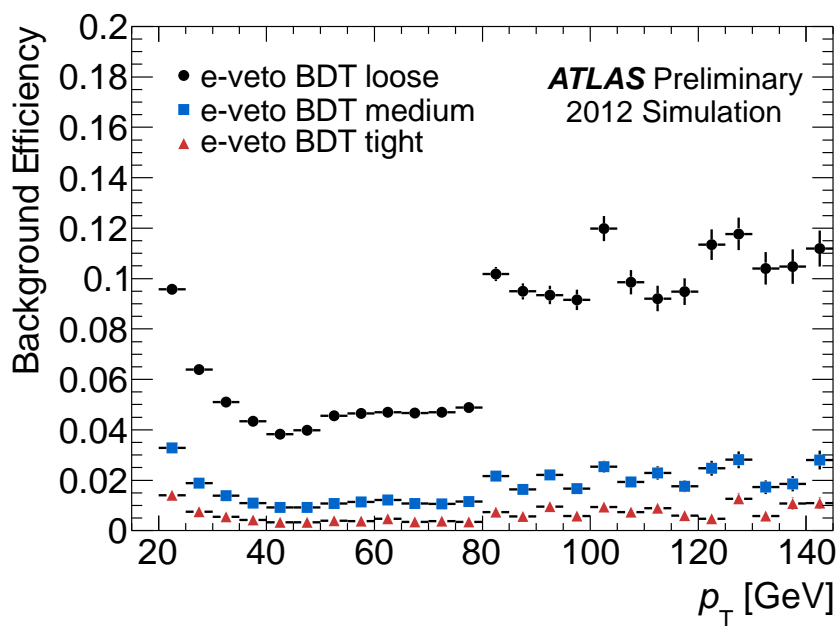
(b)

Figure 4.16: Signal (left) and background (right) efficiencies for the three BDT electron veto working points as a function of p_T. The efficiencies are obtained using 1-prong τ_h candidates from simulated $Z \to \tau\tau$ events for signal and simulated $Z \to ee$ events for background [1].
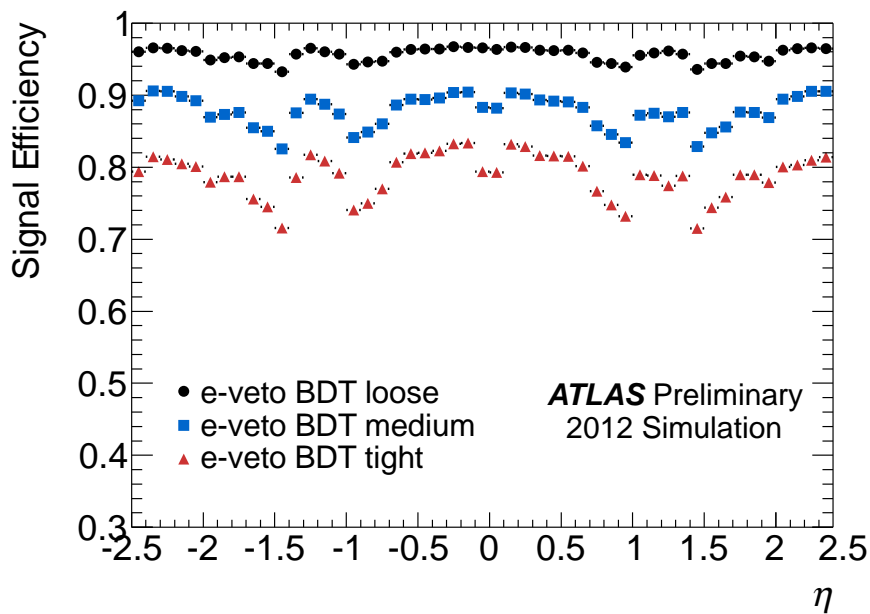
(a)
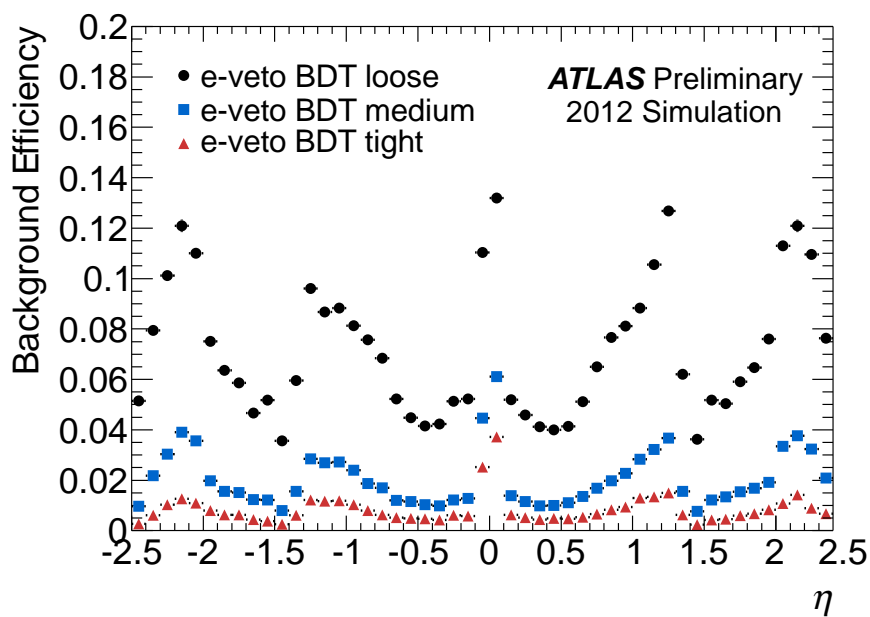
(b)

Figure 4.17: Signal (left) and background (right) efficiencies for the three BDT electron veto working points as a function of η. The efficiencies are obtained using 1-prong τ_h candidates from simulated $Z \to \tau\tau$ events for signal and simulated $Z \to ee$ events for background [1].

4.3.3 Muon Discrimination

Muons are minimally ionising particles, they are unlikely to deposit enough energy in the calorimetry to be effectively reconstructed as a τ_h candidate. However, when a sufficiently energetic cluster in the calorimeter is associated with a muon, the muon track and the calorimeter cluster together may be incorrectly identified as a τ_h. Previously a simple cut-based discriminant was optimised to differentiate between the muons from true τ_h decays.

The most efficient way of doing this is to use the default muon reconstruction algorithms, that is to say that if a τ_h candidate overlaps geometrically with a reconstructed muon it is removed from the analysis. This leaves the following cases unaccounted for:

1) The muon has passed through an inefficient region of the Muon Spectrometer and was not reconstructed,

2) The muon has deposited enough energy in the calorimeter that it's track is skewed and reconstruction in the muon spectrometer fails,

3) The muon was of very low energy, and was stopped in the calorimeter.

In case 1), the low efficiency regions occur at very low $|\eta|$, where there is a gap in the muon coverage to allow access to the inner detector. It also occurs in the transition region between the barrel and the end-cap regions in the positive η region of the detector. The increased rates can be seen in Figure 4.18a. Muons that have deposited significant energy in the calorimeter are most likely to have have done so in the hadronic calorimeter, resulting in τ_h candidates with an unusually low electromagnetic fraction f_{EM} see section 4.2.4 for more information. Additionally, for these muons the track momentum may be higher than the calorimeter energy which is also true of muons that overlap coincidentally with some other calorimeter deposit. Furthermore, the very low energy muons must overlap with a calorimeter event, this is so that it can pass the τ_h reconstruction, therefore it can be characterised by a high EM fraction and a low track momentum fraction (this could be from some final state radiation from the very same muon). In Figure 4.18b, the distribution of the EM fraction for τ_h candidates seeded by true

muons and true tau leptons is shown.

To optimise the muon veto, simulated muons from $Z \to \mu\mu$ events and hadronic tau decays from $Z \to \tau\tau$ were used. Regions of low and high EM fractions were defined, and a cut on the track momentum fraction is applied in each, with separate region definitions and cuts for τ_h in the low muon efficiency areas. The resulting efficiency is better than 96% for true τ_h events, with a reduction of muon fakes of around 40%. The performance, however, can vary depending on the τ_h ID and muon overlap removal that is being used.

4.4 Measurements of the Hadronic Tau Identification Efficiency Scale Factors

As described in the previous section, the various algorithms used to identify visible τ_h were tuned using simulations to provide specific efficiency working points. It is of the utmost importance to verify that these are performing correctly and comparably to both the predictions from simulated samples and in data. This is achieved by measuring the identification efficiency for reconstructed visible τ_h candidates directly in data. By comparing this to the same performance Figures in simulated samples, the scale factors can be calculated. These can then be used in a full analysis to account for the difference between data and simulation (which arises from the different modelling of any input variables). It is important to note that no scale factors are provided for background rejection efficiencies, as this quantity is too sensitive to the final state being studied.

To accomplish this a "tag-and-probe" method was used, this consists of selecting events with real tau leptons in their final state, and extracting a measure of the identification efficiencies directly from the number of reconstructed visible τ_h before and after identification algorithms are applied. However, it is impossible to obtain a completely pure sample of τ_h leptons, and thus, backgrounds must be taken into account. To estimate the number of background events, a variable with good separation potential is chosen, a fit is then performed using the expected distributions in this variable (referred to as "templates") for both
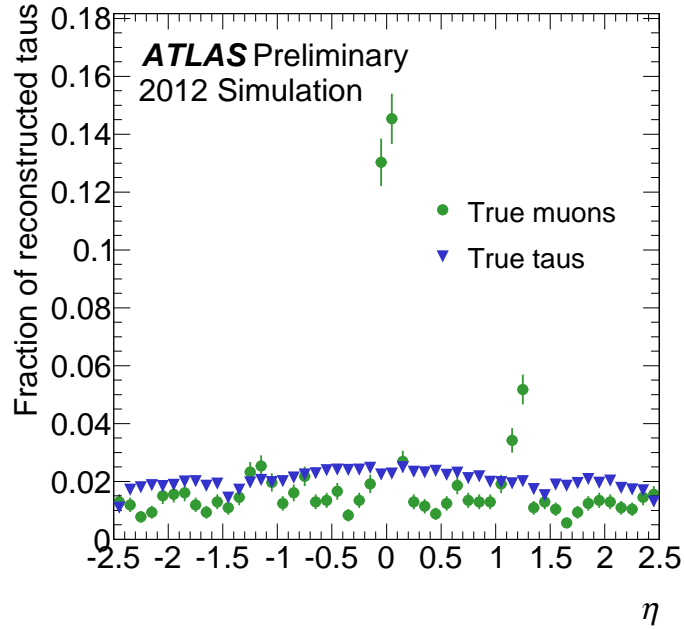
(a)
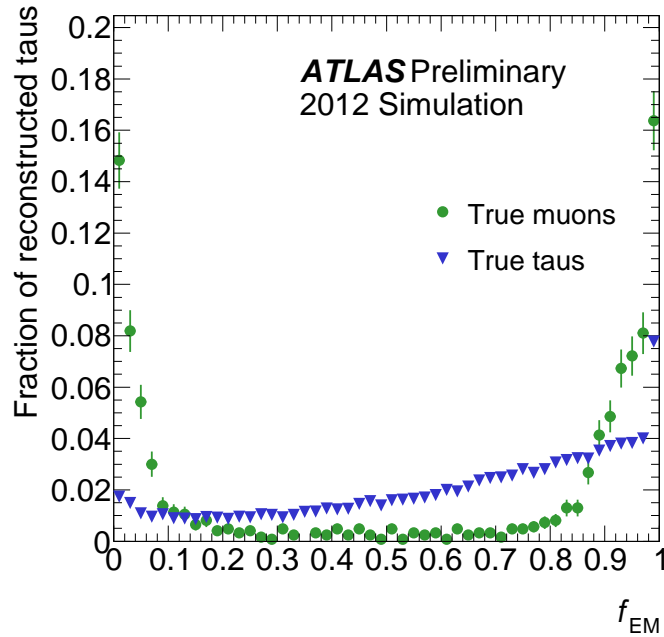
(b)

Figure 4.18: (a) Pseudorapidity, η of τ_h candidates in simulation matched to true muons and true τ_h after removing candidates which overlap with a reconstructed muon. The effect of inefficient muon reconstruction in certain regions can be seen. (b) Electromagnetic fraction f_{EM} of τ_h candidates in simulation and true muons [1].

signal and backgrounds. This fit has to be performed multiple times: once before any identification is used and once after each identification algorithm. Then, the real number of τ_h decays in data is obtained from the fitted signal template. In order to measure the tau ID efficiency for data ε_{data}, the number of real visible τ_h after the tau ID is divided by the umber of real visible τ_h measured before the tau ID. The uncertainties on the efficiency measurement are estimated by recalculating the efficiency using systematically altered templates, this is a fairly common practice for estimating the systematic uncertainties for a given process. For the simulated sample efficiencies, $\varepsilon_{simulation}$, the number of tau leptons before and after tau ID is taken directly from truth-matched visible τ_h candidates. From these two efficiencies the scale factor is calculated simply:

$$SF = \frac{\varepsilon_{data}}{\varepsilon_{simulation}} \tag{4.25}$$

Using a standard prescription the uncertainty on the scale factor is propagated from the uncertainty of the efficiency measurement in data. That is to say that the uncertainty from the data efficiency measurement has a constant factor applied to it.

It is therefore obvious that the scale factors account for the differences between data and simulation due to the modelling of the input variables for the identification algorithms. This measurement is also repeated for different final states, with a view to understand the different underlying physics processes where hadronically decaying tau leptons are involved. Three processes are chosen, $Z \to \tau_{lep}\tau_{had}$, $W \to \tau_{had}\nu_\tau$ and $t\bar{t} \to \tau_{had} + jets$. The $Z \to \tau_{lep}\tau_{had}$ channel is chosen as the main measurement as it offers the highest precision due to the low associated backgrounds. This channel offers coverage in the range $20 < p_T < 50$ GeV. The measurement in the $W \to \tau_{had}\nu_\tau$ channel is used as a cross-check, and offers coverage of the $20 < p_T < 60$ GeV regime. The $t\bar{t} \to \tau_{had} + jets$ channel offers an alternative measurement in the higher kinematic regime of $40 < p_T < 100$ GeV.
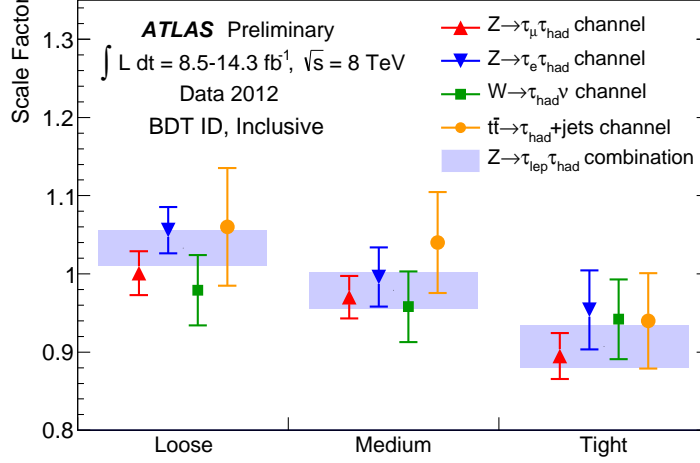
(a)
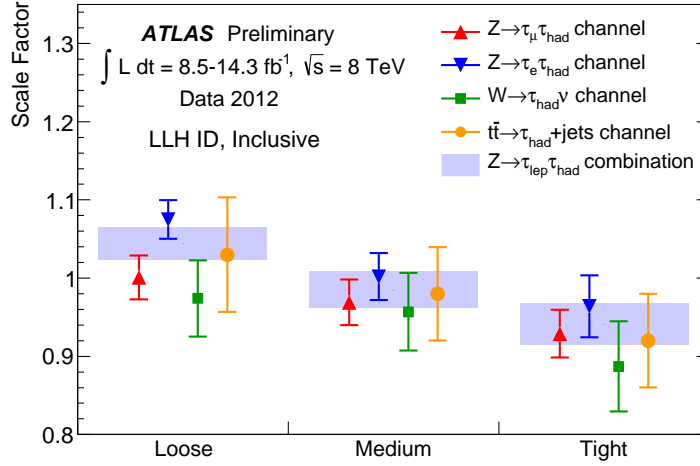
(b)

Figure 4.19: Summary showing the Scale Factors for all channels and all working points [1]

Scale factors for the visible τ_h signal efficiency measured in four different final states have been provided. In Figure 4.19 a summary of all inclusive measurements and illustrates is given and the good agreement between all channels can be seen. More information regarding the other channels used in this measurement can be found in ref. [1], but will not be discussed here, as they are not fully

relevant. An overview of the inclusive scale factors can be seen in Tables 4.2 and 4.3 In the latter table the correlation, ρ is shown, this corresponds to the total correlation between the all the measurements in both of the channels, including the effect of the statistical uncertainties.

$Z \to \tau_\ell \tau_h$ combination	Inclusive scale factors and $\pm$syst.unc. $\pm$stat.unc.		
	Overall	Barrel	End-Cap
BDT Loose	$1.033 \pm 2.0\% \pm 1.0\%$	$1.021 \pm 2.1\% \pm 1.2\%$	$1.000 \pm 2.9\% \pm 1.6\%$
BDT Medium	$0.979 \pm 2.1\% \pm 1.1\%$	$0.966 \pm 2.8\% \pm 1.3\%$	$0.954 \pm 2.2\% \pm 1.8\%$
BDT Tight	$0.907 \pm 2.6\% \pm 1.5\%$	$0.941 \pm 3.0\% \pm 1.6\%$	$0.905 \pm 2.4\% \pm 2.2\%$
LLH Loose	$1.044 \pm 1.7\% \pm 1.0\%$	$1.027 \pm 2.4\% \pm 1.2\%$	$1.000 \pm 2.5\% \pm 1.6\%$
LLH Medium	$0.985 \pm 2.1\% \pm 1.1\%$	$0.979 \pm 2.7\% \pm 1.4\%$	$0.927 \pm 3.2\% \pm 1.8\%$
LLH Tight	$0.941 \pm 2.4\% \pm 1.5\%$	$0.925 \pm 3.2\% \pm 1.8\%$	$0.901 \pm 2.8\% \pm 2.3\%$

Table 4.2: $Z \to \tau\tau$ combination: scale factors for inclusive τ_{had}^{vis} for all ID working points. The Barrel region corresponds to $|\eta(\tau_{had}^{vis})| < 1.37$, while the End-Cap to $|\eta(\tau_{had}^{vis})| > 1.52$.

4.5 Measurement of the Electron Veto Efficiency Scale Factors

As talked about previously the electron veto algorithm was tuned using simulated samples to provide very specific efficiency working points. As also stated previously it is of the utmost importance to check that this algorithm is performing comparably in both simulated samples and in data. This is achieved by performing direct measurements of the real electron veto efficiency in data for multiple combinations of the tau ID, electron veto and electron overlap removal and comparing it to the efficiency obtained from the same processes applied to simulated samples. The tag-and-prove approach chosen consists of selecting $Z \to ee$ events with real electrons in their final state, and extracting the efficiencies directly from the number of reconstructed visible τ_h before and after identification and the veto algorithm has been applied, or not.

Combination of inclusive scale factors and uncertainties (%)						
$Z \to \tau_\ell \tau_h$		BDT			LLH	
	Loose	Medium	Tight	Loose	Medium	Tight
SF $(Z \to \tau_{mu}\tau_{had})$	**1.001**	**0.970**	**0.895**	**1.001**	**0.969**	**0.929**
uncorr syst.	2.0%	2.3%	2.4%	2.3%	2.4%	2.4%
corr syst.	1.6%	0.7%	1.3%	0.9%	1.0%	1.3%
stat.	1.3%	1.5%	1.9%	1.3%	1.5%	1.9%
syst.+stat.	2.8%	2.8%	3.3%	2.8%	3.0%	3.3%
SF $(Z \to \tau_e\tau_{had})$	**1.056**	**0.996**	**0.954**	**1.075**	**1.002**	**0.964**
uncorr syst.	1.0%	2.8%	4.3%	0.8%	1.1%	2.6%
corr syst.	1.7%	1.8%	2.1%	1.7%	2.1%	2.1%
stat.	1.5%	1.7%	2.3%	1.5%	1.7%	2.3%
syst.+stat.	2.5%	3.8%	5.3%	2.3%	3.0%	4.1%
SF Combination	**1.033**	**0.979**	**0.907**	**1.044**	**0.985**	**0.941**
syst.	2.0%	2.1%	2.6%	1.7%	2.1%	2.4%
stat.	1.0%	1.1%	1.5%	1.0%	1.1%	1.5%
syst.+stat.	2.2%	2.4%	3.0%	2.0%	2.4%	2.8%
ρ (total)	0.387	0.121	0.159	0.219	0.242	0.203

Table 4.3: $Z \to \tau\tau$ combination: inclusive scale factors and uncertainties for all ID working points [1].

In this tag-and-probe method, the tag object, "tag electron", is a reconstructed electron candidate with, $p_T(e) > 35$ GeV and $|\eta| < 1.37$ or $1.52 < |\eta| < 2.47$ (barrel and end-cap fiducial regions of the detector). The tag electron is then required to pass through a tight electron identification (for more details of that see ref. [62]). The two isolation criteria that are required in addition to this (in order to suppress contamination from multi-jet events) are:

- The calorimeter energy inside of $\Delta R < 0.2$ around the tag electron is less than 5% of $p_T(e)$,

- The sum of the momenta from any additional tracks inside $\Delta R < 0.4$ around the tag electron is less than 4% of $p_T(e)$.

The probe object "probe tau" is a reconstructed tau candidate with a visible $p_T(\tau_h) > 20$ GeV and an $|\eta| < 2.5$ (the fiducial region of the entire tracking system). This probe tau is required to have exactly one track in the core cone, and it is rejected if it overlaps with an identified electron candidate. Additionally it is required to have an e-veto BDT score less than 0.75, this strongly suppresses contamination from real visible τ_h and quark-gluon initiated jets.

Each event is required to pass either of the two lowest un-prescaled electron triggers. One of the triggers selects events containing an isolated electron with $E_T > 24$ GeV. The other, requires the tag electron to have at least 60 GeV, but puts less constraints on its isolation. Additionally the tag electron and the probe tau are required to have opposite charge and the invariant mass of the tag-probe system is required to be within a Z-mass window of between 80 and 100 GeV. The transverse mass m_T of the tag electron and the E_T^{miss} as shown in Equation 4.26 is required to be less than 40 GeV to suppress unnecessary contamination from $W \to e\nu$ events. Furthermore there must be no identified muons in any of the tag electron or probe tau events.

$$m_T = \sqrt{2 \cdot p_T(\tau_{had} \cdot E_T^{miss}) \cdot (1 - \cos\phi(\tau_{had}, E_T^{miss}))} \qquad (4.26)$$
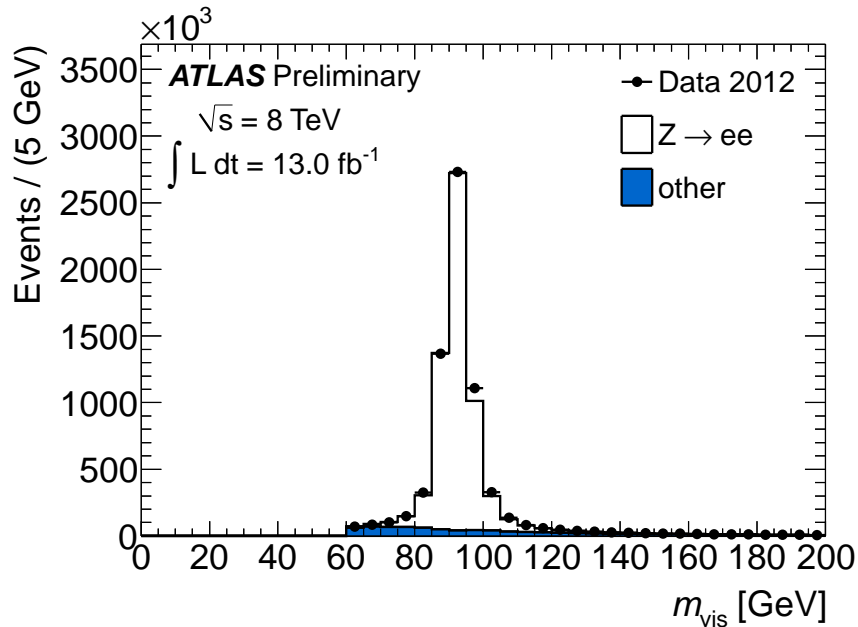
Figure 4.20: Invariant mass of the tag-probe system $m_{vis}(e, \tau_{had})$ before applying any ID, veto or any other additional selections to increase the purity of $Z \rightarrow ee$ events. The backgrounds grouped in the "other" category correspond to $W \rightarrow e\nu$, $Z \rightarrow \tau\tau$, $t\bar{t}$ and multi-jet events [1].

4.5.1 Background Samples

Before applying the electron veto, the $Z \rightarrow ee$ selection is incredibly pure (see

Figure 4.20). As one might expect after applying the electron veto to this sample,

it is then contaminated by mainly $W \rightarrow e\nu$, $Z \rightarrow \tau\tau$, $t\bar{t}$ and multi-jet events (the

"other" background in Figure 4.20), a plot resulting from this selection can be

seen in Figure 4.21
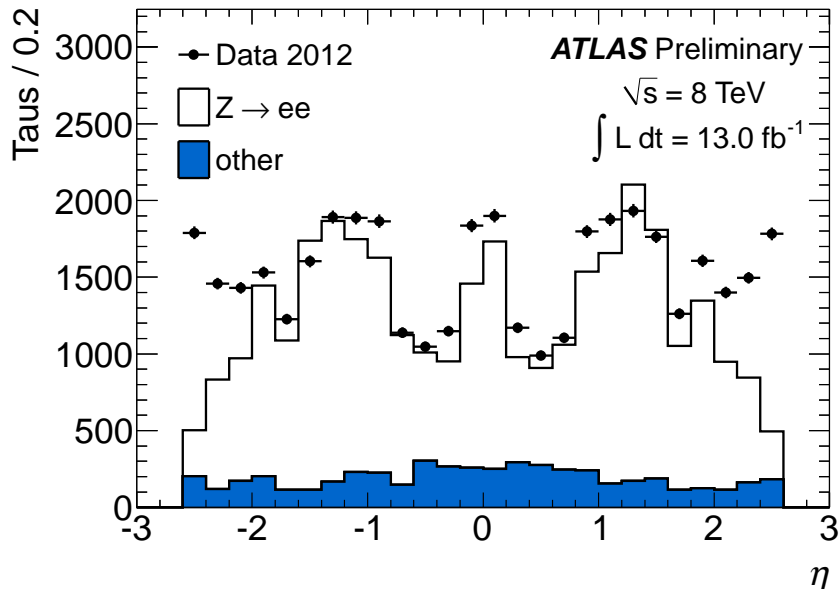
Figure 4.21: The η of the leading track of the probe tau after applying a loose tau ID and a loose electron veto, with overlap removal [1].

The contamination from multi-jet events is then estimated from a sample of $Z \to ee$ from data, that has same-sign tag electrons and probe taus. Any other contaminants with same-sign charge conjugation are simulated and simply subtracted from the multi-jet estimation.To estimate the $W \to e\nu$, $Z \to \tau\tau$ and $t\bar{t}$ backgrounds, event yields are observed in dedicated control regions for each background, for data and from simulated events. The difference between them is then taken as a data-driven normalisation for each background. These are derived for each combination of tau ID, electron veto, and electron overlap removal.

4.5.2 Systematic Uncertainties

Four variations were considered as systematic uncertainties for this measurement. These are:

- Varying the tag electron p_T threshold from 35 GeV to 40 GeV,

- Varying the tag electron isolation requirement from 5% of the momentum to 8%,

- Varying the data-driven normalisation of the simulated background by 1σ of the statistical uncertainty,

- Varying the electron veto BDT score requirement between the nominal measurement and the varied measurements

4.5.3   Results

The efficiency for the electron veto and real electrons was compared between data and simulated events, with an integrated luminosity $\mathcal{L}_{int} = 5.8\text{fb}^{-1}$. This was measured for all combinations of tau ID, electron veto and electron overlap removal. Within these selections, the efficiency was measured in six regions of $|\eta|$, four of which correspond directly to those that were used for training the electron veto and the remaining to the gap in the coverage of the Transition Radiation Tracker ($|\eta(e)| < 0.05$) and the end of the coverage of the offline electron identification ($|\eta(e)| > 2.47$). The overall results of this measurement can be viewed in Table 4.4.

Electron veto data/MC scale factor and uncertainties loose BDT tau ID, medium electron veto, and loosePP overlap removal						
$|\eta(\tau)|$	$0.00-0.05$	$0.05-1.37$	$1.37-2.00$	$2.00-2.30$	$2.30-2.47$	$2.47+$
vary tag electron p_T	12%	4.5%	7.9%	17%	7.0%	57%
vary tag electron isol.	2.3%	6.3%	2.1%	11%	39%	28%
vary background norm.	1.2%	5.3%	5.7%	1.3%	1.1%	0.1%
vary probe tau e-veto BDT	2.3%	11%	6.4%	16%	8.1%	2.9%
$\text{SF}^{syst.}$	12%	14%	12%	26%	41%	64%
$\text{SF}^{stat.}$	13%	12%	19%	13%	19%	17%
$\text{SF}^{syst.+stat.}$	17%	18%	22%	29%	44%	66%
SF	0.86	1.12	1.40	1.58	2.70	21.69

Table 4.4: Comparison of data to MC prediction of the electron veto efficiency for loose BDT tau ID, medium electron veto, and overlap removal with reconstructed electron candidates which pass loosePP offline identification, and the associated systematic uncertainties [1].

The difference in the efficiency between data and simulation is largest for $|\eta(\tau_h)| > 2.0$, as illustrated in Figure 4.21. This is because the energy deposited in the hadronic calorimeter is not modelled well in the simulations, this energy is part of the electromagnetic fraction (f_{EM}) of the probe tau and the electron veto relies heavily on the f_{EM} for $|\eta(\tau_h)| > 2.0$.

4.6 Conclusion

Some of the reconstruction and identification algorithms for hadronically decaying tau leptons in the 2012 data period have been described in this document. The variables were optimised to be robust against increasing pile-up, which is present in this data period. The resulting efficiencies are independent of this pile-up.

Chapter 5

A Study of the $Z \to \tau\tau$ Channel

5.1 Introduction

Measurements of the $Z \to \tau\tau$ cross section at $\sqrt{s} = 7$ TeV have been made before by ATLAS [63] and CMS [64], using data collected in 2010 and corresponding to an integrated luminosity of 36 pb^{-1}. In this section data recorded by the ATLAS detector during 2011 have been used corresponding to an increased luminosity of between 1.34 fb^{-1} and 1.55 fb^{-1}, depending on the channel used. With this larger sample, a new measurement of the $Z \to \tau\tau$ cross section at $\sqrt{s} = 7$ TeV in the invariant mass range $66 < M_{\tau\tau} < 116$ GeV was made. A high τ-purity dataset was obtained and has been used for studies of the distributions of variables relevant for the hadronic τ identification. In this section three final states are considered:

- $Z \to \tau\tau \to \mu + \text{hadrons} + 3\nu$ ($\tau_\mu \tau_h$), with a branching ratio of 22.50±0.09%,

- $Z \to \tau\tau \to \text{e} + \text{hadrons} + 3\nu$ ($\tau_e \tau_h$), with a branching ratio of 23.13±0.09%,

- $Z \to \tau\tau \to \text{e}\mu + 4\nu$ ($\tau_e \tau_\mu$), with a branching ratio of 6.20 ± 0.02%.

5.2 Data and Monte Carlo Samples

The data samples analysed in this specific study were collected with the ATLAS detector during 2011 at $\sqrt{s} = 7$ TeV. For the $\tau_\mu \tau_h$ and $\tau_e \tau_\mu$ channels, an isolated muon trigger requiring a $P_T > 15$ GeV was used. For the $\tau_e \tau_h$ channel, a combined hadronic tau and electron trigger is used. The threshold of the hadronic tau trigger is 16 GeV whilst the electron trigger threshold is at 15 GeV. The periods when these triggers were active result in different integrated luminosities for the channels, 1.55 fb^{-1} for the $\tau_\mu \tau_h$ and $\tau_e \tau_\mu$ channels and 1.34 fb^{-1} for the $\tau_e \tau_h$ channel.

The signal and background Monte Carlo (MC) samples used in this study were generated at $\sqrt{s} = 7$ TeV and passed through a full detector simulation based on the Geant4 Program [65]. The inclusive W and γ^*/Z signal and background samples were generated with ALPGEN [49], interfaced to HERWIG [66] and JIMMY [67], using the CTEQ6L1 [68] Parton Distribution Functions (PDFs), with the ATLAS AUET1 [69] tune. The samples are normalised to NNLO [70] cross sections. For the $t\bar{t}$ background the MC@NLO generator [71] is used with the CTEQ6.6 [68] PDFs, and the parton shower and hadronisation simulated with HERWIG. The diboson samples are generated with HERWIG. In all samples the τ decays are modelled with TAUOLA [72], and all the generators are interfaced to PHOTOS [73] to simulate the effect of final state QCD radiation.

5.3 Physics Objects

Collision Candidate events are selected by requiring at least one reconstructed primary vertex with at least four reconstructed tracks. Cleaning cuts are applied to reject events with jets or τ candidates caused by cosmic-ray events or other known noise effects in the calorimeters, as well as events with reconstructed calorimeter objects falling within a local readout problem in the Electromagnetic Calorimeter (ECAL).

In the $\tau_\mu \tau_h$ and $\tau_e \tau_h$ decay modes, events are characterised by exactly one isolated lepton (ℓ) and one hadronic τ decay (τ_h). Hadronically decaying taus produce a highly collimated jet in the detector with an odd number of charged hadrons

and possibly additional calorimetric energy deposits form neutral decay products. The $\tau_e\tau_\mu$ decay mode is characterised by two isolated leptons, typically of lower transverse momentum (p_T) than those produced in $Z \to ee/\mu\mu$ events. Finally, missing transverse energy is expected in all channels from the neutrinos produced in the τ decays. This analysis therefore relies on many reconstructed objects, making use of the entire ATLAS detector: electrons, muons, τ candidates, jets and missing transverse momentum.

The identification of τ_h decays is a difficult process and suffers from relatively high misidentification rates, because of this most of the backgrounds relevant for the $\tau_\ell\tau_h$ channels involve true leptons with a quark or gluon jet misidentified as a hadronically decaying τ lepton. This will be covered in a later chapter. However, the backgrounds in the $\tau_e\tau_\mu$ channel are generally lower due to the different flavoured leptons requirements and the higher purity for electron and muon identification, compared to τ_h decays.

In addition multi-jets are an important background, especially in the case of $\tau_\ell\tau_h$, due to the very large production cross section. The leptons(s) can be real (i.e. muons produced from heavy-flavour decays) or fake (i.e. miss-identified physics object), while the τ_h candidate is usually either a misidentified quark or gluon seeded jet. The production of γ^*/Z bosons decaying to a pair of electrons or muons is an appreciable background. This is in the case where the γ^*/Z is produced in association with a jet which has been misidentified as a τ, with an additional coincidence of being at the same time as a reconstructed real lepton or if one of the leptons has been misidentified as a τ_h. Another electroweak background of note for the $\tau_\ell\tau_h$ channels is $W+$ jets production, where the W decays leptonically whilst an associated misidentified quark or gluon jet provides the fake τ candidate. The lepton and the jet in this process tend to have opposite signs, which is the same as in the signal region. Finally, $t\bar{t}$ productions, particularly in the dilepton decay channel and including the diboson production can also be important backgrounds in the $\tau_e\tau_\mu$ channels, since they yield two real different-flavour leptons.

The following definitions of physical objects are consistent with the rest of the work detailed in this thesis, with only minor corrections to the specifics of each analysis.

5.3.1 Muons

Muon candidates are formed by associating muon spectrometer tracks with inner detector tracks after accounting for energy losses in the calorimeter [74]. A combined transverse momentum is determined using a statistical combination of the two tracks and is required to be greater than 17 GeV. Muon candidates are also required to be within a pseudorapidity range of $|\eta| < 2.4$, pass track quality criteria and have a longitudinal impact parameter of less than 10 mm with respect to the primary vertex.

5.3.2 Electrons

Electron candidates are reconstructed from clusters in the EM calorimeter matched to a track in the inner detector. Candidate electrons are selected if they have a transverse energy $E_T > 17$ GeV. They must also be within the psuedorapidity range of $|\eta| < 2.47$, also excluding the transition region between the barrel and end-cap calorimeters, $1.37 < |\eta| < 1.52$, and to pass tight identification requirements [62].

5.3.3 Jets

Jets are reconstructed using the anti-K_t algorithm [75], with a distance parameter of $R = 0.4$, using three-dimensional topological calorimeter energy clusters as input. Jet candidates are required to have $p_T > 20$ GeV and a pseudorapidity in range of $|\eta| < 4.5$.

5.3.4 Hadronic τ Candidates

The most important definition and the most changeable, is that of the τ_h candidates. In this analysis they have the following definition. Reconstruction of τ_h decays have a jet seeded by an anti-K_t jet with $R = 0.4$ and a $p_T > 20$ GeV. Inner detector tracks with $P_T > 1$ GeV fulfilling minimum quality criteria are associated with the candidate. In this section τ candidates are required to have $|\eta| < 2.47$, excluding the transition region between the barrel and end-cap

calorimeters, $1.37 < |\eta| < 1.52$, and $p_T > 20(25)$ GeV in the $\tau_\mu \tau_h$ ($\tau_e \tau_h$) channel. The higher p_T requirement in the $\tau_e \tau_h$ channel is necessary due to the τ trigger, in order to avoid the steepest part of the trigger's turn-on curve; this effect is because of the energy dependence of the trigger efficiency described in more detail in ref. [76]. Additionally τ candidates that have a leading track within $|\eta| < 0.03$ are excluded, as the rate of misidentification from electrons is much higher in this region than is acceptable; this is due to the gap in the calorimeter acceptance and reduced TRT coverage around $|\eta| = 0$.

A Boosted Decision Tree (BDT) for τ_h identification [77] is used, requiring that the τ candidates passes the "medium" selection, corresponding to a signal efficiency of approximately 45%. A τ candidate is rejected if it is found within a cone of $\Delta R < 0.4$ of a reconstructed lepton. Looser identification requirements are applied on the leptons for the purposes of overlap removal and the $P_T(E_T)$ cut on muons (electrons) is reduced to 6 (15) GeV. The reduced p_T requirement for muons allows the rejection of low-p_T muons which were found to have a non-negligible misidentification rate [76]. This is the 2011 τ_h definition and is likely to be adjusted in later sections.

5.3.5   Missing Transverse Momentum

The missing transverse momentum (E_T^{miss}) reconstruction used in all final states relies on energy deposits in the calorimeter and on reconstructed muon tracks. It is defined as the vector sum $E_T^{miss} = E_T^{miss}(\text{calo}) + E_T^{miss}(\text{muon}) - E_T^{miss}(\text{energy loss})$, where $E_T^{miss}(\text{calo})$ is calculated from the energy deposits in calorimeter cells inside three-dimensional topological clusters, $E_T^{miss}(\text{muon})$ is the sum of the muon momentum vectors, and $E_T^{miss}(\text{energy loss})$ is a correction term accounting for the energy lost by muons in the calorimeters.

5.3.6   Lepton Isolation

Leptons from $\gamma^*/Z \rightarrow \tau\tau$ decays are typically isolated from other particles. Therefore isolation requirements are applied to both the electron and muon candidates used in the three final states considered. The first isolation variable is

based on the total transverse momentum of charged particles in the inner detector, inside a cone of size $\Delta R = 0.4$ centred around the lepton direction vector, divided by the transverse momentum or energy of the muon or electron candidate respectively. A selection requiring $\Sigma p_T(\Delta R < 0.4)/p_T < 0.03$ for the muon candidate, and $\Sigma p_T(\Delta R < 0.4)/E_T < 0.06$ for the electron candidate, is used for all final states. Figure 5.1 shows the distribution of the $\Sigma p_T(\Delta R < 0.4)/p_T$ and $\Sigma p_T(\Delta R < 0.4)/E_T$ track isolation variables for muon and electron candidates respectively.

A second track isolation variable is fundamentally similar to the first, however instead of the total transverse momentum, it uses the transverse energy, E_T. For muon candidates, a cone of size $\Delta R = 0.3$ is used, thus, the requirement $\Sigma E_T(\Delta R < 0.3)/p_T < 0.04$ is applied to all final states. For electrons $\Delta R = 0.4$ is used, thus, the requirement $\Sigma E_T(\Delta R < 0.4)/E_T < 0.1$ is applied. In the calculation of all the isolation variables, the lepton p_T or E_T is excluded from the isolation sum.
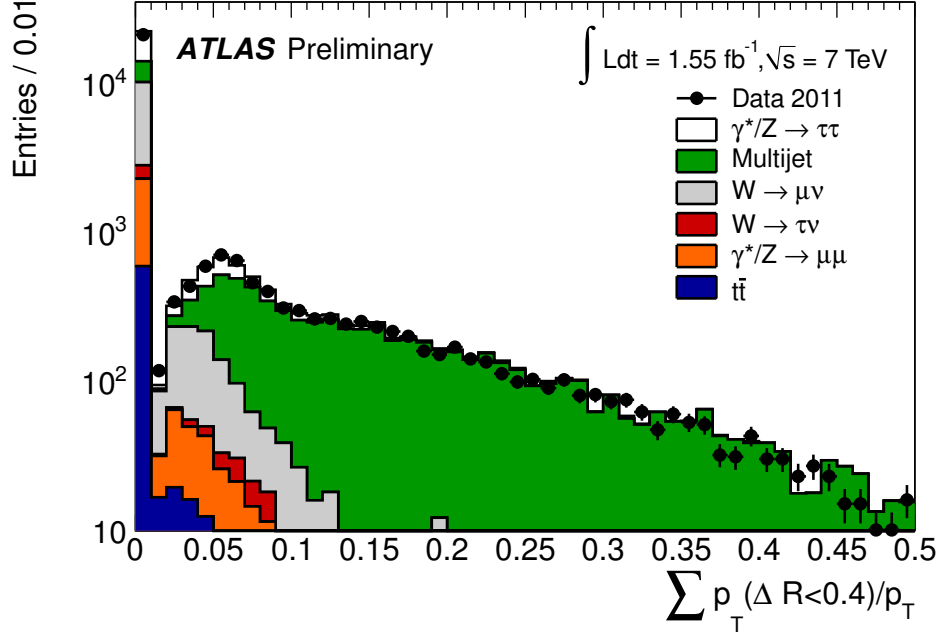
(a) $\tau_\mu \tau_h$ channel
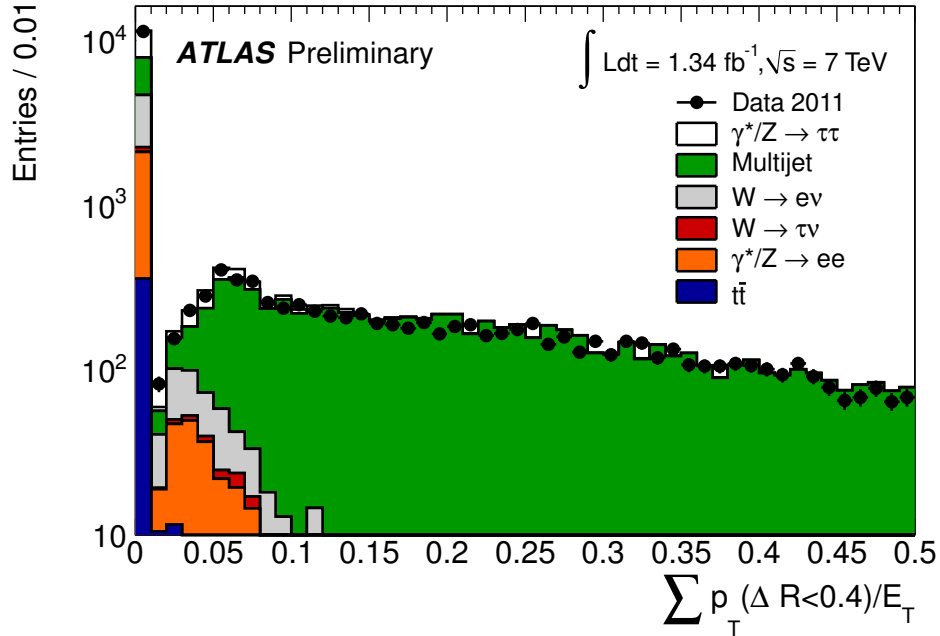
(b) $\tau_e \tau_h$ channel

Figure 5.1: Track isolation variables (a) $\Sigma p_T(\Delta R < 0.4)/p_T$ for muons and (b) $\Sigma p_T(\Delta R < 0.4)/E_T$ for electrons, for selecting one τ_h candidate and one lepton with OS in the $\tau_\mu \tau_h$ and $\tau_e \tau_h$ final states respectively. No other event selection cuts have been applied at this stage.

5.4 Event Selection

5.4.1 The $\tau_\mu\tau_h$ and $\tau_e\tau_h$ Channels

In the $\tau_\ell\tau_h$ channels, the multi-jet background is suppressed to quite a large extent by the τ identification and the lepton isolation requirements that were discussed in the previous section 5.3.6. Events from $W \to \ell\nu$, $W \to \tau\nu \to \ell\nu\nu$ and $\gamma^*/Z \to \ell\ell$ decays can be rejected with additional event-level cuts. Any event with more than one muon or electron is vetoed and thrown away, thus strongly suppressing the $\gamma^*/Z \to \ell\ell+$ jets background. The same loosened selection criteria and p_T thresholds are used for the second lepton are used, as for the overlap removal procedure described in section 5.3. Events are then selected by requiring $\Sigma \cos\Delta\phi > -0.15$, where the discriminating variable $\Sigma \cos\Delta\phi$ is defined as:

$$\Sigma \cos\Delta\phi = \cos(\phi(\ell) - \phi(E_T^{miss})) + cos(\phi(\tau_h) - \phi(E_T^{miss})) \tag{5.1}$$

Generally speaking this variable is positive when the E_T^{miss} vector points in the direction such that it would bisect those of the visible decay products and negative when pointing away. For signal events the E_T^{miss} vector is expected to fall in the azimuthal range spanned by the decay products. This cut effectively removes $W \to \ell\nu+$ jets events, where the E_T^{miss} vector will tend to point outside of the angle between the jet misidentified as a τ candidate and the lepton. The distributions for $\Sigma \cos\Delta\phi$ are shown in Figures 5.2a and 5.2b for the $\tau_\mu\tau_h$ and $\tau_e\tau_h$ final states respectively. The peak around zero comes from the $\gamma^*/Z \to \tau\tau$ events that have back-to-back decay products in the transverse plane. The W + jets backgrounds accumulate in the negative region of $\Sigma \cos\Delta\phi$, whereas the $\gamma^*/Z \to \tau\tau$ has an asymmetric tail extending into the positive area of $\Sigma \cos\Delta\phi$ values, which corresponds to events that have a high p_T Z Boson. However, the resolution of the $\phi(E_T^{miss})$ vector is degraded when it has a smaller value. Fortuitously this has no adverse effect when cutting on these variables, because such events correspond to $\Sigma \cos\Delta\phi \approx 0$ and would thus pass the selection requirements anyway.
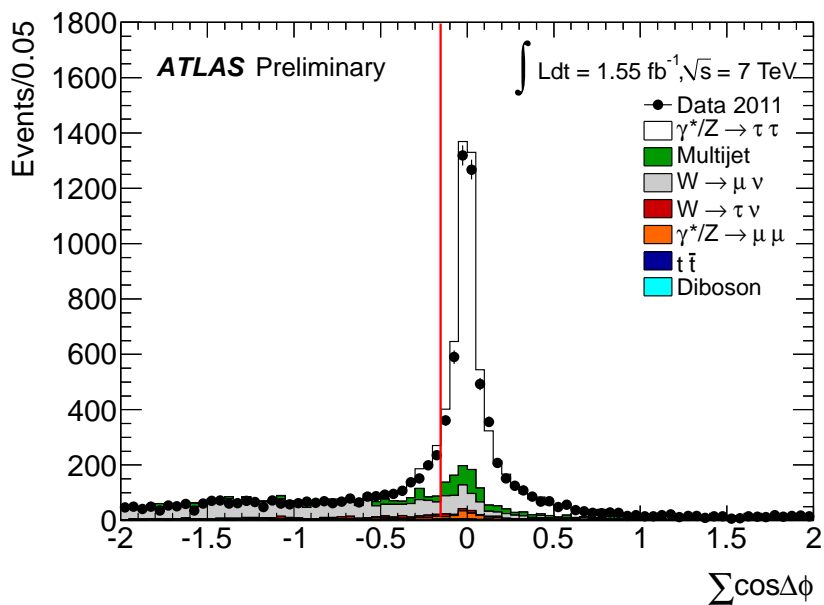
(a) $\tau_\mu \tau_h$ channel
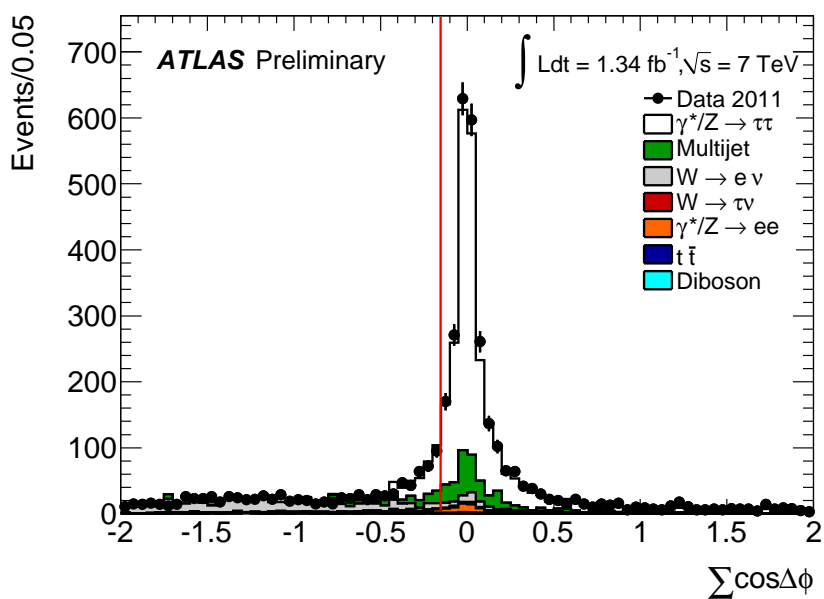
(b) $\tau_e \tau_h$ channel

Figure 5.2: The distributions of $\Sigma \cos \Delta \phi$ for the (a) $\tau_\mu \tau_h$ and (b) $\tau_e \tau_h$ final states. These distributions are shown for all events which have passed all of the selection cuts except the cut on that specific variable. The red lines show where this cut is to be applied [2]. Backgrounds are estimated as outlined in section 5.5.

After this events are selected with an upper cut on the transverse momentum which is defined as:

$$m_T = \sqrt{2 \cdot p_T(\ell) \cdot E_T^{miss} \cdot (1 - \cos \Delta\phi(\ell, E_T^{miss}))} \qquad (5.2)$$

This cut is set at $m_T < 50$ GeV. This suppresses the W + jets background further, Figures 5.3a and 5.3b show the distribution of the m_T for the $\tau_\mu \tau_h$ and $\tau_e \tau_h$ final states respectively.

The chosen τ candidate is required to have exactly 1 or 3 associated tracks and a reconstructed charge of unit magnitude, the charge is calculated from the sum of the charges of the constituent tracks. The number of tracks of the τ candidate is shown in Figure 5.4, with all the selection requirements applied apart from the number of tracks and charge requirements. A small amount of signal ends up in the 2-tracks bin, of these approximately half are 3-prong τ leptons where one of their tracks has not been properly reconstructed, while the rest are 1-prong τ leptons with an additional close-by track that is reconstructed into the τ. Finally in order to suppress $\gamma^*/Z \to \tau\tau$ events with muons misidentified as τ candidates, in the $\tau_\mu \tau_h$ channel only, the fraction of transverse of the energy of the τ candidate deposited in the electromagnetic calorimeter is required to be larger than 0.1.

There is a requirement on the visible mass m_{vis} of the τcandidate and the lepton to be in a window of $35 < m_{vis} < 75$ GeV, to increase the $Z \to \tau\tau$ signal purity and to maximise the separation from the $Z \to \ell\ell$ background. The visible mass is defined as the sum of the invariant masses of the lepton and the hadronic τcandidate. While $Z \to \ell\ell$ events are expected to accumulate at around 90 GeV, the $Z \to \tau\tau$ signal events peak at around 60 GeV due to the missing energy of the neutrinos. The visible mass distributions are shown in Figure 5.5. The E_T distributions of the τlepton candidate are shown in Figure 5.6. The p_T and E_T for the muon and electron tau candidates are shown in Figure 5.7. In both of these figures all the signal selection criteria have been applied.
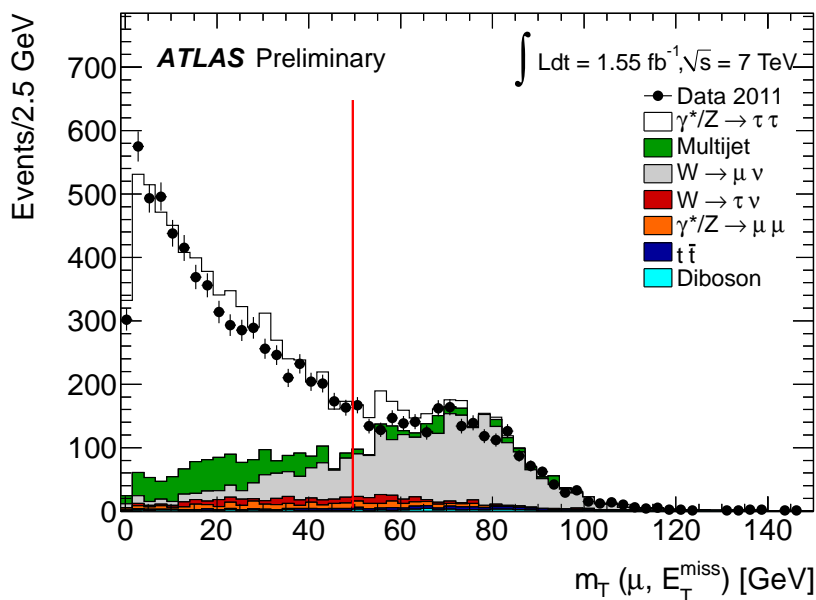
(a) $\tau_\mu\tau_h$ channel
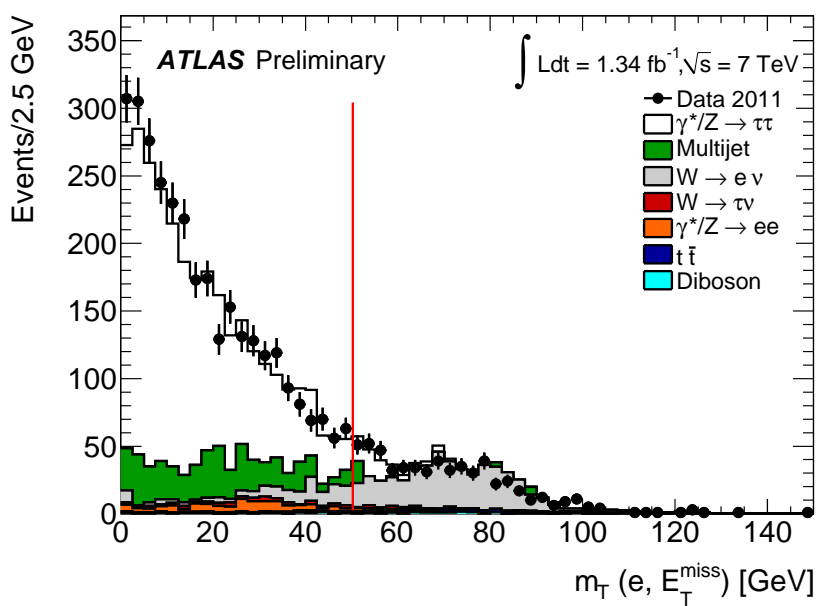
(b) $\tau_e\tau_h$ channel

Figure 5.3: The distributions of the transverse mass (m_T) for the (a) $\tau_\mu\tau_h$ and (b) $\tau_e\tau_h$ final states. These distributions are shown for all events which have passed all of the selection cuts except the cut on the variable. The red lines showing where this cut is to be applied [2]. Backgrounds are estimated as outlined in section 5.5.
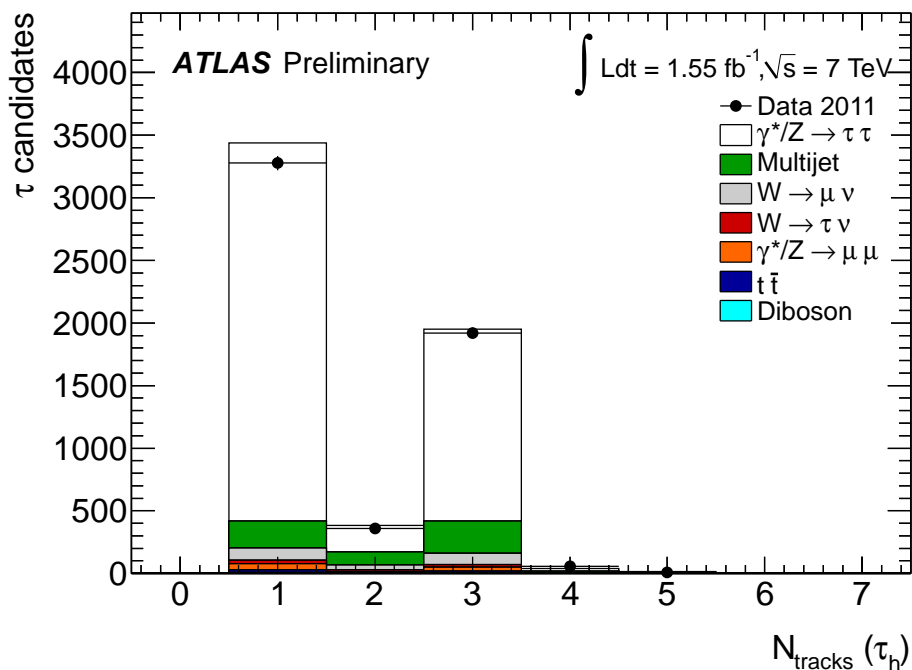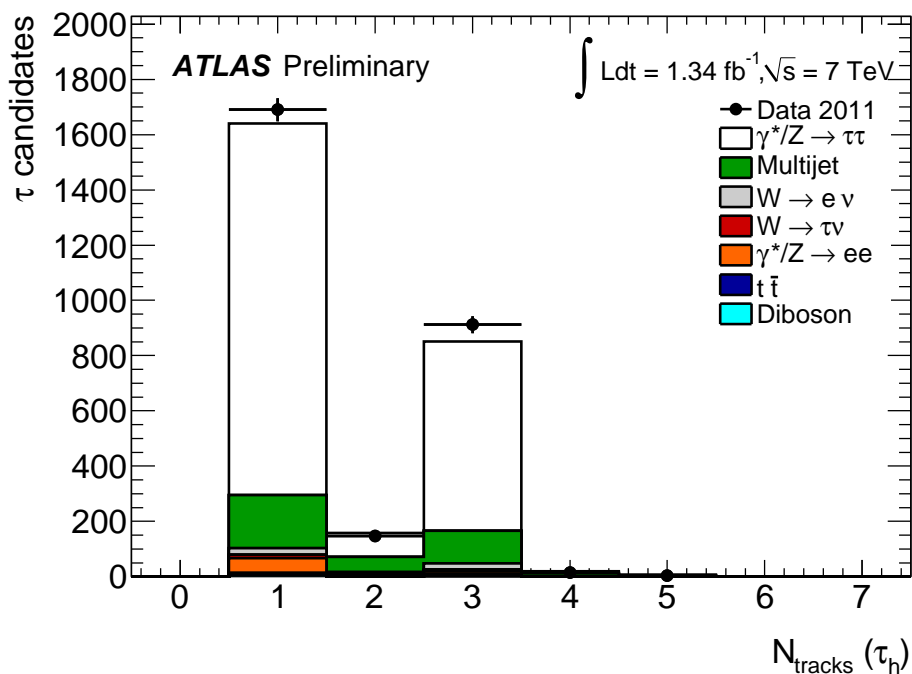
(a) $\tau_\mu\tau_h$ channel

(b) $\tau_e\tau_h$ channel

Figure 5.4: The distribution of the number of tracks associated to the τ, after all the event selection cuts except for the one on the number of tracks and the charge of the τ have been applied [2]. Backgrounds are estimated as outlined in section 5.5.
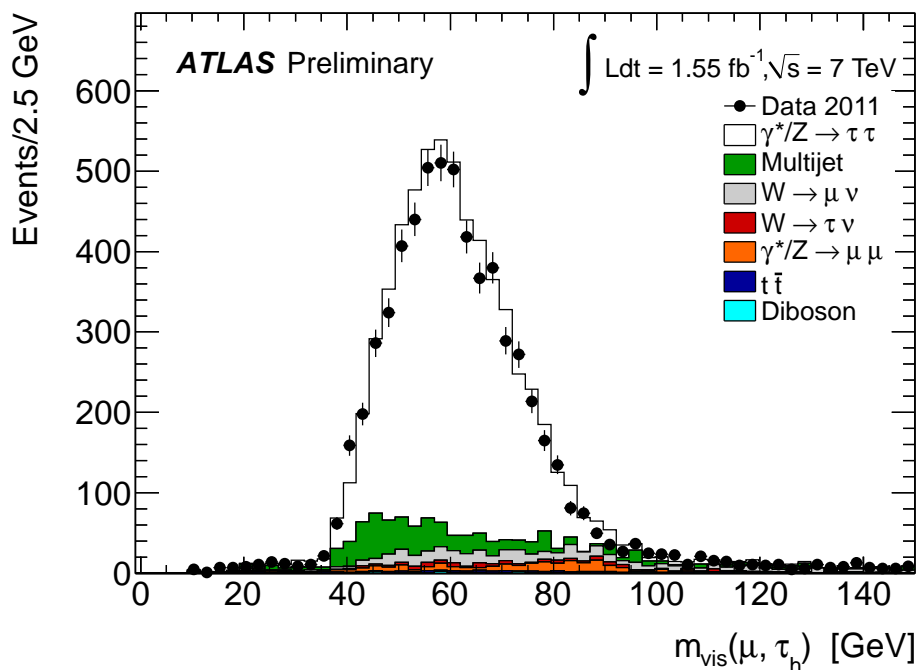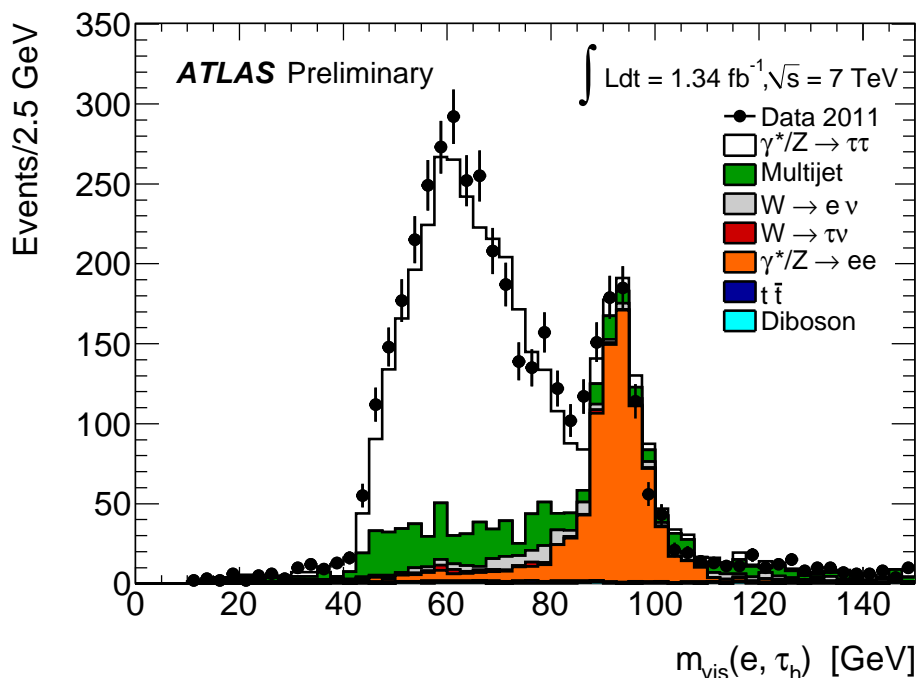
(a) $\tau_\mu \tau_h$ channel

(b) $\tau_e \tau_h$ channel

Figure 5.5: The distributions of the visible mass after all event selections cuts have been applied, except the visible mass cut, in the $\tau_\mu \tau_h$ (a) and $\tau_e \tau_h$ (b) channels. A common mass-window cut is applied in all channels, requiring the visible mass to be between 35 GeV and 75 GeV. This selects events in a region where the most signal events accumulate, while avoiding the region of the $Z \to \ell\ell$ peak [2]. Backgrounds are estimated as outlined in Section 5.5.
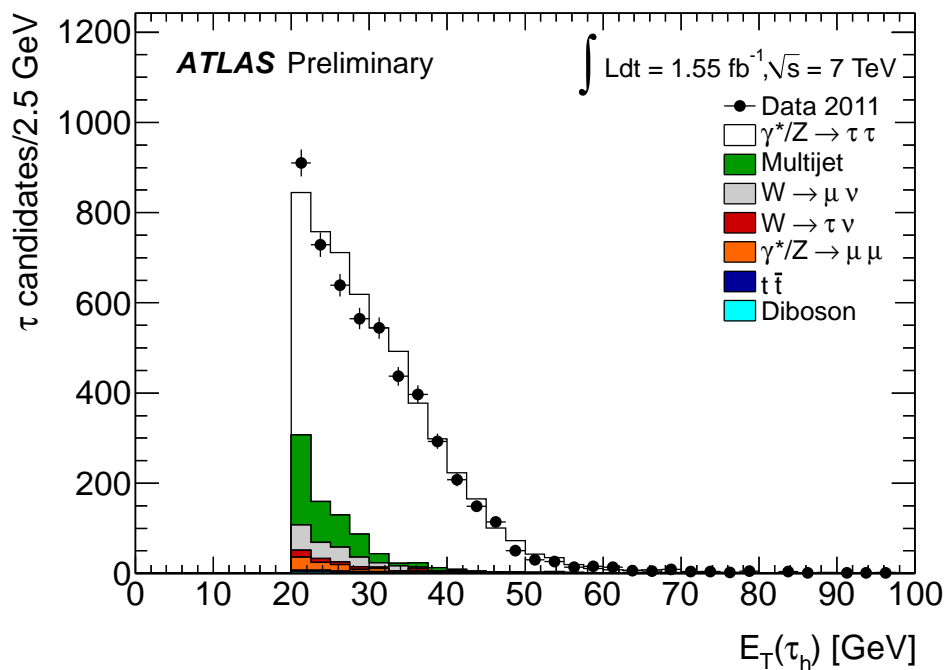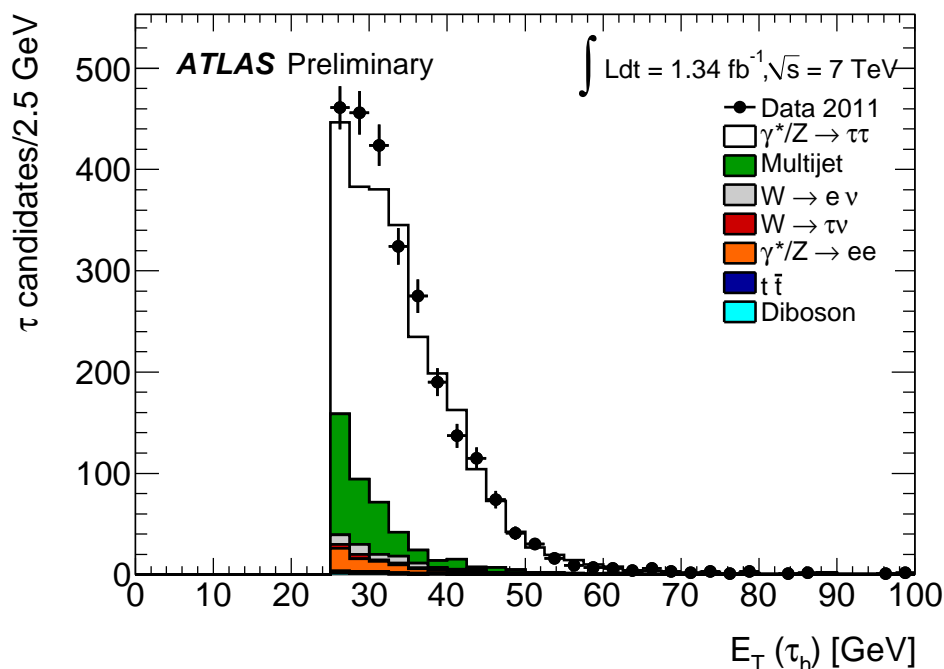
(a) $\tau_\mu\tau_h$ channel

(b) $\tau_e\tau_h$ channel

Figure 5.6: Distributions of the E_T of the τcandidate, for events passing all signal selections for the $\tau_\mu\tau_h$ and $\tau_e\tau_h$ final states [2]. Backgrounds are estimated as outlined in section 5.5.
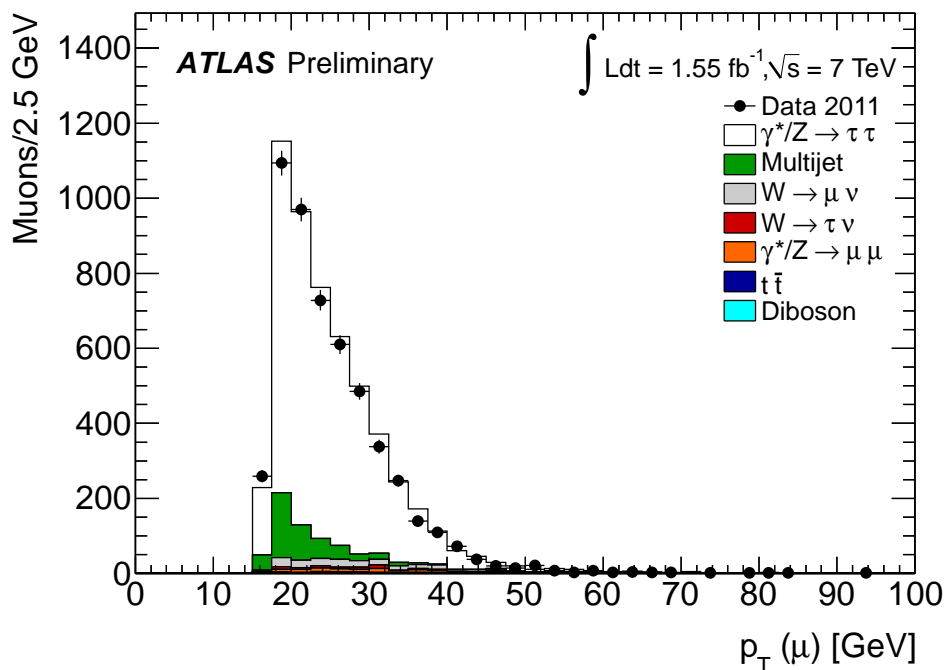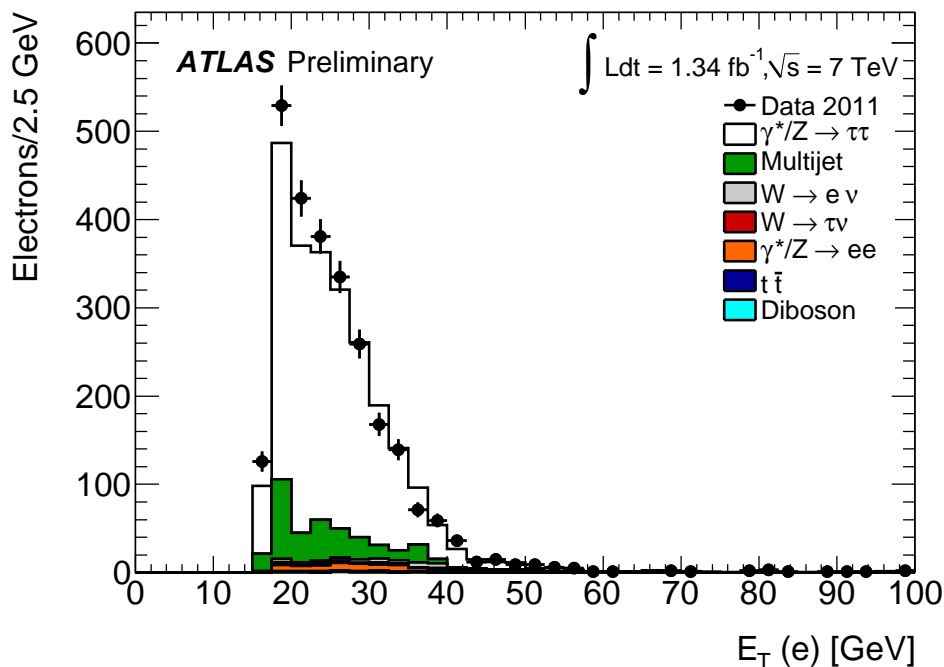
(a) $\tau_\mu \tau_h$ channel

(b) $\tau_e \tau_h$ channel

Figure 5.7: Distributions of the p_T of the muon and the E_T of the electron, for events passing all signal selections for the $\tau_\mu \tau_h$ and $\tau_e \tau_h$ final states [2]. Backgrounds are estimated as outlined in section 5.5.

The sample obtained following all these selection has a relatively high purity

in hadronic τ decays, this allows the variables used by the τ_h identification, to

be studied in depth. Figures 5.8, 5.9 and 5.10 show a number of variables

used by the τ_h identification, following the full selection of the $\tau_\mu \tau_h$ channel.

The definition of these variables is given in ref. [77]. In general for signal like

τ candidates there is a good agreement between data and Monte Carlo. Finally

in Figure 5.11, shows the distribution of the BDT score before any identification

requirements on the τ candidate have been applied but after all other object and

event selection requirements described in this section. In the $\tau_e \tau_h$ channel the use

of a hadronic τ trigger biases these distributions differently in data than in the

MC, where the trigger efficiency is applied as a p_T-dependant weighting, making

these distributions less useful for τ_h identification studies.
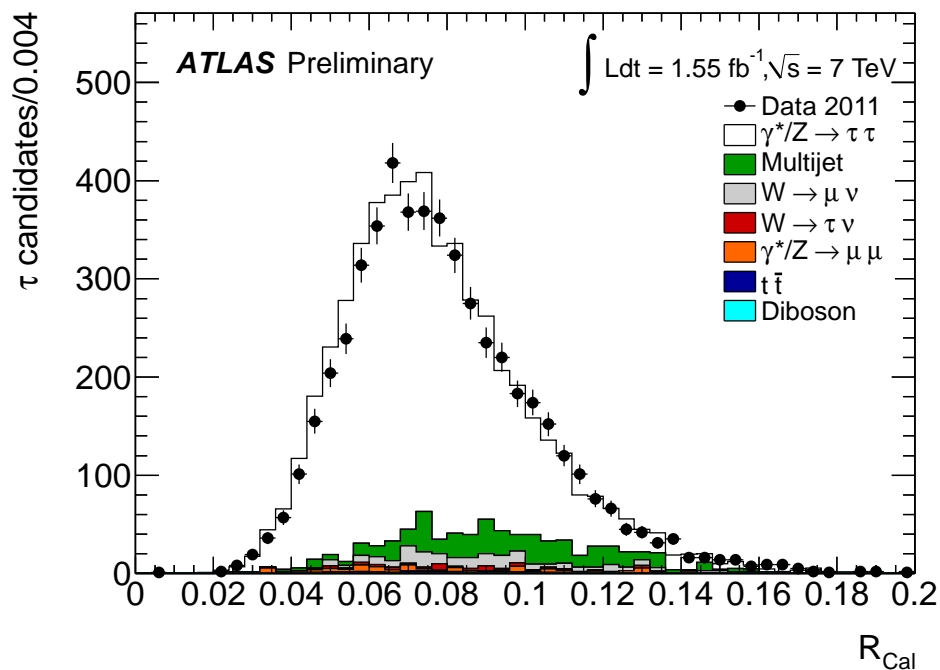
(a) (a)
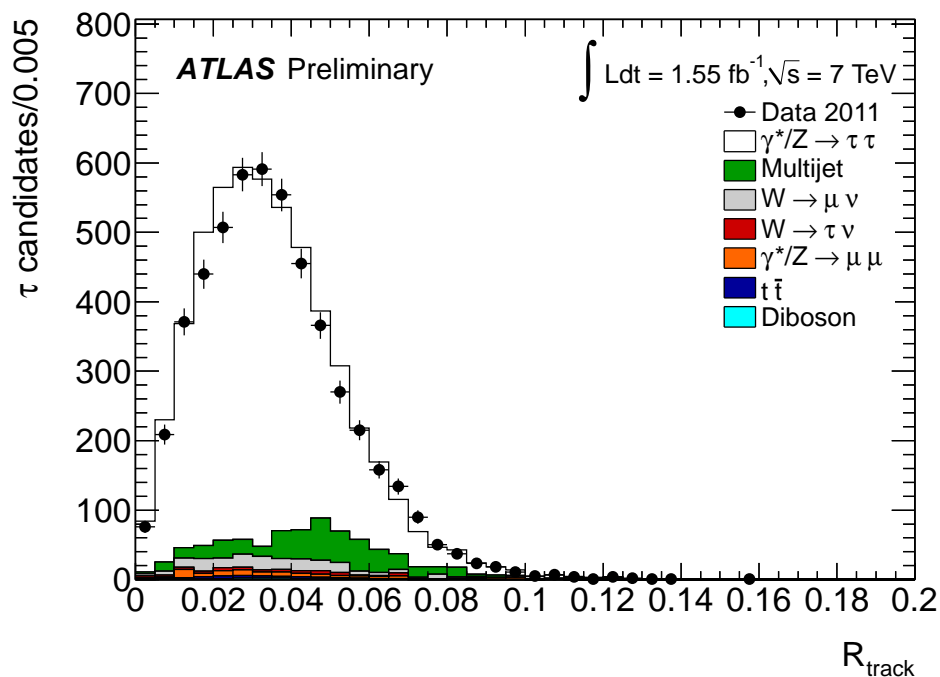
(b)

Figure 5.8: The distribution of the calorimeter radius and track radius τ_h identification variables, in the $\tau_\mu \tau_h$ channel, after the full event selection [2]. There is a more detailed definition of these variables given in ref. [77]. Backgrounds are estimated as outlined in section 5.5.
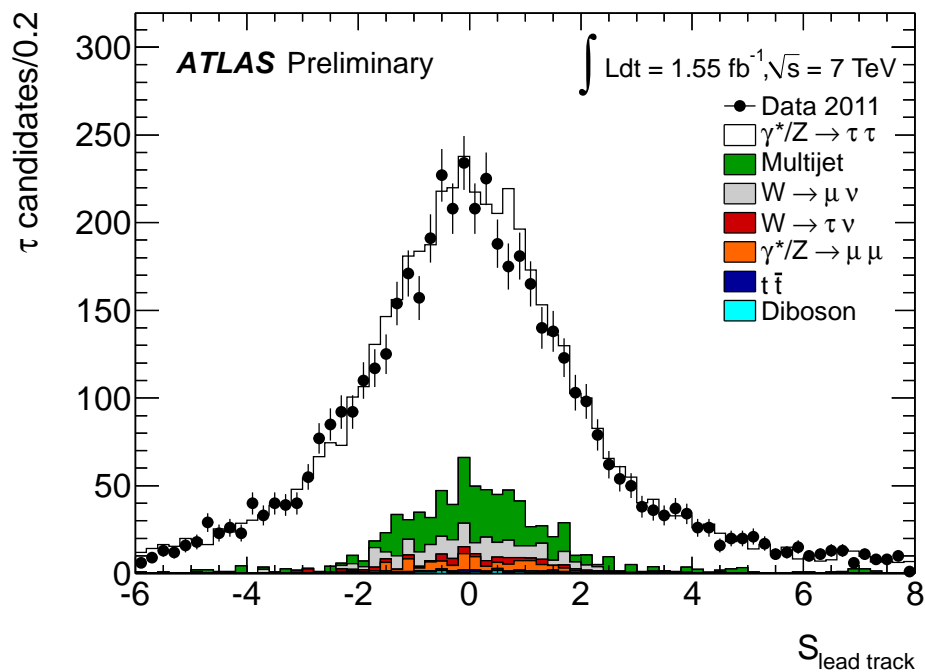
(a)
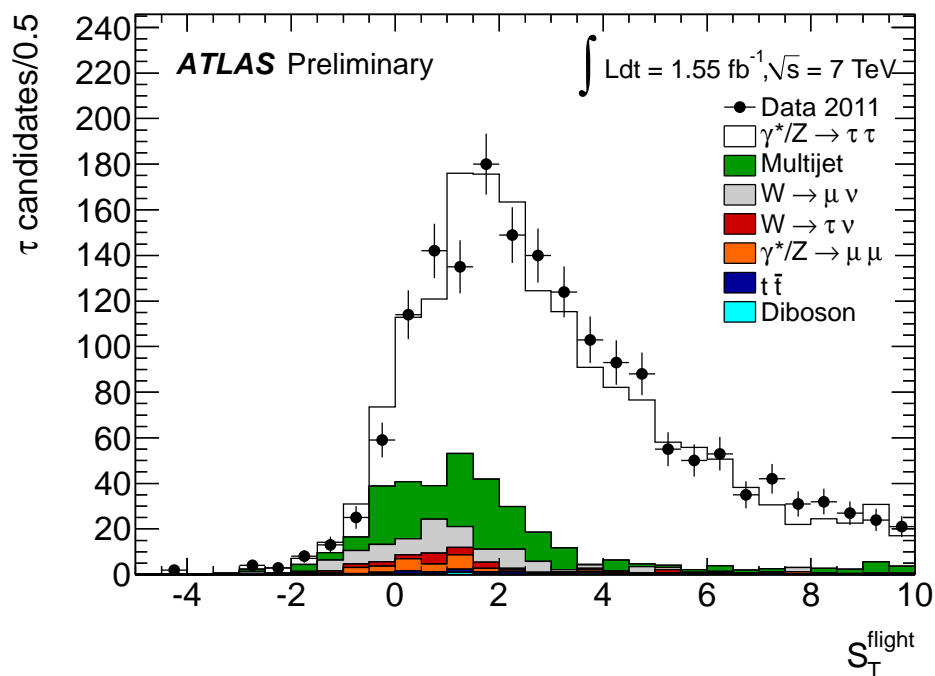
(b)

Figure 5.9: The distributions of the leading track impact parameter significance and the transverse flight path significance in the $\tau_\mu \tau_h$ channel. after the full event selection. There is a more detailed definition of these variables given in [77]. Backgrounds are estimated as outlined in section 5.5.

117
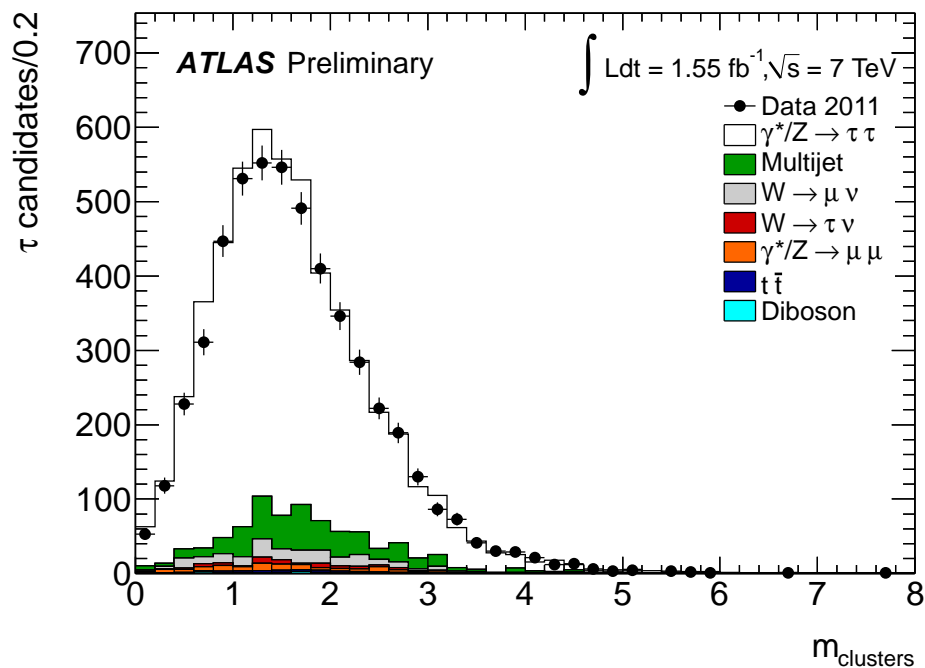
(a)
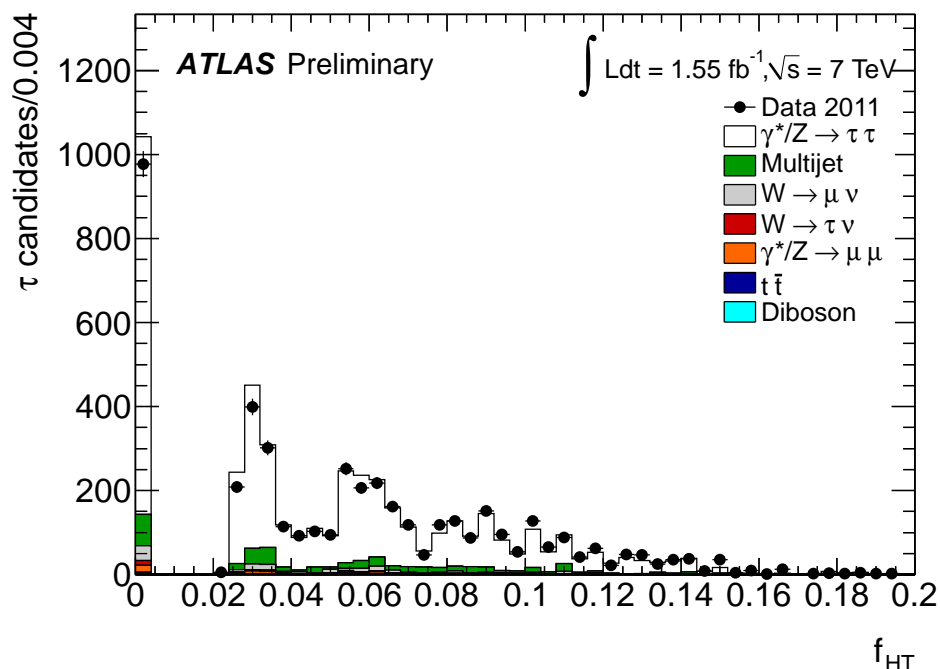
(b)

Figure 5.10: The distribution of the calorimeter cluster mass and the TRT high threshold hit fraction, in the $\tau_\mu \tau_h$ channel, after the full event selection [2]. There is a more detailed definition of these variables given in ref. [77]. Backgrounds are estimated as outlined in section 5.5.
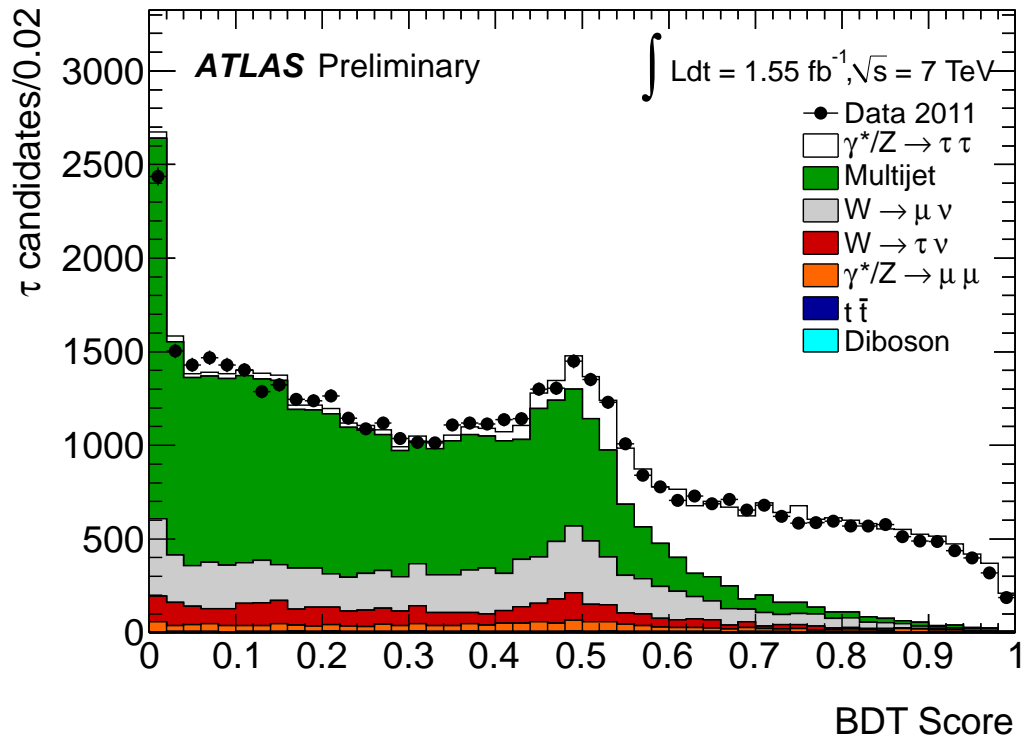
Figure 5.11: The distribution of the score from the BDT, used to discriminate τ candidates from jets, after the full selection in the $\tau_\mu \tau_h$ channel except for the cuts on the τ candidate [2]. Backgrounds are estimated as described in 5.5

5.4.2 The $\tau_e \tau_\mu$ Channel

Events in the $\tau_e \tau_\mu$ channel are characterised by two oppositely charged isolated leptons in the final state. Therefore, exactly one electron and one muon of opposite electric charge that pass the selection criteria described earlier (section 5.3) are required. By selecting events that contain two leptons of different flavours, the contributions from $\gamma^*/Z \to \mu\mu$ and $\gamma^*/Z \to ee$ process are greatly reduced. The requirement $\Sigma \cos \Delta\phi > -0.15$ is applied (the same as in the $\tau_\ell \tau_h$ channels), discriminating against the $W \to \tau\nu \to \ell\nu\nu$, WW and $t\bar{t}$ background events. This can be seen in Figure 5.13a, which shows this distribution after all cuts except on the variable itself.

Furthermore, a selection is made by requiring that events satisfy the criteria

119

$\Sigma_T < 140$ GeV, where Σ_T is defined as:

$$\Sigma_T = E_T(e) + E_T(\mu) + E_T(jets) + E_T^{miss} \tag{5.3}$$

The topology of $t\bar{t}$ events, especially in the dilepton decay channels, have multiple jets and leptons with a high p_T, as well as a large E_T^{miss} vector, this results in a higher value for Σ_T. The signal events contrastingly, $Z \to \tau\tau \to \ell\ell + \nu\nu\nu\nu$, have a low Σ_T. This is shown in Figure 5.13b, which highlights the suppression power of this cut.

Finally, the invariant mass of the two leptons is calculated, applying the same requirements as in the other channels, $35 < m_{vis} < 75$ GeV. This distribution of the muon p_T and election E_T after all the selection criteria have been applied can be seen in Figure 5.14
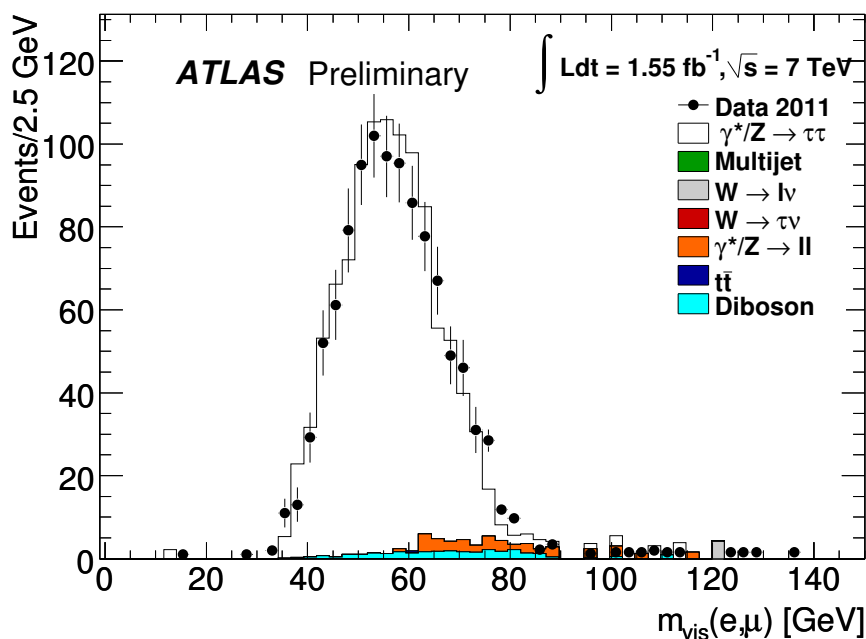
Figure 5.12: The visible mass distribution after all event selection cuts have been applied, except that on the visible mass, in the $\tau_e\tau_\mu$ channel. A common mass-window cut is applied in all channels, requiring the visible mass to be between 35 GeV and 75 GeV.
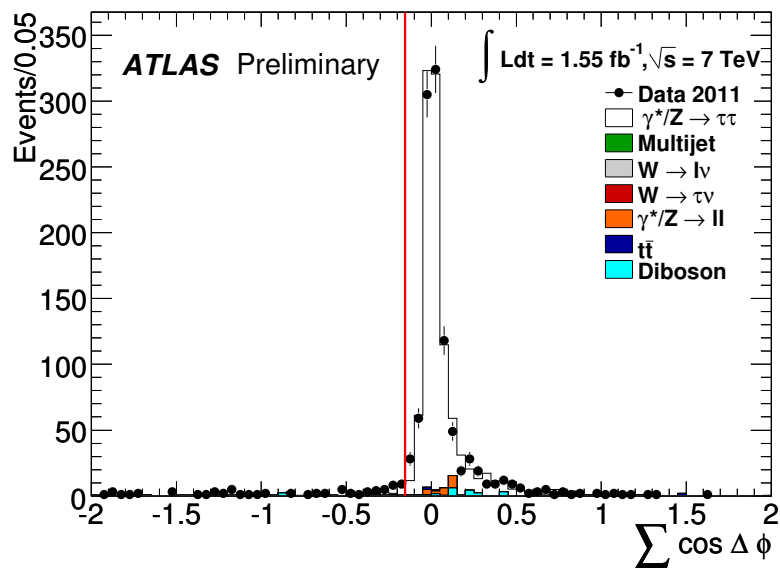
(a) $\tau_e \tau_\mu$ channel
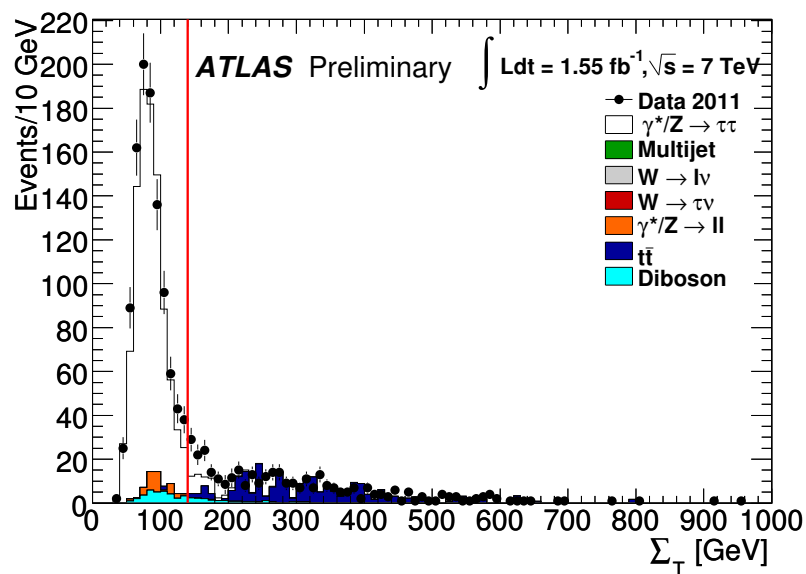
(b) $\tau_e \tau_\mu$ channel

Figure 5.13: The $\Sigma \cos \Delta \phi$ distribution (a) and Σ_T (b) after all selections except the cut on the respective variable itself. The red line shows where the cut is applied [2].
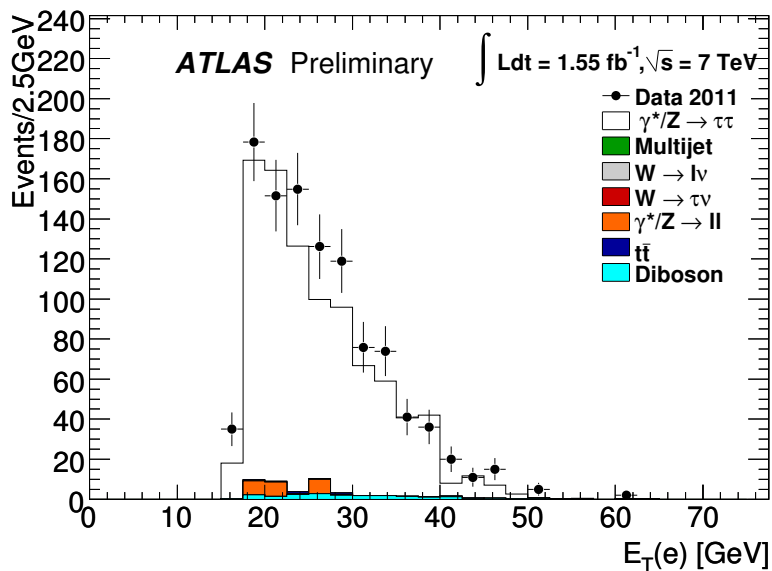
(a) E_T of the electron.
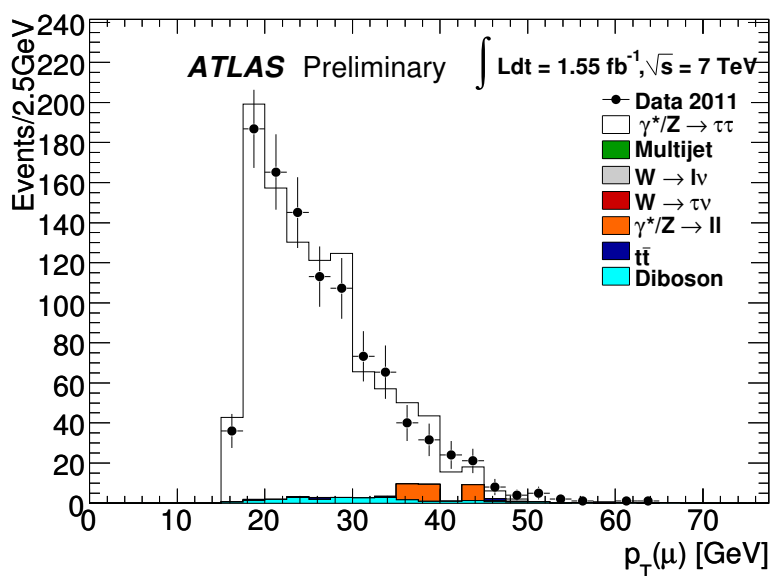
(b) p_T of the muon.

Figure 5.14: Distributions of the E_T of the election and the p_T of the muon. For events passing all selections for the $\tau_e\tau_\mu$ final state.

5.5   Background Estimation

The contributions made by the non-dominating $t\bar{t}$, diboson, W and Z backgrounds are obtained from Monte Carlo simulations, in the $\tau_e\tau_\mu$ channel. While the multi-jet background is estimated using data-driven methods, described in this section.

	$\tau_\mu\tau_h$ $(1.55fb^{-1})$	$\tau_e\tau_h(1.34fb^{-1})$	$\tau_e\tau_\mu(1.55fb^{-1})$
$\gamma^*/Z \to \ell\ell$	81±7	64±4	23±4
$W \to \ell\nu$	186±13	45±5	< 0.5
$W \to \tau\nu$	49±5	18±2	< 0.5
$t\bar{t}$	31±1	17±1	2±1
Diboson	15±2	6±1	18±2
Multi-jet	432±30	300±21	13±7
Total Background	793±34	449±22	56±8
$\gamma^*/Z \to \tau\tau$	4544±49	2029±25	981±26
N_{obs}	5184	2600	1035

Table 5.1: The expected number of events per process and number of events observed in data, after the full selection. The background estimations were obtained as described in Section 5.5. The quoted uncertainties are statistical only [2].

5.5.1   W + Jets

In the $\tau_e\tau_\mu$ final state the $W \to \ell\nu$ and $W \to \tau\nu$ backgrounds were found to be small. In the $\tau_\ell\tau_h$ final states, however, these backgrounds are important, and are constrained by normalising them with a W boson enriched control region in a data sample. This corrects the Monte Carlo for a known overestimation [78] of the probability for quark and gluon jets produced in association with the W to be misidentified as τ_h decays. The control region is defined so as to contain events passing all selection cuts, but inverting those designed to reject the W background $(m_T, \Sigma \cos \Delta\phi)$. This provides a W sample that has a very high purity. The multi-jet background contamination in this region is negligible, while the Monte Carlo estimation of the small electroweak and $t\bar{t}$ contribution is subtracted before calculating the normalisation factor. The obtained factor is 0.54 ± 0.01 (stat.) for the $\tau_\mu\tau_h$ final state and 0.44 ± 0.02 (stat.) for the $\tau_e\tau_h$ final state. The difference

between the two is expected due because the tau trigger in the $\tau_e\tau_h$ channel introduces a bias on the misidentified τ candidates in that channel.

5.5.2 Z + Jets

The $Z \to \ell\ell$+jets channel is one of the principle backgrounds for the $\tau_\ell\tau_h$ channels. This can contribute to the background in two different ways:

(a) The τ_h candidate can be a misidentified lepton from the Z decay,

(b) A misidentified jet produced in association with the Z boson.

Information garnered from truth-level events is used to separate the Monte Carlo events corresponding to each case, and a different treatment is applied.

Case (a) is mainly important in the electron channel, since the probability for electrons to be misidentified as τ_h candidates is much higher than for muons. In this case the electron misidentification probability in Monte Carlo is corrected to that measured in data using $|\eta|$-dependant scale factors obtained from a $Z \to ee$ tag-and-probe study [77].

In case (b), the τ candidate is a misidentified jet. The Monte Carlo overestimates the probability for this to happen, as discussed above for the $W+$ jet process. The number of simulated $Z \to \ell\ell +$ jets events is normalised to collision data, using a control region enriched with Z bosons. This region is obtained by requiring two electrons or muons with an invariant mass compatible with the Z mass ($66 < m_{\ell\ell} < 116$ GeV), in addition to a τ_h candidate satisfying the standard analysis selection. The obtained normalisation factor is 0.57±0.04 (stat.) for the $\tau_\mu\tau_h$ final state and 0.39±0.05 (stat.) for the $\tau_e\tau_h$ final state. These factors are applied only to the $Z \to \ell\ell$ Monte Carlo events in which the τ_h candidate is not a truth-matched lepton.

5.5.3 Multi-jet

In hadron colliders one of the main backgrounds are events with multiple jets. These backgrounds are typically composed of one or two real or fake leptons

coming from a jet, and, in the $\tau_\ell \tau_h$ channels, a jet misidentified as a τ candidate. A data-driven method is used to estimate their contribution across all three channels. A multi-jet enriched control region is constructed, requiring the two candidate τ decay products to have the same sign. The ratios of events where the decay products have the opposite sign (OS) to those where they have the same sign (SS), $R_{OS/SS}$, is then measured in an additional two control regions where the lepton isolation requirements are inverted for each lepton. In all of the channels, the control regions are defined after the full selection has been applied, as described in section 5.3.

The Z, W, diboson and $t\bar{t}$ backgrounds in all three control regions are subtracted using Monte Carlo simulations. For the same sign control regions of the $\tau_\ell \tau_h$ final states, the W normalisation factor is computed using a new W control region that is identical to the control region described above, apart from having the same sign requirement applied. The reason for this being that the same sign requirement changes the relative fraction of quark and gluon induced jets leading to different τ misidentification probabilities. A small contamination of signal events is present in the $\tau_\mu \tau_h$ channel in the anti-isolated, OS region, due to the tight isolation both at trigger level at the offline selection. These signal events are subtracted along with the electroweak backgrounds, assuming the theoretical cross section, with 5% uncertainty. Varying the normalisation of these signal events within that range was found to have a very small effect on the final measured cross section. The following values of $R_{OS/SS}$ were obtained:

- $\tau_e \tau_h$ channel, $R_{OS/SS} = 1.06 \pm 0.03$ (stat.),

- $\tau_\mu \tau_h$ channel, $R_{OS/SS} = 1.13 \pm 0.04$ (stat.),

- $\tau_e \tau_\mu$ channel, $R_{OS/SS} = 2.20 \pm 0.22$ (stat.).

These ratios are then applied on the SS, isolated events of the main control region in order to estimate the multi-jet contribution to the signal region.

5.6 Methodology for Cross Section Calculation

The measurements of the cross sections are done for each channel separately and are then combined. The calculation is performed using the same method as in previous years [79], using the formula:

$$\sigma(Z \to \tau\tau) \times Br = \frac{N_{obs} - N_{bkg}}{A_Z \cdot C_Z \cdot \mathcal{L}} \tag{5.4}$$

Where N_{obs} is the number of observed events in data, N_{bkg} is the number of estimated background events, Br is the branching ratio for the specific channels, and $\mathcal{L}$ is the integrated luminosity for the final state of interest. C_Z is the experimental correction factor that accounts for the efficiency of triggering, reconstructing and identifying the $Z \to \tau\tau$ events with the fiducial regions. A_Z is the acceptance factor that extrapolates the fiducial cross section to the entire detector space. Firstly, for C_Z the fiducial region is defined as:

- The $\tau_\mu \tau_h$ channel:

    - Muon: $p_T > 17$ GeV, $|\eta| < 2.4$

    - Tau: $E_T > 20$ GeV, $|\eta| < 2.47$, excluding $1.37 < |\eta| < 1.52$

    - Event: $\Sigma \cos \Delta\phi > 0.15$, $m_T < 50$ GeV, m_{vis} within [35, 75] GeV

- The $\tau_e \tau_h$ channel:

    - Electron: $E_T > 17$ GeV, $|\eta| < 2.47$ excluding $1.37 < |\eta| < 1.52$

    - Tau: $E_T > 25$ GeV, $|\eta| < 2.47$, excluding $1.37 < |\eta| < 1.52$

    - Event: $\Sigma \cos \Delta\phi > 0.15$, $m_T < 50$ GeV, m_{vis} within [35, 75] GeV

- The $\tau_e \tau_\mu$ channel:

    - Electron: $E_T > 17$ GeV, $|\eta| < 2.47$ excluding $1.37 < |\eta| < 1.52$

    - Muon: $p_T > 17$ GeV, $|\eta| < 2.4$

    - Event: $\Sigma \cos \Delta\phi > 0.15$, m_{vis} within [35, 75] GeV

Where the variables which at the reconstruction level make use of E_T^{miss}, m_T and $\Sigma \cos \Delta \phi$ are constructed using the transverse component of the sum of the neutrino momenta, the C_Z factor is calculated using ALPGEN with the CTEQ6L1 [68] PDF set. It is determined as the ratio between the number of events passing the entire analysis selection after full detector simulation and the number of events in the fiducial region at the generator level. The four momenta of the τ candidates are defined by including photons radiated by both the τ leptons and their decay products within a cone of size of $\Delta R = 0.4$. The correction that the C_Z factor provides the cross section with in the fiducial region of each measurement:

$$\sigma^{fid}(Z \to \tau\tau) \times Br = \frac{\mathrm{N_{obs} - N_{bkg}}}{\mathrm{C_Z} \cdot \mathcal{L}} \tag{5.5}$$

This is independent of the extrapolation procedure to the full phase space.

The acceptance factor, A_Z allows the extrapolation of σ^{fid} to the total cross section, defined by equation (5.4). The factor is determined from Monte Carlo simulations as the ratio of events at generator level whose $\tau\tau$ invariant mass, before Final State Radiation (FSR), lies within the mass window [66, 116] GeV, and the number of events at generator level that falls within the fiducial regions defined above. The A_Z factor accounts for events that migrate from outside the invariant mass window into the fiducial region. The central values for A_Z are determined using a Pythia [80] Monte Carlo sample generated with the modified leading order PDF MRSTLO* [81].

The values of A_Z and C_Z that were obtained, along with their statistical uncertainties, are given for all three channels in Table 5.2.

	$\tau_\mu \tau_h$	$\tau_e \tau_h$	$\tau_e \tau_\mu$
A_Z	0.0976 ± 0.0002(stat)	0.0687 ± 0.0002(stat)	0.0784 ± 0.0003(stat)
C_Z	0.1417 ± 0.0016(stat)	0.1009 ± 0.0013(stat)	0.1348 ± 0.0037(stat)

Table 5.2: Central values and Monte Carlo statistical uncertainty for the A_Z and C_Z factors [2].

5.7 Systematic Uncertainties

5.7.1 Trigger Efficiency

The efficiency of the isolated muon trigger used in the $\tau_\mu\tau_h$ and $\tau_e\tau_\mu$ channels is measured in $Z \rightarrow \mu\mu$ events as a function of η and ϕ, with respect to the reconstructed muons passing offline isolation requirements of the analysis. For the $\tau_e\tau_h$ channel which uses the combined electron and τ trigger, the efficiencies and associated systematics of the two components of the combined trigger are considered uncorrelated to each other and therefore can be measured and applied separately. The electron trigger efficiency is measured using $W \rightarrow e\nu$ with a tag and probe method as a function of both E_T and $|\eta|$, the correction factors that arise from this are applied to the Monte Carlo. The τ trigger efficiency with with respect to the offline τ candidates that pass all identification requirements is a function of p_T and is measured in data using a $Z \rightarrow \tau\tau$ sample obtained by triggering on a single-lepton trigger and the Monte Carlo is directly weighted by the measured efficiency.

5.7.2 Efficiency of Lepton Reconstruction, Identification and Isolation

The efficiency of the reconstruction, identification and isolation of leptons are each measured separately in data using tag and probe methods. The corresponding Month Carlo efficiency for each step is corrected to agree with the measured values. The efficiency of the electron reconstruction and identification is measured from the following samples [62]:

- $W \rightarrow e\nu$,

- $Z \rightarrow ee$,

- $J/\Psi \rightarrow ee$.

The muon reconstruction efficiency is measured in $Z \rightarrow \mu\mu$ events, following the prescription outlined in ref. [82]. The isolation efficiencies for the electrons and

muons are measured using the $Z \to ee$ and $Z \to \mu\mu$ events respectively. The corrections that are calculated from these are applied to all of the relevant Monte Carlo sampled used in this section. To estimate the effect of the uncertainties on the yield of the signal and background predictions, the individual uncertainties of the efficiency measurements are added in quadrature, including all the efficiencies on the electron and muon trigger efficiencies described in 5.7.1.

5.7.3 Hadronic τ Identification Efficiency and Misidentification Rate

The efficiency of identifying of τ candidates has been measured using both $Z \to \tau\tau$ and $W \to \tau\nu$ events (in data) collected in 2011, described fully in [77]. From this measurement, the average uncertainty on the identification efficiency for τ candidates selected with the BDT medium selection is around 5%. The rate of misidentification of electrons as τ candidates has been measured in data, using $Z \to ee$ and a tag-and-probe study, explained fully in ref. [77]. $|\eta|$-dependent correction factors were calculated and applied to Monte Carlo samples where a τ candidate had been matched with an electron, which had in turn been truth matched. These correction-factors were varied within their uncertainties and found to have a per 1×10^{-3} effect on the measured cross section in the $\tau_e\tau_h$ channel.

5.7.4 Energy Scale

The effects of the electron [62], the τ [77] and jet [83] energy scale uncertainties, including the calorimetric components of the E_T^{miss}, are evaluated by simultaneously shifting each one up or down by one standard deviation. However, the jet candidates are not considered in the $\tau_\ell\tau_h$ final states, and the τ candidates are not considered for the $\tau_e\tau_\mu$ final state. The muon energy scale, and the correlated effect on the E_T^{miss}, is also evaluated but it was found to be negligible in comparison with the other uncertainties.

5.7.5 Background Estimation

The multijet background systematic uncertainties arise from statistical uncertainties in the control regions, the subtraction of Monte Carlo in the control regions, and the degree that the ratio of Opposite sign and Same sign events ($R_{OS/SS}$) is independent of the lepton isolation efficiencies. The latter is obtained by studying the dependence of $R_{OS/SS}$ on the isolation variables, the maximum deviation of which from the average value is taken as its systematic uncertainty. In the $\tau_e\tau_h$ channel, the stability of the $R_{OS/SS}$ during the cut-flow was found to be non-negligible, and the observed 4% difference is assigned as an additional systematic uncertainty. All effects were added in quadrature to obtain the total systematic uncertainty on the multijet background estimation. Finally, all systematic uncertainties on the Monte Carlo estimates discussed in this section are also propagated into the control regions, and their impact on the multi-jet background is evaluated.

For the W and Z background estimation in the $\tau_\ell\tau_h$ channels, the statistical uncertainty on the normalisation factors is assigned as a systematic uncertainty. Additionally, all other systematic uncertainties described in this section are applied to the Monte Carlo sample and their effects are evaluated. However this was found to be lower than, approximately of the order of, the statistical uncertainty on the normalisation factors.

5.7.6 Acceptance Systematics

The theoretical uncertainty on the geometric and kinematic acceptance factor A_Z is dominated by the limited knowledge of the proton PDFs and the modelling of the Z-boson production at the LHC. The uncertainty due to the choice of PDF set is evaluated by considering the maximum deviation between the acceptance obtained using the default sample and the values obtained by reweighting the sample to the CTEQ6.6 and HERAPDF1.0 [84] PDF sets. The uncertainties within the PDF set are determined by using the 44 PDF error eigenvectors available for the CTEQ6.6 NLO PDF set [68]. The variations are obtained by reweighting the default sample to the relevant CTEQ6.6 eigenvector. The uncertainties due to the modelling of W and Z production are estimated using MC@NLO interfaced

with HERWIG for parton showering, with the CTEQ6.6 PDF set and a lower bound on the invariant mass of 60 GeV. The deviation with respect to the A_Z factor obtained using the default sample reweighted to the CTEQ6.6 PDF set central value and with an applied lower bound on the invariant mass of 60 GeV is taken as the uncertainty. In the default sample the QED radiation is modelled by PHOTOS which has an accuracy of better than 0.2%, and therefore has a negligible uncertainty compared to uncertainties from the PDFs. Summing the contributions in quadrature, total theoretical uncertainties on A_Z of 3.1%, 3.4% and 3.2% are assigned to the $\tau_\mu \tau_h$, $\tau_e \tau_h$ and $\tau_e \tau_\mu$ final states respectively.

5.7.7 Other uncertainties

There are a number of other sources of uncertainty, such as that from the object quality requirements and the effect of a local readout problem in the Electromagnetic Calorimeter. These were evaluated but have a negligible impact on the total uncertainty. The lepton resolution is found to only have a less than 1% effect on the C_Z and the background predictions, while the jet resolution has an effect of 1.7% in the $\tau_e \tau_\mu$ channel which is the only channel in which jets are used. Uncertainties due to charge misidentification are negligible. The uncertainties on the theoretical cross sections by which the background Monte Carlo samples are scaled are also found to only have a very small impact on the corresponding background prediction. Finally, the uncertainty on the luminosity is taken to be 3.7% from ref. [85].

5.7.8 Summary of Systematics

Systematic Uncertainty	$\delta\sigma/\sigma(\%)\tau_\mu\tau_h$	$\delta\sigma/\sigma(\%)\tau_e\tau_h$	$\delta\sigma/\sigma(\%)\tau_e\tau_\mu$	Correlation
Muon Efficiency	1.7	—	1.5	×
Electron Efficiency	—	5.0	6.0	×
Muon Resolution	< 0.05	—	< 0.05	×
Electron Resolution	—	0.1	0.2	×
Jet Resolution	—	—	1.7	—
τ ID Efficiency	5.2	5.2	—	×
τ Fake Rate	—	0.2	—	—
Energy Scale	8.2	9.3	4.5	×
τ Trigger Efficiency	—	4.7	—	—
W Normalisation Factor	< 0.05	< 0.05	—	—
Z Normalisation Factor	< 0.05	< 0.05	—	—
Multijet Estimation	0.8	1.3	0.4	×
Background Theoretical σ	0.1	0.2	0.2	×
Monte Carlo Statistics	1.2	1.4	2.9	—
A_Z uncertainties	3.1	3.4	3.2	×
Total Systematic unc.	10.4	13.2	8.9	
Luminosity unc.	3.7	3.7	3.7	×
Statistical unc.	1.6	2.4	3.3	—

Table 5.3: Relative statistical and systematic uncertainties in percent on the total cross section measurement. The lepton efficiency term includes the lepton trigger, reconstruction, identification and isolation uncertainties as described in 5.7.2. The last column indicates whether or not a give systematic is treated as fully correlated (×) or uncorrelated (−) among the relevant channels when combining the results [2].

The uncertainty on the experimental correction factor C_Z is given by the effect of the uncertainties described previously on the signal Monte Carlo. The theoretical uncertainties on the experimental correction factor C_Z are negligible. For the total estimated background uncertainties, the correlations between the electroweak and $t\bar{t}$ background uncertainties and the multijet background uncertainty, arising from the subtraction of the former in the control regions used on the latter. The largest systematic uncertainty comes from the energy scale in the two $\tau_\ell\tau_h$ channels. Other important uncertainties arise from the τ candidates and electron identification efficiencies and, for the $\tau_e\tau_h$ final state, the τ trigger efficiency. The

correlation between the uncertainty on C_Z and on $(N_{obs} - N_{bkg})$ is accounted for in obtaining the final uncertainties on the cross section measurements, which are summarised in the Table 5.3.

5.8 Measured $\sigma(Z \to \tau\tau)$

Final State	Fiducial cross section $\sigma^{fid}(Z \to \tau\tau) \times Br(\tau \to ...)$
$\tau_\mu \tau_h$	20.0±0.3(stat)±2.0(syst)±0.7(lumi)pb
$\tau_e \tau_h$	15.9±0.4(stat)±2.0(syst)±0.6(lumi)pb
$\tau_e \tau_\mu$	4.7±0.4(stat)±2.0(syst)±0.6(lumi)pb

Final State	Total cross section $\sigma(Z \to \tau\tau, m_{inv}[66 - 116 GeV])$
$\tau_\mu \tau_h$	0.91±0.01(stat)±0.09(syst)±0.03(lumi)nb
$\tau_e \tau_h$	1.00±0.02(stat)±0.13(syst)±0.04(lumi)nb
$\tau_e \tau_\mu$	0.96±0.03(stat)±0.09(syst)±0.04(lumi)nb

Table 5.4: The production cross section multiplied by branching ratio for the $Z \to \tau\tau$ process as measured in each of the three final states. For the fiducial cross sections, the measurements also include the branching ratio for the τ to its decay products.

Combining the numbers from the previous sections in this chapter, and following the methodology laid out in 5.6, the results of this calculation are laid out in Table 5.4. This shows the numbers obtained for both the fiducial cross sections and the total cross sections for a ditau invariant mass of $[66 - 116]$ GeV. The total cross section has had the correction for the $\tau \to l\nu\nu$ and $\tau \to \tau_{had}$ branching ratio, 0.2250 ± 0.0009 for the $\tau_\mu \tau_h$ channel, 0.2313 ± 0.0009 for the $\tau_e \tau_h$ channel and 0.0620 ± 0.0002 for the $\tau_e \tau_\mu$ channel [47] included.

The combinations of the cross section measurements form the three different final states is obtained using the Best Linear Unbiased Estimate (BLUE) method, described in full in refs. [86, 87]. This method aims to determine the best estimate of the combined total cross section measurement, while accounting for correlations between the uncertainties from each individual channel. The last column of table 5.3, shows whether or not a given systematic has been treated as correlated or uncorrelated amongst the relevant channels when calculating the combined

result. All of the systematic uncertainties that pertain to the efficiency and the resolution of the various physics objects used in the three analysis channels are assumed to be fully correlated between final states that make use of said same objects, whereas no correlations is assumed to exist between the systematic uncertainties relating to the different physics objects.

The dominant uncertainties in this study are correlated across all channels, resulting in them being much larger than any of the uncorrelated uncertainties. In the case of large positive correlations between the inputs, BLUE can yield large negative weights and a central value that does not sit within the range of the inputs; the result in these cases, is very sensitive to the values of the assumed correlations between the inputs [86]. In order to avoid this, the conservative approach is taken to exclude from the BLUE calculations the three largest correlated systematic uncertainties (energy scale, luminosity, and acceptance uncertainties). These are added instead, to the final uncertainty using standard error propagation on the linear combination of the individual channels, using the weights from the BLUE calculations, when those uncertainties are not included. However this means, that a larger total uncertainty on the combination is obtained, since these large uncertainties were not directly included in the final combination. From this the total cross section can be defined as:

$$\sigma(Z \to \tau\tau, 66 < m_{inv} < 116 GeV) = 0.92 \pm 0.02 (\text{stat.}) \pm 0.08 (\text{syst.}) \pm 0.03 (\text{lumi.}) \text{nb}$$

$$(5.6)$$

This was obtained from the three final states, $\tau_\mu\tau_h$, $\tau_e\tau_h$ and $\tau_e\tau_\mu$, which have the respective weights, 0.758, -0.130 and 0.372. A χ^2/NDF of 1.24/2 was obtained.
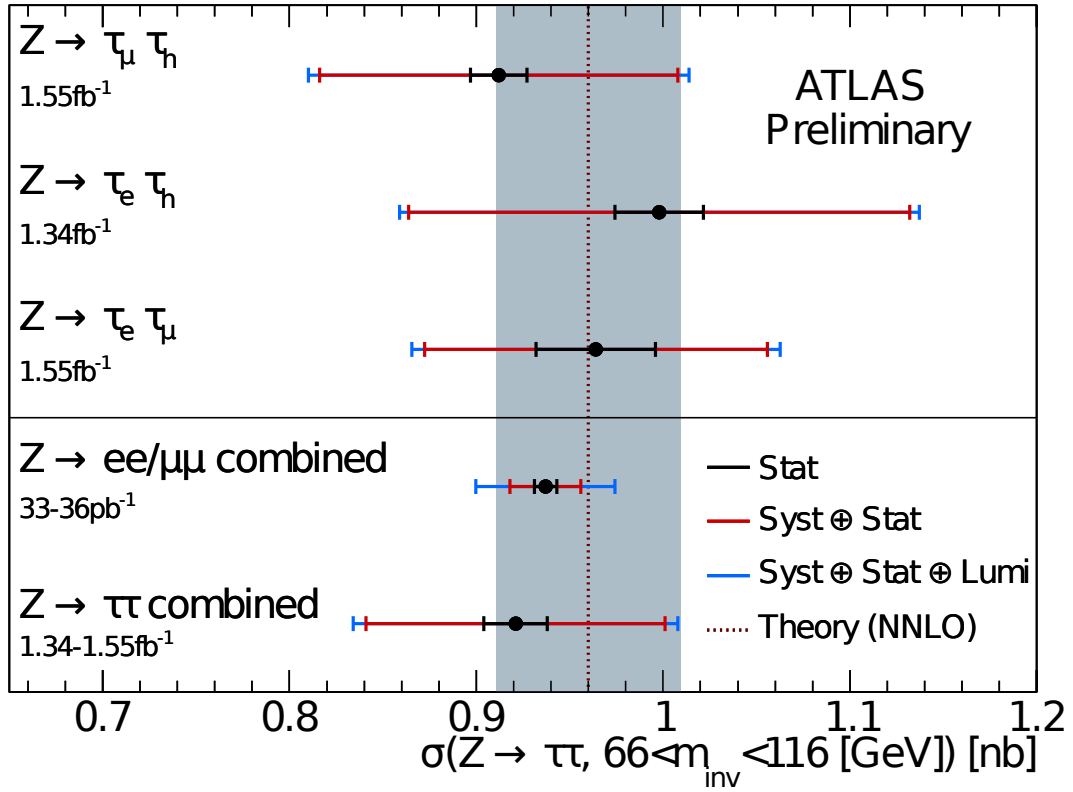
Figure 5.15: The individual cross section measurements by final state, and the combined result.

Each individual cross section obtained in each channel as well as the combined result are shown in Figure 5.15. The $Z \to \ell\ell$ combined cross section measured by ATLAS with the $Z \to \mu\mu$ and $Z \to ee$ final sates is shown for comparison [74]. The gray band indicates the uncertainty on the NNLO cross section prediction. The theoretical expectation [70, 88, 89] of 0.96±0.05 nb for an invariant mass window of [66, 116] GeV is also shown.

5.9 Conclusion

In this last chapter the author had a personal contribution towards the calculation of the acceptance factors A_Z and C_Z including all of the subsequent systematic

	$\tau_\mu \tau_h$	$\tau_e \tau_h$	$\tau_e \tau_\mu$
A_Z	$0.0976 \pm 0.0002\text{(stat)}$	$0.0687 \pm 0.0002\text{(stat)}$	$0.0784 \pm 0.0003\text{(stat)}$
C_Z	$0.1417 \pm 0.0016\text{(stat)}$	$0.1009 \pm 0.0013\text{(stat)}$	$0.1348 \pm 0.0037\text{(stat)}$

Table 5.5: Central values and Monte Carlo statistical uncertainty for the A_Z and C_Z factors [2].

calculations for these variables. The cross section (σ) for the $Z \to \tau\tau$ can be calculated using the following formula:

$$\sigma^{fid}(Z \to \tau\tau) \times Br = \frac{N_{obs} - N_{bkg}}{C_Z \cdot \mathcal{L}} \qquad (5.7)$$

This is for any specific fiducial region, which with the introduction of the factor, A_Z, can be generalised for the entire detector:

$$\sigma(Z \to \tau\tau) \times Br = \frac{N_{obs} - N_{bkg}}{A_Z \cdot C_Z \cdot \mathcal{L}} \qquad (5.8)$$

The terms for both of these equations are outlined in section 5.6. The factor, A_Z was calculated using events from Monte Carlo simulations as the ratio of events at generator level whose $\tau\tau$ invariant mass, before Final State Radiation (FSR), lies within the mass window [66, 116] GeV, and the number of events at generator level that falls within the fiducial regions defined above. The A_Z factor accounts for events that migrate from outside the invariant mass window into the fiducial region. The central values for A_Z are determined using a Pythia [80] Monte Carlo sample generated with the modified leading order PDF MRSTLO* [81]. The obtained values of the A_Z and C_Z factors, with their statistical uncertainties, are given for all three channels in Table 5.5. This resulted in the following cross-sections for $Z \to \tau\tau$.

Final State	Fiducial cross section $\sigma^{fid}(Z \to \tau\tau) \times Br(\tau \to ...)$
$\tau_\mu\tau_h$	20.0±0.3(stat)±2.0(syst)±0.7(lumi)pb
$\tau_e\tau_h$	15.9±0.4(stat)±2.0(syst)±0.6(lumi)pb
$\tau_e\tau_\mu$	4.7±0.4(stat)±2.0(syst)±0.6(lumi)pb

Final State	Total cross section $\sigma(Z \to \tau\tau, m_{inv}[66-116GeV])$
$\tau_\mu\tau_h$	0.91±0.01(stat)±0.09(syst)±0.03(lumi)pb
$\tau_e\tau_h$	1.00±0.02(stat)±0.13(syst)±0.04(lumi)pb
$\tau_e\tau_\mu$	0.96±0.03(stat)±0.09(syst)±0.04(lumi)pb

Chapter 6

Vertex Based Missing Mass Calculator

6.1 Introduction

The accurate reconstruction of mass for τ leptons is challenging because of the presence of multiple neutrinos. Despite this however, invariant mass reconstruction is still commonly used in experimental searches for new physics, principally for the Higgs boson (or Z' boson), and can also be used for properties measurements. Each τ lepton decay involves one or two neutrinos, depending on how it decays, either; hadronically $\tau_h \rightarrow \nu_\tau + hadrons$ or leptonically $\tau_\ell \rightarrow \nu_\tau + \ell + \nu_\ell$ (where $\ell = e$ or μ). In pp collisions at the LHC, the full neutrino energy cannot be determined, instead an imbalance in the transverse energy in the calorimetry can be measured (E_T^{miss}). This quantity represents the total sum of all the neutrinos in the event and therefore, when two or more neutrinos are present (as in the case of a leptonically decaying τ) the individual momenta and vector of the neutrinos cannot be reconstructed. To further complicate this, in some di-tau resonance events, the τ leptons are produced "back-to-back", that is to say that they are travelling in completely opposite directions in high η regions of the detector. This means that the neutrinos associated with the two decays can cancel

out and accurately measuring the E_T^{miss} in these events is incredibly tricky due in part to it's small size.

6.1.1 Previous Methods

In this section overviews of previous techniques will be given and give a sense of their advantages and disadvantages.

6.1.2 Colinear Approximation Technique

One of the simplest and more frequently used methods. This method is based on two important assumptions:

- The neutrinos from each τ decay are nearly collinear with the corresponding visible τ decay product, $\phi_\nu \simeq \phi_{vis}$ and $\theta_\nu \simeq \theta_{vis}$

- The E_T^{miss} in the event is only from the neutrinos.

When using this method, the total momentum carried away by the neutrinos from each τ decay can be estimated by solving the two following equations:

$$E_{\top_x}^{miss} = p_{miss_1} \sin\theta_{vis_1} \cos\phi_{vis_1} + p_{miss_2} \sin\theta_{vis_2} \cos\phi_{vis_2} \tag{6.1}$$

$$E_{\top_y}^{miss} = p_{miss_1} \sin\theta_{vis_1} \sin\phi_{vis_1} + p_{miss_2} \sin\theta_{vis_2} \sin\phi_{vis_2} \tag{6.2}$$

Where $E_{\top_x}^{miss}$ and $E_{\top_y}^{miss}$ are the x and y components of the E_T^{miss} vector, p_{miss_1} and p_{miss_2} are the combined momenta of each τ decay, and $\theta_{vis_{1,2}}$ and $\phi_{vis_{1,2}}$ are the polar and azimuthal angles of the visible decay products respectively. From this the invariant mass of the whole $\tau\tau$-system can be calculated as:

$$M_{\tau\tau} = \frac{m_{vis}}{\sqrt{x_1 \cdot x_2}} \tag{6.3}$$

Where m_{vis} is the visible mass and $x_{1,2} = p_{vis_{1,2}}/(p_{vis_{1,2}} + p_{miss_{1,2}})$ are momentum fractions carried away by visible τ decay products. Despite offering the advantage of having a fully reconstructed $M_{\tau\tau}$, the collinear approximation technique
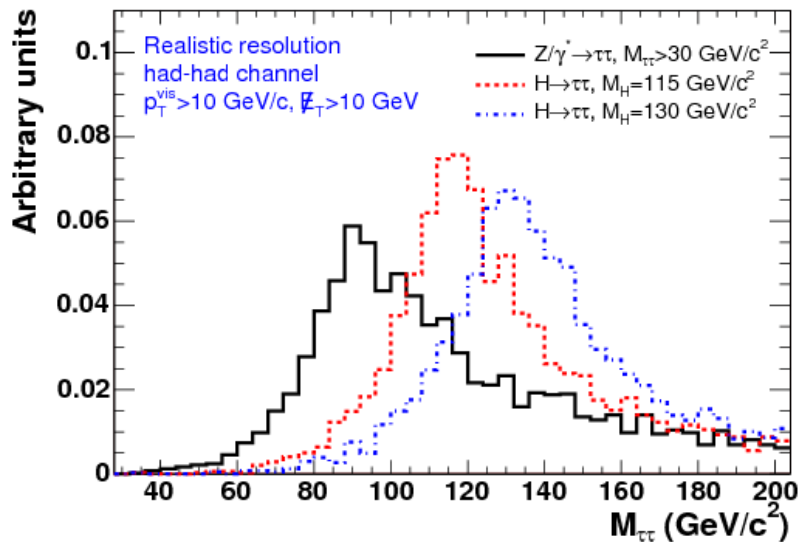
Figure 6.1: Example of the fully reconstructed mass using the collinear approximation for three events samples: inclusive $Z'/\gamma* \to \tau\tau$ and $gg \to H \to \tau\tau$ with $M_H = 115$ GeV and 130 GeV

has some disadvantages. It only gives a reasonable mass resolution for the small fraction of events where the $\tau\tau$ system is boosted, and the visible τ decay products are not back-to-back in the transverse plane. This last point can be seen mathematically in equations 6.2. If the visible decay products are back-to-back then from $\phi_{vis_1} = \phi_{vis_2} + \pi$, the solutions $p_{miss_{1,2}} \sim \sin^{-1}(\phi_{vis_1} - \phi_{vis_2})$ diverge as $|\phi_{vis_1} - \phi_{vis_2}| \to \pi$. This is especially problematic as the majority of the $H \to \tau\tau$ events are produced with the τ leptons being back-to-back. This technique, therefore, is applicable to only a very small fraction of $\tau\tau$ events. It is also sensitive to the E_T^{miss} resolution and has a tendency to over-estimate the $\tau\tau$ mass, leading to reconstructed mass distributions that have long tails, this can be seen in Figure 6.1. This long tail is very disruptive to the low-mass Higgs searches as it is completely dominated by $Z \to \tau\tau$ events.

6.1.3 Fit Based Missing Mass Calculator

The current technique for calculating the energy taken away by the neutrinos uses an algorithm that minimises a likelihood function in the kinematically allowed

detector phase space [90]. This method does not suffer from the drawbacks of the collinear approximation that can get overwhelmed in certain topologies, and can be applied to all $\tau\tau$ events without losing any resolution on the reconstructed $\tau\tau$ mass. This MMC technique was formulated using the assumption that we have perfect detector resolution and that all of the missing energy is via neutrinos only associated τ decay. For each tau decay the ΔR between the visible momentum and the assumed direction of the missing momentum is calculated. This is then calculated with the dependence of the distribution on the initial τ momentum. Furthermore, the τ polarisation can be ignored, making the ΔR distribution depend solely on the τ momentum and decay type, not on the parent of the τ. All this is scalculated using Monte Carlo simulation (PYTHIA [48] and TAUOLA [72]). The distributions obtained were then fit with a linear combination Gaussian-Landau function, parametrised as $p_0/(x + p_1 x^2) + p_2 + p_3 x + p_4 x^2$, which yields the probability of a particular tau decay having a certain missing momentum. To actually incorporate this as a more quantifiable variable the log likelihood of the event probability is calculated as follows:

$$\mathcal{L} = -\log(\mathcal{P}(\Delta R_1, p_\tau) \times \mathcal{P}(\Delta R_2, p_\tau)) \qquad (6.4)$$

Where, the functions $\mathcal{P}$ are chosen according to one of the decay types (leptonically or hadronically). To better estimate the $\tau\tau$ invariant mass in a given event, the $M_{\tau\tau}$ distribution is produced for all points on a grid of $(\phi_{mis_1}, \phi_{mis_2})$. Each point on these scan points is weighted by the corresponding probability, the argument for the logarithm in equation 6.4. The mean value for the $M_{\tau\tau}$ distribution is taken as the final estimate for the event. Examples of the log likelihood distributions probability distribution function and the $M_{\tau\tau}$ distributions can be seen in Figure 6.2 and Figure 6.3 respectively. these showcase the reasonable performance that was obtained by this method.
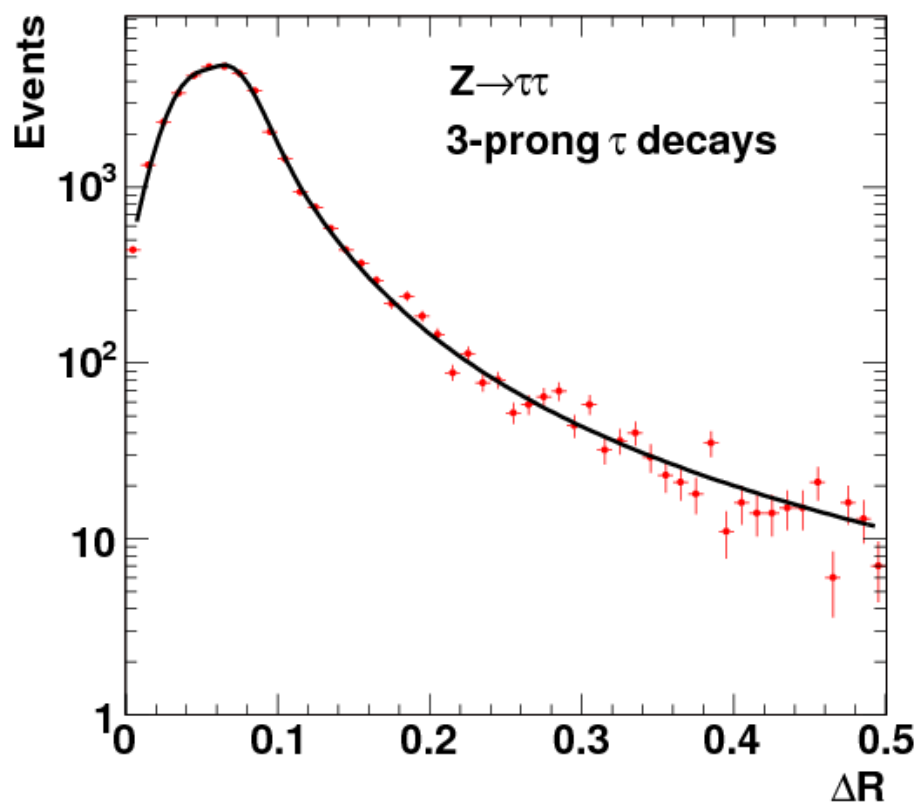
Figure 6.2: The probability distribution function for 3-prong τ decays, this is used in the calculation for the likelihood function [90].
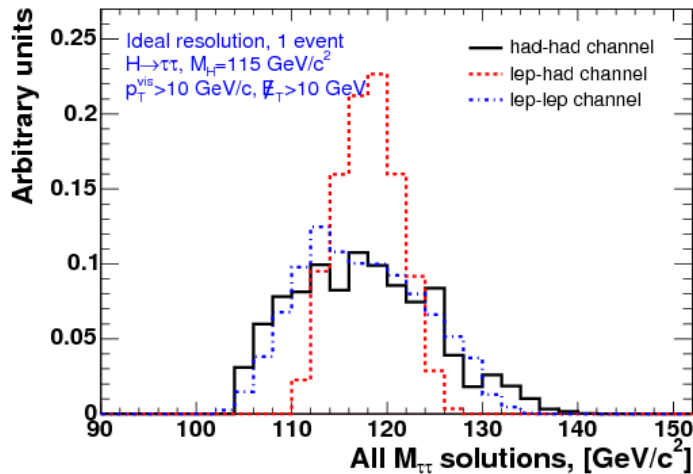
Figure 6.3: The $M_{\tau\tau}$ distribution for every grid point in each of the $\tau\tau$ decay modes. This plot is for the ideal detector resolution and weighted by the log-likelihood function [90].

6.2 Vertex Based Missing Mass Calculator

The techniques discussed previously whilst having good performance could be improved upon. Utilising the improved understanding of the ATLAS detector it is possible to accurately reconstruct the vertices involved in the tau decays, thus enabling any missing momentum to be measured. This method also provides detailed information for each of the individual tau leptons, whereas the previous MMC methods deal only with the di-tau final state as a whole. Once this has been achieved, there will be a much more complete picture of the behaviour of tau leptons in the ATLAS detector. In this section a technique that aims to achieve this will be presented and discussed.

Tau candidates that have been identified by the calorimeters and selected to have only three prongs. These tracks have no additional cuts applied to them apart from a secondary vertex fit, more detail on which can be found here [91]. Only pairs of τ candidates that have a successful secondary vertex fit are combined to form a Higgs/Z candidate. In this method we consider both opposite and same-sign combinations. Irrespective of the charge of the two τ candidates, if a

track is shared and used in both of their calculations then the result from this pair is rejected. The refitted track momenta;

$$\vec{P^i} = (P_x^i, P_y^i, P_z^i), \; i = 1, 3 \tag{6.5}$$

This is obtained from the vertex fit, and is used in all of the calculations.

6.2.1 Primary vertex selection and refit

For each Primary Vertex (PV) in the event the following quantities are calculated:

- $\vec{dR} = \frac{\vec{SV} - \vec{PV}}{|\vec{SV} - \vec{PV}|}$: unit vector in the direction between the τ decay vertex $\vec{SV} = (x, y, z)$ and the primary vertex $\vec{PV} = (x_0, y_0, z_0)$

- impact parameter (in 3D) of the τ visible momentum, calculated from the refitted momenta of the 3 tracks, $\vec{P}^{\text{vis}} = \sum_{i=1}^{3} \vec{P^i}$

- the angle θ between $\vec{dR}$ and $\vec{P}^{\text{vis}}$.

The primary vertices with the smallest impact parameter and the largest value of $\cos\theta$ are identified for both τ candidates. If the same PV satisfies both criteria for both of the τ candidates, the PV is selected as the origin of both taus, otherwise they are rejected. If any of the six tracks used in the two τ candidates is also used in the fit of the selected PV, the PV is refitted excluding such tracks. If during the process of calculation of the tracks from the PV results in less than three tracks remaining in the PV, the original PV is used. Figure 6.4 shows the change in vertex position as a result of the PV refit on the gluon-gluon fusion sample.

6.2.2 τ momentum calculation

The requirement that the direction of the τ momentum is determined by the unit vector $\vec{dR}$, gives two equations for the unknown neutrino momentum $\vec{P}^\nu = (P_x^\nu, P_y^\nu, P_z^\nu)$. These together with the fact that the τ mass is known [47]

$$m_\tau = \sqrt{(E^{\text{vis}} + E^\nu)^2 - (P_x^{\text{vis}} + P_x^\nu)^2 - (P_y^{\text{vis}} + P_y^\nu)^2 - (P_z^{\text{vis}} + P_z^\nu)^2}, \tag{6.6}$$

144

(a)

(b)

(c)
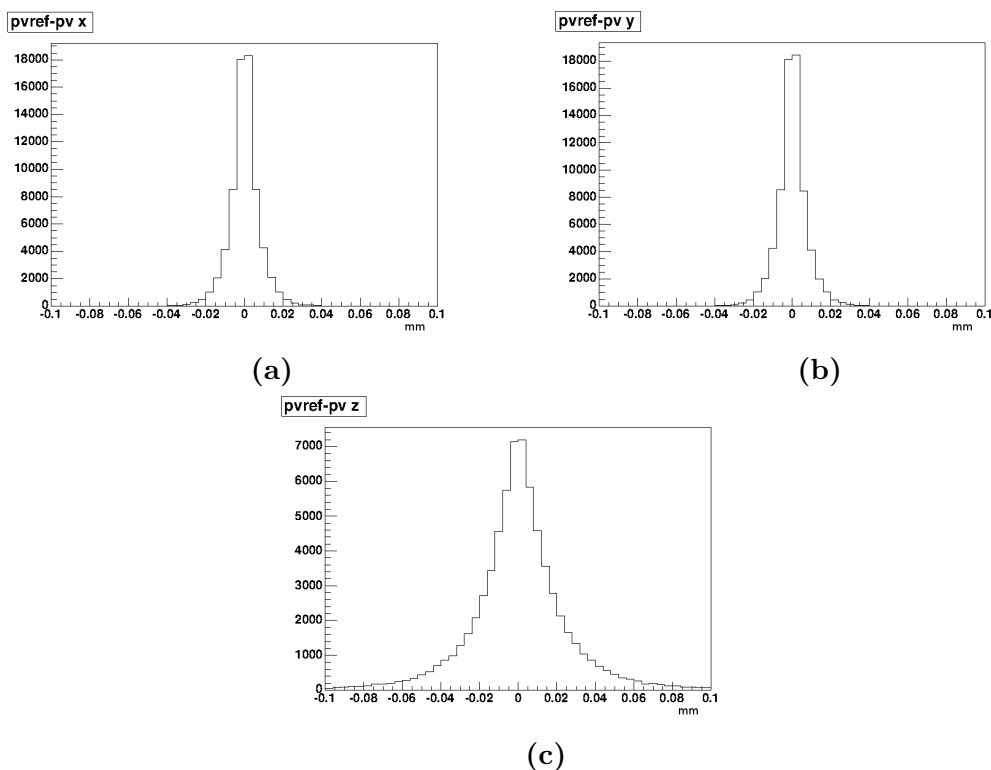
Figure 6.4: Plots of the co-ordinates of the primary vertices, a)$\delta x = x_0 - x_0^{\text{ref}}$, b) $\delta y = y_0 - y_0^{\text{ref}}$ and c) $\delta z = z_0 - z_0^{\text{ref}}$ for PV refit.

where;

$$E^{\text{vis}} = \sum_{i=1}^{3} E^i \tag{6.7}$$

$$E^i = \sqrt{(P_x^i)^2 + (P_y^i)^2 + (P_z^i)^2 + m_{\pi^+}^2} \tag{6.8}$$

and;

$$m_{\pi^+} = 139.57 \, \text{MeV} \tag{6.9}$$

and;

$$m_\tau = 1776.82 \, \text{MeV} \tag{6.10}$$

allows us to calculate the neutrino momentum $\vec{P}^\nu$. Assuming $m^\nu = 0$, the neutrino energy is $E^\nu = P^\nu$. If there are neutral particles among the decay products of the τ lepton their momenta are incorporated in $\vec{P}^\nu$.

145

For each τ lepton two solutions are obtained, from these equations it can be seen that there are four possible solutions for the resonance momentum and mass. The correct solution for Monte Carlo signal events can be identified by performing the same calculations on the truth quantities, for which the solutions always exist and the correct combination yields the generated momenta. This was used to determine how well the algorithm and the fitting methodology was performing. However, for reconstructed quantities the detector has a finite resolution (as one would expect), this means that the solution to the system of quadratic equations is not always possible. Additionally even if the solutions is indeed possible, there is no easy way of selecting the correct one from amongst the four solutions. For this task an MVA method is used to select a single solution, this will be described in more detail later.

For the cases when the parameters from the original vertex fit do not yield a solution for the neutrino momentum an additional refit is performed. In this refit the minimal change to the secondary vertex position and the visible 4-momentum:

$$\vec{P}^{\text{vis}}, E^{\text{vis}} \tag{6.11}$$

is obtained by minimising

$$\chi^2 = \Delta s^T V_{\text{cov}}^{-1} \Delta s + (m_{\text{min}} - m_\tau)^2, \tag{6.12}$$

where,

$$\vec{s} = (x, y, z, P_x^{\text{vis}}, P_y^{\text{vis}}, P_z^{\text{vis}}, E^{\text{vis}}) \tag{6.13}$$

is a vector of the measured parameters. V_{cov} is the covariance matrix of the measured parameters, obtained by error propagation from the full covariance of the original vertex fit, which takes into account all track-track and vertex-track correlations. m_{min} is the invariant mass calculated using the new parameters and the requirement that a solution for the neutrino momentum exists, i.e. the discriminant is zero. The χ^2 minimisation is done using MINUIT [92]. The minimal change to $\vec{s}$ should result in a single solution, but due to the finite step-size and limited number of iterations in MINUIT, in most cases the refit gives

two close solutions and the average is taken as the single solution. The vertex refit is also performed in the cases when the original fit allows a solution for the purpose of systematic studies to evaluate the effects of the refit on the vertex and momentum resolution.

6.2.3 Data and Monte Carlo Samples

The data samples used in this specific analysis were collected with the ATLAS detector from 2011 and 2012 at $\sqrt{s} = 7$ TeV and $\sqrt{s} = 8$ TeV respectively. There was a combined hadronic tau trigger applied to this data, this has a threshold of 16 GeV whilst the electron trigger has a threshold of 15 GeV. The signal and background Monte Carlo (MC) samples used in this study were generated with $\sqrt{s} = 8$ TeV and passed through a full detector simulation based on the Geant4 Program [65]. The inclusive W and γ^*/Z signal and background samples were generated with ALPGEN [49], interfaced to HERWIG [66] and JIMMY [67], using the CTEQ6L1 [68] Parton Distribution Functions (PDFs), with the ATLAS AUET1 [69] tune. The samples are normalised to NNLO [70] cross sections. For the $t\bar{t}$ background the MC@NLO generator [71] is used with the CTEQ6.6 [68] PDFs, and the parton shower and hadronisation simulated with HERWIG. The diboson samples are generated with HERWIG. In all samples the τ decays are modelled with TAUOLA [72], and all the generators are interfaced to PHO-TOS [73] to simulate the effect of final state radiation.

For the signal samples ggF and VBF MC were used:lower-p_T

- ggF with 100 GeV $< m_H <$ 150 GeV in 5 GeV steps,

- VBF with 100 GeV $< m_H <$ 150 GeV in 5 GeV steps.

The main background samples used were:

- $Z \to \tau\tau$ split into categories with different numbers of jets (0-5),

- $Z \to \tau\tau$ split into categories with different numbers of jets (0-5),

- The QCD background was estimated using data that had two same-sign reconstructed taus.

6.2.4 Event Selection

In this analysis the event selection is very similar to the one used in previous sections, specifically section 4. However the specific cuts are described in the following list:

- trigger,

- tauID Leading or subleading Medium and at least one Tight,

- nprongs $= 3$,

- electron overlap removal, muon veto, electron veto, loose muon,

- $\eta < 1.37$ or > 1.52 and < 2.5,

- Both τs $p_T > 25$ GeV and one with $p_T > 35$ GeV,

- $\Delta\eta < 1.5$,

- $\Delta R < 3.2$,

- $r_{xy} > 1$ mm, this is the primary vertex displacement length,

- additional tracks < 2,

- njets $>= 1$, the number of jets.

In this analysis, the two τ_h leptons are selected if they have the Opposite Sign (OS) charge conjugation requirement ($C_{\tau_1} \times C_{\tau_2} = -1$). Additionally to this, events that have been classified as mis-identified electrons or muons are rejected
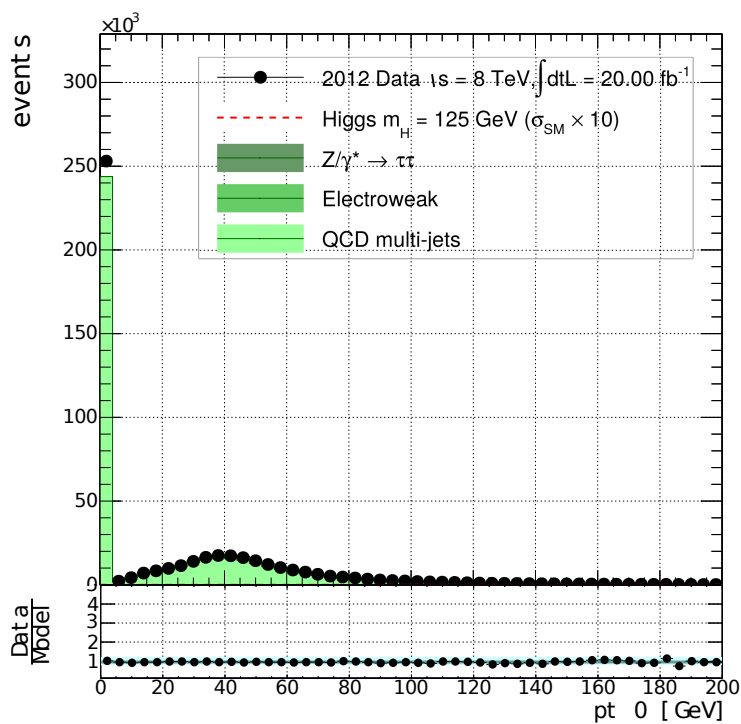
(a)
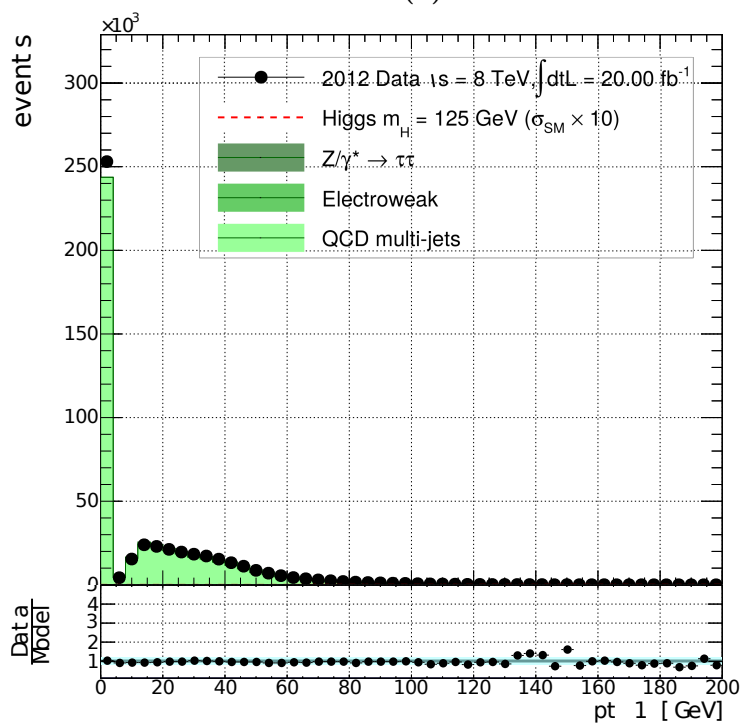
(b)

Figure 6.5: The p_T of the tau before any of the selection or clean-up cuts have been applied. (a) Is the leading tau (the one with the higher p_T) and (b) is the subleading tau.
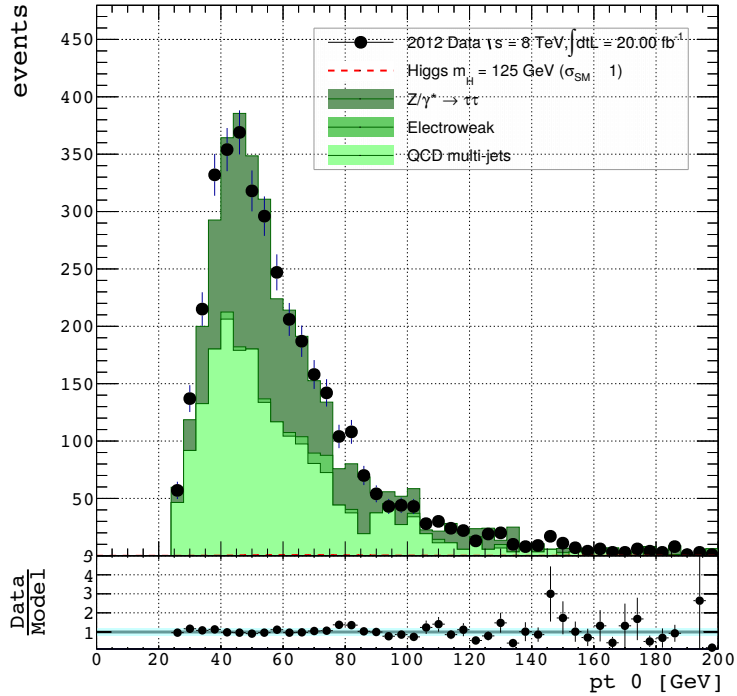
(a)
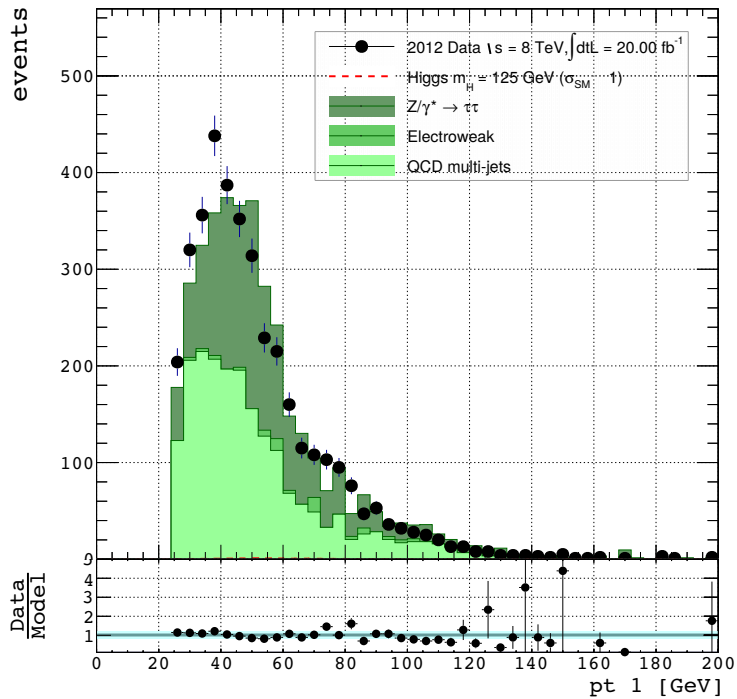
(b)

Figure 6.6: The p_T of the tau after all of the selection and clean-up cuts have been applied. (a) Is the leading tau (the one with the higher p_T) and (b) is the subleading tau.

This can be seen diagrammatically by comparing the plots in Figure 6.5 and Figure 6.6. In these plots the QCD and the $Z \rightarrow \tau\tau$ processes have been individually weighted. This is done using a fit to the $\Delta\eta$ for these two backgrounds. Originally this was a 2D fit to the number of tracks, however due to our constraint of only having 3 prong τs this was not feasible and the $\Delta\eta$ was found to be a suitable replacement.

In addition to all this, the events needed to have a weighting due to the effects of the tau identification and the specific electron veto. These were calculated using tools and prescriptions from the tau working group [93]. These scale factors have a fairly strong dependence on the pseudorapidity, which is outlined in the respective Tables 6.1 and 6.2. This dependence is inherited from the algorithm that is used to calculate the scale factors and is similarly taken into account in-situ.

$|\eta|$	Medium τ ID	Tight τ ID
0.00 - 1.52	0.97 ($\pm$0.04)	1.01 ($\pm$0.04)
1.52 - 2.00	1.04 ($\pm$0.05)	1.03 ($\pm$0.04)

Table 6.1: Table showing the Scale factors from the Medium and Tight τ ID working points, in the different $|\eta|$ regions.

The Data/MC correction factor for the tau identification efficiency is obtained through tag-and-probe studies of $Z \rightarrow \tau\tau$ events which have been varied upwards and downwards in accordance with the recommendation of the tau working group [93]. The correction factors and the corresponding variation is applied only to truth match hadronic taus. Furthermore , the correction factors on the rate of misidentification of electrons as hadronic τ candidates (electron veto) are also varied within their uncertainties. The tools to calculate this were provided by the Tau Working Group. Using these tools the scale factors shown in tables 6.2 and 6.1 were calculated these were used in-situ to weight the specific events that fit the conditions listed in those tables.

6.2.5 Solution Selection

The single solution for the resonance mass (and the tau momenta) is chosen using a BDT Multi Variate Analysis. Originally, other methods of finding this single

$|\eta|$	Electron Veto Scale Factor
0.00 - 0.05	0.85 ($\pm$1.07)
0.05 - 0.80	0.99 ($\pm$0.88)
0.80 - 1.37	1.22 ($\pm$1.40)
1.37 - 1.52	0.84 ($\pm$0.38)
1.52 - 2.00	0.83 ($\pm$0.62)

Table 6.2: Table showing the scale factors for the electron veto, through different $|\eta|$ regions.

solution were sampled. All involved finding a kinematic quality that would discriminate for the correct solution, obviously they also centred around the missing energy variables. This however proved to be a very unsatisfactory method for finding the solution. The decision was made that a MVA would fair much better for dynamically choosing the solution, it could take a wide range of information that could better influence the decision made. Below the variables that are used in the BDT MVA are outlined:

- The cosine of the angle between the missing momentum calculated from the sum of the two neutrino momenta and the missing momentum measured in the calorimeter[†], labelled as **a**,

- The same as above, instead using the missing momentum calculated from the measured tracks[†], labelled as "**at**",

- Fraction of the leading tau momentum measured in the calorimeter, which is not associated with the charged tracks, labelled as "**fraction_lead**",

- Fraction of the sub-leading tau momentum measured in the calorimeter, which is not associated with the charged tracks, labelled as "**fraction_sublead**",

- Ratio of the energy of the leading tau measured using the three charged tracks (and assuming a pion mass) and the energy measured in the calorimeter, labelled as "**fractionE_lead**",

- As above but using the sub-leading tau, labelled as "**fractionE_sublead**",

- Momentum divided by the energy of the vector boson[†], labelled as "**beta**",

- Momentum divided by the energy of the leading $\tau^{\ddagger}$, labelled as "**beta_lead**",

- Momentum divided by the energy of the sub-leading $\tau^{\ddagger}$, labelled as "**beta_sublead**",

- Magnitude of the vector difference between the missing momentum calculated from the sum of the two neutrino momenta and the missing momentum measured in the calorimeter[†], labelled as "**r**",

- Ratio of the energies of the neutrino and the τ for the leading $\tau^{\ddagger}$, labelled as "**r_lead**",

- Ratio of the energies of the neutrino and the τ for the sub-leading $\tau^{\ddagger}$, labelled as "**r_sublead**",

- ΔR between the leading τ and the sub-leading $\tau^{\ddagger}$, labelled as "**dR**",

- Proper time of the leading $\tau^{\ddagger}$, labelled as "**propertime_lead**",

- Proper time of the sub-leading $\tau^{\ddagger}$, labelled as "**propertime_sublead**",

- Sum of the p_T of the two τ[†], labelled as "**sum_pt**",

- Scalar product of 2D vectors of the missing momentum calculated from the sum of the two neutrino momenta and the missing momentum measured in the calorimeter[†], labelled as "**cet_mag**",

- As above but using the track-based missing momentum[†], labelled as "**cetTrk_mag**",

- Log of the ratio of the magnitudes of the missing momentum calculated from the sum of the two neutrino momenta and the missing momentum measured in the calorimeter[†], labelled as "**log_et_ratio**",

- Difference of the ϕ angle of the missing momentum calculated from the sum of the two neutrino momenta and the ϕ angle of the missing momentum measured from the tracks[†], labelled as "**dphi_etTrk**".

All items marked with † have 4 different values for each, each τ contributes two values each. Each item marked with ‡ has only two values, only one from the leading τ and the sub-leading τ. This is because in the latter cases one of the tau candidates has had its vertex refitted, this means that it has its components perturbed slightly and then reprocessed, this gives a definite solution and no ambiguity in the solution. The former case has none of these refitted vertices so has the original four way ambiguity. This refitting whilst giving a definite result comes at a cost of resolution. In addition it should be noted that the variables "**fraction_lead**", "**fraction_sublead**", "**fractionE_lead**" and "**fractionE_sublead**" are useful only in classifying and defining the events, they provide no discrimination for the solutions.

The rankings of the variables, that were used in the two different cases are shown in tables 6.3, 6.4 and 6.5. These show the rankings for the BDT variables that were used for the four solution case and for the subleading and the leading τ from the two solution case respectively.

The listed variables resulted in the following background rejection against signal efficiency plots, shown in Figure 6.7 are directly outputted from the TMVA framework. They show how well the BDT is performing relative to each other. However the optimal method for determining the performance is to compare the resulting mass resolutions. This is highlighted in Figure 6.8, where the Subfigures 6.8a and 6.8c show the BDT method, compared to the Subfigures 6.8b and 6.8d, which were produced with a previous method. This previous method selected the solution that had the largest angle between the tau and its missing momentum vector. As can be seen in this figure the BDT provides an improved solution selecting method. These plots were created using MC focused around either $m_H = 125$ GeV or the Z boson mass, they also take into account all of the solution options that we have either the four fold ambiguity and the 2-fold ambiguity.

Additionally there are two categories that were produced, one took the calculated solution wherever it was available and if it was not calculated a refitted vertex. The other was when the refitted vertex was used for every event. This was a test to see if there was any improvement in the performance of the method. The former can be seen in figures 6.9, 6.10 and the latter for a comparison in

Rank	Variable	Variable Importance
1	sumPt	0.106
2	r_sublead	0.089
3	r_lead	0.083
4	log_et_ratio	0.081
5	dR	0.072
6	fractionE_sublead	0.055
7	beta_sublead	0.053
8	beta	0.051
9	fractionE_lead	0.046
10	r	0.045
11	propertime_sublead	0.045
12	fraction_lead	0.044
13	at	0.043
14	a	0.042
15	fraction_sublead	0.031
16	propertime_lead	0.027
17	cet_mag	0.025
18	beta_lead	0.024
19	dphi_etTrk	0.021
20	cetTrk_mag	0.019

Table 6.3: Ranking of the variables used in the "4 solution" BDT, the top variable is best ranked.

Rank	Variable	Variable Importance
1	m_tau_sublead_pt	0.166
2	m_r_sublead	0.149
3	m_dR	0.124
4	m_beta_sublead	0.097
5	m_a	0.092
6	m_fraction_sublead	0.089
7	m_fractionE_sublead	0.087
8	m_beta	0.076
9	m_at	0.054
10	m_propertime_sublead	0.043
11	m_sumPt	0.023

Table 6.4: Ranking of the variables used in the "2 solution" cases in this instance the leading tau has had its vertex refitted. The top variable is best ranked.

Rank	Variable	Variable Importance
1	p_tau_lead_pt	0.133
2	p_r_lead	0.131
3	p_r_sublead	0.107
4	p_dR	0.086
5	p_fraction_lead	0.080
6	p_fractionE_lead	0.076
7	p_r	0.068
8	p_beta_lead	0.065
9	p_a	0.064
10	p_beta	0.060
11	p_sumPt	0.058
12	p_at	0.050
13	p_propertime_lead	0.021

Table 6.5: Ranking of the variables used in the "2 solution" cases in this instance the subleading tau has had its vertex refitted. The top variable is best ranked.

6.11. When dealing with the Higgs boson it can be seen that the vertex based MMC has a better performance than the other MMC method. This includes the case when only the refitted vertices are chosen, Figure 6.11a, however in this case the resolution is slightly worsened. In the case of the Z boson it is clear to see that the vertex based missing mass calculator does not perform as well as the other method. However when only the refitted vertices are chosen, Figure 6.11b, the performance whilst still not as good is still improved compared to the previous category. The information showing the mean and the width for the fits for each of Figures 6.8, 6.9, 6.10 and 6.11, can be seen in Tables 6.6, 6.7, 6.8 and 6.9 respectively. The fits were done using Minuit. More details of the general BDT performance can be seen in Appendix A.
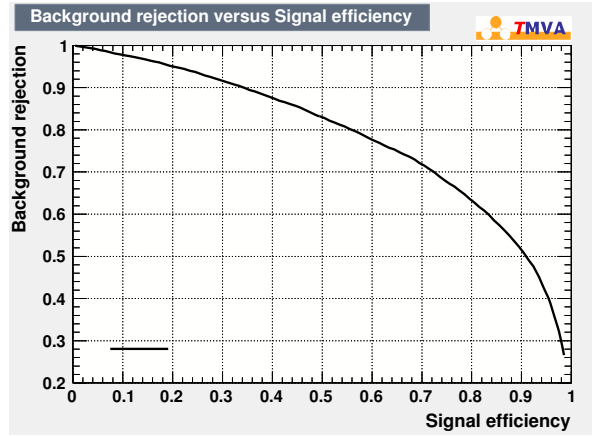
(a)
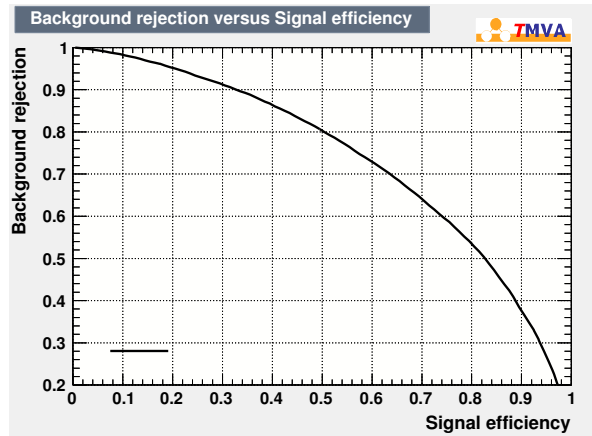
(b)
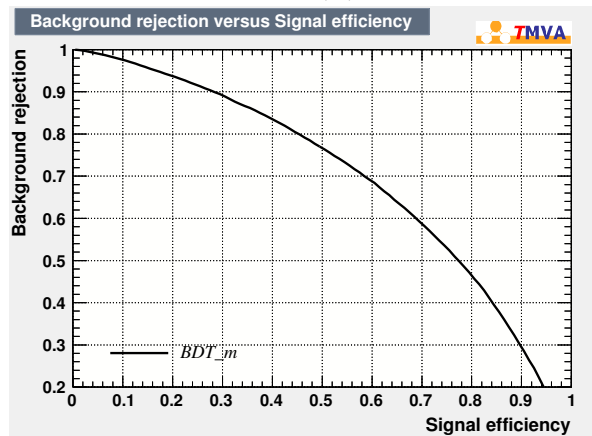
(c)

Figure 6.7: a) Background rejection Vs Signal Efficiency for the 4 solution BDT b) the same for the leading τ and c) for the sub-leading τ.

157

(a)

(b)

(c)

(d)
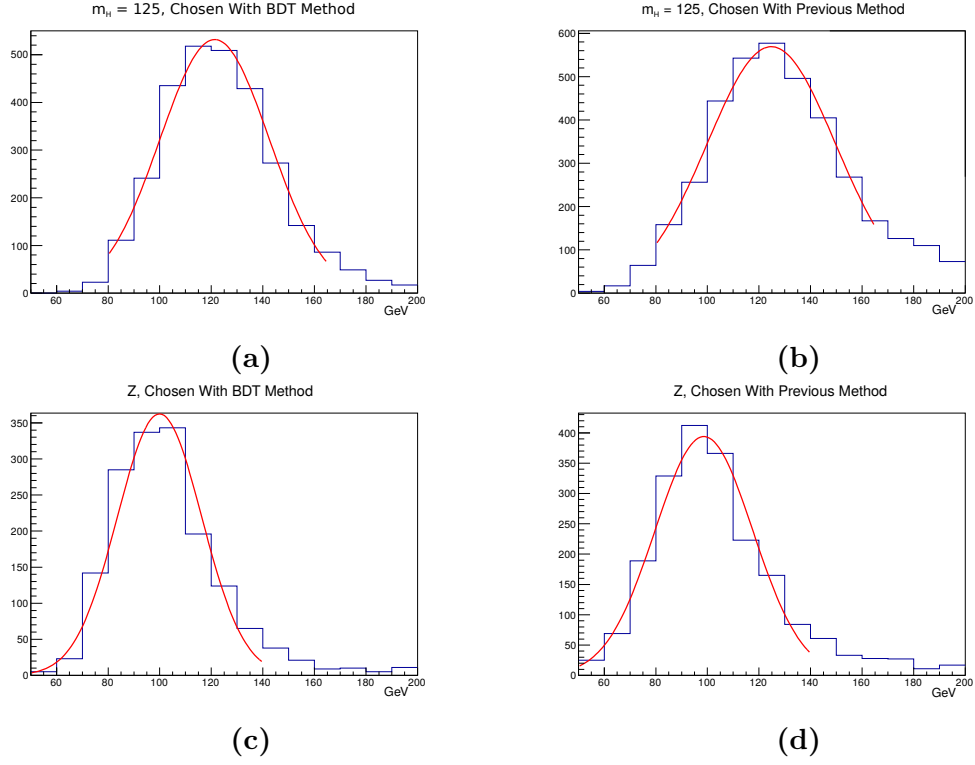
Figure 6.8: A comparison between two different methods for selecting the correct solution. The upper plots show MC events focused around the $m_H = 125$ GeV, the lower plots are focused around the Z boson mass. a) and c) show the BDT driven method compared to b) and d) which show a previous method.

	BDT Method		Previous Method	
	mean	σ	mean	σ
MC $H_{mass} = 125$	121.3±0.5	21.23±0.43	124.8±0.5	24.89±0.56
MC Z	99.93±0.49	16.34±0.35	98.64±0.5	18.97±0.43

Table 6.6: The mean and the width (σ) of the fits shown in Figure 6.8.

158

(a)

(b)

(c)
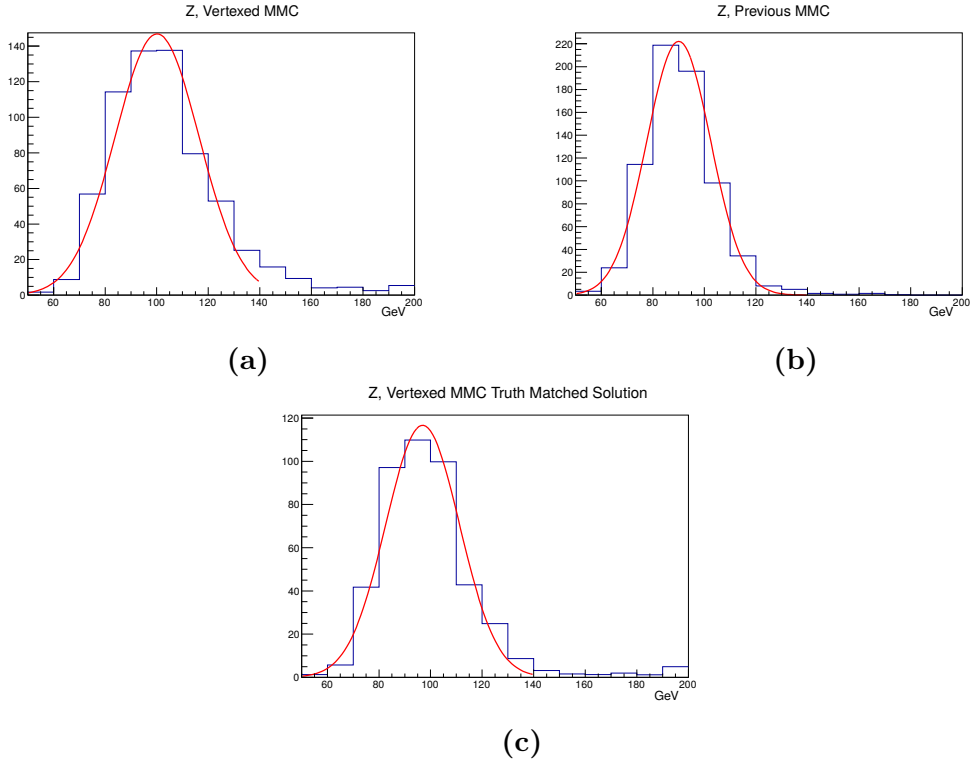
Figure 6.9: Monte Carlo simulated events focused around the Z boson mass. a) Shows the reconstructed mass using the vertex based MMC, b) the mass using the old MMC method c) the truth matched solution showing the optimum performance of the vertex based MMC method.

	mean	σ
Vertexed MMC	100.1±0.8	16.27±0.54
Previous MMC	90.04±0.49	12.42±0.38
True Vertexed MMC	96.92±0.78	14.31±0.57

Table 6.7: The mean and the width (σ) of the fits shown in Figure 6.9.

159

(a)

(b)

(c)
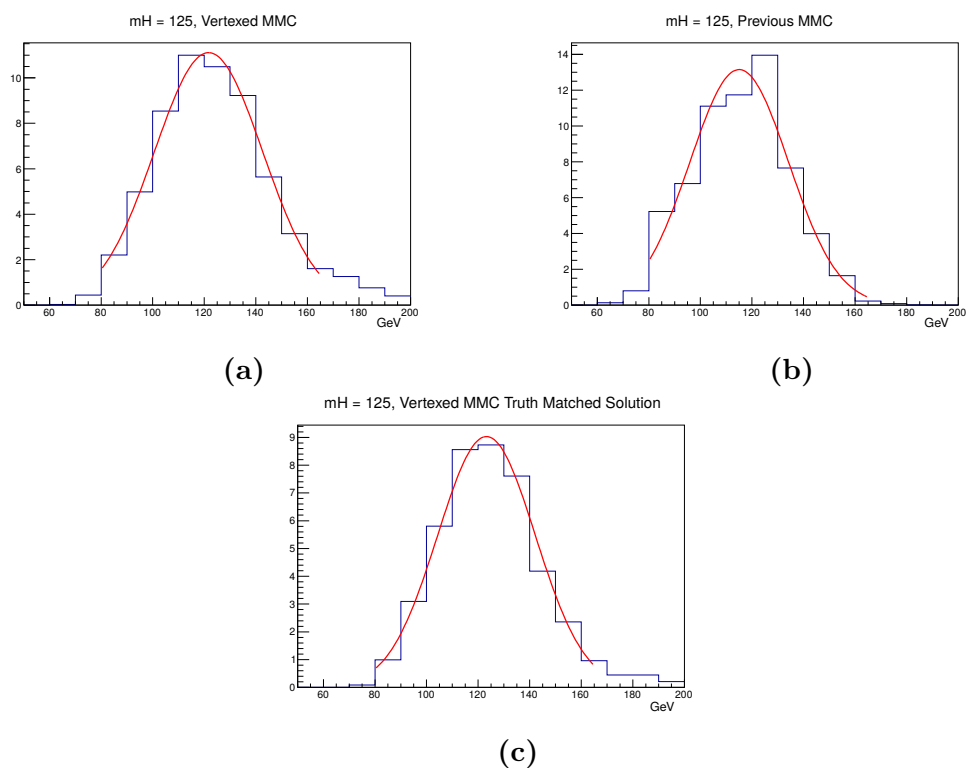
Figure 6.10: Monte Carlo simulated events focused around the Higgs boson at a $m_H = 125$ GeV. a) Shows the reconstructed mass using the vertex based MMC, b) the mass using the old MMC method c) the truth matched solution showing the optimum performance of the vertex based MMC method.

	mean	σ
Vertexed MMC	121.7±3.1	21.04±2.9
Previous MMC	115±3.1	19.16±2.28
True Vertexed MMC	123.2±3.1	18.93±2.67

Table 6.8: The mean and the width (σ) of the fits shown in Figure 6.10.

160
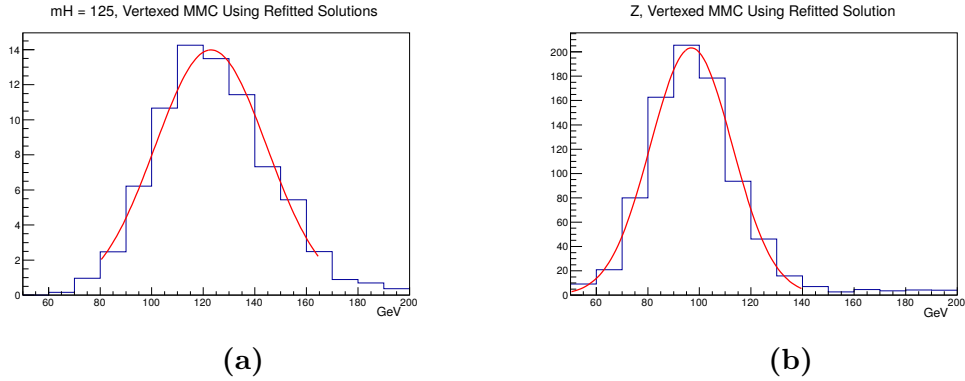
Figure 6.11: These show the reconstructed mass of MC samples that include the refitted vertices. a) Is focused on $m_H = 125$ GeV, b) is focused on the Z boson mass.

	mean	σ
MC $m_H = 125$	123±2.8	21.67±2.71
MC Z	96.88±0.58	15.88±0.48

Table 6.9: The mean and the width (σ) for the fits shown in Figure 6.11.

6.3 Systematic Uncertainties

To properly estimate the performance of this MMC, a direct comparison to the results of the main tau working group should be performed. In order to achieve this, the relevant systematic uncertainties need to be calculated. This section will give an overview of the methodology and reasoning behind the uncertainties that were included.

One of the main contributions to systematic uncertainty when measuring τ leptons is the τ Energy Scale (TES), this is simply because of the inherent difficulty in reconstructing these objects. It is obtained by varying the p_T of the tau upwards and downwards in accordance to the recommendations of the tau working group [93]. It is calculated using a mix of in-situ TES corrections (for the range of $p_T < 50$ GeV), obtained by fitting the reconstructed visible mass for $Z \to \tau\tau$ event in data, and a decomposition method (for $p_T > 70$ GeV) with an

interpolation between the two.

In Figure 6.12 the TES up and down shifted p_T can be seen for both the leading tau (6.12a and 6.12b) and the subleading tau (6.12c and 6.12d). Comparing these to the original tau p_T (which can be seen in Figure 6.6a and Figure 6.6b) an estimate for the systematic for the TES can be gathered. Specifically this was achieved by integrating over the full range of the p_T distributions then finding the percentage difference between that and the un-shifted p_T. When this was done it was found to be 5%. This number is comparable to what was used by various other analyses.

The following systematics are taken from previously completed analyses by the $H \rightarrow \tau\tau$ working group. The Jet Energy Scale, JES, uncertainty is obtained following the prescription of the Jet Performance Group [94].

The uncertainties due to pileup, consist of two components. One accounts for the residual p_T dependence of the correction as a function of the number of primary vertices and μ, this was however found to be negligible. The other accounts for residual dependence on the underlying event of the jet energy scale following jet-area based pile-up correction.

The jet Energy Resolution systematic uncertainty was obtained following the prescriptions and methods that were outlined by the Jet Performance Group [95]. From this a one sigma variation in the resolution is obtained for every jet with a factor that accounts for the uncertainty of the in-situ resolution measurements. The final effect of the variation was made to be symmetric in order to have a two-sided uncertainty. This was taken from a previous analysis as it was reasoned that the effect would be the same [31].

Trigger efficiencies are measured through tag-and-probe studies, from these studies correction factors for Monte Carlo events are calculated, and applied in-situ. These correction factors were then varied within their uncertainties to ascertain the effect that would be had. This was taken from a previous analysis as it was reasoned that the effect would be the same [31].

The uncertainty from the integrated luminosity is $\pm 2.8\%$ for data taken in 2012 at 8 TeV ref [96]. It was calculated from a preliminary calibration of the luminosity derived from beam-separation scans.
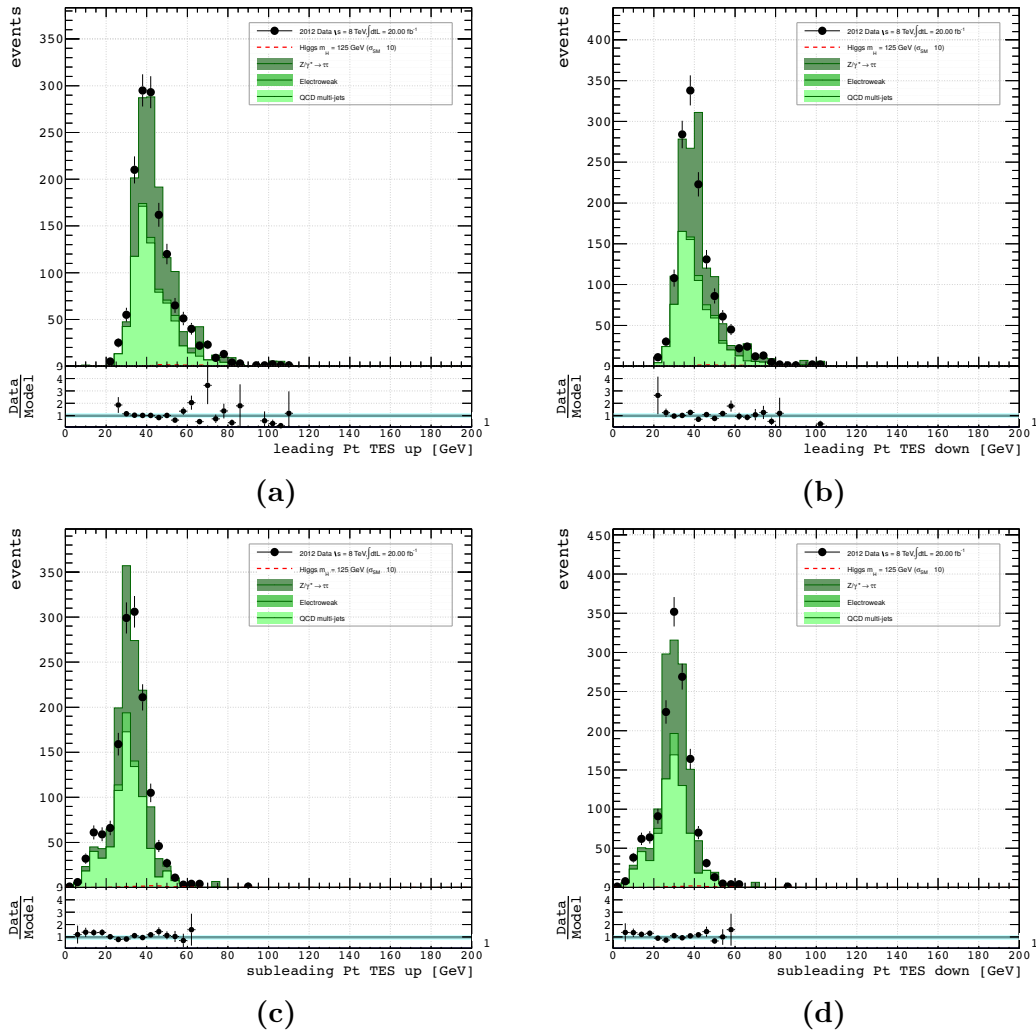
Figure 6.12: Plots showing the Tau Energy scale shifted p_T, top row for the leading τ and the bottom row shows the subleading τ.

The uncertainty that arise from the QCD scale corrections for the VBF and VH production methods are calculated by varying the factorization and normalisation scales by a factor of two up and down, around the nominal scale m_W, the resulting uncertainty for $\tau_h \tau_h$ is listed in Table 6.10 below.

The uncertainties from the Parton Distribution Functions (PDFs) are evaluated at the reconstruction level by reweigh ting the events using information about the incoming partons (the Bjorken x variables and the type of incoming parton in the hard scattering). This re-weighting is used to estimate the difference in acceptance between the CT10 PDF and MSTW2008NLO, NNPDF and the CT10 PDF sets that has been varied within its own uncertainty. The largest of these differences is used as the PDF uncertainty. As with other uncertainties described here, the specific uncertainty for this factor was taken from a previous analysis, as the difference was reasoned to be minimal. All the uncertainties described above are listed in Table 6.10. More information on the systematics can be found here [97].

| Systematic	Plus value	Minus Value
Jet Energy Scale	0.05	-0.08
Pileup	0.007	-0.014
Jet Energy Resolution	0.01	-0.01
Trigger	0.034	-0.042
Tau Energy Scale	0.05	-0.05
PDF	0.027	-0.021
Trigger	0.034	-0.042
QCD scale	0.004	-0.004
Luminosity	0.028	-0.028

**Table 6.10:** List of systematics used in the mass Limit plots.

6.4   Results

Using the BDT method the plots shown in figures 6.13 and 6.14 were produced, they show the reconstructed mass that was calculated using the method described in section 6.2 overlayed on the three backgrounds, $Z \to \tau\tau$, QCD and EW. They were plotted in the mass region $m > 60$ GeV. They show that there is reasonable agreement between the data and the background, any discrepancy cna be attributed primarily to the relatively low amount of statistics in this channel. The final plots in this section, figures 6.15 and 6.16 show the mass limit built using the prescription described here [93] and using the tools from here [98], for every available m_H point from 100 GeV to 150 GeV in steps of 5 GeV and takes into account all the systematics listed in Table 6.10. From this and using the same prescription and tools described by the tau working group [93], the signal strength (μ) was then extracted following the prescription of the $H \to \tau\tau$ working group, and the following numbers were obtained for the mass range $m > 60$ GeV:

- Using the calculated solution where available:

    - Vertex based MMC:

        $\mu = 2.42 \pm 0.82$ with a significance of 0.22,

        Expected = 2.50, Observed = 1.48,

    - Previous MMC:

        $\mu = 2.40 \pm 0.74$ with a significance of 1.04,

        Expected = 1.52, Observed = 1.35,

- Preferentially taking the refitted vertices:

    - Vertex based MMC:

        $\mu = 0.03 \pm 0.72$ with a significance of 0.05,

        Expected = 2.21, Observed = 2.25,

    - Previous MMC:

        $\mu = 2.05059 \pm 0.60$ with a significance of 1.11,

        Expected = 1.24, Observed = 1.13.

The numbers in list 6.4 are only for the 3-prong category of hadronically decaying taus. The errors on the signal strengths and the size of the central values for them are large enough that no meaningful face value conclusions can be drawn. However this was not specifically a mass measurement, it was focused on comparing the vertex based missing mass calculator to the currently used method. In this regard the vertex based method performs just as well. It also has a few other advantages that can be capitalised upon. This will be discussed specifically in Section 7.
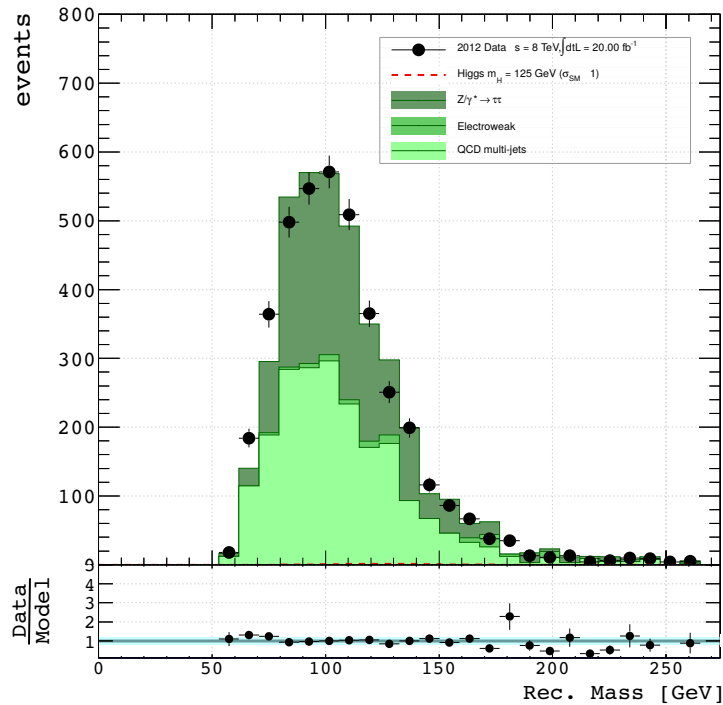
(a)
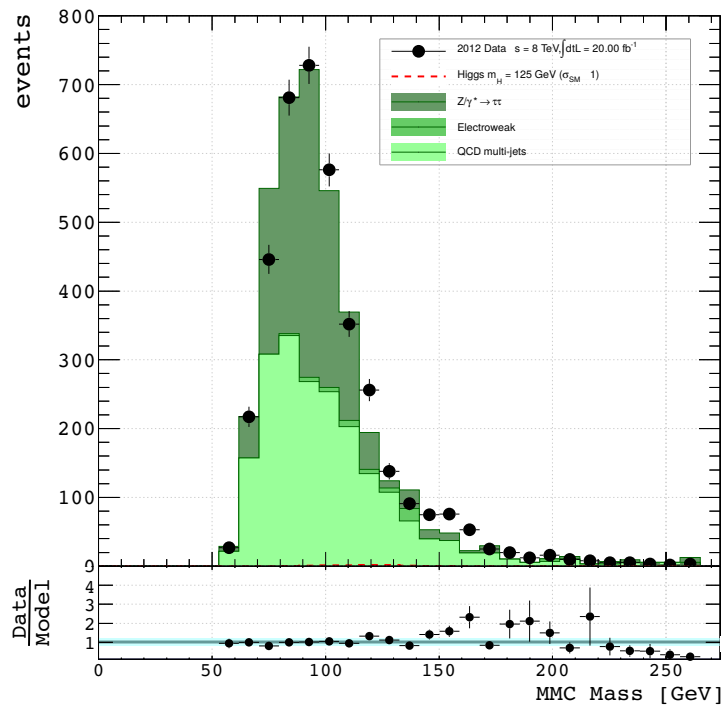
(b)

Figure 6.13: Mass plots showing all MC and signal contributions superimposed to data. a) Shows the reconstructed mass b) Shows the previous MMC method. Using events that where available use the calculated solution.
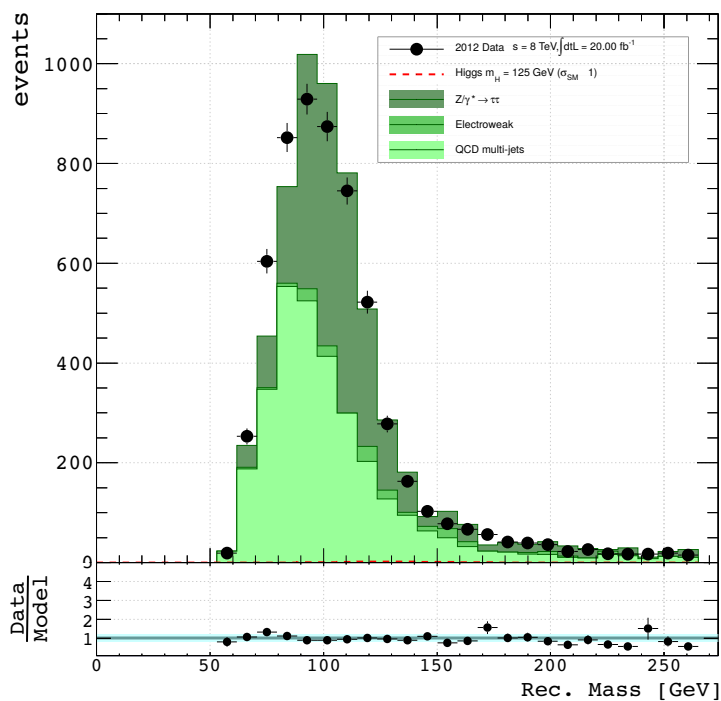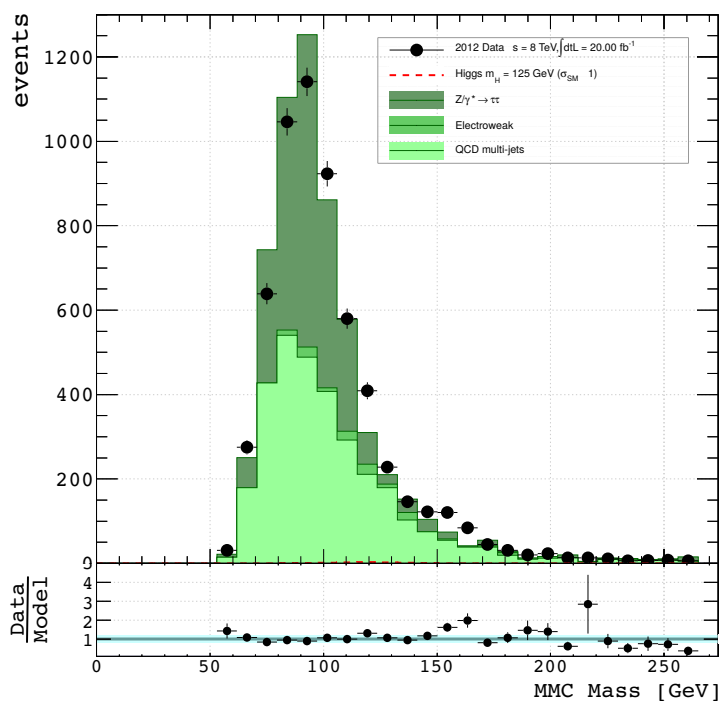
Figure 6.14: Mass plots showing all MC and signal contributions superimposed to data inside the mass region > 60 GeV. a) Shows the reconstructed mass using the vertex based MMC b) Shows the previous MMC method. Using only events that have had their vertices refitted.
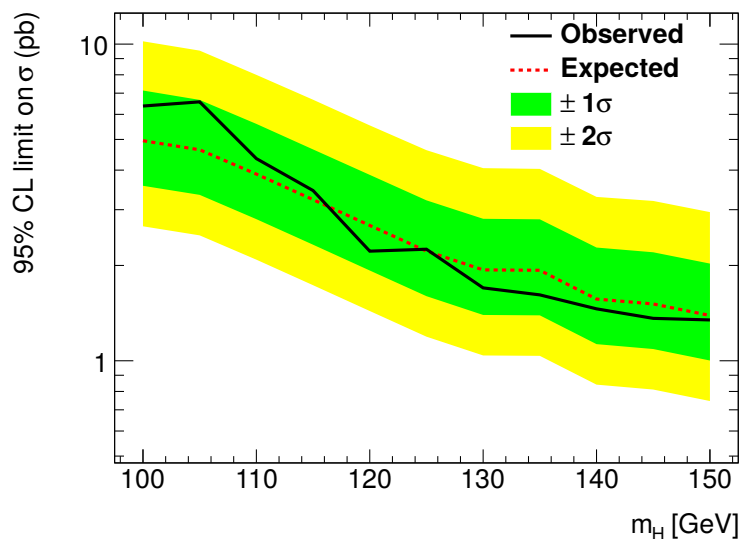
(a)
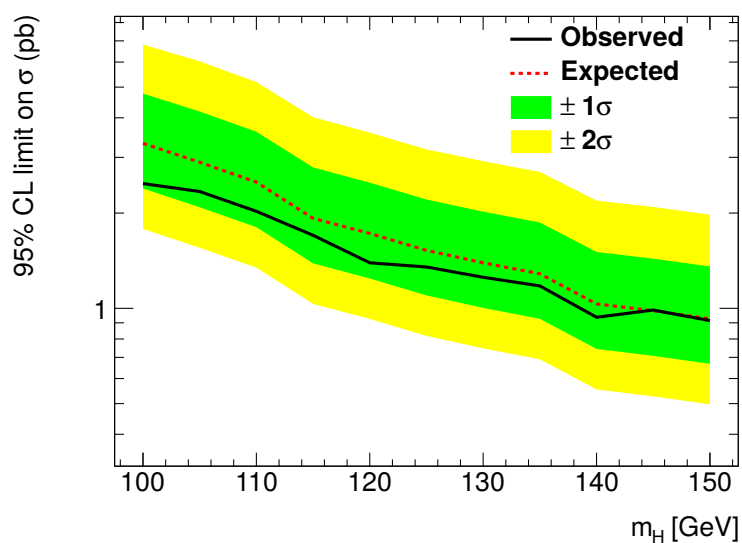
(b)

Figure 6.15: The mass limits showing up to $\pm 2\sigma$ for the full range of the $m_H = 100$ to $m_H = 150$, in the category where the calculated solution is used and if not a valid solution the vertex is refitted. a) Using the vertex based MMC b) is made with the previous MMC method.
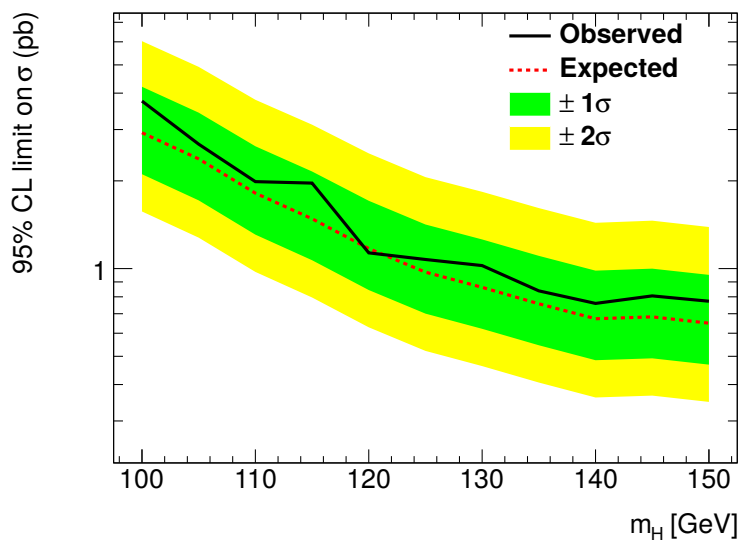
(a)
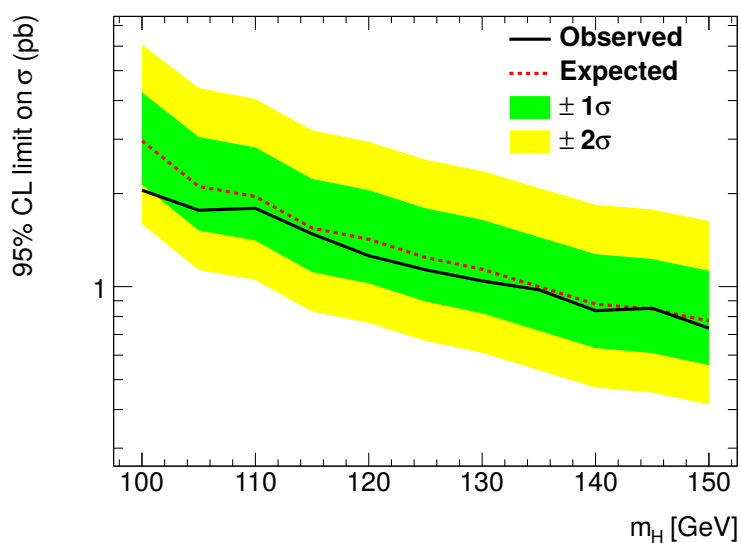
(b)

Figure 6.16: The mass limits showing up to $\pm 2\sigma$ for the full range of the $m_H = 100$ to $m_H = 150$, in the category where the vertex was always refitted. a) Using the vertex based MMC b) is made with the previous MMC method.

6.4.1 Recent Results from Other Analyses

The official $\tau\tau$ analysis is releasing its latest results from Run 1 of the LHC using the ATLAS experiment, that will now be briefly explained, using integrated luminosities of $4.5fb^{-1}$ and $20.3fb^{-1}$ at centre-of-mass energies of $\sqrt{s} = 7$ TeV and $\sqrt{s} = 8$ TeV respectively. All the combinations of leptonic and hadronic tau decay channels are included and event categories selecting both VBF and highly boosted $\tau\tau$ signatures are considered in a multivariate analysis. It was observed that an excess of events over the expected background signature from other Standard Model processes is found with an observed (expected) significance of 4.5 (3.5) standard deviations. This is consistent with being as a result of $H \to \tau\tau$ decays with $m_H = 125$ GeV. The measured signal strength, normalised to the Standard Model expectation for a Higgs boson of this mass is:

$$\mu = 1.38^{+0.26}_{-0.25}(\text{Stat.})^{+0.33}_{-0.26}(\text{Syst.}) \qquad (6.14)$$

This is consistent with the predicted Yukawa coupling strength of the Higgs boson in the Standard Model (section 2.7). For more information on this please see reference [99].

Chapter 7

Conclusion

The work outlined in this thesis was carried out for the high energy physics department at Lancaster University, during the period 2010 to 2014. During this time four main bodies of work were carried out, three of which were outlined in this thesis. Briefly, acceptance study for the $Z \to \tau\tau$ analysis, work to update the electron veto for the tau lepton identification, the development of a new vertex based missing mass calculator for 3-prong hadronically decaying tau leptons.

The cross-section (σ) for the $Z \to \tau\tau$ process can be calculated using the following formula:

$$\sigma^{fid}(Z \to \tau\tau) \times Br = \frac{N_{obs} - N_{bkg}}{C_Z \cdot \mathcal{L}} \qquad (7.1)$$

This is for any specific fiducial region, which with the introduction of the factor, A_Z, can be generalised for the entire detector:

$$\sigma(Z \to \tau\tau) \times Br = \frac{N_{obs} - N_{bkg}}{A_Z \cdot C_Z \cdot \mathcal{L}} \qquad (7.2)$$

The terms for both of these equations are outlined in section 5.6. The factor, A_Z was calculated using events from Monte Carlo simulations as the ratio of events at generator level whose $\tau\tau$ invariant mass, before Final State Radiation (FSR), lies within the mass window [66, 116] GeV, and the number of events at generator level that falls within the fiducial regions defined above. The A_Z factor accounts for events that migrate from outside the invariant mass window into

172

	$\tau_\mu\tau_h$	$\tau_e\tau_h$	$\tau_e\tau_\mu$
A_Z	0.0976 ± 0.0002(stat)	0.0687 ± 0.0002(stat)	0.0784 ± 0.0003(stat)
C_Z	0.1417 ± 0.0016(stat)	0.1009 ± 0.0013(stat)	0.1348 ± 0.0037(stat)

Table 7.1: Central values and Monte Carlo statistical uncertainty for the A_Z and C_Z factors [2].

the fiducial region. The central values for A_Z are determined using a Pythia [80] Monte Carlo sample generated with the modified LO PDF MRSTLO* [81]. The obtained values of the A_Z and C_Z factors, with their statistical uncertainties, are given for all three channels in Table 7.1.

This resulted in the following cross-sections for $Z \to \tau\tau$.

Final State	Fiducial cross section $\sigma^{fid}(Z \to \tau\tau) \times Br(\tau \to ...)$
$\tau_\mu\tau_h$	20.0 ± 0.3(stat)± 2.0(syst)± 0.7(lumi)pb
$\tau_e\tau_h$	15.9 ± 0.4(stat)± 2.0(syst)± 0.6(lumi)pb
$\tau_e\tau_\mu$	4.7 ± 0.4(stat)± 2.0(syst)± 0.6(lumi)pb

Final State	Total cross section $\sigma(Z \to \tau\tau, m_{inv}[66 - 116 GeV])$
$\tau_\mu\tau_h$	0.91 ± 0.01(stat)± 0.09(syst)± 0.03(lumi)pb
$\tau_e\tau_h$	1.00 ± 0.02(stat)± 0.13(syst)± 0.04(lumi)pb
$\tau_e\tau_\mu$	0.96 ± 0.03(stat)± 0.09(syst)± 0.04(lumi)pb

The electron veto is an important feature of tau identification, it allows for the characteristics of electrons that have been misidentified as taus to be rejected. The study that was performed was to update the definitions and performance for the 2012 tau identification performance paper. This was accomplished by training a Boosted Decision Tree (BDT) which is a form of Multi Variate Analysis (MVA), on $Z \to ee$ events to train for background and simulated $Z \to \tau\tau$ events for the signal. The efficiency for the electron veto and real electrons was compared between data and simulated events, with an integrated luminosity $\mathcal{L}_{int} = 5.8 fb^{-1}$. This was measured for all combinations of tau ID, electron veto and electron overlap removal. Within these selections, the efficiency was measured in six regions of $|\eta|$, four of which correspond directly to those that were used for training the electron veto and the remaining to the gap in the coverage of the Transition Radiation Tracker ($|\eta(e)| < 0.05$) and the end of the coverage of the offline

electron identification ($|\eta(e)| > 2.47$). The overall results of this measurement can be viewed in table 4.4. The overall aim of this was that the variables were optimised to be robust against increasing pile-up, which is present in this data period. The performance that is resultant from these identification algorithms show efficiencies which are independent of this pile up.

The vertex based MMC shows great potential. With the addition of the insertable B-layer (IBL) into the ATLAS detector, the performance of the vertex based MMC will drastically increase. The IBL will be located 3.3 cm from the beam axis (current pixel detector is 5 cm), it also has a much small pixel size ($50\mu m \times 250\mu m$ compared to the current $50\mu m \times 400\mu m$). This will massively increase the effectiveness of the vertex based MMC, whilst the previous methods will not be significantly affected. It should be noted that this is only a comparison for the 3-prong hadronically decaying taus, so can only be compared to other such things, which was shown in this thesis. This method performs just as well as the previous method that has been similarly constrained. Furthermore it should be noted that this method is entirely model independent, this means that in its calculation it does not rely on some probability distribution from an assumed model, that would be specific to each case. This is not the case for the previous MMC methods which do depend on some probability distributions. This is an important factor to consider for the upcoming run II of the LHC and the CP measurements that will take place, as these need to be model independent.

Additionally given more time it should have been possible to include a proper categorisation method, this would properly split the analysis up into the VBF and boosted categories present in the main analysis. This was not meant to be an analysis to supply an accurate measurement of the di-tau mass, that would have required more man power and time than was available. However it was a very good example of how well this algorithm performs. The plan for the future is to get it included in the official $H \to \tau\tau$ analysis to replace the current method. When this accomplished a much more thorough performance study can be performed.

Appendix A

Additional BDT plots for the MMC Solution Selection

Plots the detail the specific response from the BDT TMVA method that was used to select the correct solution for our MMC in the three different circumstances. The four solution, leading tau and subleading tau specific solutions.

A.1 Four Solutions
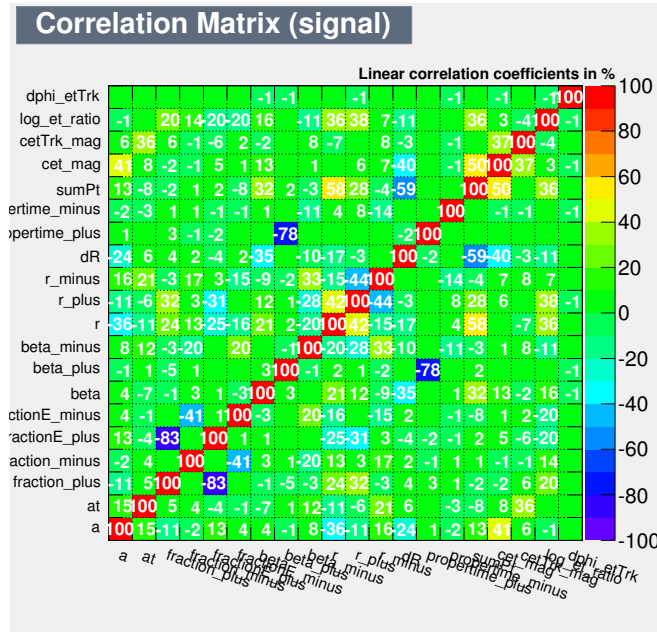
Figure A.1: Signal correlation matrix using the 4 solution method.
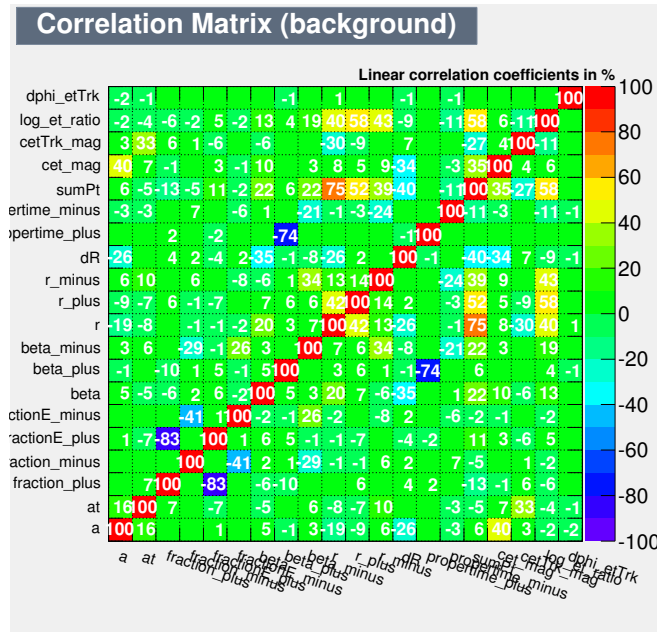
Figure A.2: Background correlation matrix using the 4 solution method.
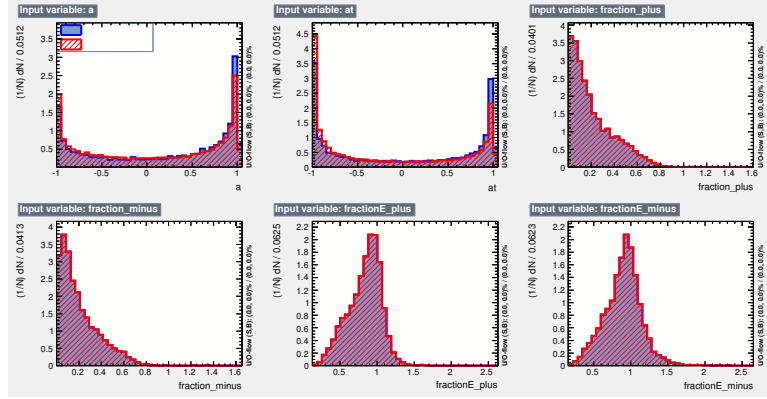
Figure A.3: Distributions of the variables used in the 4 solution method.
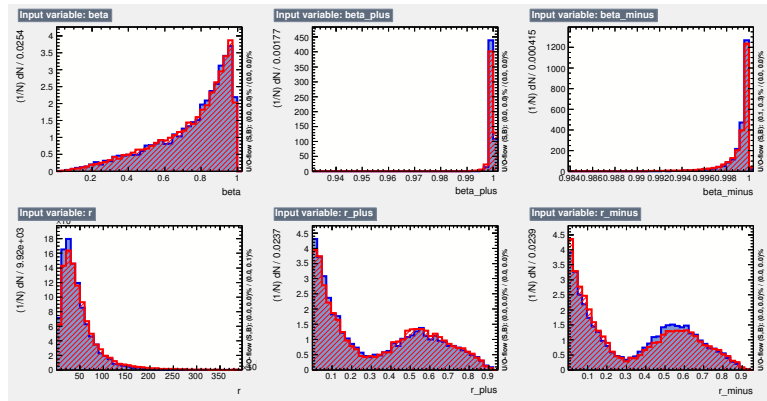
Figure A.4: Distributions of the variables used in the 4 solution method.
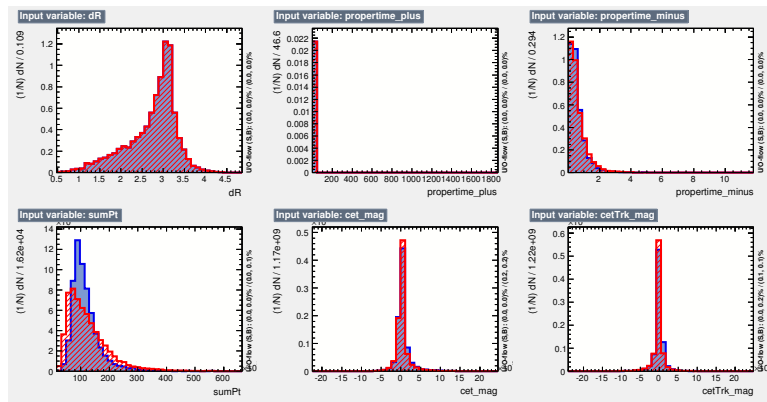
Figure A.5: Distributions of the variables used in the 4 solution method.
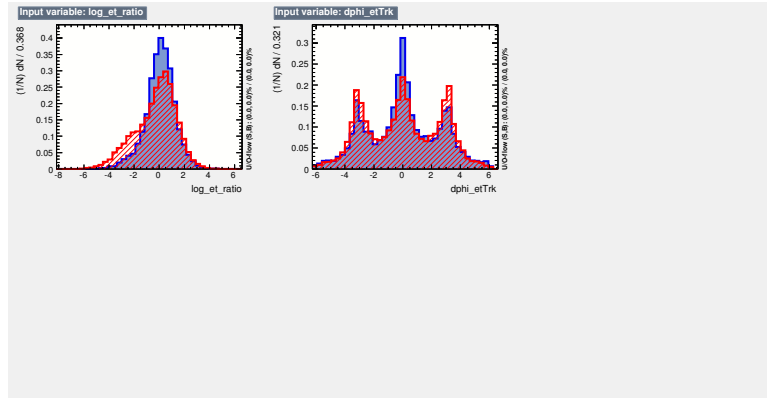
Figure A.6: Distributions of the variables used in the 4 solution method.

A.2 Leading Tau

Figure A.7: Signal correlation matrix using the 2 solution method focusing on the leading tau.

179

Figure A.8: Background correlation matrix using the 2 solution method focusing on the leading tau.

Figure A.9

Figure A.10: Distributions of the variables for the 2 solution method focusing on the leading tau.
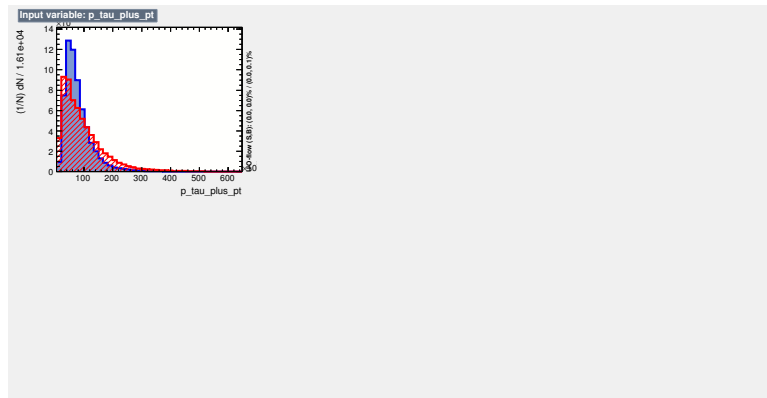
Figure A.11: Distributions of the variables for the 2 solution method focusing on the leading tau.

A.3   Subleading Tau
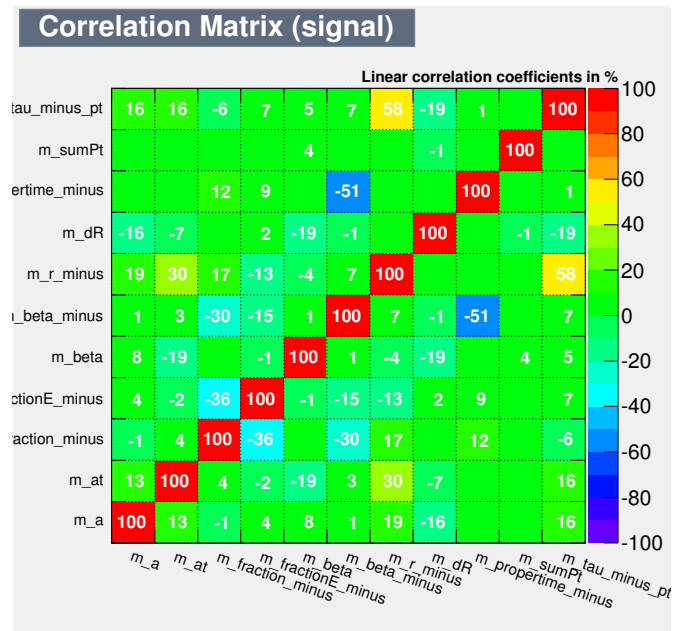
Figure A.12: Signal correlation matrix using the 2 solution method focusing on the subleading tau.
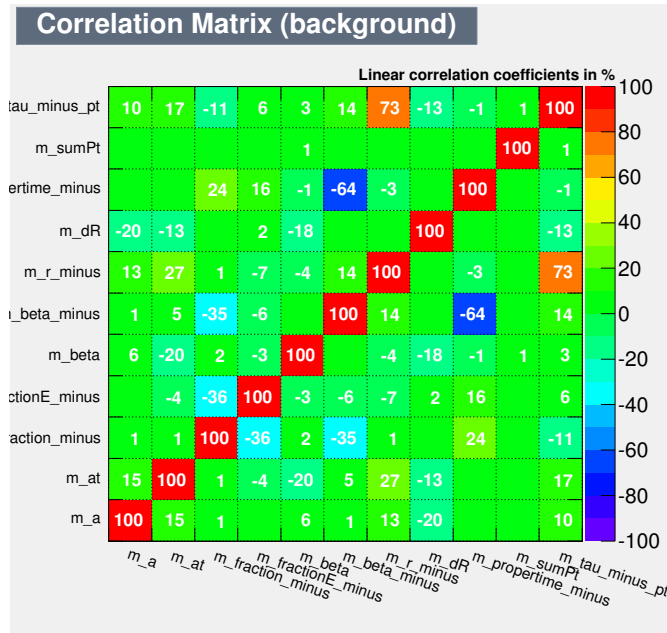
Figure A.13: Background correlation matrix using the 2 solution method focusing on the subleading tau.

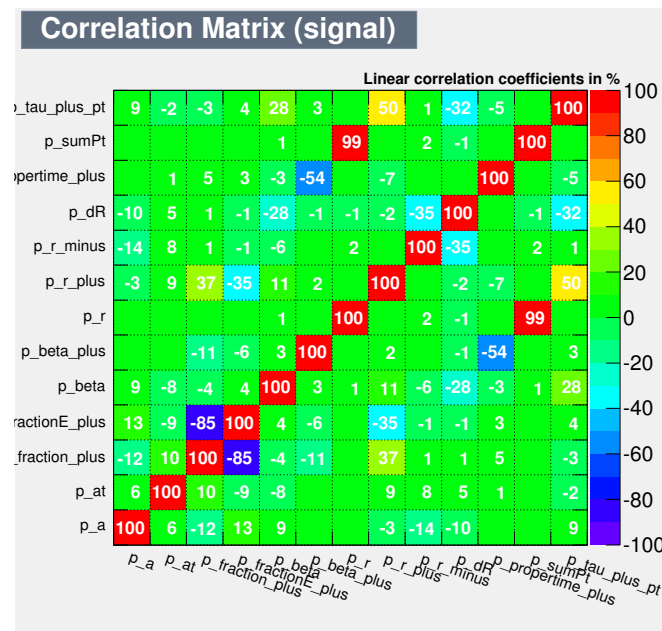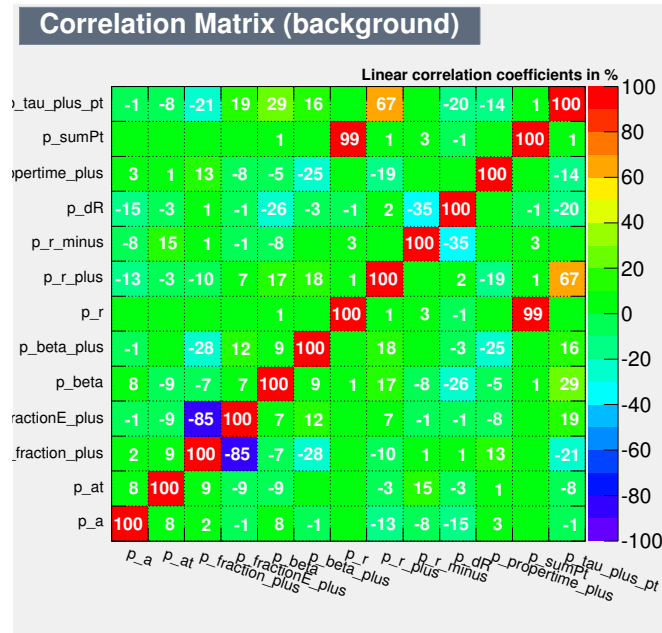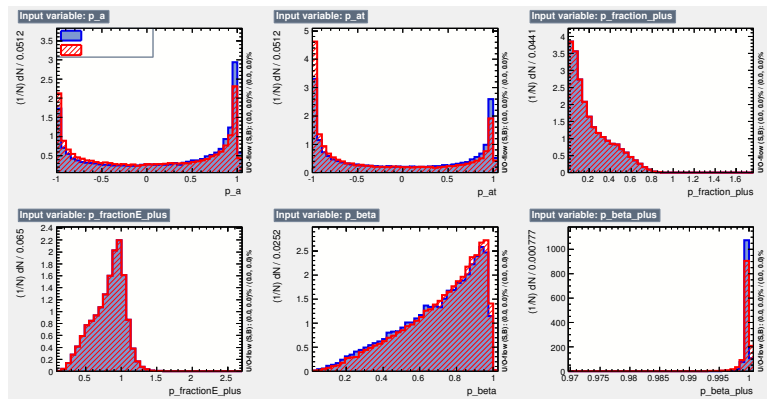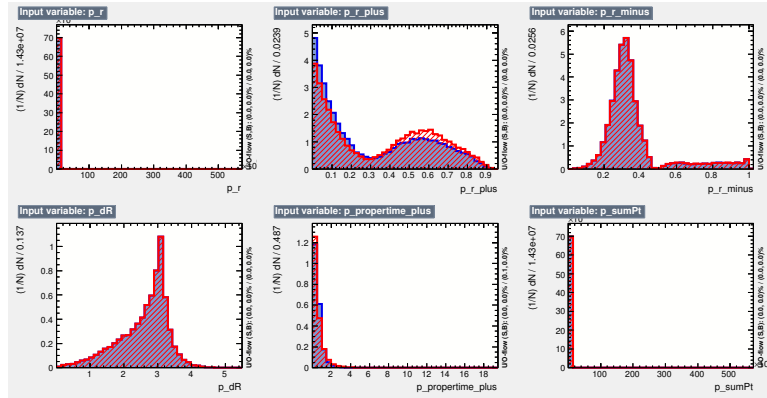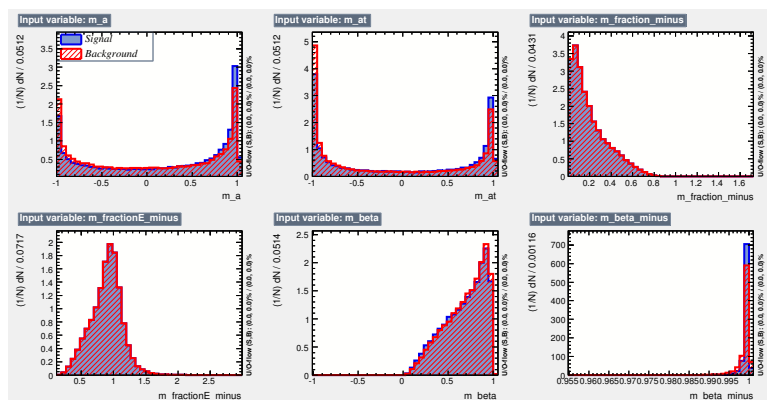**Figure A.14:** Distributions of the variables for the 2 solution method focusing on the subleading tau.
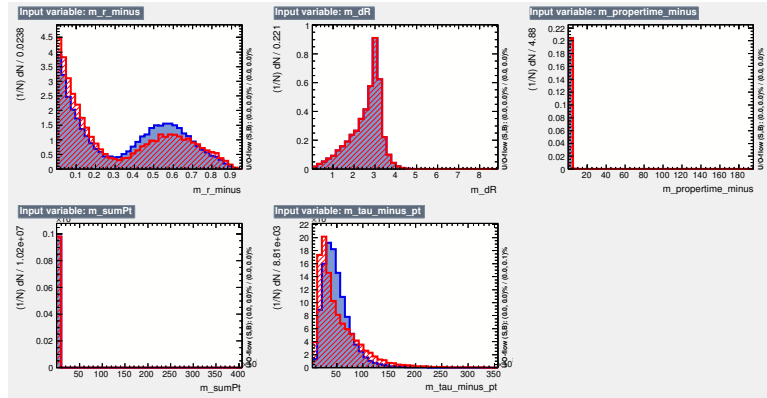
Figure A.15: Distributions of the variables for the 2 solution method focusing on the subleading tau.

Bibliography

[1] Identification of the Hadronic Decays of Tau Leptons in 2012 Data with the ATLAS Detector. Technical Report ATLAS-CONF-2013-064, CERN, Geneva, Jul 2013. xii, xiii, xiv, xix, 2, 73, 76, 77, 79, 85, 86, 87, 90, 92, 94, 96, 97, 98

[2] Z tau tau cross section measurement in proton-proton collisions at 7 TeV with the ATLAS experiment. (ATLAS-CONF-2012-006), 2012. xiv, xv, xvi, xix, xx, 2, 108, 110, 111, 112, 113, 114, 116, 118, 119, 121, 123, 127, 132, 136, 173

[3] G A Stewart, W B Breaden-Madden, H J Maddocks, T Harenberg, M Sandhoff, and B Sarrazin. ATLAS Job Transforms: A Data Driven Workflow Engine. *Journal of Physics: Conference Series*, 513(3):032094, 2014. 2

[4] Website, showcasing the standard model of particle physics. `http://www.stfc.ac.uk/2861.aspx`. Accessed: 2014-26-08. ix, 4

[5] S. L. Glashow. Partial symmetries of weak interactions. *Nucl. Phys.*, B 22:579, 1961. 6

[6] S. Weinberg. A Model of Leptons. *PRL*, 19:1264, 1967. 6

[7] A. Salam. *Elementary Particle Theory.* Almqvist and Wiksells, Stockholm, 1968. 6

[8] Peter W. Higgs. Spontaneous Symmetry Breakdown without Massless Bosons. *Phys.Rev.*, 145:1156–1163, 1966. 11

[9] Peter W. Higgs. Broken symmetries and the masses of gauge bosons. *Phys. Rev. Lett.*, 13:508–509, Oct 1964. 11

[10] Peter W. Higgs. Broken symmetries, massless particles and gauge fields. *Phys.Lett.*, 12:132–133, 1964. 11

[11] F. Englert and R. Brout. Broken symmetry and the mass of gauge vector mesons. *Phys. Rev. Lett.*, 13:321–323, Aug 1964. 11

[12] G. S. Guralnik, C. R. Hagen, and T. W. B. Kibble. Global conservation laws and massless particles. *Phys. Rev. Lett.*, 13:585–587, Nov 1964. 11

[13] Diagram of the higgs potential. `http://www.nature.com/nphys/journal/v7/n1/fig_tab/nphys1874_F1.html`. Accessed: 2014-31-06. ix, 12

[14] Abdelhak Djouadi. The Anatomy of electro-weak symmetry breaking. I: The Higgs boson in the standard model. *Phys.Rept.*, 457(LPT-ORSAY-05-17):1–216, 2008. 15, 18

[15] Julien Baglio. Phenomenology of the Higgs at the hadron colliders: from the Standard Model to Supersymmetry. (LPT-11-91), 2011. ix, 17

[16] R. Barate et al. Search for the standard model Higgs boson at LEP. *Phys.Lett.*, B565(CERN-EP-2003-011):61–75, 2003. ix, 18, 19

[17] Combined CDF and D0 Search for Standard Model Higgs Boson Production with up to 10.0 fb^{-1} of Data. (FERMILAB-CONF-12-065-E, CDF-NOTE-10806, D0-NOTE-6303), 2012. x, 19, 20

[18] John Ellis, Mary K. Gaillard, and Dimitri V. Nanopoulos. A Historical Profile of the Higgs Boson. (KCL-PH-TH-2012-04, LCTS-2012-01, CERN-PH-TH-2012-009, LBNL, UCB-PTH-12-01, ACT-1-12, MIFPA-12-01), 2012. x, 21

[19] M. Baak, M. Goebel, J. Haller, A. Hoecker, D. Ludwig, et al. Updated Status of the Global Electroweak Fit and Constraints on New Physics. *Eur.Phys.J.*, C72(DESY-11-107, CERN-OPEN-2011-033):2003, 2012. x, 22

[20] Website for the higgs cross section group. `https://twiki.cern.ch/twiki/bin/view/LHCPhysics/CrossSectionsFigures`. Accessed: 2014-02-07. x, 24, 25, 29

[21] X. Ruan and Z. Zhang. Impact on the Higgs Production Cross Section and Decay Branching Fractions of Heavy Quarks and Leptons in a Fourth Generation Model. (LAL-11-109), 2011. x, 28, 29

[22] A. Denner, S. Dittmaier, A. Muck, G. Passarino, M. Spira, et al. Higgs Production and Decay with a Fourth Standard-Model-Like Fermion Generation. *Eur.Phys.J.*, C72(FR-PHENO-2011-022, MPP-2011-135, PSI-PR-11-03, TTK-11-57):1992, 2012. 29

[23] T.D. Lee. A Theory of Spontaneous T Violation. *Phys.Rev.*, D8:1226–1239, 1973. 29

[24] Fatemeh Arbabifar, Sahar Bahrami, and Mariana Frank. Neutral Higgs Bosons in the Higgs Triplet Model with nontrivial mixing. *Phys.Rev.*, D87(1):015020, 2013. 29

[25] Georges Aad et al. Observation of a new particle in the search for the Standard Model Higgs boson with the ATLAS detector at the LHC. *Phys.Lett.*, B716(CERN-PH-EP-2012-218):1–29, 2012. 30

[26] Measurements of the properties of the Higgs-like boson in the two photon decay channel with the ATLAS detector using 25 fb^{-1} of proton-proton collision data. (ATLAS-CONF-2013-012, ATLAS-COM-CONF-2013-015), 2013. 30

[27] Serguei Chatrchyan et al. Searches for Higgs bosons in pp collisions at sqrt(s) = 7 and 8 TeV in the context of four-generation and fermiophobic models. *Phys.Lett.*, B725(CMS-HIG-12-013, CERN-PH-EP-2013-011):36–59, 2013. 30

[28] Search for charged Higgs bosons in the τ+jets final state with pp collision data recorded at $\sqrt{s} = 8$ TeV with the ATLAS experiment. Technical Report ATLAS-CONF-2013-090, CERN, Geneva, Aug 2013. 30

[29] Search for Neutral MSSM Higgs bosons in $sqrts = 7$ TeV pp collisions at ATLAS. Technical Report ATLAS-CONF-2012-094, CERN, Geneva, Jul 2012. 30

[30] Measurements of the Higgs boson production and decay rates and coupling strengths using pp collision data at s = 7 and 8 TeV in the ATLAS experiment. Technical Report ATLAS-CONF-2015-007, CERN, Geneva, Mar 2015. x, 31

[31] Georges Aad et al. Identification and energy calibration of hadronically decaying tau leptons with the ATLAS experiment in pp collisions at $\sqrt{s}$=8 TeV. (CERN-PH-EP-2014-227), 2014. 162

[32] Vardan Khachatryan et al. Precise determination of the mass of the Higgs boson and tests of compatibility of its couplings with the standard model predictions using proton collisions at 7 and 8 TeV. (CMS-HIG-14-009, CERN-PH-EP-2014-288), 2014. xi, 32

[33] CERN. ATLAS: Detector and physics performance technical design report. Volume 1. (CERN-LHCC-99-14, ATLAS-TDR-14), 1999. xi, 34, 42, 46, 47, 48

[34] The cern accelerator complex. `"http://te-epc-lpc.web.cern.ch/te-epc-lpc/machines/lhc/general.stm"`, 2008. xi, 37

[35] G. Aad et al. Studies of the performance of the ATLAS detector using cosmic-ray muons. *Eur.Phys.J.*, C71:1593, 2011. xi, 41

[36] CERN. ATLAS: Detector and physics performance technical design report. Volume 2. (CERN-LHCC-99-15, ATLAS-TDR-15), 1999. 42

[37] Collaboration, ATLAS. The ATLAS Inner Detector commissioning and calibration. *Eur. Phys. J.*, C 70:787–821, 2010. xi, 43

[38] M.S. Alam et al. ATLAS pixel detector: Technical design report. (CERN-LHCC-98-13), 1998. 43

[39] A. Ahmad, Z. Albrechtskirchinger, P.P. Allport, J. Alonso, L. Andricek, et al. The Silicon microstrip sensors of the ATLAS semiconductor tracker. *Nucl.Instrum.Meth.*, A578:98–118, 2007. 43

[40] Joao Pequenao. Computer Generated image of the ATLAS calorimeter. Mar 2008. xi, 45

[41] A. T. L. A. S. Collaboration. The atlas experiment at the cern large hadron collider. *JINST*, 3, 2008. xi, 49

[42] Antonio Salvucci. Measurement of muon momentum resolution of the ATLAS detector. *EPJ Web Conf.*, 28:12039, 2012. xii, 50

[43] Per Hansson Adrian. The ATLAS b-Jet Trigger. Technical Report ATL-DAQ-PROC-2011-035, CERN, Geneva, Nov 2011. Comments: 4 pages, 6 figures, conference proceedings for PIC2011. xii, 52

[44] Diagram showing the grid tiers of atlas. `http://www.isgtw.org/feature/how-grid-computing-helped-cern-hunt-higgs`. Accessed: 2014-02-06. xii, 54

[45] ATLAS Collaboration. ATHENA, The ATLAS Common Framework - Developer Guide. 54

[46] Rene Brun and Fons Rademakers. Root - an object oriented data analysis framework, proceedings aihenp'96 workshop, lausanne, sep. 1996, nucl. inst. and meth. in phys. res. a 389 (1997) 81-86. See also http://root.cern.ch/. 54

[47] K. Nakamura et al. Review of particle physics. *J.Phys.*, G37(FERMILAB-PUB-10-665-PPD):075021, 2010. 55, 133, 144

[48] Torbjorn Sjostrand, Stephen Mrenna, and Peter Z. Skands. A Brief Introduction to PYTHIA 8.1. *Comput.Phys.Commun.*, 178(CERN-LCGAPP-2007-04, LU-TP-07-28, FERMILAB-PUB-07-512-CD-T):852–867, 2008. 57, 141

[49] Michelangelo L. Mangano, Mauro Moretti, Fulvio Piccinini, Roberto Pittau, and Antonio D. Polosa. Alpgen, a generator for hard multiparton processes in hadronic collisions. *JHEP*, 0307(CERN-TH-2002-129, FTN-T-2002-06):001, 2003. 57, 101, 147

[50] G. Aad et al. The atlas simulation infrastructure. *Eur.Phys.J.*, C70:823–874, 2010. 57

[51] G. Folger and J.P. Wellisch. String parton models in GEANT4. *eConf*, C0303241(CHEP-2003-MOMT007):MOMT007, 2003. 57

[52] Bo Andersson, G. Gustafson, and B. Nilsson-Almqvist. A Model for Low p(t) Hadronic Reactions, with Generalizations to Hadron - Nucleus and Nucleus-Nucleus Collisions. *Nucl.Phys.*, B281(LU-TP-86-3):289, 1987. 57

[53] Matteo Cacciari, Gavin P. Salam, and Gregory Soyez. The Anti-k(t) jet clustering algorithm. *JHEP*, 0804(LPTHE-07-03):063, 2008. 58

[54] W. Lampl, S. Laplace, D. Lelas, P. Loch, H. Ma, et al. Calorimeter clustering algorithms: Description and performance. (ATL-LARG-PUB-2008-002, ATL-COM-LARG-2008-003), 2008. 58

[55] T. Barillari et al. Local hadronic calibration. (ATL-LARG-PUB-2009-001-2, ATL-COM-LARG-2008-006), 2009. 58

[56] Performance of the ATLAS Inner Detector Track and Vertex Reconstruction in the High Pile-Up LHC Environment. (ATLAS-CONF-2012-042, ATLAS-COM-CONF-2012-014), 2012. 59

[57] Performance of the Reconstruction and Identification of Hadronic Tau Decays in ATLAS with 2011 Data. (ATLAS-CONF-2012-142, ATLAS-COM-CONF-2012-080), 2012. xii, 60, 62

[58] The ATLAS collaboration. Determination of the tau energy scale and the associated systematic uncertainty in proton-proton collisions at $\sqrt{s} = 8$ TeV with the ATLAS detector at the LHC in 2012. (ATLAS-CONF-2013-044, ATLAS-COM-CONF-2013-040), 2013. 63, 64

[59] E. Abat et al. The ATLAS Transition Radiation Tracker (TRT) proportional drift tube: Design and performance. *JINST*, 3:P02013, 2008. 68

[60] TMVA - Toolkit for Multivariate Data Analysis. http://tmva.sourceforge.net/, Jan 2011. version 4.0.4 (available as part of ROOT version 5.26). 72, 75

[61] Reconstruction, Energy Calibration, and Identification of Hadronically Decaying Tau Leptons. Technical Report ATLAS-CONF-2011-077, CERN, Geneva, May 2011. 74

[62] Georges Aad et al. Electron performance measurements with the ATLAS detector using the 2010 LHC proton-proton collision data. *Eur.Phys.J.*, C72(CERN-PH-EP-2011-117):1909, 2012. 95, 103, 128, 129

[63] A. T. L. A. S. Collaboration. Measurement of the z to $\tau\tau$ cross section with the atlas detector. *Phys.Rev.*, D84:112006–112006, 2011/// 2011. 100

[64] Serguei Chatrchyan et al. Measurement of the inclusive z cross section via decays to tau pairs in *pp* collisions at 7 tev. *JHEP*, 1108(CERN-EP-PH-2011-035, CMS-EWK-10-013):117, 2011. 100

[65] J. Apostolakis, M. Asai, A. G. Bogdanov, H. Burkhardt, G. Cosmo, S. Elles, G. Folger, V. M. Grichine, P. Gumplinger, A. Heikkinen, I. Hrivnacova, V. N. Ivanchenko, J. Jacquemier, T. Koi, R. P. Kokoulin, M. Kossov, H. Kurashige, I. McLaren, O. Link, M. Maire, W. Pokorski, T. Sasaki, N. Starkov, L. Urban, and D. H. Wright. Geometry and physics of the geant4 toolkit for high and medium energy applications. *Radiation Physics and Chemistry*, 78(10):859–873, 2009. Workshop on Use of Monte C4arlo Techniques for Design and Analysis of Radiation Detectors. 101, 147

[66] G. Corcella, I. G. Knowles, G. Marchesini, S. Moretti, K. Odagiri, et al. Herwig 6: An event generator for hadron emission reactions with interfering gluons (including supersymmetric processes). *JHEP*, 0101(CAVENDISH-HEP-99-03, CERN-TH-2000-284, RAL-TR-2000-048):010, 2001. 101, 147

[67] J. M. Butterworth, Jeffrey R. Forshaw, and M. H. Seymour. Multiparton interactions in photoproduction at hera. *Z.Phys.*, C72(CERN-TH-96-82, M-C-TH-96-05, UCL-HEP-96-02):637–646, 1996. 101, 147

[68] Pavel M. Nadolsky, Hung-Liang Lai, Qing-Hong Cao, Joey Huston, Jon Pumplin, et al. Implications of cteq global analysis for collider observables. *Phys.Rev.*, D78(MSUHEP-080125, UCRHEP-T447):013004, 2008. 101, 127, 130, 147

[69] First tuning of herwig/jimmy to atlas data. (ATL-PHYS-PUB-2010-014, ATL-COM-PHYS-2010-858), 2010. 101, 147

[70] Stefano Catani, Leandro Cieri, Giancarlo Ferrera, Daniel de Florian, and Massimiliano Grazzini. Vector boson production at hadron colliders: a fully exclusive qcd calculation at nnlo. *Phys.Rev.Lett.*, 103:082001, 2009. 101, 135, 147

[71] Stefano Frixione and Bryan R. Webber. Matching nlo qcd computations and parton shower simulations. *JHEP*, 0206(CAVENDISH-HEP-02-01, LAPTH-905-02, GEF-TH-2-2002):029, 2002. 101, 147

[72] S. Jadach, Z. Was, R. Decker, and Johann H. Kuhn. The tau decay library tauola: Version 2.4. *Comput.Phys.Commun.*, 76(CERN-TH-6793-93):361–380, 1993. 101, 141, 147

[73] Piotr Golonka and Zbigniew Was. PHOTOS Monte Carlo: A Precision tool for QED corrections in Z and W decays. *Eur.Phys.J.*, C45(IFJPAN-V-05-01, CERN-PH-TH-2005-091):97–107, 2006. 101, 147

[74] Georges Aad et al. Measurement of the inclusive W and Z/gamma cross sections in the electron and muon decay channels in pp collisions at 7 TeV with the ATLAS detector. *Phys.Rev.*, D85(CERN-PH-EP-2011-143):072004, 2012. 103, 135

[75] Matteo Cacciari and Gavin P. Salam. Dispelling the N^3 myth for the k_t jet-finder. *Phys.Lett.*, B641(LPTHE-05-32):57–61, 2006. 103

[76] Performance of the ATLAS tau trigger in 2011. Technical Report ATLAS-CONF-2013-006, CERN, Geneva, Jan 2013. 104

[77] Performance of the Reconstruction and Identification of Hadronic Tau Decays with ATLAS. Technical Report ATLAS-CONF-2011-152, CERN, Geneva, Nov 2011. xv, 104, 115, 116, 117, 118, 124, 129

[78] Measurement of the Mis-identification Probability of Leptons from Hadronic Jets and from Electrons. (ATLAS-CONF-2011-113, ATLAS-COM-CONF-2011-067), 2011. 123

[79] ATLAS Collaboration. Measurement of the z to cross section with the atlas detector. *Phys.Rev.*, D84:112006 – 112006, 2011/// 2011. 126

[80] Torbjorn Sjostrand, Stephen Mrenna, and Peter Z. Skands. PYTHIA 6.4 Physics and Manual. *JHEP*, 0605(FERMILAB-PUB-06-052-CD-T, LU-TP-06-13):026, 2006. 127, 136, 173

[81] A. Sherstnev and R.S. Thorne. Parton Distributions for LO Generators. *Eur.Phys.J.*, C55(CAVENDISH-HEP-2007-12):553–575, 2008. 127, 136, 173

[82] Muon reconstruction efficiency in reprocessed 2010 LHC proton-proton collision data recorded with the ATLAS detector. Technical Report ATLAS-CONF-2011-063, CERN, Geneva, Apr 2011. 128

[83] A. T. L. A. S. Collaboration. Jet energy measurement with the atlas detector in proton-proton collisions at 7 tev. *http://arxiv.org/abs/1112.6426v1arXiv:1112.6426v1*, 2011. 129

[84] F.D. Aaron et al. Combined measurement and qcd analysis of the inclusive e+- p scattering cross sections at hera. *JHEP*, 1001(DESY-09-158):109, 2010. 130

[85] G. Aad et al. Luminosity Determination in pp Collisions at sqrt(s) = 7 TeV using the ATLAS Detector in 2011. (ATLAS-CONF-2011-116, ATLAS-COM-CONF-2011-130), 2011. 131

[86] Louis Lyons, Duncan Gibaut, and Peter Clifford. How to Combine Correlated Estimates of a Single Physical Quantity. *Nucl.Instrum.Meth.*, A270(PRINT-88-0048 (OXFORD), OXFORD-NP-5-88):110, 1988. 133, 134

[87] A. Valassi. Combining correlated measurements of several different physical quantities. *Nucl.Instrum.Meth.*, A500:391–405, 2003. 133

[88] Ryan Gavin, Ye Li, Frank Petriello, and Seth Quackenbush. FEWZ 2.0: A code for hadronic Z production at next-to-next-to-leading order. *Comput.Phys.Commun.*, 182(ANL-HEP-PR-10-60):2388–2403, 2011. 135

[89] Kirill Melnikov and Frank Petriello. Electroweak gauge boson production at hadron colliders through O(alpha(s)**2). *Phys.Rev.*, D74(UH-511-1092-06):114017, 2006. 135

[90] A. Elagin, P. Murat, A. Pranko, and A. Safonov. A New Mass Reconstruction Technique for Resonances Decaying to di-tau. *Nucl.Instrum.Meth.*, A654(FERMILAB-PUB-11-918-PPD):481–489, 2011. xvi, 141, 142, 143

[91] V. Kostyukhin. VKalVrt - package for vertex reconstruction in AT-LAS. (ATL-PHYS-2003-031, ATL-COM-PHYS-2003-033, CERN-ATL-PHYS-2003-031), 2003. 143

[92] F. James. MINUIT Function Minimization and Error Analysis: Reference Manual Version 94.1. (CERN-D-506, CERN-D506), 1994. 146

[93] Tau working group recommendations. https://twiki.cern.ch/twiki/bin/view/AtlasProtected /TauRecommendationsWinterConf2013. 151, 161, 165

[94] jet working group recommendations. https://twiki.cern.ch/twiki/bin/viewauth /AtlasProtected/JetUncertainties. 162

[95] Jet resolution working group. https://twiki.cern.ch/twiki/bin/viewauth /AtlasProtected/ApplyJetResolutionSmearing. 162

[96] Georges Aad et al. Improved luminosity determination in *pp* collisions at $\sqrt{s}$ = 7 TeV using the ATLAS detector at the LHC. *Eur.Phys.J.*, C73(CERN-PH-EP-2013-026):2518, 2013. 162

[97] Evidence for Higgs Boson Decays to the $\tau^+\tau^-$ Final State with the ATLAS Detector. Technical Report ATLAS-CONF-2013-108, CERN, Geneva, Nov 2013. 164

[98] Limit plot workspace. "https://svnweb.cern.ch/trac/atlasphys/browser/Physics/Higgs/HSG4/software/hadhad/MultiVariateAnalysis/". 165

[99] Georges Aad et al. Identification and energy calibration of hadronically decaying tau leptons with the ATLAS experiment in pp collisions at $\sqrt{s}$=8 TeV. (CERN-PH-EP-2014-227), 2014. 171